ΠΑΝΕΠΙΣΤΗΜΙΟ ΚΡΗΤΗΣ
UNIVERSITY OF CRETE

Development of implant treatments with neuroprotective and neurogenic activities for Central Nervous System injuries

Ανάπτυξη εμφυτευμάτων με νευροπροστατευτικές και νευρογεννητικές ιδιότητες ως θεραπεία σε βλάβες του Κεντρικού Νευρικού Συστήματος

PhD Thesis

Konstantina Georgelou

May 2023

*Creative****Commons

Attribution-ShareAlike: This license allows the user to share and adapt this material under the following terms: (a) Attribution — You must give appropriate credit, provide a link to the license, and indicate if changes were made. You may do so in any reasonable manner, but not in any way that suggests the licensor endorses you or your use. (b) ShareAlike — If you remix, transform, or build upon the material, you must distribute your contributions under the same license as the original.

Αναφορά-Παρόμοια Διανομή (CC BY-SA): Η άδεια αυτή επιτρέπει στο χρήστη να χρησιμοποιεί, μοιράζεται και δημιουργεί παράγωγα έργα επί του αδειοδοτούμενου περιεχομένου και να το διαμοιράζεται με την προϋπόθεση να κάνει αναφορά στο δημιουργό, ή το δικαιούχο ή/και το φορέα που κάνει το περιεχόμενο διαθέσιμο καθώς επίσης και να μοιράζεται οποιοδήποτε νέο περιεχόμενο δημιουργεί με βάση το αδειοδοτημένο περιεχόμενο (π.χ. μια διασκευή ή μια μετάφραση) με την ίδια άδεια που έλαβε το αρχικό περιεχόμενο (δηλαδή την CreativeCommons Αναφορά Παρόμοια Διανομή).

This thesis was conducted at the Department of Pharmacology at School of Medicine at University of Crete and at Neural Tissue Engineering Laboratory at Institute of Molecular Biology & Biotechnology (IMBB), Foundation for Research & Technology – Hellas (FORTH).

The implementation of the thesis was co-financed by Greece and the European Union (European Social Fund-ESF) through the Operational Programme «Human Resources Development, Education and Lifelong Learning» in the context of the Act "Enhancing Human Resources Research Potential by undertaking a Doctoral Research" Sub-action 2: IKY Scholarship Programme for PhD candidates in the Greek Universities».

Moreover, this thesis was financially supported by the Hellenic Foundation for Research and Innovation (HFRI) and the General Secretariat for Research and Technology (GSRT) under grand agreement No 1635.

Konstantina Georgelou was also awarded scholarship by Maria Michail Manassaki Foundation for the 3rd year of PhD as well as EMBO Short-term Fellowship for 2-month visit at Grenoble Institute of Neuroscience.

ΠΑΝΕΠΙΣΤΗΜΙΟ ΚΡΗΤΗΣ
UNIVERSITY OF CRETE

FORTH
INSTITUTE OF MOLECULAR BIOLOGY & BIOTECHNOLOGY

Ευρωπαϊκή Ένωση
European Social Fund

Operational Programme
Human Resources Development, Education and Lifelong Learning
Co-financed by Greece and the European Union

ΕΣΠΑ 2014-2020

H.F.R.I.
Hellenic Foundation for Research & Innovation

GSRI
GENERAL SECRETARIAT FOR RESEARCH AND INNOVATION

EMBO

Advisory Committee

- **Achille Gravanis**, Professor, School of Medicine, University of Crete
- **Domna Karagogeos**, Professor, School of Medicine, University of Crete
- **Ioannis Zacharakis**, Principal Researcher, Institute of Electronic Structure and Laser (IESL), Foundation for Research & Technology – Hellas (FORTH)

Examination Committee

- **Achille Gravanis**, Professor, School of Medicine, University of Crete
- **Domna Karagogeos**, Professor, School of Medicine, University of Crete
- **Ioannis Zacharakis**, Principal Researcher, Institute of Electronic Structure and Laser (IESL), Foundation for Research & Technology – Hellas (FORTH)
- **Ioannis Charalampopoulos**, Associate Professor, School of Medicine, University of Crete
- **Kyriaki Thermos**, Professor, School of Medicine, University of Crete
- **Marina Vidaki**, Assistant Professor, School of Medicine, University of Crete
- **Dimitrios Tzeranis**, Lecturer, Department of Mechanical & Manufacturing Engineering, University of Cyprus

Acknowlegments

This thesis would not have been possible without the help and support of the people to whom I would like to express my gratitude.

I would like to thank Prof. Achille Gravanis and Ioannis Charalampopoulos who gave me the opportunity to be part of their research group, become more qualified in the field and develop my scientific career.

Many thanks to my thesis supervisor Dr. Dimitrios Tzeranis for the sharing of knowledge and practical skills as well as our prosperous scientific discussions, his trust, support and advice.

I would also like to thank Prof. Domna Karagogeos and Dr. Ioannis Zacharakis for being members of my advisory committee, as well as Prof. Kyriaki Thermos and Marina Vidaki for being members of my examination committee.

Thanks for the great collaboration to all the ones who helped me to proceed and complete the various projects of my thesis: Dr. Kanelina Karali, Dr. Maria Savvaki, Erika Saridaki, Xenofon Mallios, Fei Bampoula, Iro Papagiannaki, Fereniki Moschogiannaki and Chrysa Apostolidou. In addition, thanks to the rest of the members of the research group for the good atmosphere, their help and cooperation: Dr. Konstantina Chanoumidou, Ioanna Zota, Despoina Charou, Thanasis Rogdakis, Marianna Papadopoulou, Alexandros Tsimpolis and Maria Kokkali. Moreover, thanks to all the ones who helped me being part of IMBB, facilitating my everyday life there starting from administrative help till experimental procedures, such as the animal facility staff.

I would also like to acknowledge the Foundation of Maria Michail Manassaki and the IKY Scholarship Programme in the award of scholarships that provided me with the necessary financial support during my PhD thesis as well as EMBO that provided me with the Short-term Fellowship giving me the opportunity to visit Grenoble Institute of Neuroscience.

Most importantly, I would like to thank the persons that were by my side all this period: my brothers Giorgos and Dimitris, my cousins Constantina and Nota, and my friends Victoria, Katerina, Artemis and Danae. They all listened to me, supported and advised me as well as they shared with me unforgettable moments that were precious in order to cope with my tiredness, anxiety or any disappointments after the working hours.

Last but not least, my parents deserve special thanks for their constant support, trust, love and encouragement that enabled me to create my personality, follow my dreams and complete all the steps of my academic career till now. And of course, I am grateful to Leonidas, the one who is every moment by my side, made me believe into myself and gave me strength to complete the present thesis.

Heraklion, May 2023

Konstantina Georgelou

TABLE OF CONTENTS

I. Introduction 1

1. Central Nervous System 2

1.1. Eye Anatomy and Physiology 2

1.2. Spinal Cord Anatomy and Physiology 4

2. The Pathophysiology of Central Nervous System Injury 5

2.1. Overview 5

2.2. Inability of Axonal Regeneration 7

3. Optic Nerve Injury 8

3.1. Traumatic Optic Neuropathy & Current Therapies 8

3.2. Animal Models in Optic Nerve Injury Research 8

4. Spinal Cord Injury 10

4.1. Traumatic Spinal Cord Injury & Current Therapies 10

4.2. Animal Models in Spinal Cord Injury Research 11

5. Therapeutic Approaches for Central Nervous System Injuries 13

5.1. Molecular therapies 14

5.1.1.Overview 14

5.1.2.Neurotrophins 16

5.1.3.Microneurotrophins 19

5.2. Stem Cell therapies 20

5.2.1.Overview 20

5.2.2.Neural Stem Cells 22

5.3. Biomaterials 23

5.3.1.Overview 23

5.3.2.Porous Collagen-based Scaffolds 24

5.4. From Preclinical Studies to Effective Treatments for Central Nervous System Injuries 24

II. Aim of the Thesis 26

III. Materials and methods 28

1. Animals 29

2. Scaffold Fabrication 29

3. Primary Neural Stem Cell Isolation and Culture 29

4. Neural Stem Cell *In Vitro* Proliferation Assay 30

5. Neural Stem Cell *In Vitro* Differentiation assay 30
6. Immunocytochemistry and Image Processing of Neural Stem Cell Samples 30
7. Adult Retina Explant Isolation and Culture 32
8. Adult Retina Explant Survival and Axonal Elongation Assays 32
9. Immunostaining of Adult Retina Explant Cultures 32
10. Optic Nerve Crush Model 33
11. Optomotor Response Assay 34
12. Evaluation of BNN27 Delivery in Eye Tissues via Mass Spectrometry 35
13. Eye Tissue Collection and Preparation 35
14. Immunohistochemistry of Retina and Optic Nerve Sections 36
15. Eye Tissue Sections Imaging and Image Processing 36
16. Spinal Cord Injury Model 38
17. Horizontal Ladder Walking Assay 40
18. Rotarod Assay 41
19. Spinal Cord Tissue Collection and Preparation 42
20. Immunohistochemistry of Spinal Cord Sections 42
21. Spinal Cord Tissue Sections Imaging and Image Processing 42
22. Hematoxylin & Eosin staining of Tissue Sections 43
23. Statistical analysis 44

IV. Results 45

1. Evaluation of Microneurotrophin Effects on Optic Nerve Injury 46
   1.1. *In vivo* Characterization of the Mouse Optic Nerve Crush Model 46
   1.2. *In vivo* Design of BNN27 Delivery via Eye Drops in the Mouse Optic Nerve Crush Model 49
   1.3. *In vivo* Design of BNN27 Delivery via CGS Grafts at the Mouse Optic Nerve Crush Injury Site 51
   1.4. Detection of Delivered BNN27 in Eye Tissues via Mass Spectrometry 51
   1.5. *In vivo* Evaluation of BNN27 Effects on the Mouse Optic Nerve Crush Model 2 weeks Following Injury 52
      1.5.1. BNN27 Effects on RGC Survival 53
      1.5.2. BNN27 Effects on Gliosis in Retina 54
      1.5.3. BNN27 Effects on Axonal Elongation, Inflammation and OPC Recruitment 54
      1.5.4. BNN27 Effects on Vision Recovery 58
   1.6. *In vivo* Evaluation of BNN27 Effects on the Mouse Optic Nerve Crush Model 10 weeks Following Injury 59

1.6.1. BNN27 Effects on RGC Survival 60
1.6.2. BNN27 Effects on Axonal Elongation 60
1.6.3. BNN27 Effects on Vision Recovery 61
1.7. *Ex vivo* Evaluation of Microneurotrophin Effects on Mouse Adult Retina Explants 62
2. Evaluation of Combinatorial Treatments on Spinal Cord Injury 64
2.1. *In vivo* Evaluation of the Effects of Mouse Embryonic NSC-seeded CS Grafts at the Injury Site in the Mouse Dorsal Column Crush Spinal Cord Injury Model (Study A) 64
2.1.1. Integration of Cell-seeded and Cell-free CS Grafts 65
2.1.2. Effects of NSC-seeded CS Grafts on Locomotion Recovery Following Injury 66
2.1.3. Effects of NSC-seeded CS Grafts on Astrogliosis at 12 weeks Following Injury 68
2.1.4. Effects of NSC-seeded CS Grafts on Neuron Density at the Injury Site at 12 weeks Following Injury 69
2.1.5. Effects of NSC-seeded CS Grafts on Axonal Elongation at 12 weeks Following Injury 70
2.1.6. Effects of NSC-seeded CS Grafts on Synapse Formation at the Injury Site at 12 weeks Following Injury 72
2.1.7. Effects of NSC-seeded CS Grafts on Myelin Presence at the Injury Site at 12 weeks Following Injury 73
2.1.8. Localization of NSCs Delivered at the Injury Site via Injection 74
2.2. *In vivo* Evaluation of the Effects of Systemic of BNN27 Combined with Mouse Embryonic NSC-seeded CS Grafts in the Mouse Dorsal Column Crush Spinal Cord Injury Model (Study B) 75
2.2.1. *In vitro* evaluation of BNN27 Effects on Mouse Embryonic NSCs 76
2.2.2. Effects of Systemic Administration of BNN27 Combined with NSC-seeded CS Grafts on Locomotion Recovery Following Injury 78
2.2.3. Effects of Systemic Administration of BNN27 Combined with NSC-seeded CS Grafts on Astrogliosis at 12 weeks Following Injury 78
2.2.4. Effects of Systemic Administration of BNN27 Combined with NSC-seeded CS Grafts on Neuron Presence at the Injury Site at 12 weeks Following Injury 78
2.2.5. Effects of Systemic Administration of BNN27 Combined with NSC-seeded CS Grafts on Axonal Elongation at 12 weeks Following Injury 81
2.2.6. Effects of Systemic Administration of BNN27 Combined with NSC-seeded CS Grafts on Synapse Formation at the Injury Site at 12 weeks Following Injury 82
2.2.7. Effects of Systemic Administration of BNN27 Combined with NSC-seeded CS Grafts on Angiogenesis at the Injury Site at 12 weeks Following Injury 82
2.2.8. Fate of Implanted NSCs 85

2.2.9. Effects of Systemic Administration of BNN27 on Implanted NSC Survival and Differentiation at 12 weeks Following Injury 87
2.3. Comparison of the Horizontal Ladder Walking Assay and the Rotarod Assay in the Evaluation of Locomotion Recovery in the Mouse Dorsal Column Crush Spinal Cord Injury Model 88
V. Discussion 90
1. Treatments for Optic Nerve Injury based on Microneurotrophins and PCS Grafts 91
2. Treatments for Spinal Cord Injury based on NSC-seeded PCS Grafts and Microneurotrophins 95
VI. Conclusions 99
References 102
Appendix: Publications 116

LIST OF ABBREVIATIONS

3TH	Tyrosine Hydroxylase
ANOVA	Analysis of Variance
BBB	Blood Brain Barrier
BB&B	Basso, Beattie & Bresnahan
BDA	Biotinylated Dextran Amine
BDNF	Brain Derived Growth Factor
BMS	Basso Mouse Scale
BrdU	Bromodeoxyuridine
BSA	Bovine Serum Albumin
CCW	Counterclockwise
CGS	Collagen-GAG Scaffold
ChABC	Chondroitinase ABC
CNS	Central Nervous System
CS	Collagen Scaffold
CSPG	Chondroitin Sulfate Proteoglycans
CST	Corticospinal Tract
CTB	Cholera Toxin B
CW	Clockwise
DHEA	Dehydroepiandrosterone
DIV	Day *in vitro*
DPSC	Dental Pulp Stem Cell
ECM	Extracellular Matrix
EGF	Epidermal Growth Factor
ESC	Embryonic Stem Cell
FGF2	Fibroblast Growth Factor 2
FITC	Fluorescein Isothiocynate
GAD67	Glutamic Acid Decarboxylase 67
GCL	Ganglion Cell Layer
GFAP	Glial Fibrillary Acidic Protein
GFP	Green Fluorescent Protein
i.p.	intraperitoneal
i.v.	intravitreal
Iba1	Ionized calcium-binding adaptor molecule 1
INL	Inner Nuclear Layer
IPL	Inner Plexiform Layer
iPSC	induced Pluripotent Stem Cell
LC-MS	Liquid Chromatography-Mass Spectrometry
MAG	Myelin Associated Glycoprotein
MBP	Myelin Basic Protein
MNT	Microneurotrophin
MSC	Mesenchymal Stem Cell
NeuN	Neuronal Nuclei
NF	Neurofilament pan-axonal

NG2	Neuroglial-2-Proteoglycan
NGF	Nerve Growth Factor
NgR	Nogo Receptor
NSC	Neural Stem Cell
NSPC	Neural Stem/Progenitor Cell
NT	Neurotrophin
NTR	Neurotrophin Receptor
Ocm	oncomodulin
OEC	Olfactory Ensheathing Cell
OMgp	Oligodendrocyte-Myelin Glycoprotein
OMR	Optomotor Response
ONC	Optic Nerve Crush
ONI	Optic Nerve Injury
ONL	Outer Nuclear Layer
ONT	Optic Nerve Transection
OPC	Oligodendrocyte Precursor Cell
OPL	Outer Plexiform Layer
PB	Phosphate Buffer
PBS	Phosphate-Buffered Saline
PBST	Triton X-100 in PBS
PCL	Poly(caprolacone)
PCS	Porous Collagen-based Scaffold
PDGFRα	Platelet-Derived Growth Factor α
PDL	Poly-D-Lysine
PFA	Paraformaldehyde
PGA	Polyglycolic acid
PLA	Poly(lactic acid)
PLGA	Poly(lactic-co-glycolic acid)
PLL	Poly-L-Lysine
PNS	Peripheral Nervous System
RGC	Retinal Ganglion Cell
RNFL	Retinal Nerve Fibre Layer
RPE	Retinal Pigment Epithelium Layer
SCI	Spinal Cord Injury
SEM	Standard Error of the Mean
TON	Traumatic Optic Neuropathy
Trk	Tyrosine Receptor Kinase
VGLUT1	Vesicular glutamate transporter 1
wpi	Weeks Post Injury
YFP	Yellow Fluorescent Protein
αSMA	α-Smooth Muscle Actin

ABSTRACT

Central Nervous System (CNS) injuries, such as spinal cord or optic nerve injuries (SCI, ONI), affect thousands of individuals worldwide. Still no cure can handle the complex multifactorial nature of CNS injury. Along this direction, the present thesis evaluates novel combinatorial treatments for CNS injuries that contain three components: 1) Porous collagen-based scaffolds (PCS), biomaterials that provide structural support, inflammation regulation, a substrate for cellular migration and axonal elongation as well as a delivery system of therapeutic molecules or cells, 2) Neural Stem Cells (NSC), multipotent cells that can replace neuronal cells lost during CNS injuries, 3) Microneurotrophins (MNT), small-molecule mimetics of endogenous neurotrophins, that have demonstrated significant therapeutic effects on various animal models of human neurological diseases, but have not been evaluated in rodent models of CNS injuries yet.

The first part of this thesis focuses on evaluating the effects of BNN27, the seminal MNT, on the mouse optic nerve crush (ONC) model. Results provide the first evidence on the effects of BNN27 on animal models of ONI. In particular, BNN27 administration significantly increased RGC survival and decreased microglia-mediated inflammation at 2 weeks post injury (wpi). BNN27 was delivered via eye drops or via a PCS graft. Interestingly, this study presents the first administration of MNT via a biomaterial graft and it highlights a more consistent and efficient neuroprotective effect provided by a targeted delivery at the injury site.

The second part of this thesis focuses on evaluating the effects of combinatorial treatments on the dorsal column crush mouse SCI model. The first SCI study evaluated mouse embryonic NSC-seeded PCS grafts in this SCI model. The second SCI study combined NSC-seeded PCS grafts with systemic administration of BNN27. This thesis highlights PCS grafts as a promising delivery method of NSCs in SCI lesions, contrary to the widely used method of delivering NSCs in suspension via injection. NSC-seeded PCS grafts decreased glial scar and enhanced crucial events following SCI, such as neuron density, synaptogenesis, axonal elongation and angiogenesis at 12 wpi. Notably, NSC-seeded PCS grafts also led to statistically significant locomotion recovery starting at 9-10 wpi. This thesis also demonstrates the first evidence on the effects of BNN27 on animal models of SCI. Systemic administration of BNN27 decreased astrogliosis and neuronal loss following SCI**.** In addition, when BNN27 administration was combined with the implantation of NSC-seeded PCS grafts, BNN27 significantly increased the density of implanted NSC-derived cells, possibly addressing a major challenge of emerging NSC-based cell therapies.

In conclusion, this thesis presents novel combinatorial treatments that could cope with the complexity of CNS injuries and could hopefully be new tools in regenerative medicine leading to the design of more effective therapies with clinical application.

ΠΕΡΙΛΗΨΗ

Τα τραύματα του Κεντρικού Νευρικού Συστήματος (ΚΝΣ), συμπεριλαμβανομένων των τραυμάτων στο οπτικό νεύρο και το νωτιαίο μυελό, πλήττουν χιλιάδες ασθενείς κάθε χρόνο. Παρά την πρόοδο στην κατανόηση των μηχανισμών απόκρισης του ΚΝΣ στο τραύμα, οι διαθέσιμες θεραπείες παραμένουν ελάχιστα αποτελεσματικές. Οι μακροχρόνιες δραματικές επιπτώσεις στους ασθενείς τραύματος ΚΝΣ, καθιστούν επιτακτική την ανάγκη ανάπτυξης αποτελεσματικών θεραπευτικών στρατηγικών που θα μπορούν να επιδράσουν θετικά στην επούλωση των πληγών του ΚΝΣ. Λόγω της πολυπαραγοντικής φύσης της διαδικασίας επούλωσης στο ΚΝΣ, είναι πλέον αποδεκτό ότι απαιτούνται συνδυαστικές θεραπείες, οι οποίες θα μπορούν να επιδράσουν σε πολλαπλά σημεία της.

Η παρούσα διδακτορική διατριβή εστιάζει στην ανάπτυξη και πειραματική αξιολόγηση νέων θεραπειών για τραύματα του ΚΝΣ που συνδυάζουν τις συμπληρωματικές δράσεις τριών συστατικών: (1) Πορώδη ικριώματα κολλαγόνου (ΠΙΚ), (2) Νευρικά Βλαστικά Κύτταρα (ΝΒΚ) και (3) Μικρονευροτροφίνες (ΜΝΤ). Τα ΠΙΚ είναι βιοϋλικά με εκτενή χρήση στην κλινική πρακτική της αναγεννητικής ιατρικής, καθώς παρέχουν φυσική στήριξη, έλεγχο της φλεγμονής στην περιοχή του τραύματος και μέσο για επιμήκυνση των αξόνων, ενώ δρουν και ως φορείς για τη μεταφορά βλαστικών κυττάρων και θεραπευτικών μορίων στο σημείο του τραύματος. Τα ΝΒΚ είναι πολυδύναμα κύτταρα που μπορούν να διαφοροποιηθούν και να αναπληρώσουν νευρικά κύτταρα που χάθηκαν στο σημείο του τραύματος. Οι ΜΝΤ είναι μικρά μόρια με δράσεις που μιμούνται τις ενδογενείς νευροτροφίνες και έχουν δείξει σημαντικές νευροπροστατευτικές και νευρογεννητικές δράσεις σε διάφορα είδη νευρώνων και ζωικά μοντέλα νευροεκφυλιστικών ασθενειών, αλλά δεν έχουν δοκιμαστεί ακόμα σε τραύματα του ΚΝΣ.

Το πρώτο μέρος της διατριβής αξιολογεί τα αποτελέσματα της τοπικής χορήγησης της BNN27, την καλύτερα μελετημένη ΜΝΤ *in vitro* και *in vivo*, σε ένα μοντέλο τραύματος οπτικού νεύρου ποντικού (optic nerve crush). Συγκεκριμένα, εστιάζει στις δράσεις της BNN27 στην προστασία των γαγγλιακών νευρώνων του αμφιβληστροειδούς (ΓΝΑ) από απόπτωση και την βελτίωση της αναγέννησης των αξόνων τους στο σημείο του τραύματος. Η BNN27 χορηγήθηκε είτε μέσω σταγόνων στο μάτι είτε μέσω εμποτισμού σε ένα ΠΙΚ, το οποίο τοποθετήθηκε γύρω από το οπτικό νεύρο στο σημείο όπου είχε προηγουμένως προκληθεί τραυματισμός με σύνθλιψη του οπτικού νεύρου, με σκοπό την τοπική απελευθέρωση της ΜΝΤ στο σημείο του τραύματος. Η αξιολόγηση των δράσεων της BNN27 πραγματοποιήθηκε 2 και 10 εβδομάδες μετά τον τραυματισμό χρησιμοποιώντας ανοσοϊστοχημεία (για δείκτες απόπτωσης, φλεγμονής και αξονικής επιμήκυνσης) και πειράματα συμπεριφοράς (Optomotor Response assay). Σε δεύτερο στάδιο, αξιολογήθηκαν περισσότερες ΜΝΤ *ex vivo* σε αμφιβληστροειδείς ποντικιών για την επίδρασή τους στην αναγέννηση των αξόνων των ΓΝΑ.

Τα αποτελέσματα έδειξαν για πρώτη φορά την επίδραση της BNN27 σε ζωικό μοντέλο οπτικού τραύματος, καθώς η χορήγηση της BNN27 οδήγησε στην αύξηση της επιβίωσης των ΓΝΑ και τη μείωση της φλεγμονής 2 εβδομάδες μετά το τραύμα. Παρ' όλ' αυτά, η BNN27 δεν ώθησε την αξονική επιμήκυνση, ενώ η νευροπροστατευτική της δράση δεν ήταν μακροχρόνια, καθώς δεν παρατηρήθηκε στις 10 εβδομάδες μετά το τραύμα. Αυτά τα αποτελέσματα οδηγούν στην ανάγκη για περαιτέρω διερεύνηση των μηχανισμών δράσης των ΜΝΤ, καθώς και τον πιθανό συνδυασμό της BNN27 με άλλες ΜΝΤ ή άλλα θεραπευτικά μόρια. Σημαντικό σημείο του πρώτου μέρους της διατριβής αυτής είναι επίσης η χορήγηση της ΜΝΤ για πρώτη φορά μέσω ΠΙΚ, η οποία έδειξε μεγαλύτερη αποτελεσματικότητα σε σύγκριση με τη χορήγηση μέσω σταγόνων, αναδεικνύοντας τη σημασία της στοχευμένης χορήγησης θεραπευτικών μορίων στο σημείο του τραύματος.

Το δεύτερο μέρος της διατριβής αξιολογεί τα αποτελέσματα συνδυαστικών θεραπειών σε ένα μοντέλο τραύματος νωτιαίου μυελού ποντικού (dorsal column crush). Αρχικά, αξιολογεί τη χορήγηση εμφυτευμάτων ΠΙΚ με ΝΒΚ στο σημείο του τραύματος και στη συνέχεια, το συνδυασμό του εμφυτεύματος με την υποδόρια (pellet) χορήγηση της BNN27. Πιο συγκεκριμένα, εστιάζει στην εκτίμηση της ικανότητας των θεραπειών αυτών να σώσουν τους νευρώνες του νωτιαίου μυελού από την απόπτωση ύστερα από το τραύμα. Παράλληλα, διερευνά την ικανότητα της BNN27 να βελτιώσει την επιβίωση και διαφοροποίηση των ΝΒΚ του εμφυτεύματος, καθώς και την ενσωμάτωση τους με τον γειτονικό ιστό. Η αξιολόγηση των επιδράσεων των θεραπειών αυτών πραγματοποιήθηκε 12 εβδομάδες μετά τον τραυματισμό χρησιμοποιώντας ανοσοϊστοχημεία (για δείκτες απόπτωσης, πολλαπλασιασμού, διαφοροποίησης, φλεγμονής, αξονικής επιμήκυνσης, συναπτογένεσης και αγγειογένεσης) και πειράματα συμπεριφοράς που ποσοτικοποιούν τη βάδιση του ζώου (Horizontal Ladder Walking assay).

Τα αποτελέσματα ανέδειξαν τη σημασία των ΠΙΚ στη μεταφορά των ΝΒΚ στο σημείο του τραύματος σε αντίθεση με τη μέθοδο ενέσιμης εισαγωγής διαλύματος ΝΒΚ. Η χορήγηση εμφυτευμάτων ΠΙΚ με ΝΒΚ μείωσε την ουλή γύρω από το τραύμα και αύξησε την πυκνότητα των νευρώνων, τη συναπτογένεση, την αξονική επιμήκυνση και την αγγειογένεση 12 εβδομάδες μετά το τραύμα. Επιπλέον, βελτίωσε σημαντικά τη βάδιση των ζώων κατά την $9^{η}$-$10^{η}$ εβδομάδα. Το δεύτερο μέρος της διατριβής αυτής δείχνει επίσης για πρώτη φορά την επίδραση της BNN27 σε ζωικό μοντέλο τραύματος στο νωτιαίο μυελό, καθώς η χορήγηση της BNN27 οδήγησε στη μείωση της ουλής γύρω από το τραύμα και της απώλειας των νευρώνων. Επιπλέον, κατά την ταυτόχρονη χορήγηση της BNN27 με τα εμφυτεύματα ΠΙΚ με ΝΒΚ, η BNN27 αύξησε σημαντικά την πυκνότητα των κυττάρων που προέρχονταν από τα ΝΒΚ, πιθανώς αντιμετωπίζοντας έτσι ένα από τα σημαντικότερα προβλήματα των ΝΒΚ θεραπειών.

Συμπερασματικά, η διατριβή αυτή παρουσιάζει καινοτόμες συνδυαστικές θεραπείες που θα μπορούσαν να δώσουν την ευκαιρία για ανάπτυξη πιο αποτελεσματικών θεραπειών για την αντιμετώπιση των τραυμάτων στο ΚΝΣ, επικεντρώνοντας στη μεγάλη σημασία της προκλινικής έρευνας και θέτοντας την ως βάση για περαιτέρω κλινική εξέλιξη.

I. Introduction

1. Central Nervous System

Central (CNS) and Peripheral (PNS) Nervous System are the two parts of the mammalian Nervous System. CNS consists mainly of the brain and the spinal cord. Optic nerve is a CNS structure, as well. For the purpose of this thesis, the following sections focus on two parts of the CNS: the spinal cord and the optic nerve.

1.1. Eye Anatomy and Physiology

Eyes are organs that provide organisms with vision via the visual pathway, which includes anatomical structures that convert light signals into action potentials that reach the brain. The visual pathway consists of the retina, the optic nerve, the optic chiasm, the optic tracts, the lateral geniculate nucleus, the optic radiations and, eventually, the visual cortex (1,2).

Eyeballs, the peripheral organs of vision, are located in the skeletal cavity of orbit. In the central front of the eyeball, there is the *pupil*, where light enters the eye, surrounded by the *iris*, which controls the size of the pupil and consequently the amount of light that enters. *Cornea*, the first lens of the eyebulb, covers both pupil and iris. In continuity with cornea, there is *sclera*, the second component of the external layer of the eye. The intermediate layer is divided into the anterior (*iris* and *ciliary body*) and the posterior (*choroid*) part, while the internal neural layer consists of the retina. Another *lens* is located behind the iris, attached to the ciliary body, which changes the shape of the lens via muscle contraction or relaxation, in order to control the imaging plane that focuses into the retina. The light is focused on the *fovea* located in *macula* of human retina. The eyeball contains three fluid chambers: the *anterior chamber* between cornea and iris, the *posterior chamber* between iris and *lens* and the *vitreous chamber* between lens and retina. The anterior and posterior chambers are filled with *aqueous humor*, while the vitreous chamber is filled with *vitreous humor* (2,3) **(Fig. I-1A)**.

Retina is a circular disc in the back of the eyeball that extends till the ora serrata and the ciliary processes. Central retina near the *optic disk* is thicker than peripheral retina. Retina consists of five layers: three layers of nerve cell bodies and two layers of synapses. Beginning from the *outer* to the *inner limiting membrane*, the *outer nuclear layer (ONL)* contains cell bodies of *photoreceptors* (*rods* and *cones*), *the inner nuclear layer (INL)* contains cell bodies of the *bipolar, horizontal and amacrine cells* and the *ganglion cell layer (GCL)* contains cell bodies of *retinal ganglion cells (RGC)* and displaced amacrine cells. Between ONL and INL is the *outer plexiform layer (OPL)*, a neuropil, where photoreceptors are connected with bipolar and horizontal cells. Between INL and GCL is the *inner plexiform layer (IPL)*, the second neuropil of retina, where the bipolar cells connect to RGC. The inner retinal layers are nourished from the *central retinal artery* coming from the optic nerve head, while the outer retina is supplied with blood by the *choroidal blood vessels*. *Retinal pigment epithelium layer (RPE)* is located between the blood flow of the choroid and the outer segments of the photoreceptors that follow the *outer limiting membrane*. The tight epithelium of RPE functions as a blood/retina barrier that controls photoreceptors nutrients supply, ion homeostasis and elimination of water and metabolites from retina (2,3) **(Fig. I-1B)**.

Each retina cell type has a specific role. *Photoreceptors* (rods, cones) convert photons into electrical signals; *rods* detect low light levels, while *cones* detect moderate and high light levels (4). *Bipolar cells* transfer electric signals from photoreceptors to RGCs. *Horizontal cells* are inhibitory interneurons that modulate the communication between photoreceptors and bipolar cells. *Amacrine cells* modulate the communication between bipolar cells and RGCs (5).

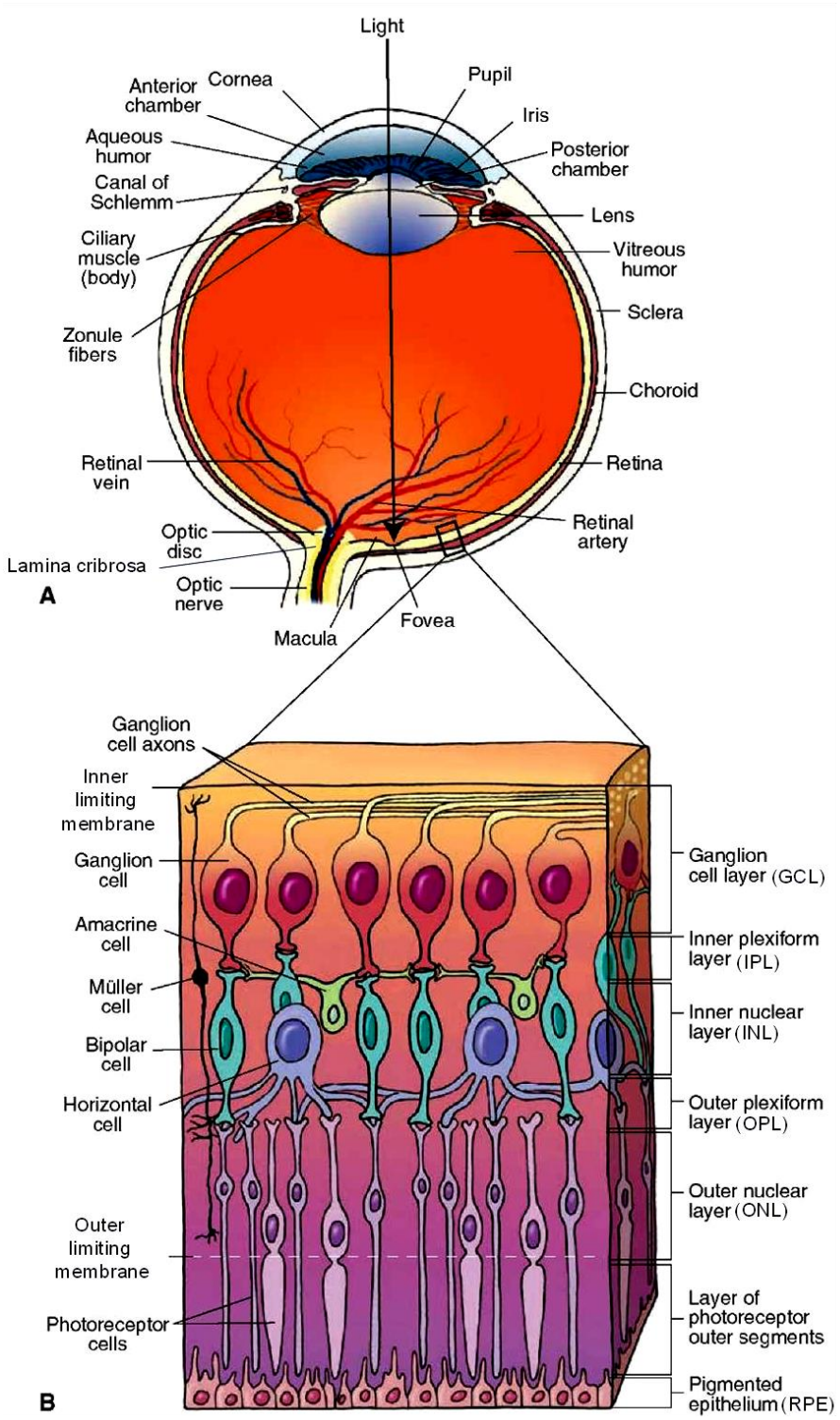

Figure I-1. A. Eye anatomy. **B.** Retinal layers. (Adapted from (6))

RGC axons converge in the optic disc and form the **optic nerve** in order to transfer visual information to the brain. RGC axons are organized into bundles, separated and ensheathed by glial cells. RGC axons are initially unmyelinated and become myelinated as they traverse the *lamina cribrosa* **(Fig. I-1A)**. The optic nerve (like other CNS tissues) is enclosed in three sheaths called *meninges*: the outer dura mater, which connects with the sclera, the middle arachnoid mater and the inner pia matter. Between the sheaths, there is the subdural and subarachnoid space (1,3).

There are three types of **glial cells in retina**: Müller cells, astrocytes and microglia. *Müller cells* are the principal glial cells of retina. Their bodies are located in the INL and they project processes to the outer and inner limiting membrane. Müller cells support mechanically the retina and metabolically the neurons, control homeostasis and are involved in debris phagocytosis. *Astrocytes* enter retina along the optic nerve and contribute to homeostasis and nutrient supply, along with Müller cells. *Microglia* are found mainly in the IPL but also in the other retinal layers. Microglia participate in the immune response (2). *Astrocytes* and *microglia* are also present in **optic nerve**. In addition to their roles on homeostasis and metabolism, astrocytes contribute to axon fasciculation and protect the optic nerve from the surrounding tissues by forming glial limiting membranes. Finally, *oligodendrocytes* are present in the optic nerve anterogradely to lamina cribrosa, where they myelinate axons (1).

1.2. Spinal Cord Anatomy and Physiology

Spinal cord is one of the main parts of CNS. Spinal cord transmits signals between the brain and the rest of the body. Specifically, spinal cord receives sensory information from the body (skin, joints and muscles) and transmits it to the brain. Spinal cord also transfers motor signals from the brain to the rest of the body. Additionally, spinal cord includes neural circuits for reflexes, bypassing the brain (7) .

Spinal cord is a cylindrical structure located and protected inside the *vertebral column*, which consists of 33 *vertebrae*. Spinal cord starts from the bottom of brain stem (*medulla oblongata*) and reaches the lower back. Spine consists of five parts: *cervical, thoracic, lumbar, sacral* and *coccygeal* vertebrae. Spinal cord reaches the first lumbar vertebrae, where it continues as a collection of nerves called *cauda equina* (3,8) **(Fig. I-2)**.

Spinal cord is protected by three *meninges*: the dura mater (outer layer), the arachnoid mater (middle layer) and the pia mater (inner layer). The epidural space lies between the dura mater and the arachnoid mater. The subarachnoid space is located between the arachnoid and the pia mater and contains *cerebrospinal fluid*. Cerebrospinal fluid also exists in the central canal that starts from the ventricular system of the brain, traverses the spinal cord longitudinally and is lined by ependymal cells. The central canal is located anteriorly or centrally in the spinal cord depending on the spine level (3,8) **(Fig. I-2)**.

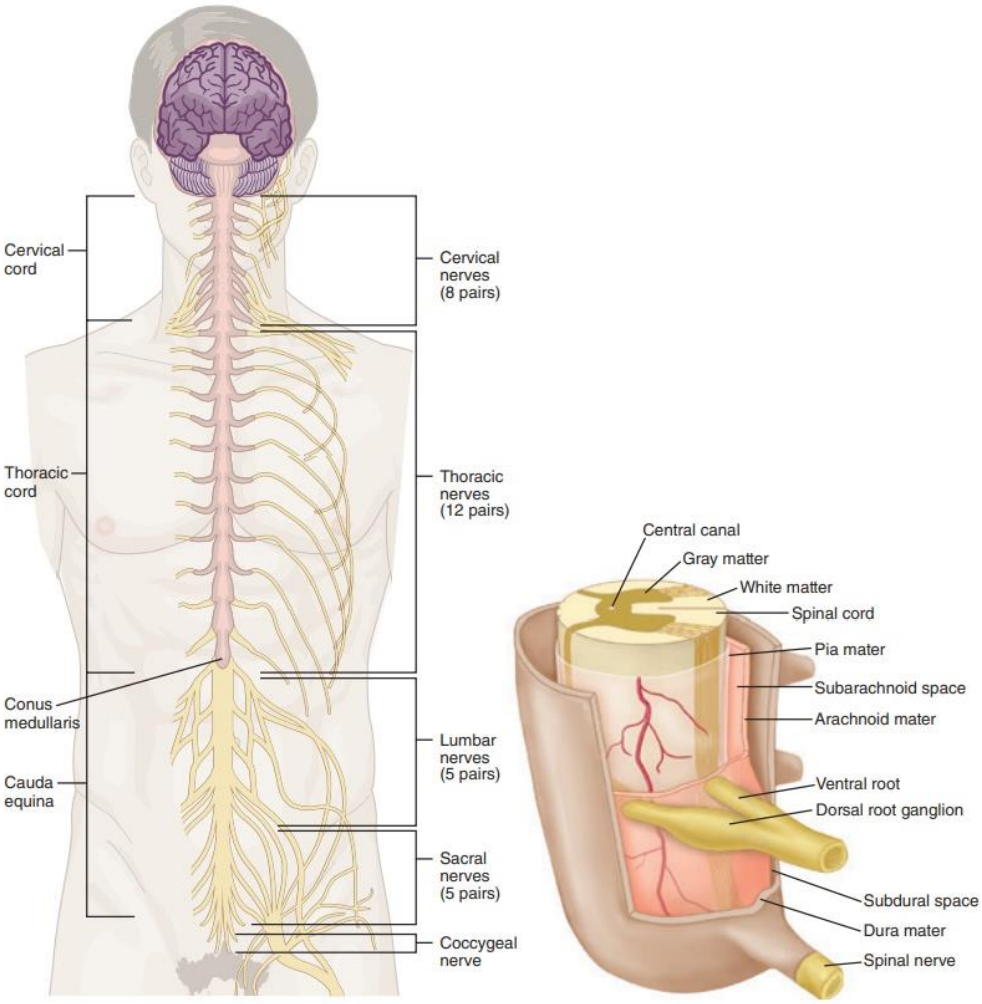

Figure I-2. Spinal cord anatomy (9).

A cross section of spinal cord consists of *grey matter* shaped like the letter H with four "horns"; 2 front horns that contain motor neurons and two back horns with sensory neurons. Grey matter is surrounded by *white matter*, which contains mostly groups of myelinated axons. Axon groups create two types of *fiber tracts*: ascending (sensory) tracts that enter the spinal cord via the posterior (Dorsal) root and whose bodies are located in the Dorsal Root Ganglia, and descending (motor) tracts that exit via the anterior (Ventral) root. For instance, the corticospinal tract (CST) begins in the cerebral cortex and descends the spinal cord. Each pair of dorsal and ventral roots creates one of the 31 spinal nerves that enters and exits the vertebral column in each vertebra. Both grey and white matter contain neuroglia and blood vessels (3,8) **(Fig. I-2)**.

2. The Pathophysiology of Central Nervous System Injury

2.1. Overview

CNS disorders, such as traumatic brain, spinal cord or optic nerve injuries and neurodegenerative diseases, affect thousands of individuals each year with still no cure (10). Over the past decades, many efforts have attempted to unravel the mechanisms of neurological damage. CNS injury induces a complex cascade of events that resembles wound healing (11). Initial primary injury leads to secondary injury (acute and sub-acute phase) within the next few hours to weeks and extends as a chronic pathology over the next months to years (8,12–14) **(Fig. I-3)**.

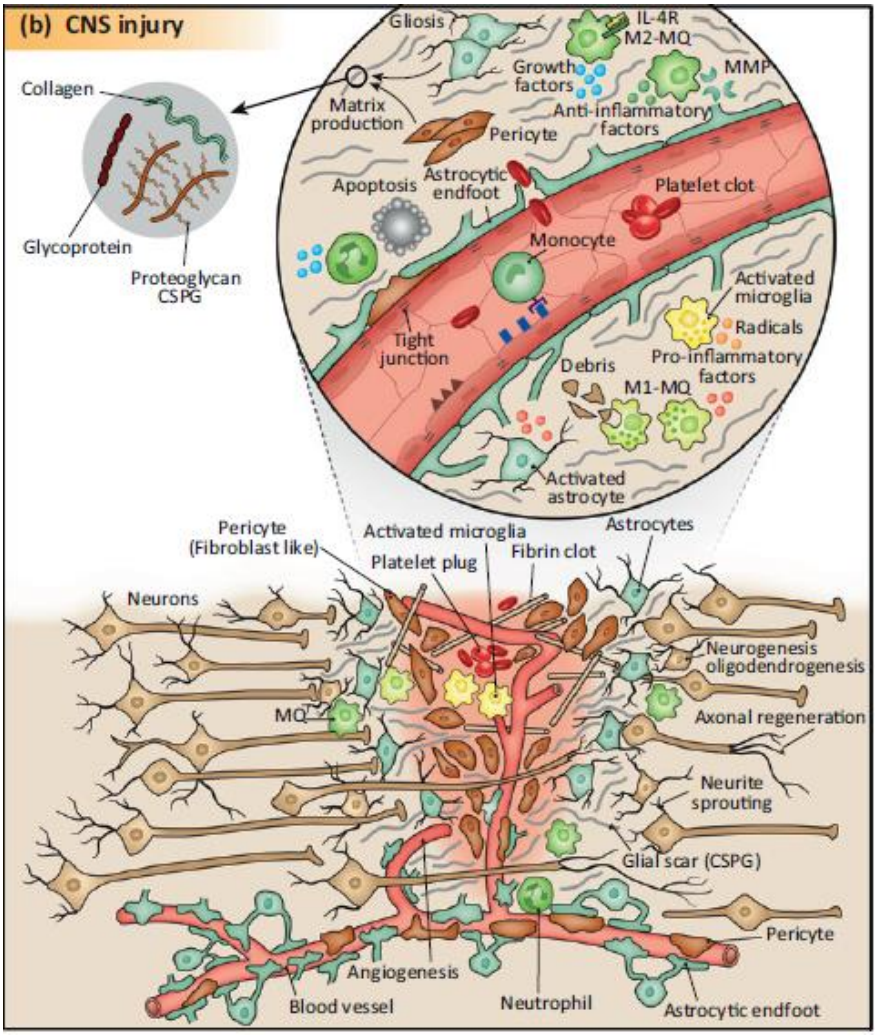

Figure I-3. The pathophysiology of CNS injury (11).

More specifically, a few minutes after **primary injury** and acute cell necrosis, a *clot* is formed followed by *edema*, in order to protect the exposed tissue. The resulting *hypoxia* leads to further neuronal damage and ischemia (11). Various *biochemical changes* are triggered, such as the uncontrolled release of glutamate that binds to NMDA and AMPA receptors. Glutamate effects are observed on neurons, glial cells and endothelial cells. Additionally, there is production of free radicals and nitric oxide. The resulting excitotoxicity, increased calcium influx into cells, DNA fragmentation, lipid peroxidation, autophagy dysregulation and neurotoxicity lead to **cellular death** by necrosis or apoptosis. At the same time, hemorrhage induces further *oxidative stress* due to the release of excitatory amino acids, iron and thrombin (14,15).

Inflammation is activated within the first minutes to hours following injury and involves many cell types, such as neutrophils, microglia, dendritic cells, macrophages, B- and T-lymphocytes as well as excessive release of pro- and anti-inflammatory cytokines. The resulting impaired blood brain barrier (BBB) function and permeability causes extensive edema and hypoxia. *Microglia* are resident CNS cells, while *macrophages* are derived from blood monocytes that reach the lesion via the disrupted BBB. Upon activation, microglia and macrophages cannot be distinguished and their main role is to clean the lesion site of dead cells and foreign material via phagocytosis (11,14–17).

The role of inflammation in CNS injury is controversial. On the one hand, limiting inflammation by blocking microglia activation exaggerates injury pathology since inflammation enhances cell survival and axonal growth (18). On the other hand, inflammation can lead to further tissue damage and neuronal death (15).

Moreover, microglia has been shown to affect the organism systemically leading to CNS injury-induced immune deficiency syndrome (CIDS) (19). Interestingly, studies revealed that there are two types of macrophages/microglia related to the two different inflammation effects; *M1 macrophages* are associated with neurotoxicity and axon dieback, while *M2 macrophages* are associated with neuroprotection (18). Neuroprotective effects of activated macrophages have been linked to the expression of neurotrophins (NTs) (19).

Another important cell type in CNS injury sites is *astrocytes*. Under normal conditions, astrocytes regulate CNS homeostasis and synaptic plasticity (20). One hour after CNS injury, astrocytes begin to become reactive and migrate to the lesion boundaries, where they proliferate, upregulate the expression of glial fibrillary acidic protein (GFAP) and other intermediate filament proteins, become hypertrophic and form the **glial scar** the following 4 days to several weeks. Glial scar surrounds the CNS lesion by rearranging astrocyte orientation in order to obstruct elongating axons (17,18,20). Interestingly, it was observed that dystrophic axon tips do not interact directly with the astrocytes; instead they interact with *oligodendrocyte precursor cells* (OPCs) that significantly proliferate in the glial scar region (18). Similarly, fibroblast-like stromal cells and *pericytes* also proliferate and invade the lesion site, interact with reactive astrocytes and together with macrophages they form a cell layer within the astrocyte cell layer, the **fibrotic scar** (18,21).

2.2. Inability of Axonal Regeneration

Already in the early 20th century, Ramón y Cajal demonstrated the first evidence that CNS possess limited regeneration ability (22). Interestingly, CNS neurons were found to regenerate their injured axons when they were in the permissive environment of a peripheral nerve graft (12). Contrary to the injured PNS, the injured CNS environment is non-permissive to axonal regeneration due to the presence of inhibitory molecules, the deficiency of trophic support and the lack of endogenous mechanisms that drive neuronal regeneration and microtubule stability (12,23). Even when a growth cone is formed in an injured CNS neuron, there is insufficient guidance and no further elongation (15). Instead, observations report retrograde axonal degeneration transferred to the somas leading to neuronal death, axonal dieback or the formation of retraction bulbs in the axonal endings. There are a few cases of sprouting, but the appropriate pruning or suppression of aberrant sprouting is essential for functional recovery (17).

Intrinsic factors that limit axon regeneration in the CNS include transcription factors (e.g. c-Jun, Atf3, Stat3) and regeneration-associated genes (e.g. Gap43, Cap23, tubulins), whose expression is decreased or even lost (15). Contrary to mature CNS axons that lose their ability to grow, PNS axons express specific genes capable to promote axonal growth after injury (12,24).

Extrinsic factors that limit axon regeneration in the CNS include *myelin-associated inhibitory proteins* and *proteoglycans in glial scar* (15). CNS myelin is enriched with neurite growth inhibitory factors, such as NogoA, myelin-associated glycoprotein (MAG) and oligodendrocyte-myelin glycoprotein (OMgp) (18). These three molecules bind to Nogo Receptor (NgR) located on the growth cones to detect the CNS inhibitory cues, leading to the collapse of growth cones and the inhibition of axonal regeneration (12,17). Contrary to Schwann cells that enhance axonal elongation following PNS injury (25), CNS glia do not participate in myelin clearance; oligodendrocytes have limited phagocytic ability and are susceptible to death, whereas astrocytes downregulate phagocytosis or lose the ability to recognize phagocytosis signals after injury (26).

Glial scar, as described in section I-2.1, is essential in CNS injury in order to protect the surrounding CNS tissue from the infiltrated inflammatory agents via creating a wall surrounding the lesion site (17,18).

Indeed, depletion of reactive astrocytes and pericytes resulted in impaired wound healing (17). Nevertheless, the role of glial scar in CNS injury is controversial. Astrocytes, OPCs and meningeal cells produce proteoglycans, such as chondroitin sulfate proteoglycans (CSPGs) including neuroglial-2-proteoglycan (NG2), which have growth-inhibiting properties (8,18). Consequently, glial scar is considered a major barrier for axonal regeneration because its structure obstructs axon pathways and its cellular components secrete inhibitory molecules (12,18).

Chronic wounds are characterized by prolonged inflammation, detected for months and even years, that promotes fibrosis, scarring and further tissue damage, limiting regeneration (11,19). Thus, inflammation and scarring need to be terminated so as for wound healing to progress (11).

3. Optic Nerve Injury

3.1. Traumatic Optic Neuropathy & Current Therapies

Traumatic Optic Neuropathy (TON) is a condition in which indirect or direct trauma of the optic nerve results in vision loss. *Indirect optic nerve injury* (ONI) is more common and usually occurs as a consequence of head trauma. *Direct ONI* results from cases such as penetrating trauma, displaced bone fragments or localized hemorrhages. Injury severity varies from a simple contusion to a complete avulsion of the optic nerve (27).

Epidemiologically, 1 in 1,000,000 persons suffers from TON (based on a 2-year British surveillance). The majority of patients are young adult males (79-85%) with average age of 33.5 years old, while approximately 20% of cases occur during childhood. The most common cause is road accidents (49%), whereas approximately two thirds of TON patients had associated head injuries (28,29).

Although half of the patients with indirect ONI show visual recovery without any interventions, direct ONI results in irreversible vision loss. None of the available treatments can halt or reverse the progress of visual loss induced by TON. Current TON management is controversial and includes observation, system steroids, surgical decompression of the optic canal or combination of steroids and surgery. Nevertheless, there are limitations and no evidence base on these current interventions (27,29).

3.2. Animal Models in Optic Nerve Injury Research

Animal models are used in ONI research to study its underlying pathophysiological mechanisms **(Fig. I-4)** and evaluate novel therapeutic methods. They are simpler compared to spinal cord injury or brain injury models (17). Although rodents, such as rats and mice, differ from humans in terms of behavior and anatomy, such as UV sensitivity of their cones and the fact that the majority of optic nerve axons target superior colliculus instead of visual cortex, they are popular compared to non-human primates that better resemble human neuroanatomy and physiology but have a higher cost and are difficult to handle (30,31).

Three popular **rodent models** that mimic direct ONI are the *optic nerve transection (ONT) model*, the *optic nerve crush (ONC) model* and the controlled orbital impact model. Two rodent models that mimic indirect ONI are the ocular blast model and the sonication-induced TON model. In the ONT model, optic nerve is transected with a blade knife behind the globe via an intra-orbital approach. As a result, 50% of RGCs die in 4 days, 70% in 1 week and more than 95% in 2 weeks (30,32). In the ONC model, the optic nerve is crushed (via forceps or other devices, such as balloon) via an intra-orbital or intracranial approach. The duration of

crush (in seconds) defines the severity of the injury. The variability of the force applied to the forceps is a drawback of this technique. Compared to ONT, used mostly for studying RGC apoptosis, ONC results in less RGC death, allowing the investigation of both RGC apoptosis and regeneration (30,32). In the *controlled orbital impact model*, the impact is performed in the optic nerve via a metallic impactor tip. This model requires specialized apparatus and software to adjust the parameters of trauma (32).

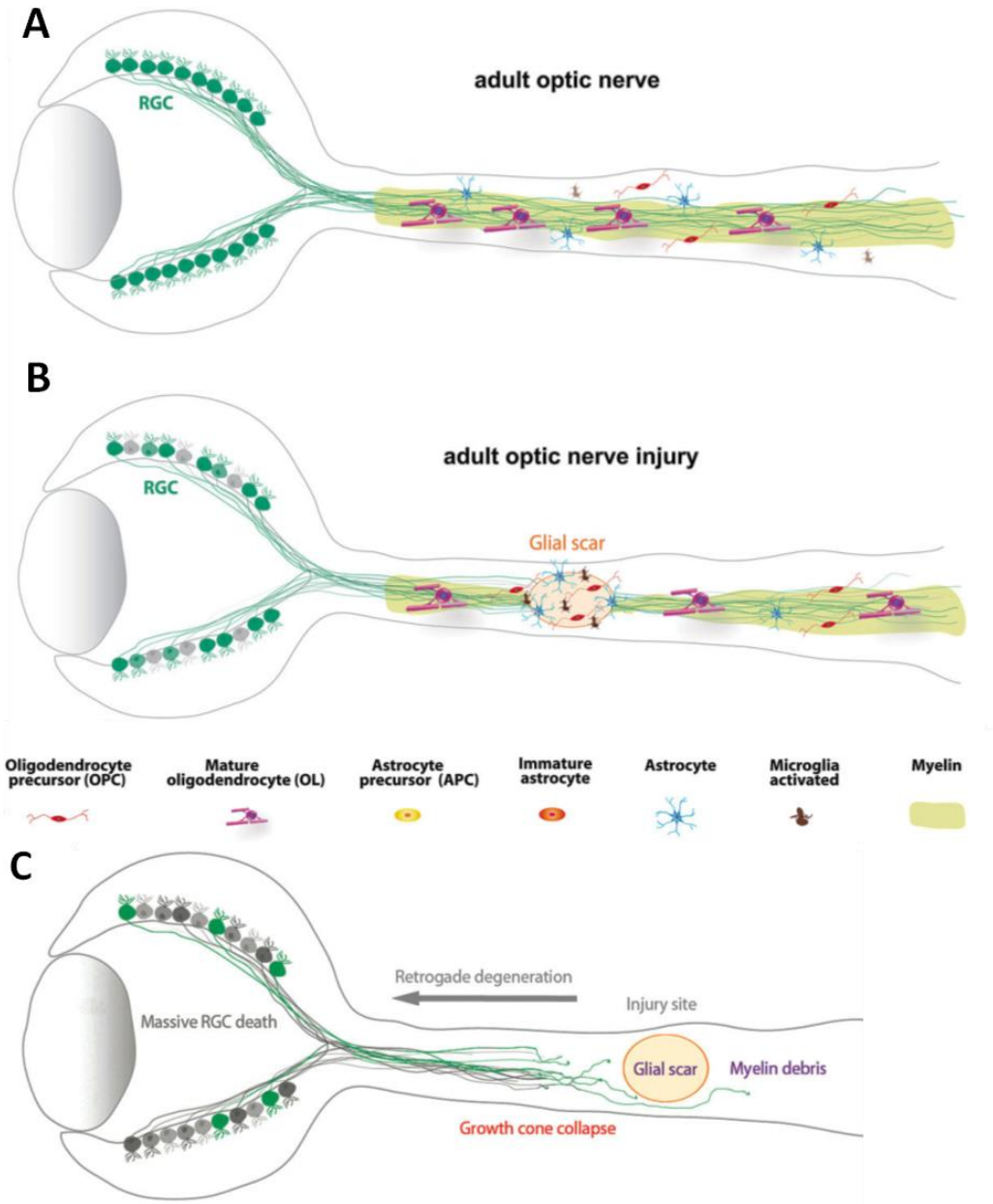

Figure I-4. Schematic overview of ONI pathophysiology that includes inflammation, glial scar formation, axonal degeneration and RGC death (Adapted from (33)).

The ocular blast model and the sonication-induced TON model are noninvasive. The *ocular blast model* allows precise modulation of the force delivered to the eye, but it leads to high mortality rates because of severe anterior and posterior segment injuries. In the *sonication-induced TON model*, injury is created via ultrasonic pulses. Its drawback is the damage that may be created in the contralateral optic nerve or surrounding tissues (32).

The **evaluation of functional recovery following ONI** mainly includes non-invasive imaging, behavioral assays and histological analysis. Regarding imaging, optical coherence tomography (OCT) is a non-invasive imaging technique that can quantify the retinal nerve fibre layer (RNFL) thickness and axonal loss *in vivo* (1).

Commonly used behavioral assays include the eye blink response assay, the visual cliff assay and the optomotor response (OMR) assay. The *eye blink response assay* is simple and fast: an animal with vision ability blinks when an object approaches its eyes before touching the cornea. The *visual cliff assay* includes a field of glass below of which there is a high-contrast checkboard pattern placed attached to the glass on one side of the field and on a lower level on the other side, creating the impression of a cliff between the two sides. The evaluation is based on the percentage of time the animal walks in each region; "safe" versus "dangerous" region. While the previous two assays evaluate only the animal ability to see, the *OMR assay* allows the evaluation of visual acuity, contrast threshold and motion sensitivity. In the OMR assay, the animal is placed on an elevated platform surrounded by a rating drum that presents vertical gratings of various patterns. As the drum rotates, the animal moves its head or body in the same direction as a reflex. By increasing the grating parameters (spatial frequency, contrast) reflexes are altered. Animal motions are recorded and videos are processed by software for the detection and quantification of movements. The OMR assay can assess the vision of each eye separately without mechanical occlusion of the other (31,34).

Histological analysis uses immunohistochemistry to detect appropriate biomarkers, in order to assess specific pathophysiological features either in retina tissue (e.g. Brn3a and RBPMS for RGC survival) or in the optic nerve (e.g. GAP43 and L1 for axonal elongation). Axonal tracers are used to identify regenerated axons or spared RGCs. Anterograde tracers, such as cholera toxin B (CTB), are injected intravitreally (i.v.), transported from cell bodies to axons and are used to trace regenerating axons. Retrograde tracers, such as Fluoro-Gold, are injected into the superior colliculus region, are transported from axons to cell bodies and are used to count spared RGCs whose axons reach superior colliculus (35).

4. Spinal Cord Injury

4.1. Traumatic Spinal Cord Injury & Current Therapies

Spinal Cord Injury (SCI) refers to the damage of spinal cord as a result of traumatic or non-traumatic etiologies. *Traumatic SCI* results from an external physical impact, such as a road accident or a sports-related injury. *Non-traumatic SCI* occurs when the spinal cord is affected by acute or chronic disease, such as a tumor, infection or degenerative disease. The clinical outcome of SCI depends on the severity of the injury and its location on spinal cord. Depending on the severity, SCI results in incomplete or complete loss of sensory and/or motor functions. Depending on the location of the trauma, different parts of the body are affected. For instance, higher cervical lesions can lead to partial or complete tetraplegia (paralysis of the four limbs), while lower lesions can lead to paraplegia (paralysis of the lower limbs) (14).

According to the World Health Organization, 250,000 - 500,000 individuals around the world suffer SCI each year. A study conducted over the last decade (2011 – 2020) revealed 26.5 traumatic SCI cases per 1,000,000 inhabitants with mean age of 59.2 years, 68.3% of which were males. Traffic crashes were the most common cause of SCI (29.9%). Cervical lesions resulted in greater mortality rates, which were also increased with age (36).

Existing clinical treatments are limited to surgical intervention for spinal cord decompression and the controversial administration of methylprednisolone, a corticosteroid that has serious adverse effects and poor efficacy (37). Current guidelines for SCI are against the use of methylprednisolone (38). Physical

rehabilitation is usually performed, but the development of effective SCI treatments remains an unmet clinical need.

4.2. Animal Models in Spinal Cord Injury Research

Animal models are used in SCI research to study the pathophysiological mechanisms of SCI **(Fig. I-5)** and evaluate novel therapeutic methods. Although larger animals, such as non-human primates, emulate better human neuroanatomy and physiology, rodents, such as mice and rats, are the most commonly used animals due to their lower cost, higher availability and ease of use. Between rats and mice, there are small differences in the content of lesion site and the inflammatory cells infiltration. Rats resemble better human SCI pathophysiology (14).

The three most common **animal SCI models** are transection, contusion and compression. *Transection SCI models* are the most severe and the least representative of human traumatic SCI. However, transection models are appropriate for studying axonal regeneration as well as developing biomaterial grafts that can bridge severed lesions. Moreover, partial transection models are developed, such as hemi-section, unilateral transection and dorsal column lesions (8,14).

Contusive SCI models are more clinically relevant, as they mimic the human lesion induced by an external physical impact. A spinal cord contusion can be generated by three different types of devices: weight-drop apparatus, electromagnetic impactor and air gun device. Such apparatuses allow the precise definition of SCI severity, whereas, depending on the device, controlled impact and reliability of the clamps can also be defined. A disadvantage of contusion SCI models is that spare and regenerated tissues are not easily distinguished (8,14).

Compressive SCI models introduce a prolonged force application in spinal cord, most commonly via the use of aneurism clips. The force of the clip and the duration of compression control the SCI severity. The spinal cord is injured both dorsally and ventrally, mimicking clinical conditions. Alternatives are the use of calibrated forceps or a catheter with an inflatable balloon that is inserted in the epidural or subdural space. Compressive SCI models are less expensive compared to contusive models, but they suffer from significant animal-to-animal variability (8,14).

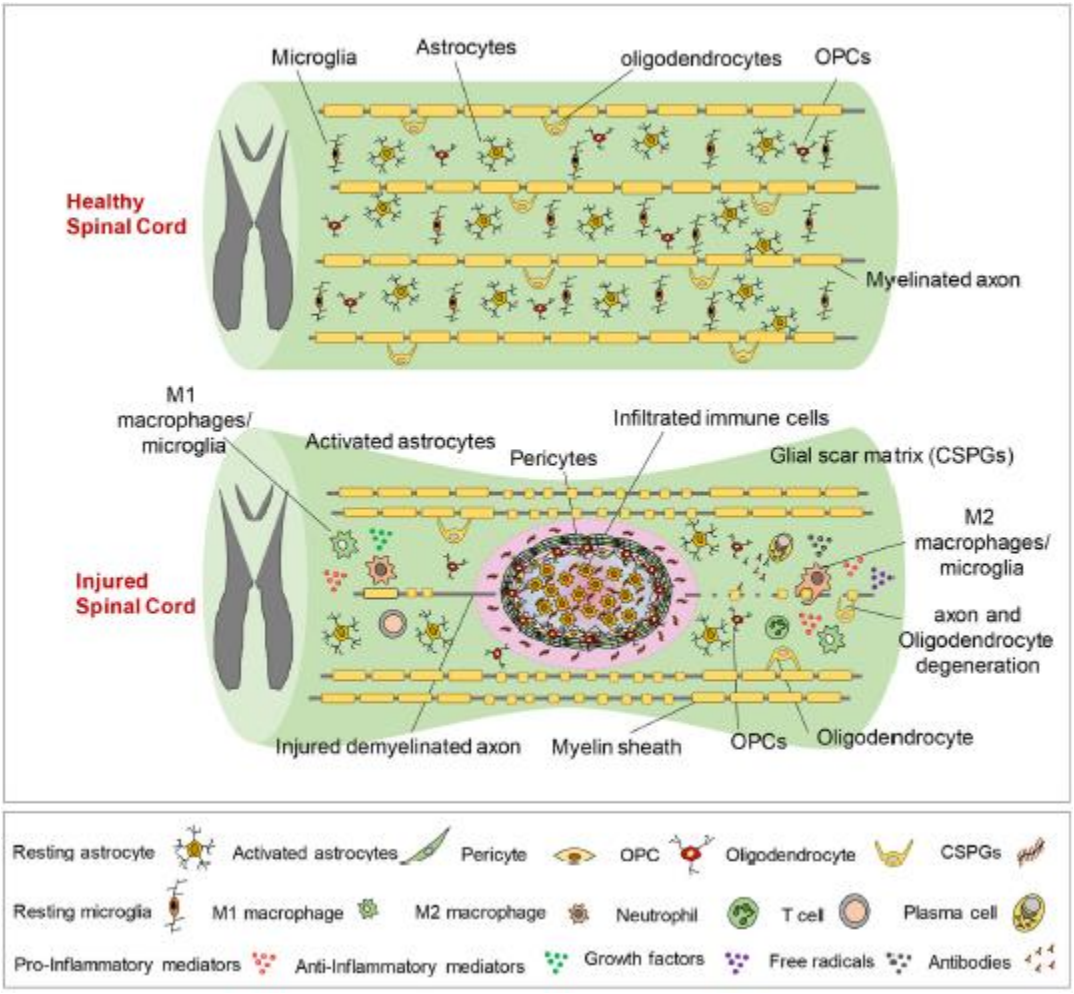

Figure I-5. Schematic overview of SCI pathophysiology (14).

The **evaluation of functional recovery following SCI** mainly includes behavioral assays and histological analysis. The most commonly used behavioral assays are the Basso, Beattie & Bresnahan (BB&B) locomotor scale, the horizontal ladder walking assay, the CatWalk assay and the hot plate assay. The choice of assay depends on the animal model, the severity of the injury and the tract that is affected (8).

The *BB&B locomotor scale* is an open field test that can evaluate the recovery of rat hind limb motor function after thoracic SCI using a 21-point scale. *Basso Mouse Scale (BMS)* is the corresponding 9-point scale developed for mice. BB&B scale is reliable and reproducible and does not require significant animal training. However, BB&B has been developed mainly for mid/lower thoracic contusion injury, therefore it cannot assess all types of SCI lesions (8,39).

In the *Horizontal ladder walking assay* rodents cross a horizontal ladder with rung spacing. Animals' locomotion recovery is evaluated via measuring the fraction of step faults. This assay is used in less severely SCI models as animals need to retain some locomotion ability. It is cheap and can discriminate details in motor recovery. However, animals need training and the analysis of locomotion videos is tedious and subjective (8).

The *CatWalk assay* is another assay for locomotion evaluation. Animals cross an elevated dark walkway floor made of glass. As animals walk, their paws in contact with the floor are illuminated based on the principle of total internal reflection. Illuminated paws are filmed and processed by computer software to quantify various gait parameters. The main drawback of this assay is that image analysis can be time-consuming (39).

In the *hot plate assay* animals are placed on a heat source in order to measure their hind paw withdrawal latency. While this is considered an example of sensory assessment, sensory tests can be affected by motor deficits resulted by SCI (8).

Histological analysis usually uses immunohistochemistry to detect appropriate biomarkers such as GFAP (for astrogliosis), Iba1 (for microglia-induced inflammation) and L1 (for axonal elongation). Axonal tracers are also used for identifying injured or regenerated axons. Axonal tracers can be either anterograde, such as biotinylated dextran amine (BDA), or retrograde, such Fluoro-Gold (8).

5. Therapeutic Approaches for Central Nervous System Injuries

The effective treatment of CNS injuries remains a major unmet scientific and therapeutic challenge. The complex multifactorial nature of CNS injury needs to be considered in the development of successful treatments. A key point is also the temporal nature of these events. Thus, there is need of combinatorial therapies that can control and encounter various events by directly targeting them specifically in space and time **(Fig. I-6)**.

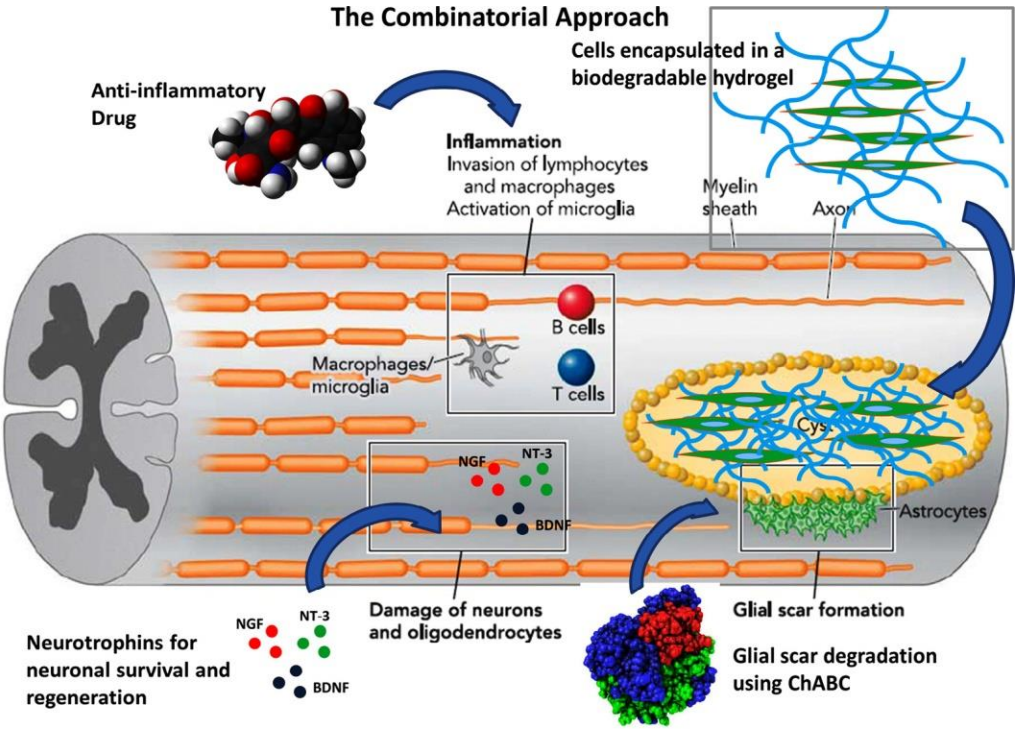

Figure I-6. Conceptual schematic representation of a combined therapy for SCI (8).

The present thesis focuses on targeted therapies for CNS injuries (ONI and SCI) with neuroprotective and neurogenic properties. Both optic nerve and spinal cord share the complexity of CNS injury pathophysiology. However, each organ has unique characteristics that need to be considered in the development of a treatment. For instance, the intravitreal cavity of the eye provides an advantage for drug delivery closer to the retina and optic nerve head leading to high drug concentrations at the site of interest (40). Non-invasive topical administration (e.g. via eye drops) has limited penetration, bioavailability and potency to reach the posterior eye segment (e.g. retina) due to physiological and anatomical barriers. On the other hand, i.v. injection is more efficient for drug delivery in the posterior eye and requires less frequent administration. However, it can result in side effects such as endophthalmitis, retinal detachment or damage (41,42).

The field of **regenerative medicine** aims to develop novel treatments that can minimize the adverse effects of injury and induce the *de novo* synthesis of tissue of normal structure and function in order to eventually recover the structure and function of the injured organ. Overall, regenerative medicine treatments combine three kinds of "components" in order to cope with the complexity of CNS injury: biomaterials, cells and therapeutic molecules (43). Despite some encouraging preclinical research results, so far these treatments have not reached clinical applications in humans (44). Thus, there is need to design treatments of improved safety and effectiveness, whose design considers the characteristics of cells, the type and properties of biomaterial, and the type, target and pharmacokinetics of therapeutic molecules involved.

5.1. Molecular therapies

5.1.1. Overview

Various kinds of **therapeutic molecules** (small molecule compounds or biologics) have been evaluated for their ability to block factors that lead to neurodegeneration or inhibit axon regeneration after ONI and SCI **(Fig. I-7)**. The present thesis focuses on neurotrophic factors, which have been included in several ONI and SCI treatments due to their role in neuronal survival, axonal guidance and synapse formation (45,46). This section provides an overview of molecular therapies, while the following section focuses on neurotrophic factors.

In order to protect neural tissue from **excitotoxicity**, sodium channel blockers, such as riluzole, or NMDA antagonists, such as magnesium, have been evaluated. Riluzole has been approved by FDA for amyotrophic lateral sclerosis and has been tested in clinical trials for human SCI (8). However, more trials are needed, since preliminary results are controversial showing decreased neuropathic pain and improved motor recovery accompanied with adverse effects (47). Furthermore, Ca^{2+} and Zn^{2+} influx control has been shown to enhance RGC survival and axonal regeneration after ONI (48).

Except for the controversial use of the anti-inflammatory drug methylprednisolone, several other therapeutic molecules have also been evaluated for their ability to limit **inflammation**. IL-10 (Interleukin-10) reduced lesion volume in SCI and enhanced neuronal survival and functional recovery. The antibiotic minocycline decreased lesion cavity and enhanced functional outcome following SCI, as well (8). Although more preclinical studies are needed to enhance the reproducibility of these findings, minocycline has tested in human clinical trials, which has shown safety but not efficacy (49). Furthermore, nonsteroid anti-inflammatory drugs (NSAIDs), such as indomethacin and ibuprofen, have been tested in SCI and resulted in reduced edema, microglia and astrocytes, but no functional improvement (8).

Regarding **intrinsic inhibitors of axonal elongation**, several therapeutic molecules have been developed to target inhibitory and growth-promoting pathways. Inhibition of PTEN (phosphatase and tensin homologue) has been linked to axon regeneration in CNS, as this leads to Akt and mTOR activation that promote axonal growth. Excluding numerous studies that used genetic PTEN manipulations, only one PTEN-specific small peptide has been developed. This PTEN antagonist peptide (PAP) enhanced growth of descending serotonergic fibers following SCI (48). Nevertheless, there are still limitations in PTEN inhibition, since the regeneration (axon number and growth distance) and functional recovery are limited and age-dependent (21). Inhibition of SOCS3 (suppressor of cytokine signaling 3) is also related to axon regeneration via induction of STAT3. SOCS3 and PTEN could also work synergistically to further increase axon regeneration after ONI and SCI (48).

Rho GTPase is activated by myelin-associated inhibitors and by glial scar components, leading to actin depolymerization, growth cone collapse and p75^{NTR}-mediated apoptosis. Rho pathway has been targeted by direct RhoA blocking via C3 transferase or by inhibiting ROCK (Rho-associated coiled-coil-containing protein kinase) via Y-27632, promoting actin polymerization and regeneration after SCI (50). As cytoskeleton stabilization is essential for axon regrowth, direct modulation of cytoskeleton has been achieved with low doses of the microtubule-stabilizing compounds paclitaxel and epothilone. These compounds have been also shown ability to modulate the inhibitory fibrotic scar (48).

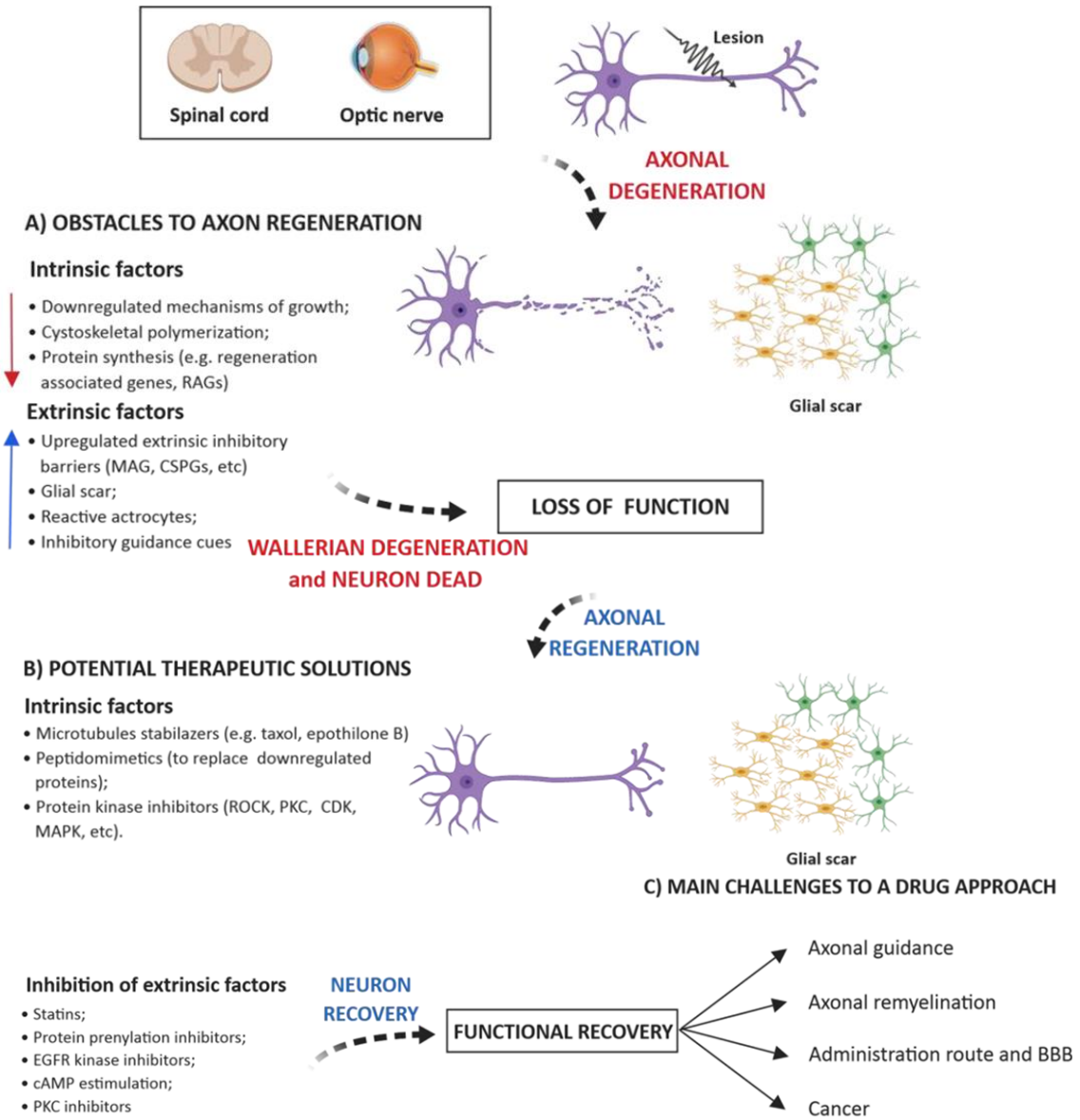

Figure I-7. Candidate molecular therapeutic solutions to target intrinsic and extrinsic factors that inhibit axonal regeneration after ONI and SCI (Adapted from (48)).

Regarding **extrinsic inhibitors of axonal elongation**, several therapeutic molecules have been evaluated for their ability to neutralize the inhibitory components of glial scar and myelin. Myelin-associated inhibitors have been targeted either via antibodies, such as the IN-1 (a blocking antibody of CNS myelin), or via NgR antagonists, such as NEP 1-40 (a binding inhibitor of Nogo-66) and NgREcto (a binding inhibitor of all NgR ligands). IN-1 administration has led to improved functional recovery after SCI, while NEP 1-40 administration promoted regeneration in rat SCI models. Glial scar has been targeted via chondroitinase ABC

(ChABC), which removes chondroitin sulfate chains in CNS lesion sites to neutralize glial scar enhancing regeneration (8,50). However, ChABC treatment resulted in less regeneration compared to an IN-1 antibody treatment because myelin-associated inhibitors are present even in neutralized glial scar, highlighting the importance of multifactorial targeting (8,50).

Limitations of molecular CNS therapies include the inability of multiple therapeutic molecules to pass the BBB and their unfavorable pharmacokinetics and adverse effects when delivered at high doses. Furthermore, many therapeutic molecules are associated with cancer via activation of related signaling pathways. Last but not least, axonal regeneration requires effective axonal guidance, formation of functional synapses and remyelination, highlighting the need for combinatorial treatments (48,51).

5.1.2. Neurotrophins

Neurotrophins (NT) are a protein family that consists of *nerve growth factor (NGF)*, *brain derived growth factor (BDNF)*, *NT-3* and *NT-4/5*. They are synthesized initially as pro-neurotrophins (pro-NT) and get converted into carboxy-terminal mature NTs via intracellular cleavage by furin or pro-convertases (52,53). Each NT binds with high affinity and activates a specific neurotrophin receptor (NTR); NGF binds to tyrosine receptor kinase A (*TrkA*), BDNF and NT-4 to *TrkB* and NT-3 to *TrkC* as well as to TrkA and TrkB with lower affinity (52). All mature NTs also bind with low affinity to the $p75^{NTR}$, a member of TNFR (tumour necrosis factor receptor) superfamily that contains a cytoplasmic death domain. Finally, all pro-NTs bind only to $p75^{NTR}$ with high affinity (52,54,55) **(Fig. I-8)**.

NTs are implicated in neuronal development and survival as well as in axonal outgrowth, guidance and synaptic plasticity in both PNS and CNS (52,54). NTs can even enhance the expression of some growth-associated proteins that are normally downregulated in adults. This has been achieved for example by BDNF treatment in injured RGCs (50). Different neuronal types express different NTRs and, consequently, respond to different NTs (8,50). For instance, NGF administration following SCI did not induce axon outgrowth in CST, which was instead observed under NT-3 administration (56,57).

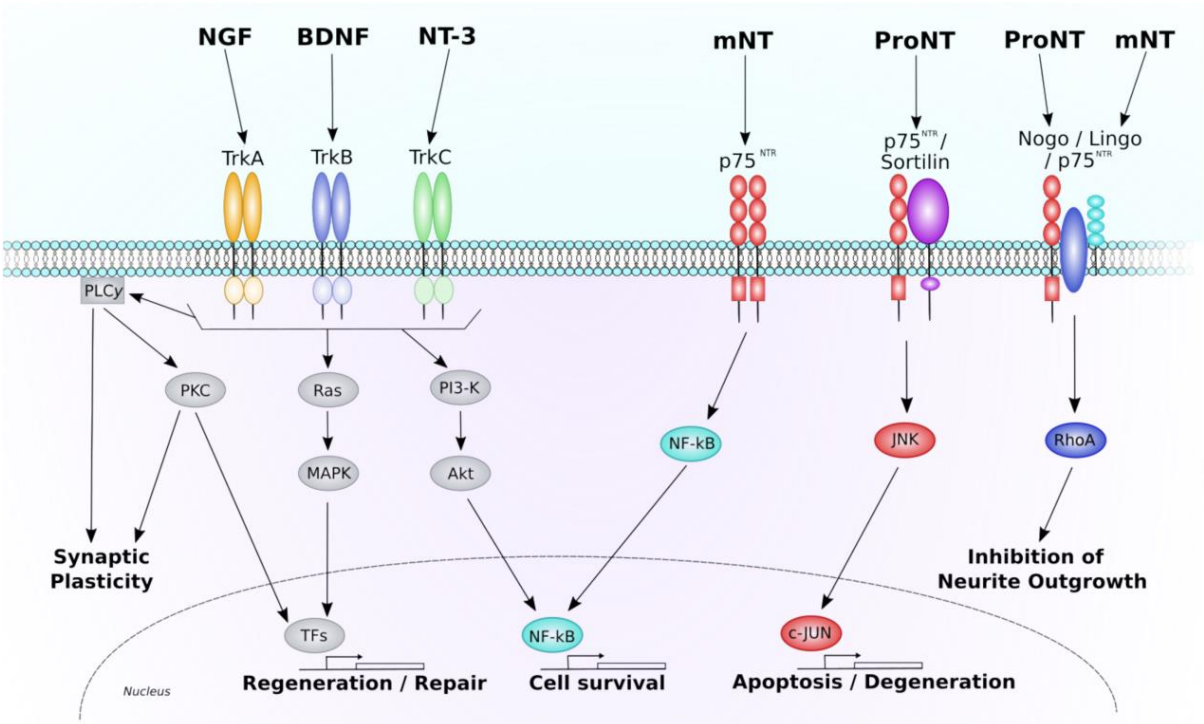

Figure I-8. Schematic overview of NT and pro-NT binding to NTRs, downstream intracellular pathways and main resulting cellular phenotypes (58).

Trk activation by NT binding leads to its dimerization and kinase transphosphorylation in its cytoplasmic domain, leading to the activation of several intracellular signaling pathways; Ras activation activates the MAP kinase pathway, Ras or Gab1 activation leads to phosphatidyl inositol-3 (PI3)-kinase activation, PLC-g1 activation results in the activation of Ca^{2+} / PKC (protein kinase C) pathways. These pathways promote neuronal survival, differentiation, growth and synaptic plasticity (54,55) **(Fig. I-8)**.

Contrary to Trk receptors, $p75^{NTR}$ does not have intrinsic catalytic activity. $p75^{NTR}$ forms a complex with sortilin for pro-NT binding, leading to apoptosis via activation of c-Jun N-terminal kinase (JNK). Several other signaling pathways are activated upon $p75^{NTR}$ activation via adaptor proteins (such as TRAF6, Rip2) recruited to the $p75^{NTR}$ intracellular domain (ICD). RhoGDI adaptor binds to the ICD leading to RhoA activation and, consequently, neurite outgrowth inhibition and growth cone collapse. $p75^{NTR}$ acts as coreceptor of NgR controlling MAG binding. $p75^{NTR}$ can even form a complex with Trk receptors, increasing NT affinity to Trk, and promoting survival via the nuclear factor-kB (NF-kB) activation (52,54,59).

NTs are not only locally produced (e.g. NTs are produced by RGCs or glial cells in retina), but they are also retrogradely transported from distant axons. Axonal bi-directional transport of molecules and organelles (retrogradely and anterogradely) is of high importance since axons can extend over long distances. Transportation of NTs-NTRs occurs via the formation of specific signaling endosomes that contain these complexes (60). More specifically, the ligand-receptor complex gets internalized in axon terminals and active signaling vesicles are formed and transported via microtubules to cell bodies, where the endosomal signaling complex maintains its signaling capacity until its lysosomal degradation. However, the most internalized axonal Trk receptors get recycled to the plasma membrane or proteolyzed in axons, whereas only a few of them undergo transportation (61). Retrogradely transported Trk receptors are replenished via anterograde transport of new ones to the growth cones via the secretory pathway of Golgi transport vesicles. Alternatively, TrkA has been found to be transported anterogradely via a NGF-dependent endocytosis manner, called transcytosis, under a Rab11 recycling endosome. When NGF was added on the distal axon

compartments of sympathetic neurons *in vitro*, its consequent retrograde transport promoted anterograde transcytosis of TrkA (60).

When axonal transport is disrupted in either direction, communication between axons and somas is lost and responses to environmental cues (e.g. following injury) are impeded resulting in axonal degeneration and neuronal apoptosis (62). Thus, the poor survival and regenerative capacity of CNS has been partly attributed to inadequate trophic support. Indeed, NT expression is reduced following CNS injury, while there is also decreased activity of Trk receptors and increased activity of $p75^{NTR}$ not only in neurons, but also in oligodendrocytes, astrocytes and microglia (52,55,59,63). These observations suggest trophic factor supplementation as a potential therapeutic strategy for CNS injury in order to promote neuronal survival and regeneration. Alternatively, $p75^{NTR}$ targeting has been tested via a $p75^{NTR}$ antibody or siRNA (50,55). However, $p75^{NTR}$ targeting is controversial, because $p75^{NTR}$ may also have a positive effect by increasing Trk activation or suppressing inappropriate growth and axon targets (59).

Among NTs, the present thesis focuses on **NGF**, the prototypic member of the NT family. Regarding the role of NGF in SCI, NGF and its receptors (TrkA, $p75^{NTR}$) are expressed in spinal cord under normal conditions (64–66), while low levels of NGF are observed following SCI. Following SCI, NGF expression was detected just in meningeal cells and Schwann cells in nerve roots (45). SCI does not induce NGF expression in spinal cord oligodendrocytes, in contrast to PNS axotomy that induces robust NGF expression in Schwann cells. Following SCI, NGF administration induced tract-specific neurite growth (56,57), reduced neuronal death (67–69), inhibited autophagy (69) and led to behavioral improvement (67–70).

Regarding the role of NGF in ONI, RGCs express NGF and its receptors (TrkA, $p75^{NTR}$) under normal conditions (71). $p75^{NTR}$ has low expression in RGCs and robust expression in Müller cells (72). It is proposed (NT hypothesis) that the obstruction of retrograde transport at the optic nerve head following ONI results in the deprivation of NT support to RGC leading to apoptotic cell death (73). TrkA and $p75^{NTR}$ expression alterations after ONI are contradictory depending on the time and method of quantification. Nevertheless, the key point is not their alteration, but mainly the balance between proNGF/NGF and TrkA/$p75^{NTR}$, since NGF/TrkA signaling favors survival while proNGF/$p75^{NTR}$ can induce apoptosis (74). Following ONI, ocular administration of NGF (i.v. or via eye drops) reduced RGC loss (75–77). Specifically, NGF administration reduced $p75^{NTR}$ and proNGF expression, enhanced TrkA phosphorylation and promoted axonal regrowth via reducing the number of cells co-expressing Nogo-A/$p75^{NTR}$ at crush site borders (76). These observations indicated that NGF administration can restore the balance between TrkA and $p75^{NTR}$, which is perturbed by injury in ways that favor proNGF/$p75^{NTR}$ binding (63,76). Contrariwise, proNGF led to RGC death in the adult rodent retina indirectly via TNFα production by Müller cells and the cooperation of $p75^{NTR}$, sortilin and NRAGE adaptor protein (78).

NT treatments for CNS injuries have demonstrated enhancement mainly in histological outcomes but not in behavioral ones (8). One explanation on the limited efficiency of NTs on chronic CNS injury models could be the loss of NTRs in injured neurons (e.g. RGCs) leading to transient effects (8,73). Indeed, it has been shown that the effect of exogenous BDNF in ONI-induced RGC death was transient because of reduced TrkB expression (79). Moreover, compartmentalized neuronal cultures have also shown that the location of NGF application matters for axonal elongation. When NGF was added in axons only, they could be extended, while when added in cell somas only, neurons survived, but axons degenerated (61). In addition, studies have highlighted the importance of combining NTs with other therapeutic molecules or transplants. For example, combination of NT-3 with the IN-1 antibody led to a non-inhibitory myelin environment in a spinal cord lesion and resulted in improved axonal outgrowth compared to NT-3 alone (50).

A major **limitation** for NT-based therapeutics is their unfavorable pharmacological properties including pharmacokinetics (short half-life and inability to pass the BBB) and side effects, such as NGF-induced hyperalgesia and $p75^{NTR}$ activation (55,80). Such limitations have led to the development of small-molecule NT mimetics such as D3, a TrkA agonist that has already been evaluated in a Phase 3 clinical trial for dry eye (55). In addition, significant research has focused on developing means of NT administration that can bypass the BBB (81), including intranasal delivery (66), local BBB disruption using ultrasound (68) and the delivery of NGF-expressing genetically modified cells in the lesion site such as fibroblasts (57,82,83), Schwann cells (84) or NSCs (69,70). This thesis focuses on a specific type of small-molecule NT mimetics, microneurotrophins (MNT), as well as their local administration via porous collagen-based scaffolds (PCS).

5.1.3. Microneurotrophins

Key limitations of endogenous NTs regarding therapeutic applications can be bypassed by **MNTs**. MNTs are C17-spiroepoxy small-molecule derivatives of dehydroepiandrosterone (DHEA) that specifically activate NTRs and can pass the BBB (85). DHEA is a neurosteroid produced in brain. DHEA levels decline with aging and degenerative diseases (86). It has been demonstrated that DHEA has the ability to bind and activate all NTRs leading to neuroprotective effects (85). For instance, DHEA administration protected retina from AMPA excitotoxicity via TrkA (87). DHEA also inhibited acute microglia-mediated inflammation via activation of the TrkA-Akt1/2 pathway (88). Contrary to DHEA, MNTs are not metabolized to estrogens and androgens and do not activate steroid hormone receptors, avoiding the side effects that limit the clinical use of DHEA (89).

This thesis focuses on the MNT **BNN27 (Fig. I-9)**, a NGF analog that can activate both its receptors (TrkA, $p75^{NTR}$). The permeability of BNN27 in rodent CNS was evaluated by previous pharmacokinetic studies that demonstrated the presence of BNN27 in rodent brain and retina 30 min after intraperitoneal (i.p.) injection. BNN27 concentration peaked in the retina 2 hours after i.p. injection and could not be detected 4 hours later (90,91).

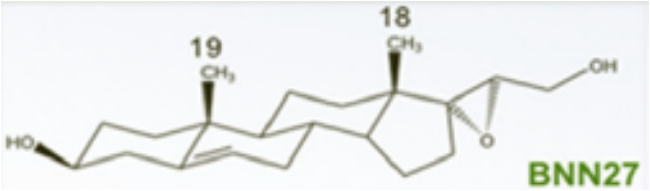

Figure I-9. The structure of MNT BNN27 (92).

BNN27 has demonstrated various effects related to CNS injury response. It has demonstrated neuroprotective effects on various kinds of neurons (e.g. Superior Cervical Ganglion cells, Cerebellar Granule Neurons) *in vitro* mediated via both NGF receptors and downstream pro-survival pathways as well as decreased apoptosis of $TrkA^{+}$ sensory neurons in E13.5 NGF-null mice embryos (92,93). BNN27 administration decreased retina cell apoptosis in a rat model of diabetes-induced retinal damage via the activation of TrkA and the downstream pathways, $p75^{NTR}$ downregulation, decrease of caspase 3 activation and pro-inflammatory cytokines and increase of anti-inflammatory cytokines (94,95). BNN27 has also demonstrated effects on glial cells: BNN27 rescued cuprizone-challenged oligodendrocytes, increased their maturation and reduced microglia activation *in vitro* as well as rescued oligodendrocytes and reduced astrogliosis and microgliosis in a mouse cuprizone-induced demyelination model (96). Interestingly, BNN27 lacks the hyperalgesia effects of NGF and, as recently demonstrated, it has even analgesic effects via NGF inhibition in DRG and activation of TrkA and downstream AKT2 pathway (97). Nevertheless, prior to this thesis, the effects of BNN27 have not been evaluated in any CNS injury model, either in the form of a monotherapy or as a part of a combinatorial therapy.

5.2. Stem Cell therapies

5.2.1. Overview

Cells are key components of regenerative medicine treatments. Several kinds of **stem cell therapies** have shown promising results in preclinical CNS injury models. Their use focuses on replacing neural cells lost during injury and re-establishing connectivity in the lesion site (98). Such therapies include various stem cell types such as embryonic stem cells (ESC), mesenchymal stem cells (MSC), olfactory ensheathing cells (OEC), neural stem cells (NSC) and induced pluripotent stem cells (iPSC) (8) **(Fig. I-10)**. The application of NSCs, the focus of this thesis, is presented in detail in the following section.

ESCs are pluripotent cells that can self-renew indefinitely and differentiate to cell types derived from all three germ layers. ESC-derived neurons, OPCs or oligodendrocytes led to remyelination and functional recovery when transplanted in SCI animals. However, the potential of ESCs clinical translation is limited by ethical concerns and the risk of teratoma formation (8,99).

Over the past decade, there is an increasing number of experiments that use **iPSCs**, which are generated by reprogramming of terminally differentiated cells into pluripotent ones. Compared to ESCs, iPSCs have no ethical concerns, yet teratoma formation remains a risk. Interestingly, iPSCs can be used as source for autologous transplantation (e.g. from patient's skin) (8,99). However, iPSCs preparation takes at least 4 months, while SCI transplantation is more efficient the first few weeks following SCI. Thus, stocks of iPSCs with various human leukocyte antigens (HLAs) have started to be constructed for safe regenerative medicine without immunological rejection problems (100). In order to reduce the time production and avoid teratoma formation, a new strategy has been rapidly advanced with direct reprogramming of somatic cells into NSCs or neurons bypassing the pluripotency stage (100).

MSCs are multipotent cells that can be isolated from adult or post-natal tissues, such as bone marrow, adipose and umbilical cord. MSCs have low immunogenicity and can be used in autologous transplants (8). Although their mechanism of action has not been defined accurately, transplanted MSCs have demonstrated decreased astrogliosis and microglia activation as well as functional recovery following SCI (101). Compared to ESCs, MSCs offer easier isolation and expansion without ethical concerns. Clinical trials of MSCs have reported their safety in SCI patients, but trials of larger scale are needed to confirm the preliminary findings of functional improvement (102).

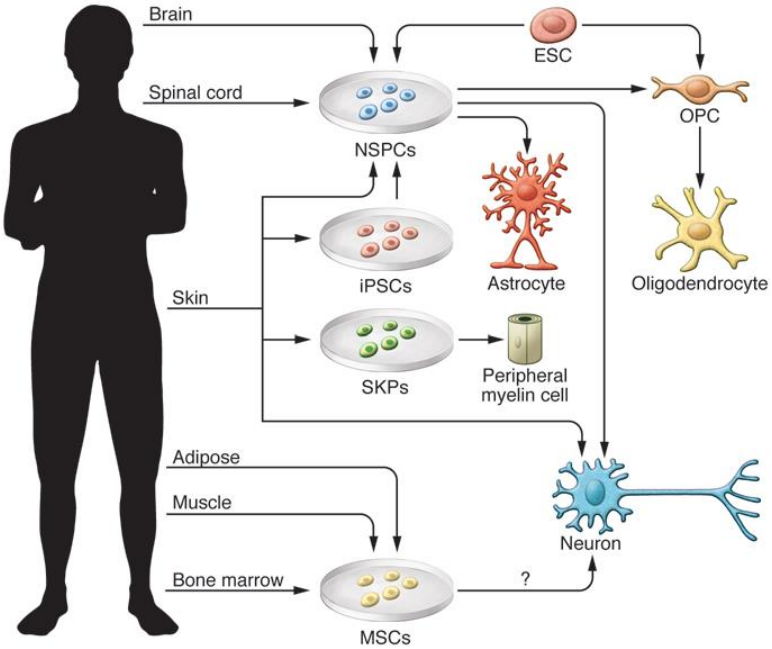

Figure I-10. Source of stem cells for transplantation in CNS injury (99).

OECs are glial cell types that support olfactory neurons and guide their axons into the olfactory bulb. Their transplantation in SCI models has resulted in improved histological and behavior response. OECs have led to astrogliosis decrease and secretion of neurotrophic factors. In addition, OECs can remyelinate regenerated axons via their ability to migrate for long distances in the injured CNS. Clinical trials have demonstrated safety and a few cases of improvement in SCI patients. However, more experiments are needed since OEC mechanism of action is not clear yet and their therapeutic effects are not always replicable (8,50).

Except for stem cells, **Schwann cell** implantation has been used in SCI. Schwann cells promote axon regeneration in PNS via growth factors secretion, expression of surface adhesive molecules and production of ECM molecules that promote axon growth. Similarly, transplanted Schwann cells in SCI resulted in reduced cavity, enhanced outgrowth and myelination of axons and functional recovery (8,103). However, Schwann cells have limitations, such as poor regeneration of CST and no exit of axons that enter grafts under their presence. Thus, they have been used in combination with other agents, such as NTs or blockers of inhibitory molecules, in order to emphasize Schwann cells advantageous effects and limit the inhibitory cues of the lesion (8,50).

The previous paragraphs of this section focused on cell therapies for SCI. There are a few studies where cell transplantation has been evaluated following ONI. MSC paracrine-mediated neuroprotection has been observed in several retinal degenerative conditions (104). Dental Pulp Stem Cells (DPSC) and bone marrow-derived MSCs were i.v. injected in an ONC model and induced significant RGC survival and axonal outgrowth. An *in vitro* study showed that both MSCs and DPSCs provided NT to RGCs and that these effects were abolished upon Trk receptor inhibition (105). MSC effect on RGC survival and long-distance axon regeneration was maintained even 240 days post injury, but did not lead to visual recovery (106). While retinal cells can be generated from iPSCs in 3D organoid cultures *in vitro*, these findings have not been clinically applied yet. RGCs or retinal progenitors transplantation by i.v. injection had promising results by migrating in retina and differentiating into neurons, yet their efficacy needs to be improved (107,108).

Despite the significant progress in stem cell therapies, there are still **limitations** that impede their clinical use. More effort is needed in order to elucidate their mechanisms of action and to find solutions to control

their survival, proliferation and differentiation in lesion sites as well as their spatial and temporal integration into the host neural circuitry (103,109). Another challenge to be faced is the necessity to acquire high quantity of purified stem cells for their clinical use (44).

5.2.2. Neural Stem Cells

NSCs are multipotent cells that can differentiate into neurons, astrocytes and oligodendrocytes. NSCs can be isolated from embryonic and adult CNS or derived by differentiating iPSCs or by transdifferentiating somatic cells (110). NSCs are expanded *in vitro* usually as neurospheres, but their differentiation potential decreases through passages. In adults, NSCs are found in the subventricular zone of forebrain and the dentate gyrus of the brain hippocampus (99). Interestingly, potential endogenous NSCs, called ependymal cells, are found in the central canal of spinal cord, as well. Following SCI, ependymal cells get recruited and proliferate in the lesion site, but they do not have the ability to replace lost neurons; they mostly differentiate into astrocytes and to a lesser degree into oligodendrocytes and participate in the glial scar formation (100,111).

As transplants in SCI lesions, NSCs replace lost neuronal cells and secrete neurotrophic factors (8,103). NSC-based therapies have shown promising preclinical results in SCI, including the extension of a high number of axons outside the lesion over long distances and synapse creation with CST axons resulting to functional recovery (112,113). The same results were demonstrated upon human NSC or human iPSC-derived NSC transplantation in rats and monkeys, as well, suggesting no species specificity and translational potential (112,114–116). A more detailed and long-term study (18 months) showed that when human NSCs were transplanted in rodents, they retained their intrinsic rate of maturation over this period, an important finding to consider for the design of clinical trials (117). Functional recovery was linked to both neuronal and glial maturation (117). For instance, differentiation of transplanted NSCs into oligodendrocytes led to increased axon myelination that has important role in functional improvement (103). Interestingly, different forms of transplanted NSCs (differentiated and non-differentiated unicellular NSCs or neurospheres) in a transected SCI model resulted in functional recovery and demonstrated that their effect was associated with their NT secretion and not their form (118). Similarly, both developing and fully mature NPC grafts resulted in CST regeneration, indicating that various differentiation stages enhance regeneration, provided that they are derived from the same region (NPCs isolated from spinal cord) (113).

Although NSC-based treatments are progressing towards human clinical evaluation (119), much work remains to enhance their efficacy and suppress limitations concerning their survival, differentiation and unavailable autologous sourcing (99,120). Within a CNS lesion, NSCs have low survival and differentiate mainly towards glial cells as a consequence of the provided environmental cues. For instance, NSC implanted in the neurogenic region of hippocampus differentiated into neurons, while their transplantation into the spinal cord resulted in glial cells (8,121,122). The differentiation of grafted NSCs into astrocytes has even been associated with allodynia (99). One approach to bypass poor neuronal differentiation of NSCs is the utilization of neuronal- or glial-restricted precursors (NRPs or GRPs), which differentiate into neurons or glial cells respectively, independently of the environmental cues (123). Ethical concerns and NSC autologous preparation can be addressed by the use of iPSCs to generate NSCs (100).

One approach to enhance the efficacy of NSC-based treatments is to combine them with therapeutic molecules or biomaterials (further discussed in section I-5.3). Cells can be accompanied with therapeutic molecules or be genetically manipulated to secrete factors that face the inhibitive cues of injury site and promote axonal growth (103). For instance, ChABC enhanced NPC transplantation (integration, migration and differentiation) in spinal cord lesion site by reducing the glial scar. Moreover, combination of NPCs, growth factors and ChABC induced axonal plasticity and improved behavior in the same model compared to

NPC alone (124). Regarding NGF effects on NSCs, various types of embryonic rodent NSCs have been reported to express both $p75^{NTR}$ and TrkA NGF receptors (125,126). NGF could increase *in vitro* proliferation of NSCs isolated from embryonic E14 rat brain or adult rat spinal cord (127,128). Implantation of NSCs that overexpress NGF reduced lesion cavity and astrogliosis and enhanced functional recovery in a SCI rat model (70).

5.3. Biomaterials

5.3.1. Overview

Biomaterials are a key component of regenerative medicine treatments. Once placed in an injury site, biomaterials provide structural support, inflammation regulation and a substrate for cellular migration and axonal elongation. For doing so, biomaterials need to have optimized physicochemical properties (chemical composition, surface chemistry, structure, mechanical stiffness, degradation rate) and low immunogenicity (37,44,103,129). The present thesis focuses on PCS, a particular type of sponge-like biomaterials fabricated via freeze-drying. This section provides an overview of biomaterials and is followed by a more detailed report on PCS.

Many biomaterials are made of *biopolymers* [usually components of the CNS extracellular matrix (ECM)] that can regulate cellular proliferation, differentiation and migration, such as hyaluronic acid, collagen, gelatin and fibrin. Other biomaterials are made of *synthetic polymers*, such as poly(caprolactone) (PCL), poly(lactic acid) (PLA), polyglycolic acid (PGA), and poly(lactic-co-glycolic acid) (PLGA). Most biomaterials are fabricated as *hydrogels*, others (*scaffolds*) are fabricated in dry state via freeze-drying or electrospinning (37,51).

A large number of *in vitro* studies have shown that the physicochemical properties of a biomaterial have strong influence on its ability to regulate the phenotypes of seeded cells. For example, scaffolds made of CNS-derived ECM led NSC differentiation to neurons compared to non-CNS-derived ECM that did not (130). NPC differentiation into oligodendrocytes is more effective in hydrogels composed of collagen, hyaluronic acid and laminin compared to hydrogels composed of combinations of any two of them or only one material (131).

Regarding the applications of biomaterials on **implants for CNS injuries**, biomaterials have been used as **bridges** that can guide axons into the CNS lesion, improve the lesion environment and allow infiltration of host cells (103,132). Self-assembling peptide nanofiber scaffold provided the appropriate environment in injured optic nerve resulting in axonal regeneration, partial reconnection to the brain and functional recovery (133).

Biomaterials are also used to develop **delivery systems of therapeutic molecules** locally at lesion sites. Bolus injection of a therapeutic molecule near or into the lesion site results in a transient effect due to diffusion and clearance and, consequently, in multiple injections that can cause infections. Moreover, intrathecal or i.v. infusion as invasive can cause further damage, while systemic delivery can cause off-target effects or be inappropriate for therapeutic molecules that do not pass the BBB. Contrariwise, when therapeutic molecules are delivered via biomaterials, biomaterial degradation, binding affinity and diffusion speed of therapeutic molecules allow the control of their time release, bioavailability and toxicity (132,134,135). For example, NT-3 loaded in chitosan carriers resulted in neurogenesis and functional recovery after being placed in transected spinal cord (136). A PGA/chitosan conduit coated with the neural cell adhesion molecule L1-Fc induced further axonal regeneration and remyelination in an ONI model compared to PGA/chitosan conduit alone (137). NTs conjugated to magnetic nanoparticles reduced RGC loss induced by oxidative stress

compared to NTs alone (138). However, a challenge of this delivery method is the maintenance of therapeutic molecule activity and desirable dose (132).

As described in section I-5.2, injury environment highly affects the viability and fate of implanted stem cells. Moreover, cell transplantation in solution can result in cell aggregation, cell death and dispersion instead of integration into the lesion site (139). For instance, RGCs injected into the vitreous did not have spatial organization and did not integrate correctly (140). Thus, biomaterials are also utilized to develop **delivery systems of cells** into lesion sites. Their specific type and defined 3D architecture provide a physical support, ameliorate the injury microenvironment and help the cells integration, viability, differentiation and orientation as well as axonal guidance, elongation and myelination (141). PGA scaffold seeded with human NPCs was transplanted in a hemisection SCI model and led to vascularization, decreased glial scar, axon elongation and functional recovery (142).

Finally, the efficacy of cell-seeded biomaterial grafts can be enhanced via their combination with biologically active therapeutic molecules. Controlled release of therapeutic molecules can benefit both implanted cells and host tissue. On the one hand, it improves cell delivery and integration as well as modulates cell differentiation fate. On the other hand, it enhances the host tissue regeneration (132). For instance, combination of growth factors, fibrin scaffold and ES-derived NPCs in a SCI model enhanced NPC survival and differentiation into neurons compared to scaffold-NPCs only (73). Decellularized optic nerve scaffold seeded with NT-3-overexpressing Schwann cells resulted in axon regeneration and remyelination in a SCI model (143). The degree of RGC regeneration following ONI was more increased upon the combination of matrigel graft seeded with Schwann cells and BDNF and/or NT-4 compared to graft with cells only placed in the transected optic nerve (144).

5.3.2. Porous Collagen-based Scaffolds

As biopolymer, collagen is biodegradable, has natural binding sites for cells and provokes less immune response (103,145). **PCS**, a particular type of sponge-like biomaterial that will be utilized in this thesis, has been shown to induce regeneration following trauma and has received FDA approval for PNS injuries (146,147). This specific and well-characterized PCS has been tested in a transected SCI model. In this study, PCS-alone or seeded with adult NSCs decreased lesion cavity 6 weeks post injury (wpi), but did not result in functional recovery (148).

Several studies have reported the application of other collagen scaffolds in SCI models. Implantation of collagen scaffolds in a SCI model increased neurofilament expression within the injury site at 4 wpi (149). When combined with BDNF, collagen scaffolds have even resulted in functional improvement in SCI (134,150). Transplantation of NSCs seeded in collagen scaffold in a transected SCI model resulted in functional recovery, as well (118). Another study showed that although collagen/silk fibroin scaffolds only decreased cavity and glial scar in a transected SCI model, when seeded with NSCs they led to even more significant result (151). Interestingly, collagen scaffolds have also been used as supportive matrix in human umbilical cord MSCs in rats, canines as well as humans in phase I clinical trial without serious complications and resulted in neurological function recovery during their 12 month follow-up (152).

5.4. From Preclinical Studies to Effective Treatments for Central Nervous System Injuries

A key consideration about CNS injury is its multifactorial nature of events highlighting the need of combinatorial treatments. Thereafter, regenerative medicine field is of high importance, yet very challenging. As described in the chapter I-5, various therapeutic molecules, cells and biomaterials as well as

various combinations among them have been tested with promising results. Nevertheless, the most appropriate combination for the clinical application has not been designed yet. Thus, there is need to select and characterize the components of each treatment more precisely.

Additionally, the physiopathology of CNS injury is dynamic and the different kinds of events need to be targeted in different time points. Thus, not only the treatment components, but also the time of administration/transplantation is important. For instance, the implants are required immediately after the injury for targeting the acute and subacute events, but the control of the long-term release of therapeutic molecules that promote axon regeneration and connectivity needs to be developed for the chronic phase, as well (44,129).

Another challenge is the animal models that are used in preclinical studies. Most of them are transection ones. Although these models are good to study regeneration, they are not close to clinical cases, so more contusion and compression models should be investigated (8).

Last but not least, combination of knowledge and effort from various fields including biology, chemistry, materials science, bioengineering and neurosurgery is essential for designing and introducing the efficient treatment into the clinic (153).

II. Aim of the Thesis

The main objective of this thesis is the design of combinatorial treatments by integrating state-of-the-art cellular therapies (neural stem cells, NSC), 3D biomaterials (porous collagen scaffolds, PCS) and small molecule compounds (microneurotrophins, MNT) that can cope with the complexity of CNS injuries and provide neuroprotection and/or neurogenesis emphasizing on their clinical translation. For this purpose, the treatments are evaluated in two established animal models of CNS injury of clinical relevance: the optic nerve crush (ONC) model and the dorsal column crush spinal cord injury (SCI) model, dividing the thesis in the following 2 parts:

I. Evaluation of the effects of BNN27 administration on the mouse ONC model

The first part of the thesis aims to investigate:

- BNN27 effects on crucial events following ONC via histology
- BNN27 effects on vision impairment following ONC via behavioral assays
- The effects of two different methods of BNN27 delivery: (1) eye drops administration and (2) entrapment in a PCS via a self-assembled peptide and placement around the optic nerve at the injury site
- BNN27 delivery to the target tissues (retina, optic nerve) via Liquid Chromatography-Mass Spectrometry (LC-MS)
- BNN27 release from PCS *in vitro* via spectroscopy
- Effects of more MNTs on crucial events following ONC *ex vivo* or *in vivo*

II. Evaluation of the effects of NSC-seeded PCS grafts combined or not with systemic administration of BNN27 on the mouse dorsal column crush SCI model

The second part of the thesis aims to investigate:

- Effects of NSC-seeded PCS grafts on crucial events following SCI via histology
- Effects of NSC-seeded PCS grafts on locomotion recovery following SCI via behavioral assays
- BNN27 effects on crucial events following SCI via histology
- BNN27 effects on locomotion recovery following SCI via behavioral assays
- BNN27 effects on proliferation and differentiation of mouse embryonic E13.5 NSCs *in vitro*
- BNN27 effects on survival and differentiation of implanted NSCs in injury site following SCI *in vivo*

III. Materials & Methods

1. Animals

Animal care and experimentation protocols were performed according to the Veterinary Directorate of the Region of Crete and FORTH ethics committee, in compliance with EU guidelines 2010/63/EU. C57/BL6 (154) and Rosa26-YFP mice [contain a floxed yellow fluorescent protein (YFP) gene] (155) were maintained in climate-controlled conditions (30–50% humidity, 21 ± 2 °C, 12:12 h light/dark cycle) with *ad libitum* access to food and water. Rosa26-YFP mice were crossed with CMV-Cre transgenic mice (156) to obtain mice that expressed YFP in all tissues.

2. Scaffold Fabrication

Collagen scaffold (CS) sheets and collagen-GAG scaffold (CGS) sheets were fabricated [by Dr. D. Tzeranis (IMBB-FORTH and University of Cyprus)] by lyophilizing a 5 mg/ml microfibrillar collagen I suspension in 50 mM acetic acid (CGS suspension includes 0.44 mg/ml chondroitin-6-sulfate), as described in (157). The resulting 2.5-mm-thick dry sheets were cross-linked via dehydro-thermal treatment (105°C, 50 mTorr, 24 h). Scaffold structure was verified by Scanning Electron Microscopy **(Fig. III-1)**. CS or CGS samples were cut from sheets via laser ablation [by F. Moschogiannaki (University of Crete)].

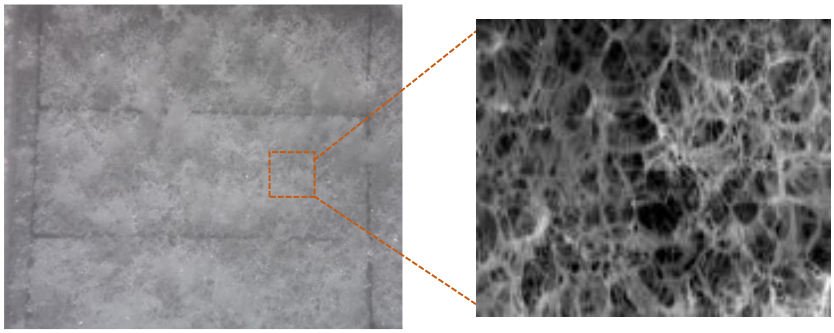

Fig. III-1. Microscopy image of CGS samples cut in a CGS sheet (left). Scanning Electron Microscopy image of a CGS sample (right).

3. Primary Neural Stem Cell Isolation and Culture

NSC isolation was performed from brain tissue (cortex) of mouse embryos (E13.5) via enzymatic digestion of the cortex [adapted from (158,159)]. Mouse embryos were obtained either by crossing wild type C57/BL6 mice or by crossing Rosa26-YFP with CMV-Cre transgenic mice. Specifically, pregnant mice (gestational day 13.5) were sacrificed via cervical dislocation and embryos were carefully removed. Embryos' cortical hemispheres were washed gently in Hank's balanced salt solution (HBSS; Thermo #14185-045) with 5% penicillin/streptomycin (Thermo #15140122) and were mechanically dissociated for NSC isolation in complete NSC medium [Dulbecco's modified Eagle's medium (DMEM)/F12 (Thermo #41966029), B27 supplement minus Vitamin A (Thermo #12587010), 0.6% D-glucose (Sigma #G8769-100ML), 50 mg/ml primocin (InvivoGen #ant-pm-1), 20 μg/ml Fibroblast growth factor 2 (FGF2; R&D #233-FB-025), 20 μg/ml Epidermal growth factor (EGF; R&D #236-EG-200)]. $2.5 \cdot 10^5$ NSCs were seeded in T25 flasks in 5 ml complete NSC medium and were kept at 37°C and 5% CO_2. 1 ml of fresh medium was added every other day. Neurospheres were formed within 2 days and were dissociated by accutase (Sigma #A6964) at 4 or 5 days *in vitro* (DIV). Dissociated NSCs were either passaged or used for experiments (passages 3–8).

In case of embryos harvested from Rosa26-YFP and CMV-Cre mice crossings, care was taken in the first passage to pick and keep neurospheres of YFP-expressing embryos: the dissociated NSCs of each embryo were seeded in a separate well. Neurospheres of YFP-expressing embryos were selected under a fluorescent microscope the day of the first passage for further culture **(Fig. III-2)**.

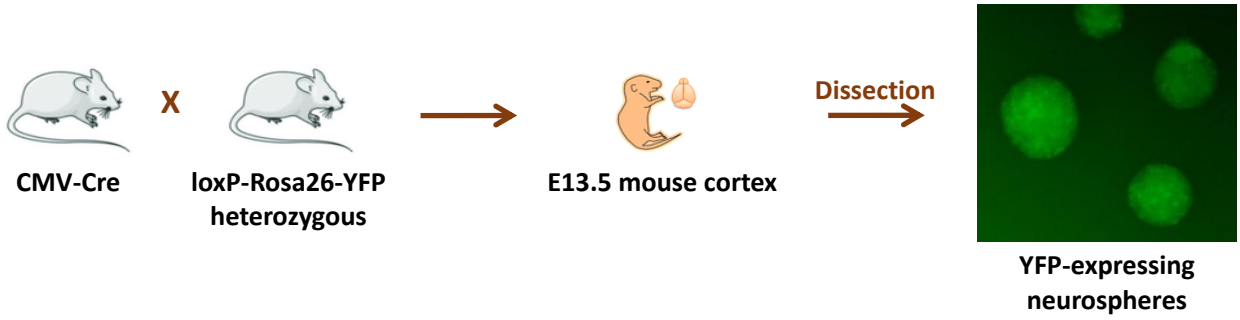

Fig. III-2. Schematic representation of YFP-expressing NSC isolation from the cortex of E13.5 mouse resulting from crossing CMV-Cre and Rosa26-YFP mice.

4. Neural Stem Cell *In Vitro* Proliferation Assay

Dissociated NSCs ($3 \cdot 10^4$/well) were seeded in 48-well-plate coated with Poly-D-Lysine (PDL; Thermo #A3890401) and laminin (Sigma #L2020) in NSC complete medium (2D culture). At 2 DIV, medium was replaced with complete NSC medium that lacked FGF2 and EGF with or without BNN27 [obtained by Dr. T. Kalogeropoulou (National Hellenic Research Foundation); 0.1 μM or 1 μM diluted in 1% DMSO], resulting in the following experimental conditions: (a) "Complete Medium": complete NSC medium, (b) "No Factors": complete NSC medium without FGF2 and EGF, (c) "No Factors + DMSO": "No Factors" medium with 1% DMSO, (d) "No Factors + 0.1 μM BNN27": "No Factors" medium with 0.1 μM BNN27, (e) "No Factors + 1 μM BNN27": "No Factors" medium with 1 μM BNN27. 24 hours after treatment (3 DIV), cells were fixed (as described in section III-6). 4 hours before fixation, cells were pulsed with 1 μM Bromodeoxyuridine (BrdU; BD Pharmingen #550891).

5. Neural Stem Cell *In Vitro* Differentiation Assay

Dissociated NSCs were seeded in a 1×1×1.5 mm CS sample (3D culture) by placing a 2 μl drop containing $3 \cdot 10^4$ NSCs on a 48-well-plate well, placing the CS sample on it to absorb them, incubating the cell-seeded scaffold at 37°C for 15 min (let NSCs attach to the CS) and adding 300 μl complete NSC medium per well. At 2 DIV, complete NSC medium was replaced by complete NSC medium that lacked FGF2 and EGF with or without BNN27 (0.1 μM or 1 μM diluted in 1% DMSO), resulting in the following experimental conditions: (a) "Complete Medium", (b) "No Factors", (c) "No Factors + 0.1 μM BNN27", (d) "No Factors + 1 μM BNN27". NSC-seeded CS were fixed 5 days later (as described in section III-6).

6. Immunocytochemistry and Image Processing of Neural Stem Cell Samples

At indicated days, NSCs grown on 48-well-plates or inside 1×1×1.5mm CS samples were washed twice in Phosphate-Buffered Saline (PBS) and fixed with 4% paraformaldehyde (PFA) in PBS at 4°C for 15 min. Samples were washed twice in PBS, once in 0.1% Triton X-100 (Sigma #X100) in PBS (PBST), blocked in 0.1% bovine serum albumin (BSA), 10% goat or horse serum in 0.3% PBST at room temperature for 1 h, incubated in primary antibodies **(Table III-1)** diluted in 1% goat or horse serum in 0.1% PBST at 4°C overnight, washed twice in 0.1% PBST, incubated in fluorophore-conjugated secondary antibodies **(Table III-2)** diluted in 0.1% PBST at room temperature for 1 h, washed twice in 0.1% PBST, once in PBS, counterstained with Hoechst 33342 (Thermo) and washed twice in PBS. For BrdU immunocytochemistry, after PFA fixation, NSCs were incubated in 2N HCL at 37°C for 30 min and then were neutralized with 0.1 M sodium borate buffer pH 8.5 at room temperature for 10 min.

Stained NSCs were imaged either in an epifluorescence microscope (AXIO Vert A1, Zeiss, Jena, Germany) using a ×32 objective lens or in an inverted confocal microscope (TCS SP8, Leica Microsystems, Wetzlar, Germany) using a ×40 water-immersion objective lens.

Table III-1. Primary antibodies used in immunocytochemistry protocols.

Antigen	Primary antibody	
	Vendor, Catalogue #	Dilution
BrdU	Thermo #B35128	1:200
GFAP	Millipore #AB5541	1:1000
Green Fluorescent Protein (GFP)	Minotech #701-1	1:200
Nestin	Novus #NB100-1604	1:1000
RBPMS	Millipore #ABN1376	1:200
Tubulin β3 (Tubb3)	Covance #MMS-435P (clone Tuj1)	1:400
Tubulin β3 (Tubb3)	Biolegend #801201 (clone Tuj1)	1:1000

Table III-2. Secondary antibodies used in immunocytochemistry and immunohistochemistry protocols.

Secondary antibody	Vendor, Catalogue #	Dilution
anti-Chicken IgY (H+L), Alexa Fluor 546	Thermo #A11040	1:1000
anti-Goat IgG (H+L), Alexa Fluor 488	Thermo #A-11055	
anti-Guinea Pig IgG (H+L), Alexa Fluor 647	Jackson #106-605-003	
anti-Mouse IgG (H+L), Alexa Fluor 488	Thermo #A-11029	
anti-Mouse IgG (H+L), Alexa Fluor 488	Jackson #115-545-003	
anti-Rabbit IgG (H+L), Alexa Fluor 488	Thermo #A-11008	
anti-Rabbit IgG (H+L), Alexa Fluor 546	Thermo #A10040	
anti-Rabbit IgG (H+L), Alexa Fluor 647	Thermo #A21244	
anti-Rat IgG (H+L), Alexa Fluor 633	Thermo #A-21094	

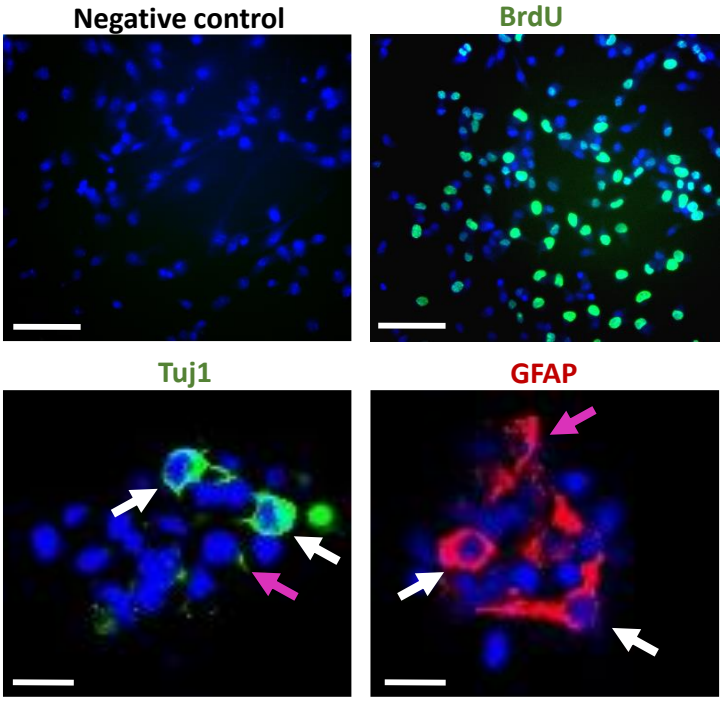

Fig. III-3 Representative fluorescence microscopy images of NSC-derived cells immunostained for BrdU, Tuj1 and GFAP. NSCs were stained for BrdU (2D culture), Tuj1 or GFAP (3D culture). Negative control (top left) of BrdU staining corresponds to staining of cells without adding a primary antibody. BrdU$^+$ cells (top right) express BrdU in their nucleus. Tuj1$^+$ (bottom left) and GFAP$^+$ cells (bottom right) express Tuj1

and GFAP in their cytoplasm and were confirmed in each z-stack. White arrows show Tuj1$^+$ and GFAP$^+$ cells. Purple arrows show staining that is not confirmed in this z-stack to represent a specific stained cell. Scale bars: 50 µm (top) and 10 µm (bottom).

The fraction of BrdU$^+$, Tuj1$^+$ and GFAP$^+$ cells was counted manually using the "Cell Counter" plugin of the Fiji software. Cell nuclei were counted based on the channel that contains Hoechst emission. Counting of Tuj1$^+$ and GFAP$^+$ cells was based on the staining pattern in multiple consecutive confocal z-stacks due to staining pattern complexity **(Fig. III-3)**. NSC *in vitro* assays, immunocytochemistry and image processing were performed in collaboration with I. Papagiannaki during her Master's Thesis (University of Crete).

7. Adult Retina Explant Isolation and Culture

Adult Retina Explant isolation was performed according to a previously described protocol (160) and the training of Prof. Nawabi (Grenoble Institut des Neurosciences, GIN). Specifically, 4-week-old wild type mice were sacrificed by cervical dislocation and eyes were removed quickly using a pair of Dumont #5 fine forceps and placed in Hibernate A medium without calcium (BrainBits, #HA-CA). Under a stereoscope, eyeball was cut along the line between the anterior and posterior chambers using spring scissors and the retina was dissected from the posterior part by using a pair of Dumont #5 fine forceps and placed in a new dish containing Hibernate A medium without calcium. The retina was cut into small pieces (about 500 µm in diameter) using a scalpel blade, which have a slight curvature with the GCL on their concave side. Then, Neurobasal-A (Thermo #10888022) was removed from glass coverslips (24-well-plate) previously coated with Poly-L-Lysine (PLL; Sigma #P1399) and laminin, a thin layer (20-30 µl) of coating medium [Hibernate A (BrainBits, #HA), Methyl cellulose (Sigma #M0512), 2% B-27 (Thermo #12587-010), L-glutamine (Thermo #25030164)] was added, and retina explants were placed so that GCL faces the coated side of coverslip. 5 min later, 500 µl explants culture medium [Neurobasal-A, 2% B-27, 20mM L-glutamine and 100 units/ml of penicillin/streptomycin (Thermo #15140122)] at room temperature was gently added. At this step, only the retina explants that adhered to the coverslip were further cultured at 37°C and 5% CO_2 up to 2 weeks.

8. Adult Retina Explant Survival and Axonal Elongation Assays

For survival and axonal elongation assays, retina explants from 4-week-old wild type mice were cultured in the presence and absence of MNTs for 2 weeks post-dissection, resulting in the following experimental conditions: (a) DMSO 1 µM, (b) NGF [Alomone #N-100] 100 ng/ml, (c) BNN27 1 µM, (d) MNT10 1 µM, (e) MNT11 1 µM, (f) MNT61 1 µM. All MNTs were obtained by Dr. T. Kalogeropoulou. Treatments were added in the culture medium 1 h after explants isolation, without changing the explants culture medium. In each well, half of the explants culture medium was replenished every 3 days with fresh treatment.

9. Immunostaining of Adult Retina Explant Cultures

At each indicated day, adult retina explants were fixed by adding gently the same volume of fixative (8% formaldehyde, 3% sucrose) as the volume of culture medium directly in each well and incubating for 15 min. Then, explants were washed 3 times in PBS, once in 0.1% PBST, incubated with primary antibodies **(Table III-1)** diluted in blocking solution (3% BSA in PBS) at room temperature for 2 h, washed three times in PBS, incubated in fluorophore-conjugated secondary antibodies **(Table III-2)** diluted 1:500 in blocking solution at room temperature for 1 h, washed three times in PBS and got mounted using Fluoromount-G with DAPI (Thermo #00-4959-52).

Immunostained retina explants were imaged in an epifluorescence microscope (Zeiss) using a ×10 objective lens. Despite various modifications of the immunostaining protocol (e.g. increase of incubation time of

primary and secondary antibodies, adding of blocking step), the resulting images of explants immunostained for the RBPMS RGC marker were blurry and were not utilized in further analysis. RGC axonal elongation was quantified by counting outgoing Tuj1-stained RGC neurites in various distances from explant boundaries ("number of neurites intersects") via image processing using the "Sholl analysis" (with a step of 50 mm) plugin of the Fiji software. Subsequent statistical analysis included retina explants with > 6 outgoing neurites.

10. Optic Nerve Crush Model

This study adapted a standard mouse ONC model (161) in order to evaluate the effects of MNTs delivered via eye drops and biomaterial grafts placed around the ONC lesion [under the training of Dr. M. Savvaki (University of Crete)]. All surfaces, tools and instruments utilized had been sterilized carefully. 2-month-old C57/BL6 male mice underwent systemic anesthesia with i.p. injection of ketamine/xylazine. After verifying the absence of paw reflexes, each mouse was transferred on a heat pad, where ophthalmic ointment was applied to the non-operated eye to avoid eye dryness (right eye; "Intact" group). Then, the conjunctiva of the left eye was incised and the optic nerve was exposed at its exit from the eye globe by gently putting aside the orbital muscles. The optic nerve of the left eye was crushed approximately 1 mm away from the eyeball using a pair of Dumont #5 fine forceps for 10 sec **(Fig. III-4a)**. Great care was taken in order not to damage the ophthalmic artery.

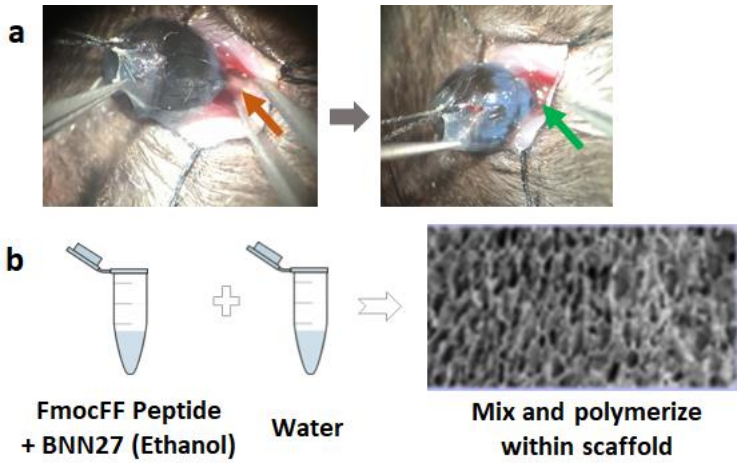

Fig. III-4. ONC Model. (a) Representative images of the ONC surgery. Images highlight the optic nerve before (orange arrow) and after (green arrow) CGS graft placement. **(b)** Schematic description of BNN27 entrapment in FmocFF peptide inside the scaffold.

Mice were organized in five animal groups. In the "Crush" animal group, animals did not receive any treatment following optic nerve crush. In the two grafted animal groups ["Crush (Scaffold)", "Crush+BNN27 (Scaffold)"], a 4x3x1.5mm CGS graft (0.5% mass fraction, 95 µm mean pore diameter) was placed around the crushed nerve site immediately after the crush **(Fig. III-4a)**. In the "Crush (Scaffold)" group, the CGS was soaked in 6 µl FmoFF peptide [2mg/ml; Bachem #B-2150], a self-assembled peptide. In the "Crush+BNN27 (Scaffold)" group, the CGS was soaked in 6 µl solution of BNN27 (30 mM) and FmoFF peptide (2 mg/ml). More specifically, FmoFF with or without BNN27 was diluted in ethanol. The resulting ethanol solution was mixed with H_2O in 1:3 v/v, inducing peptide polymerization. The resulting mix was placed immediately on the top of the CGS graft in order to be absorbed and the peptide to get polymerized into a hydrogel inside PCS pores [in collaboration with C. Apostolidou (University of Crete)]. Consequently, BNN27 was entrapped inside the CGS via the formation of the peptide gel **(Fig. III-4b)**. Two animal groups were treated with BNN27 delivered via eye drops ["Crush+BNN27 (1 drop/day)" and "Crush+BNN27 (2 drops/day)" groups]. Starting one day after surgery, mice were administered with 5 µl BNN27 drops (50 mM diluted in 100% DMSO) in

each eye daily once [“Crush+BNN27 (1 drop/day)” group] or twice [“Crush+BNN27 (2 drops/day)” group]. All animal groups were provided with meloxicam (Metacam) the operation day and the following day for analgesia.

While initially each animal group consisted of 9-10 mice, some of them were excluded from the final results in order to ensure consistent injury in all animals. Exclusion criteria were based on both OMR performance and histology. Mice were excluded when 1) a positive clockwise (CW) response was detected 1 day following ONC or 2) when immunohistochemistry for L1 or Iba1 revealed that the ONC lesion was absent or inadequate. Retina samples were included only if > 2 regions of peripheral retina were well imaged.

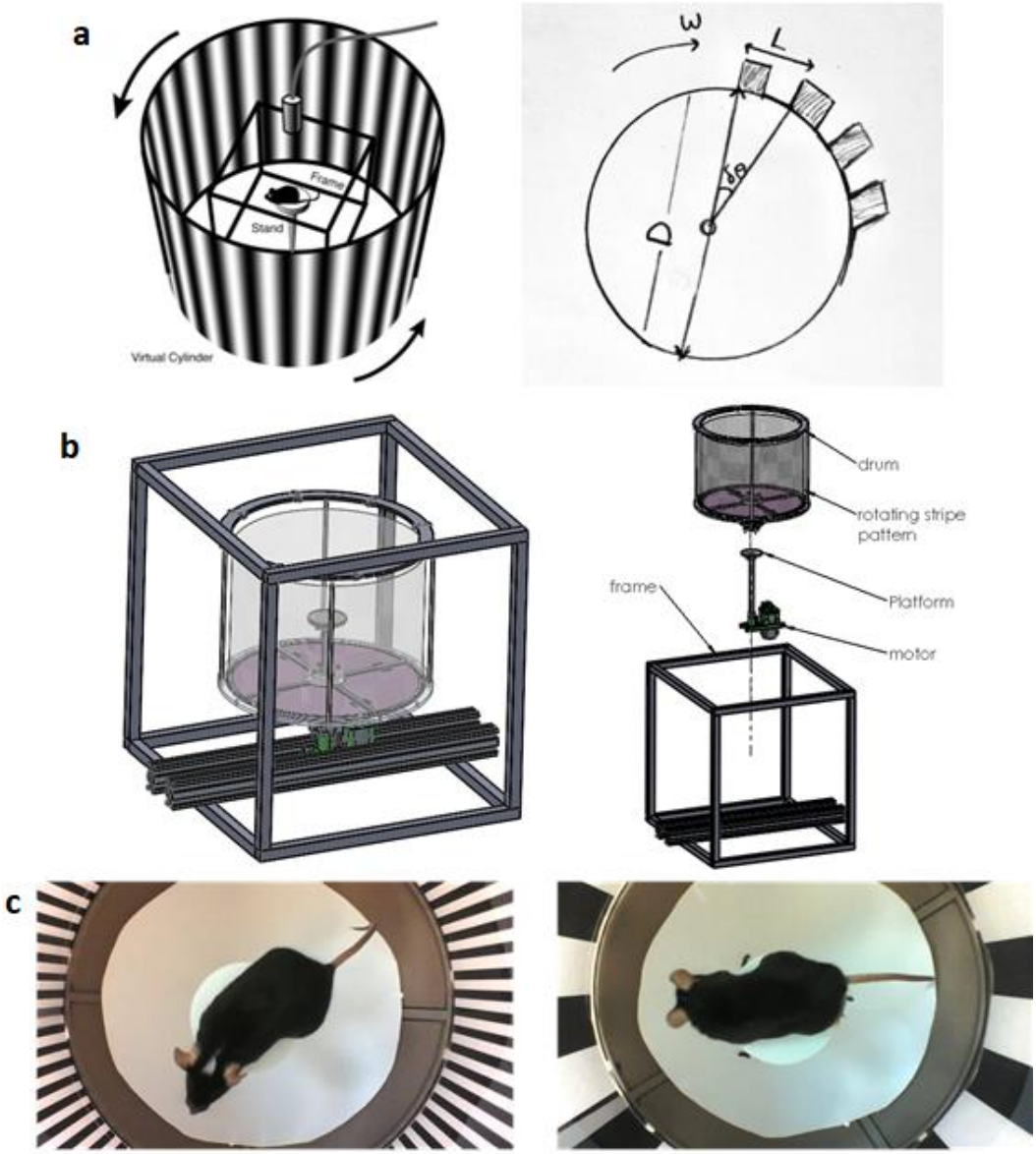

Fig. III-5. Quantifying vision performance following ONC via the OMR assay. (a) Left: Schematic representation of the optomotor assay. Right: Optomotor design parameters. **(b)** Drawings of the custom OMR apparatus used. **(c)** Representative images of mice during the OMR assay using stripes of different spatial frequencies K: 0.5 cpd (left) and 0.01 cpd (right).

11. Optomotor Response Assay

Vision performance (visual acuity) of mice following ONC over a 2-week or 10-week period was assessed via the OMR assay (162) using a custom-made apparatus **(Fig. III-5a,b)**. Mice were placed on a small white

elevated platform (Ø53 mm diameter), where they could move freely. While on the platform, mice were surrounded by a rotating (angular velocity of 2 rpm) cylindrical drum (Ø267 mm diameter, 200 mm height) that rotated (drive via a direct-current motor) in either the CW or the counterclockwise (CCW) direction. **(Fig. III-5c)**. The inner surface of the drum contained a periodic pattern of high-contrast stripes. The head motion of the mice was monitored during drum rotation for 1 minute for given stripe pattern. The process was repeated for CW and CCW rotation and for using a set of stripe patterns of progressively decreasing or increasing spatial frequency K [0.5, 0.37, 0.23, 0.10, 0.05, 0.03, 0.02, 0.01 cycles per degree (cpd)]. The spatial frequency K of each stripe pattern is the inverse of the pattern's angular period δθ (in deg) and can be expressed as a function of the drum's diameter D and the stripe pattern's period L:

$$K = \frac{1}{\delta\theta} = \frac{\pi}{360} \cdot \frac{D}{L}$$

This study utilized stripes whose thickness (equals L/2) ranged between 2.33 and 116 mm.

For handling and acclimation of mice, prior to surgery, mice settled down in the animal facility for approximately 3 days to become familiarized. One day prior to testing, animals were handled for 5 min by the examiner, were left to move freely on the platform for 5 min, and then the OMR assay was performed for 5 more min for reducing their stress during the testing procedure.

During the testing procedure, the trial was video recorded. Before each test, each mouse was placed on the platform for 3 min for habituation. Then each animal was tested for 1 min for each stripe spatial frequency rotation at CCW rotation (test response of intact eye), starting from highest spatial frequency K and proceeding to stripes of lower spatial frequency till mouse response was observed. Then each animal was tested for 1 min rotation CW (test response of injured eye), starting from the lowest spatial frequency K till mouse response was observed. Positive response was counted if the mouse head direction was caught to follow the drum rotation. For response analysis, the maximum spatial frequency with response was noted for each mouse once per day (2-week study) or once per week (10-week study).

12. Evaluation of BNN27 Delivery in Eye Tissues via Mass Spectrometry

In order to detect the presence of BNN27 in eye tissues, mice were sacrificed 1 week following ONC and 24 hours after the last eye drop administration ["Crush+BNN27 (1 drop/day)" group] or 2 weeks following ONC ["Crush+BNN27 (Scaffold)" group]. Following sacrifice, both eyes (injured and intact) were collected, eye tissues were divided in three samples (retina, optic nerve, remaining tissues) and were frozen at −70°C. BNN27 was detected in these three tissue samples via LC-MS by Dr. Katsila in collaboration with Dr. Kalogeropoulou (National Hellenic Research Foundation). The detection limit of this method for BNN27 was 0.7 ng/ml.

13. Eye Tissue Collection and Preparation

For the histological evaluation of retina and optic nerve tissues, mice were sacrificed 2 or 10 wpi. In the 2-week study, eyes were enucleated, fixed in 4% PFA overnight and cryopreserved in 30% sucrose solution in 0.1M Phosphate Buffer (PB) at 4°C for 24 h. In the 10-week study, injured eyes were i.v. injected with CTB (Thermo #C34778; 1mg/ml diluted in PBS), a retrograde neuroanatomical tracer that labels RGC axons that constitute the optic nerve (163). 3 days later mice were deeply anesthetized using isoflurane and transcardially perfused with ice-cold heparinized (10 U/mL) saline followed by 4% PFA in PBS. Then, eyes and brain were dissected, post-fixed in 4% PFA at 4°C for 1 h, washed in PBS and immersed in 30% sucrose solution in 0.1M PB at 4°C for 24 h. In both 2- and 10-week studies harvested cryopreserved eye bulbs were placed in small cylindrical molds (approximately 1 cm diameter and 2 cm length) that were then filled with

OCT embedding matrix (VWR #361603E) and snap frozen by immersion in isopentane cooled at −70°C. Eye bulbs and optic nerves were cryosectioned in super-frost slides in 20 µm cross sections and 10 µm longitudinal sections, respectively.

14. Immunohistochemistry of Retina and Optic Nerve Sections

Slides with eye tissue (retina, optic nerve) sections were placed in ice-cold acetone for 5 min, air-dried for 10 min in laminar flow, washed twice in PBS, once in 0.1% PBST and once in 0.3% PBST, then blocked in 0.1% PBST supplemented with 0.1% BSA and 10% goat or horse serum at room temperature for 1 h, incubated in primary antibodies **(Table III-3)** diluted in blocking solution at 4°C overnight, washed three times in 0.1% PBST, incubated with fluorophore-conjugated secondary antibodies **(Table III-2)** diluted in PBS at room temperature for 1 h, washed once in 0.1% PBST, once in PBS, counterstained with Hoechst 33342, washed once in PBS, once in PB and mounted. For TrkA and TrkB immunohistochemistry, sections were incubated in preheated (85°C) citrate buffer (10 mM sodium citrate in PBS, pH=6.0) at 85°C for 10 min, cooled down at room temperature and then washed in 0.1% PBST before blocking.

Table III-3. List of primary antibodies used in immunohistochemistry protocols.

Antigen	Primary antibody	
	Vendor, Catalogue #	Dilution
α-Smooth Muscle Actin (αSMA)	Sigma #A5228	1:200
BrdU	Novus	1:200
GFAP	Millipore #AB5541	1:2000
GFP	Minotech #701-1	1:200
Glutamic acid decarboxylase 67 (GAD67)	Sigma #MAB5406	1:1000
Ionized calcium-binding adaptor molecule 1 (Iba1)	Wako #019-19741	1:1000
L1	obtained by Dr. Fritz G. Rathjen	1:000
Myelin Associated Glycoprotein (MAG)	Cell Signaling #9043	1:200
Myelin Basic Protein (MBP)	Chemicon #AB980	1:200
Neurofilament pan-axonal (NF)	Biolegend #837904	1:200
Neuronal Nuclei (NeuN)	Millipore #MAB377	1:200
$p75^{NTR}$	Promega #G3231	1:100
Platelet-Derived Growth Factor α (PDGFRα)	R&D #AF1062	1:200
Synaptophysin	Millipore #MAB368	1:200
TrkA	Millipore #06-574	1:100
TrkB	Abcam #ab33655	1:200
TrkC	Cell Signaling #c44HS	1:200
Tubulin β3 (Tubb3)	Biolegend #801201 (clone Tuj1)	1:1000
Tyrosine Hydroxylase (3TH)	Thermo #MA1-24654	1:40
Vesicular glutamate transporter 1 (VGLUT1)	Synaptic systems #135304	1:400

15. Eye Tissue Sections Imaging and Image Processing

Immunostained sections of retina or optic nerve tissues were imaged in an inverted confocal microscope (TCS SP8, Leica Microsystems, Wetzlar, Germany) using a 40× or a 63× oil-immersion objective lens.

Retina images were acquired (3-4 pictures per section) in peripheral retina **(Fig. III-6a)**. The presence of neurons in GCL was quantified by counting the density of $NeuN^+$ cells in peripheral GCL. Results were expressed as linear density (RGC cells per 100 µm GCL length). Gliosis was quantified by counting the number of $GFAP^+$ processes of activated Müller cells in the retinal layers. Results were expressed as linear

density (GFAP$^+$ processes per 100 µm GCL length). NTR expression was quantified by calculating the fraction of p75^{NTR+}, TrkA$^+$, TrkB$^+$ and TrkC$^+$ pixels in the GCL (GCL boundaries were defined manually) (**Fig. III-6b)**.

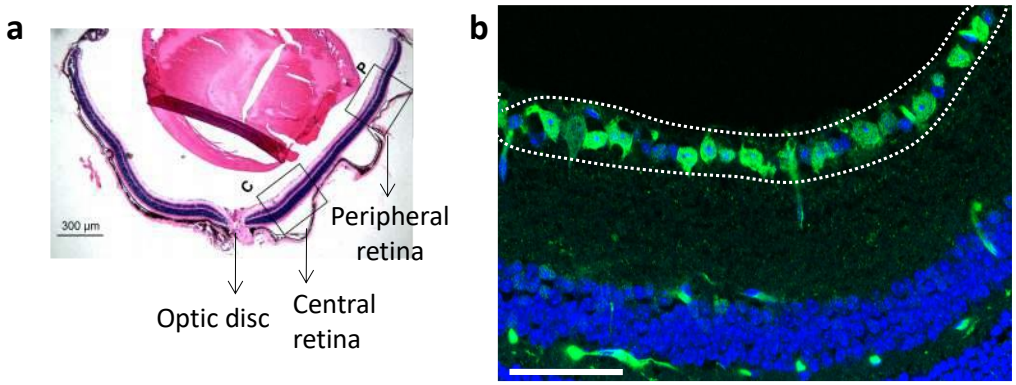

Fig. III-6. Peripheral retina used for histological evaluation of ONC. (a) H&E staining shows the location of central and peripheral retina. Central retina, located near the optic disk, is thicker than peripheral retina and has multilayered GCL [adapted from (164)]. **(b)** Representative fluorescence image of a peripheral retina cross section immunostained for NeuN (green). GCL boundaries are marked via dotted lines. Scale bar: 100 µm.

Images of optic nerve longitudinal sections were acquired in the ONC lesion and after it (towards the direction to the optic chiasm). Axonal elongation was quantified by counting the number of L1$^+$ axons in various distances (250 µm, 500 µm, 750 µm, 1000 µm) from the proximal end of the injury site **(Fig. III-7a,b)**. Results were expressed as linear density (axons per 100 µm of optic nerve). Microglia-mediated inflammation was quantified by counting the fraction of Iba1$^+$ pixels within the injury site after appropriate thresholding of the Iba1 image **(Fig. III-7c,d)**. OPC recruitment was quantified by counting the density of PDGFRα$^+$ cells (expressed as PDGFRα$^+$ cells per mm^2) in various distances (250 µm, 500 µm, 750 µm, 1000 µm) from the proximal end of the ONC injury site **(Fig. III-7e,f)**. OPC recruitment at the injury site was quantified by counting the fraction of PDGFRα$^+$ pixels within the injury site after appropriate thresholding of the PDGFRα image.

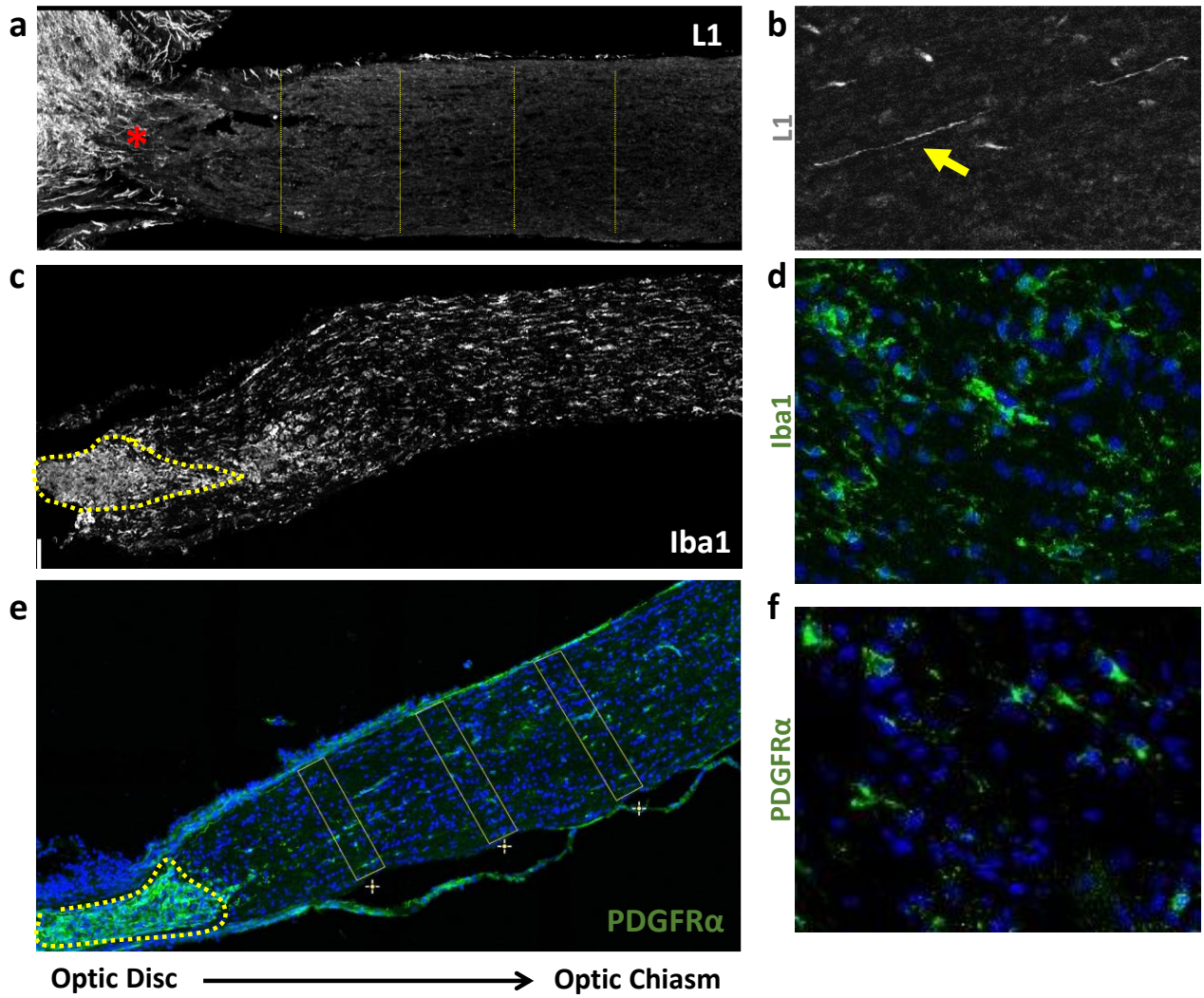

Fig. III-7. Representative images utilized for the quantification of L1⁺ axons, Iba1⁺ pixels and PDGFRα⁺ cells in optic nerve longitudinal sections. The location of the ONI site was determined by the accumulation of L1⁺ axons in the proximal end of the lesion **(a**; red asterisk**)** or the accumulation of Iba1⁺ and PDGFRα⁺ cells within the injury site **(c,e**; surrounded by a dotted yellow line**)**. L1⁺ axons and PDGFRα⁺ cells were counted in 250 μm, 500 μm, 750 μm, 1000 μm (marked in **a, e**) from the proximal end of the injury site. **(b,d,f)** Representative high-magnification images of L1⁺ axons, Iba1⁺ cells and PDGFRα⁺ cells in the optic nerve after the distal end of the lesion (yellow arrow indicates an L1⁺ axon).

All image analysis tasks were performed in the Fiji software. In thresholding operations, care was taken to avoid counting the background of each staining and define positive staining using a common value chosen by an expert user. Eye tissue preparation, immunohistochemistry and image processing were performed in collaboration with X. Mallios and E. Saridaki during their Master's Thesis (University of Crete).

16. Spinal Cord Injury Model

As shown in **fig. III-8**, two experimental studies were performed for SCI. The first one (study A) included 6 experimental groups ("Uninjured control", "Crush only", "Scaffold only", "Scaffold NSC", "NSC injection", "Scaffold+NIH3T3"). Regarding the cells used in study A, three days prior to injury, $3 \cdot 10^4$ cells (embryonic E13.5 NSCs for the "Scaffold+NSC" group and NIH3T3 for the "Scaffold+NIH3T3" group) were seeded into 1×1×1.5mm CS samples or on 48-well-plate (embryonic E13.5 NSCs for "NSC-injection" group). In both cases, NSCs were cultured in complete NSC medium. Starting 2 days prior to injury and repeating once every 12 h,

cell-seeded scaffolds or wells were pulsed with 1 µM BrdU. The second study (study B) included 5 experimental groups ("Uninjured control", "Placebo", "BNN27", "Scaffold NSC+Placebo", "Scaffold NSC+BNN27"). In study B, YFP-expressing E13.5 embryonic NSCs were used, in order to avoid BrdU pulse step. In both studies, prior to implantation, grafts were washed for 30 min in PBS, while 2D cultures were detached with accutase, diluted in 3 µl complete NSC medium and placed (1.5 µl) in a Hamilton microsyringe.

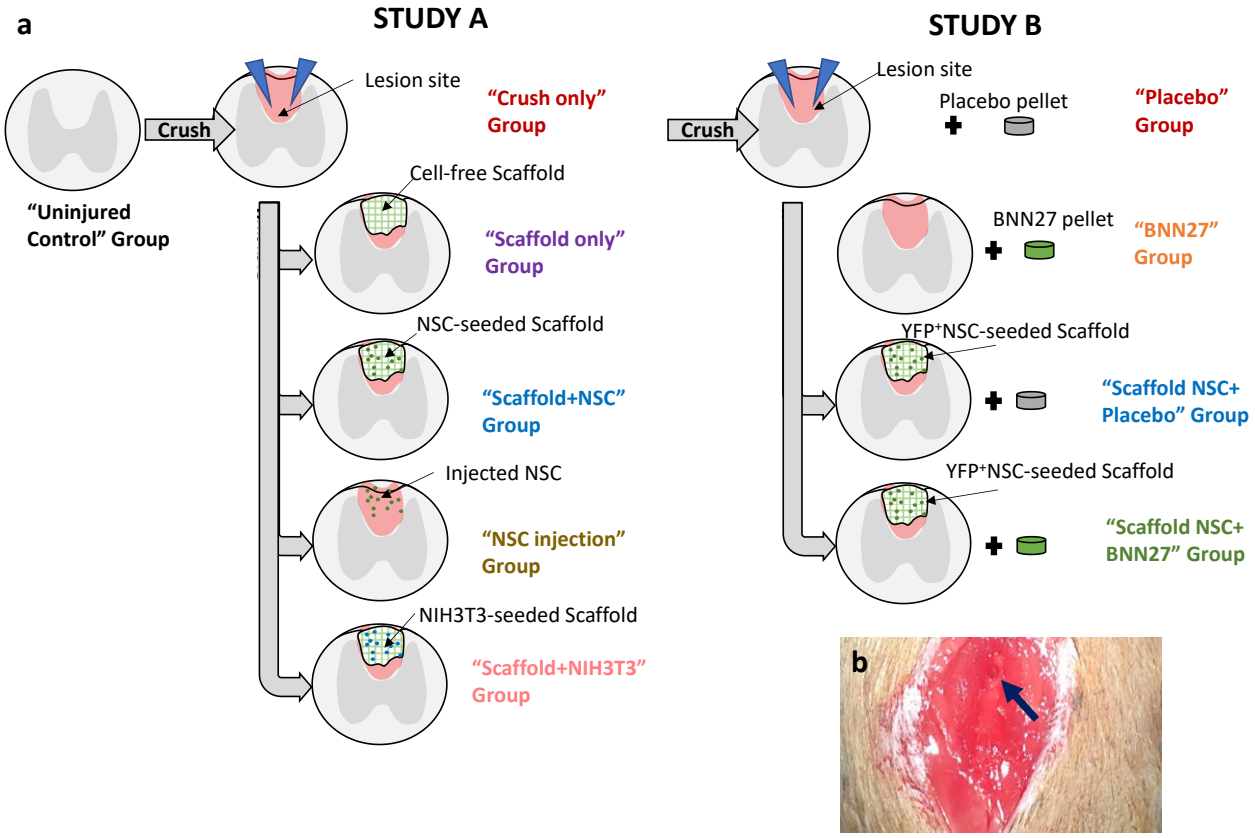

Fig. III-8. SCI model. (a) Schematic representation of the 2 SCI studies that were performed including 6 and 5 experimental groups, respectively. **(b)** Representative image of the spinal cord lesion during the SCI surgery. The blue arrow highlights the spinal cord lesion after graft placement.

All surfaces, tools, and instruments utilized had been sterilized carefully. C57/BL6 male mice approximately 4-week old were anesthetized by 2.5:1 isoflurane:oxygen mix inhalation for 5 min in a scavenger box until breathing slowed down. Before anesthesia, a drop of meloxicam was introduced per os. After verifying the absence of paw reflexes, each mouse was shaved in the level of the humpback and the exposed skin was disinfected. Each mouse was then transferred on a heat pad, where ophthalmic ointment was applied to avoid eye dryness and 2:1 isoflurane:oxygen mix was applied to maintain deep anesthesia via a mask.

In all animal groups ("Uninjured control", "Crush only", "Placebo", "BNN27", "Scaffold only", "Scaffold+NSC", "Scaffold NSC+Placebo", "Scaffold NSC+BNN27", "Scaffold+NIH3T3", "NSC injection") a skin incision was made from the base of the humpback until the higher point of the rib cage and exposed muscles were carefully torn. After removing surrounding ligaments, the bone of T10 vertebra was removed and an incision was made in the dura mater above the T13 segment (165). In the injured animal groups ("Crush only", "Placebo", "BNN27", "Scaffold only", "Scaffold+NSC", "Scaffold NSC+Placebo", "Scaffold NSC+BNN27", "Scaffold+NIH3T3", "NSC injection") the dorsal column was crushed by inserting Dumont #5 fine forceps 1 mm deep into the white matter and keeping them closed for 10 sec. This step was repeated once to create a

≈1 mm^3 pocket (lesion). In the "Scaffold only" animal group a cell-free CS graft was placed in the pocket immediately following injury. In three animal groups ("Scaffold+NSC", "Scaffold NSC+Placebo", "Scaffold NSC+BNN27") a NSC-seeded CS graft was placed in the pocket immediately following injury. In the "Scaffold+NIH3T3" a NIH3T3-seeded CS graft was placed in the pocket immediately following injury. In the "NSC injection" group, NSCs (1.5 µl NSCs diluted in complete NSC medium) were injected in the lesion (0.1 µl per 5 sec) and the syringe was kept at that point for 5 minutes after the injection. In all animal groups, the exposed spinal cord tissue was covered by a Geistlich membrane (Geistlich Bio-Gide) and then a hemostatic agent (Lyostypt, B. Braun Company), the muscles and skin were sutured and the skin was disinfected. In animals of the "BNN27" and "Scaffold NSC+BNN27" groups, a small incision was made close to the shoulder and a pellet that contained 18 mg BNN27 (60-day release period; Innovative Research of America #SX999) was implanted under the skin. After inserting the pellet, the skin was sutured and disinfected. Similarly, in animals of the "Placebo" and "Scaffold NSC+Placebo" groups, mice were implanted a pellet that lacked an active pharmaceutical ingredient (Innovative Research of America #SC111). All animal groups were provided with meloxicam for the next 3 days for analgesia. SCI injuries in study A were conducted by Dr. K. Karali (University of Crete).

CST axons in the spinal cord were labeled by anterograde tracing (only in study B). 3.2 µl of BDA solution (10% BDA in water for injection) was injected into the sensorimotor cortex at four sites (AP coordinates from bregma in mm: AP 2.0/1.5, 1/1.5, 0/1.5, −1.0/1.5 all at a depth of 0.5 mm into cortex) 2 weeks before mouse sacrifice.

17. Horizontal Ladder Walking Assay

Locomotion performance of mice following SCI was assessed via the horizontal ladder walking assay (166). Mice crossed a 1-meter-long horizontal ladder consisted of sidewalls made of clear plexiglass connected by ø2 mm aluminum rods spaced approximately 1 cm from each other. The ladder was elevated above the ground at the height of two cages. Animals were trained to cross the ladder from a neutral cage to their home cage and always in the same direction **(Fig. III-9a)**.

For handling and acclimation, the week prior to surgery, mice settled down in the animal facility to become familiarized. For 6 consecutive days prior to testing, animals were handled for 5 min by the examiner and walked through the ladder for 5 min in order to reduce their stress during the testing procedure. During the testing procedure, each animal was tested 5 times per session. Before each session, mice crossed the ladder twice for habituation. Each trial was video recorded for locomotion analysis. Videos of walking mice were analyzed frame-by-frame by two researchers blind to the animal's condition (group, week) analyzed to identify locomotion errors, defined as steps where a hind limb missed or slipped off or was misplaced on a rod. Each fault was classified using a 7-category scale (0: total miss, 1: deep slip, 2: slight sleep, 3: replacement, 4: correction, 5: partial placement, 6: correct placement) as described previously (166) **(Fig. III-9b-d)**. Locomotion performance was described via the fault rate (the fraction of steps classified in categories 0 to 5). The last step before and the first step after a stop were excluded; only consecutive steps were included in the analysis. Assay processing and video analysis were performed in collaboration with Dr. K. Karali, X. Mallios and F. Bampoula (study A) as well as E. Saridaki and I. Papagiannaki (study B) (University of Crete).

While initially each animal group consisted of 9-10 mice, some of them were excluded in order to ensure consistent injury in all animals. Exclusion criteria were based on mice locomotion performance:

- Mice of the "Uninjured Control" group were excluded when their mean fault rate over the monitoring period exceeded 10%.

- Mice of the injured groups were excluded when there were strong indications of insufficient injury (e.g. fault rate <20% the day following injury or <15% at 1 wpi) or excessive injury (e.g. fault rate >90% the day following injury or > 45% at 1 wpi or >35% at 2 wpi).

Mice exclusions were confirmed by histology based on the magnitude of the observed lesion in mice spinal cord sections.

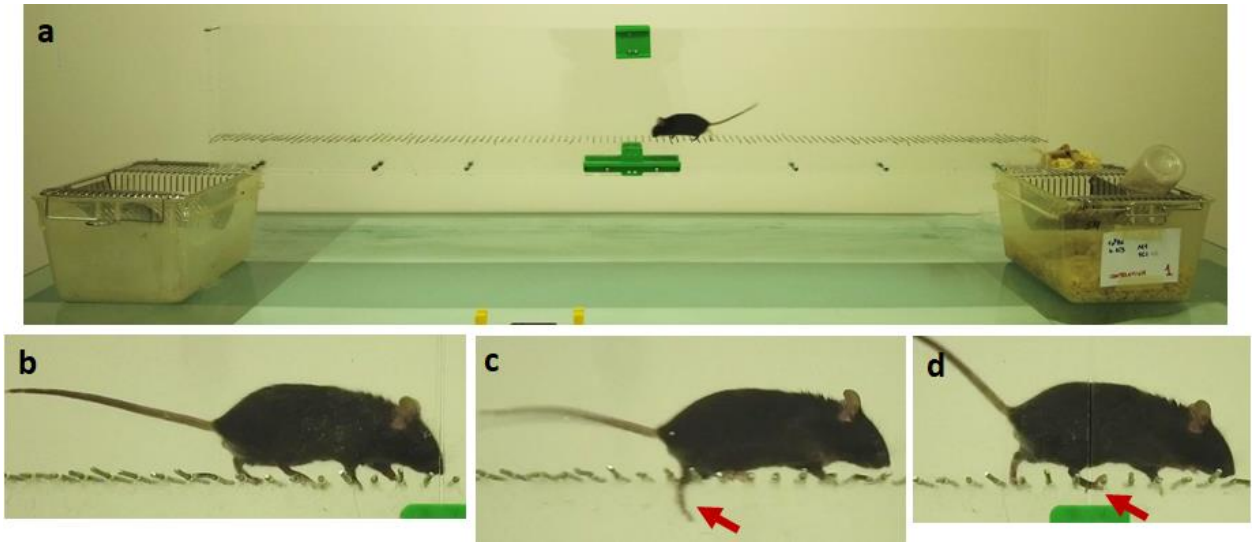

Fig. III-9. Evaluating mouse locomotion performance via the Horizontal Ladder Walking assay. (a) Representative image of a mouse performing the horizontal ladder walking assay. **(b-d)** Examples of mouse steps: (b) correct placement, (c) deep slip, (d) partial placement. Red arrows denote the leg that steps incorrectly on the rod (fault step).

18. Rotarod Assay

Locomotion performance of mice over a 6-week period following SCI was also assessed via the Rotarod assay (167). The rotarod apparatus consists of a circular rod rotating at constant or increasing angular speed. Animals placed on the rotating rod try to remain on it rather than falling onto the platform located below **(Fig. III-10)**.

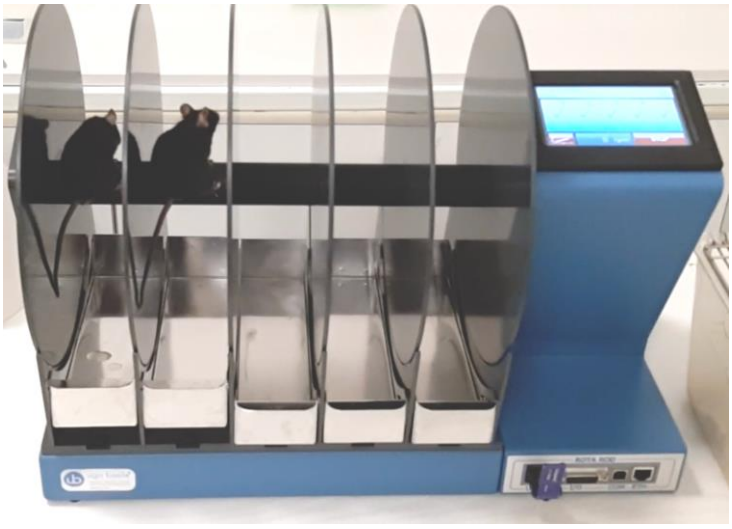

Fig. III-10. Representative image of mice during a Rotarod Assay.

For acclimation, one day prior to testing, mice were placed on the rod when it was rotating at constant 5 rpm for 240 sec, 3 times with an interval of 5 min. During the testing procedure, mice were placed on the

rod rotating at a constant 5 rpm. Then, the rod began to linearly accelerate from 5 to 20 rpm over 120 sec. Then, the rod's angular velocity remained constant at 20 rpm for another 120 sec. The time spent (latency) by each mouse on the rod was measured automatically. When a mouse was able to stay on the rod until the cut-off time (240 sec), the mouse was removed from the rod, and the maximum time (240 sec) was recorded. Testing was completed 3 times with an interval of 5 min. The average latency of the 3 trials was used for statistical analysis. When a mouse hung onto the rod for a full rotation or turned around backwards, the trial was stopped and scored as a fall. Assay processing and analysis were performed in collaboration with A. Moniakis during his Master's studies (University of Crete).

19. Spinal Cord Tissue Collection and Preparation

For histological evaluation of spinal cord tissues, 12 weeks following SCI, mice were deeply anesthetized using isoflurane and transcardially perfused with ice-cold heparinized (10 U/mL) saline followed by 4% PFA in PBS. Then, spinal cords were dissected, post-fixed in 4% PFA at 4°C for 1 h, washed in PBS and immersed in 30% sucrose solution in 0.1M PB at 4°C for 24 h. The 1 cm long part of the spinal cord tissue centered around the lesion was placed in molds (Sigma #E6032) that were then filled with 15% sucrose 7.5% gelatin in PB and snap-frozen by immersion in isopentane cooled at −70°C. 20 μm-thick parasagittal sections were cut in super-frost slides.

20. Immunohistochemistry of Spinal Cord Sections

Slides with spinal cord tissue sections were placed in ice-cold acetone for 5 min, air-dried for 10 min in laminar flow, washed twice in PBS, once in 0.1% PBST and once in 0.3% PBST, then blocked in 0.1% PBST supplemented with 0.1% BSA and 10% goat or horse serum at room temperature for 1 h, incubated in primary antibodies **(Table III-3)** diluted in blocking solution at 4°C overnight, washed three times in 0.1% PBST, incubated with fluorophore-conjugated secondary antibodies **(Table III-2)** diluted in PBS at room temperature for 1 h, washed once in 0.1% PBST, once in PBS, counterstained with Hoechst 33342, washed once in PBS, once in PB and mounted. For BrdU immunohistochemistry (study A), sections were incubated in 2 N HCl at 37°C for 30 min, rinsed in 0.1 M sodium tetraborate pH 8.5 for 10 min and washed twice in PBS before blocking.

21. Spinal Cord Tissue Sections Imaging and Image Processing

Immunostained sections of spinal cord tissues were imaged in an inverted confocal microscope (TCS SP8, Leica Microsystems, Wetzlar, Germany) using a 40× or a 63× oil-immersion objective lens. Images of stained spinal cord sections were acquired at the epicenter, caudally and rostrally to the lesion.

The presence of neurons in the epicenter was quantified by counting the density of Tuj1$^+$ cells within a region of interest defined by the user within the injury site. Astrogliosis was quantified by calculating the fraction of GFAP$^+$ pixels immediately around the lesion boundary, by selecting up to 5 regions (approximately 0.025 mm^2 each) per section. The presence of implanted NSC-derived cells was quantified by counting the density of GFP$^+$ cells in the lesion epicenter using images acquired by a 63× objective lens. Results were expressed as GFP$^+$ cells per volume. Synapse formation was quantified by calculating the fraction of Synaptophysin$^+$ pixels in the lesion epicenter. Axonal elongation was quantified by calculating the fraction of L1$^+$ pixels in the lesion epicenter as well as in the dorsal region rostrally and caudally to the lesion. Angiogenesis in the lesion epicenter was quantified by counting the number of αSMA$^+$ vessels in the lesion epicenter. The presence of myelin in the lesion epicenter was quantified by calculating the fraction of MBP$^+$ pixels in the lesion epicenter.

All image analysis tasks were performed in the Fiji software. In thresholding operations, care was taken to avoid counting the background of each staining and define positive staining using a common value chosen by an expert user. In study A, spinal cord tissue collection, preparation, immunohistochemistry and image processing were performed in collaboration with Dr. K. Karali and F. Bampoula (University of Crete).

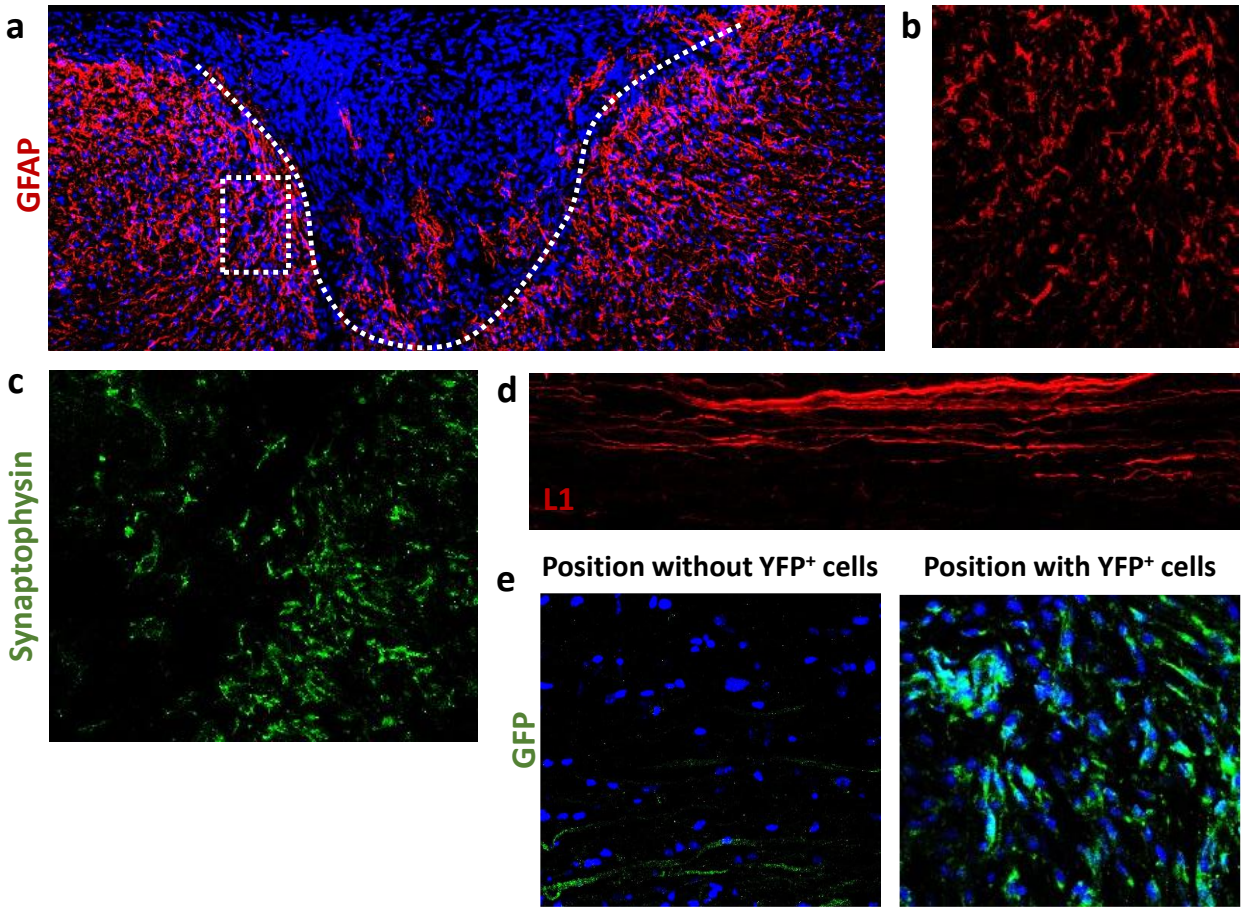

Fig. III-10. Representative images in spinal cord tissue samples utilized for the quantification of GFAP$^+$ pixels, Synaptophysin$^+$ pixels, L1$^+$ pixels and GFP$^+$ cells in spinal cord parasagittal sections. (a) The dorsal column injury site was determined by the GFAP$^+$ glial scar formed around the lesion. The boundaries of the injury site are marked via dotted lines. GFAP$^+$ quantification was performed in 5 regions immediately around the lesion boundary like the one marked via a dotted rectangular. **(b-d)** Representative images of spinal cord sections immunostained for GFAP, Synaptophysin and L1 after removing non-specific background signal to quantify the positive pixels. **(e)** YFP$^+$ cells (green) were well-distinguished as GFP signal is very low in positions that lack implanted NSCs.

22. Hematoxylin & Eosin Staining of Tissue Sections

Tissue slides (retina, optic nerve, spinal cord) were washed 3 times in tap water to remove cryoprotection medium, were air-dried for 5-10 min, washed in running tap water for 5 min and rehydrated by washing in 100%, 90% and 70% ethanol solutions consecutively. Then, slides were placed in haematoxylin solution (abcam, #ab245880) for 2-3 min, washed in running tap water, rinsed in 1% acid alcohol (0.6 M HCl in 70% ethanol), washed in running tap water, washed in Scott's tap water substitute (0.17 M $MgSO_4$, 0.42 M $NaHCO_3$ in dH_2O) until tissue sections turn blue, washed in running tap water, placed in Eosin Y solution (abcam, #ab245880) for 15 sec and washed in running tap water. Then, slides were immersed in 70% ethanol

for 30 sec, 90% ethanol for 2 min and 100% ethanol for 5 min and xylene for 5 min, and finally were mounted in DPX (Sigma #06522).

23. Statistical analysis

Experimental data are expressed as mean ± standard error of the mean (SEM). Statistical analysis was performed using the Prism software (Graphpad, La Jolla, CA, USA).

In ONC experiments, statistically significant effects in the quantification of NeuN$^+$ cell density, GFAP$^+$ processes number and Iba1$^+$, L1$^+$, PDGFRα$^+$ pixel fractions were assessed by 1-way analysis of variance (ANOVA; for evaluating the overall effects of injury or treatment among the groups) followed by Tukey's post-hoc test (for pairwise comparisons between groups). Statistically significant effects of ONC on NTR expression were assessed by unpaired two-tailed Student's t-tests. In adult retina explants experiments, statistically significant effects of MNTs on the number of neurites intersects were assessed by 1-way ANOVA followed by Tukey's post-hoc test.

In SCI experiments, statistically significant effects in locomotion fault rate were assessed by 1-way ANOVA (for evaluating the overall effects of injury among the groups in postop and 1 wpi) and by 2-way ANOVA (for evaluating the effects of BNN27 and NSC-seeded graft treatments) followed by Tukey's post-hoc test (for pairwise comparisons between groups at 2-10 wpi)**.** Statistically significant effects in the quantification of GFAP$^+$, Synaptophysin$^+$, MBP$^+$, L1$^+$ pixel fractions, Tuj1$^+$ cell density and αSMA$^+$ vessel number were assessed by 2-way ANOVA (for evaluating the effects of BNN27 and NSC-seeded graft treatments) followed by Tukey's post-hoc test (for pairwise comparisons between groups). Statistically significant effects of BNN27 on the density of GFP$^+$, Tuj1$^+$ and GFP$^+$ Tuj1$^+$ cells were assessed by unpaired two-tailed Student's t-tests.

In NSC proliferation *in vitro* experiments, statistically significant effects of BNN27 administration were assessed by 1-way ANOVA (for evaluating the overall effects of treatment among the groups) followed by Tukey's post-hoc test (for pairwise comparisons between groups). Statistically significant effects of BNN27 on NSC differentiation *in vitro* were assessed by 1-way ANOVA (for evaluating the overall effects of treatment among the groups) followed by Dunnett's post-hoc test (for pairwise comparisons between the "No Factors" group and other groups). All statistical tests assumed a statistical significance level of 0.05.

All the experimental processes and analyses described above were performed under the supervision of Dr. D. Tzeranis (IMBB-FORTH and University of Cyprus).

III. *Results*

This chapter presents experimental results and is organized in two parts. The first part presents results on the evaluation of MNT administration in a mouse ONC model. The second part presents results on the evaluation of combinatorial treatments (MNT, NSC-seeded scaffold grafts) in a dorsal column crush mouse SCI model.

1. Evaluation of Microneurotrophin Effects on Optic Nerve Injury

1.1. *In vivo* Characterization of the Mouse Optic Nerve Crush Model

ONC model is a simple yet informative CNS injury model that resembles clinical ONI cases (30). For the histological evaluation of ONC, the preparation of tissue sections from mouse retina and optic nerve is challenging due to the delicate nature of these tissues. Thus, in order to confirm the proper preparation of tissues, the morphology of retinal layers and the optic nerve was assayed via H&E staining in tissue sections. According to retina morphology, peripheral retina was chosen for further experimental evaluation due to its monolayer GCL, contrary to central retina **(Fig. III-6, IV-1)**.

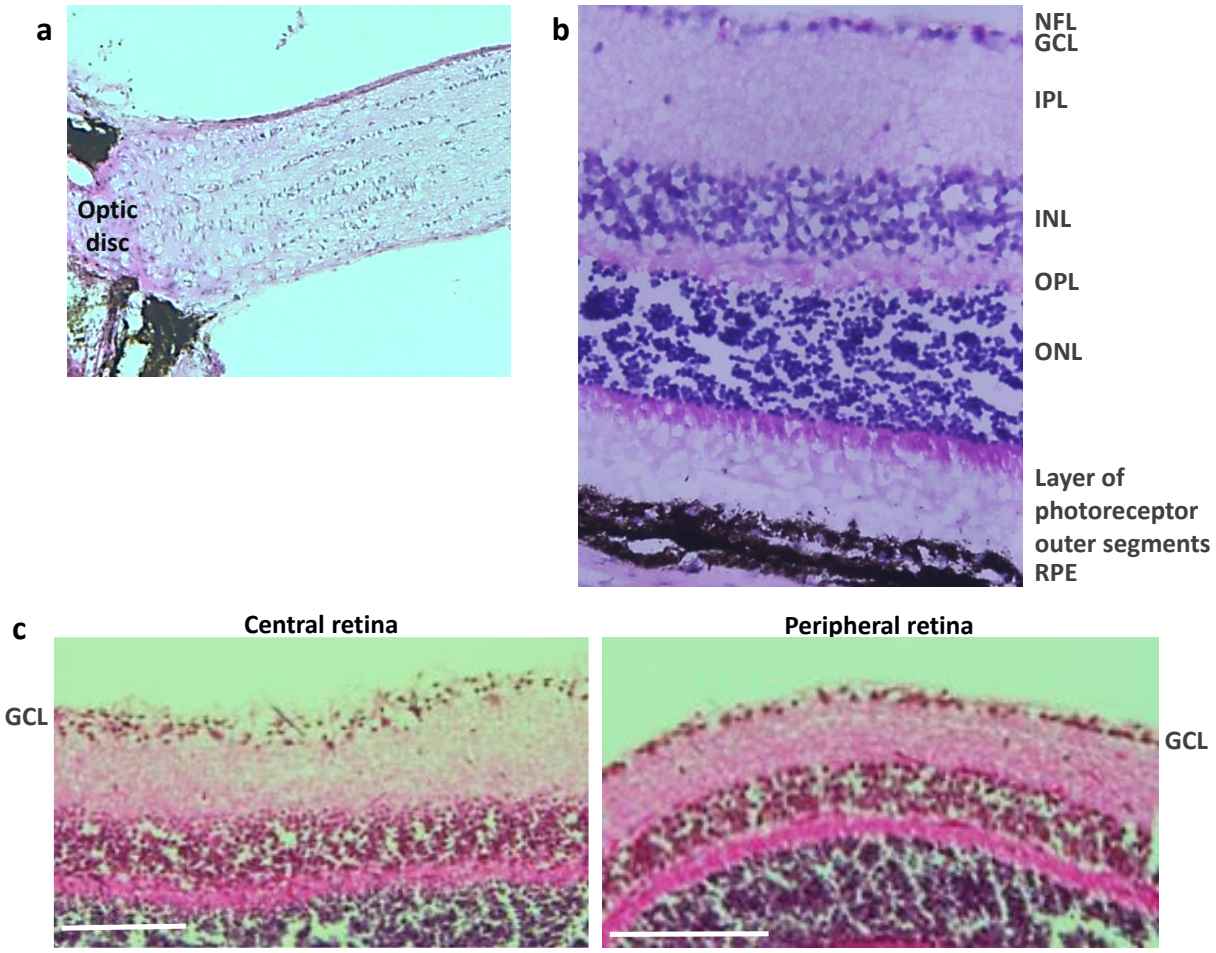

Fig. IV-1. Morphology of optic nerve and retina revealed via H&E staining. H&E staining of **(a)** intact optic nerve longitudinal sections and **(b)** retina cross sections show the morphology of optic nerve and retinal layers, respectively (NFL: nerve fibre layer, GCL: ganglion cell layer, IPL: inner plexiform layer, INL: inner nuclear layer, OPL: outer plexiform layer, ONL: outer nuclear layer, RPE: Retinal pigment epithelium). **(c)** Representative images of retina cross sections stained with H&E show the different organization of the GCL in central and peripheral retina. Scale bars: 100 µm.

Another challenge of ONC model is the delicate error-prone surgery that leads to variability among different conditions and operators (30). Thus, the model was also histologically evaluated regarding the injury effects on RGC survival, gliosis and NTR expression in GCL as well as on axonal degeneration in optic nerve, in order to confirm its accuracy and repeatability by a specific operator for the purposes of this thesis.

In order to quantify ONC effects on RGC survival and validate the correct implementation of ONC, RGC survival at 1- and 2- wpi was evaluated by immunostaining retina cross sections for NeuN (neuronal marker) and calculating the linear density of NeuN$^+$ cells in the GCL **(Fig. IV-2a)**. It is important to note that NeuN is a generic neuronal marker and, consequently, it does not mark only RCGs, but also a few amacrine cells displaced in GCL. However, for the purposes of this thesis, NeuN was used for detecting RGCs in GCL. Trial retina immunohistochemistry using an antibody for Brn3a, a specific marker utilized in literature to label RGCs, provided poor staining that was inappropriate for reliable RGC quantification. Results showed a significant decrease in NeuN$^+$ cell linear density in GCL and, consequently, in RGC survival in retinas of injured eyes at 1 and 2 wpi compared to retinas of intact (contralateral) eyes ("Intact": 9.5$\pm$0.7 cells/100μm, n=5; "Crush 1 wpi": 5.9$\pm$1.0 cells/100μm, n=4, P=0.006; "Crush 2 wpi": 3.7$\pm$0.3 cells/100μm, n=7, P<10^{-4}) **(Fig. IV-2b)**. Result consistency in each group indicated that the crush was performed in an accurate and repeatable manner.

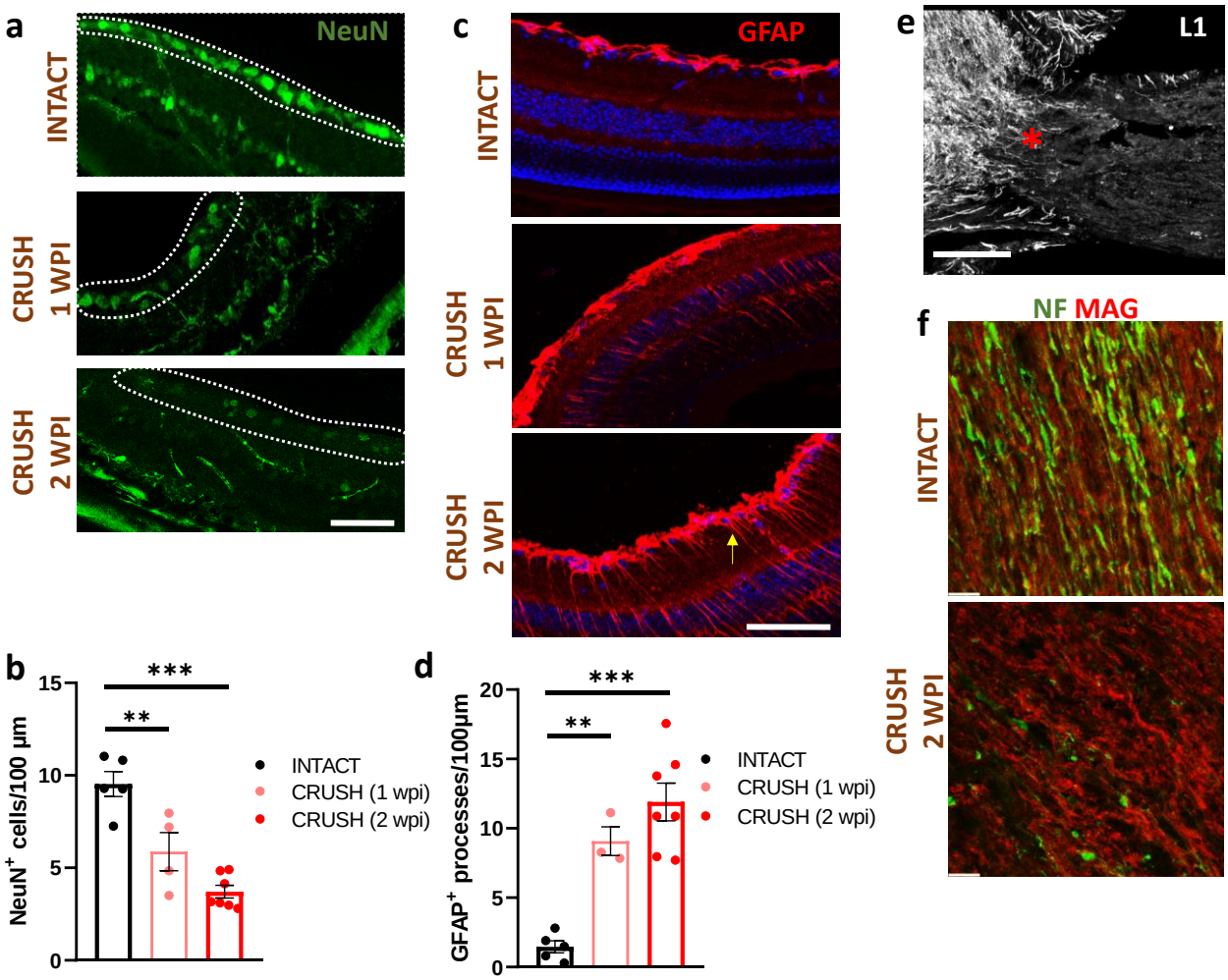

Fig. IV-2. ONC effects on RGC survival, gliosis and axonal degeneration at 1 and 2 wpi. (a) Representative fluorescence images of retina cross sections from intact and injured eyes at 1 and 2 wpi immunostained for NeuN (green). GCL boundaries are denoted by dotted lines. Scale bar: 50 μm. **(b)** Quantification of the linear density of NeuN$^+$ cells in the GCL of intact and injured eyes at 1 and 2 wpi

("Intact": n=5, "Crush 1 wpi": n=4, "Crush 2 wpi": n=7). **(c)** Representative fluorescence images of retina cross sections from intact and injured eyes at 1 and 2 wpi immunostained for GFAP (red). The yellow arrow indicates a $GFAP^+$ process of an activated Müller cell. Scale bar: 50 µm. **(d)** Quantification of the linear density of $GFAP^+$ processes in the retina of intact and injured eyes at 1 and 2 wpi ("Intact": n=5, "Crush 1 wpi": n=3, "Crush 2 wpi": n=7). **(e)** Representative fluorescence image of an optic nerve longitudinal section from an injured eye at 2 wpi immunostained for the L1 marker. The proximal end of the injury site is highlighted via a red asterisk. Scale bar: 100 µm. **(f)** Representative fluorescence images of optic nerve longitudinal sections from intact and injured eyes at 2 wpi immunostained for NF (green) and MAG (red) markers. Scale bars: 10µm. Results are presented as mean ± SEM. **P < 0.01, ***P < 0.001; Tukey's post-hoc pairwise test assuming $P_{1\text{-}way\text{-}ANOVA} < 0.05$.

Gliosis in the retina at 1 and 2 wpi was evaluated by immunostaining retina cross sections for GFAP (a marker of astrocytes and activated Müller cells) and then calculating the linear density of $GFAP^+$ processes of activated Müller cells that cross retina layers **(Fig. IV-2c)**. Results (expressed as number of $GFAP^+$ processes per 100 µm) showed a significant increase in $GFAP^+$ processes linear density and, consequently, in reactive gliosis in injured eyes at 1 and 2 wpi compared to the intact eyes ("Intact": 1.5±0.4 processes/100 µm, n=5; "Crush 1 wpi": 9.1±1.0 processes/100 µm, n=3, P=0.006; "Crush 2 wpi": 11.9±1.4 processes/100 µm, n=7, $P<10^{-4}$) **(Fig. IV-2d)**.

Following ONC, significant axonal degeneration was observed in the optic nerve at 2 wpi. Immunostaining of optic nerve sections for the L1 cell adhesion molecule [upregulated in elongating axons (163)] highlighted the proximal end of the injury site, where high accumulation of $L1^+$ RGC axons was observed **(Fig. IV-2e)**. Double immunostaining of optic nerve sections using a pan-NF (neuronal marker) antibody and a MAG (myelin marker) antibody revealed significant loss of axon myelin integrity, since MAG (a known inhibitor of axon regeneration) was released from damaged myelin **(Fig. IV-2f)**.

The expression of NTRs in the GCL at 2 wpi was evaluated by immunostaining retina cross sections for the $p75^{NTR}$, TrkA, TrkB and TrkC proteins and then calculating the fraction of pixels in GCL that stain positively for each marker **(Fig. IV-3a)**. Results showed that a substantial part of GCL cells (not necessary RGCs) express $p75^{NTR}$, TrkA or TrkB, while a small fraction of GCL cells express TrkC. Results also showed small ONC-induced NTR expression alterations at 2 wpi, such as upregulation of $p75^{NTR}$ and downregulation of TrkA. However, these ONC effects were limited and not statistically significant (*$p75^{NTR}$*: "Intact" 27.9±4.5 %, n=3; "Crush 2 wpi" 30.7±3.0 %, n=3, P=0.63. *TrkA*: "Intact" 34.6±3.3 %, n=5; "Crush 2 wpi" 29.7±1.7 %, n=3, P=0.32. *TrkB*: "Intact" 27.8±1.2 %, n=3; "Crush 2 wpi" 25.0±0.8 %, n=2, P=0.20. *TrkC*: "Intact" 4.5±1.3 %, n=4; "Crush 2 wpi" 1.2±0.5 %, n=3, P=0.09) **(Fig. IV-3b-e)**.

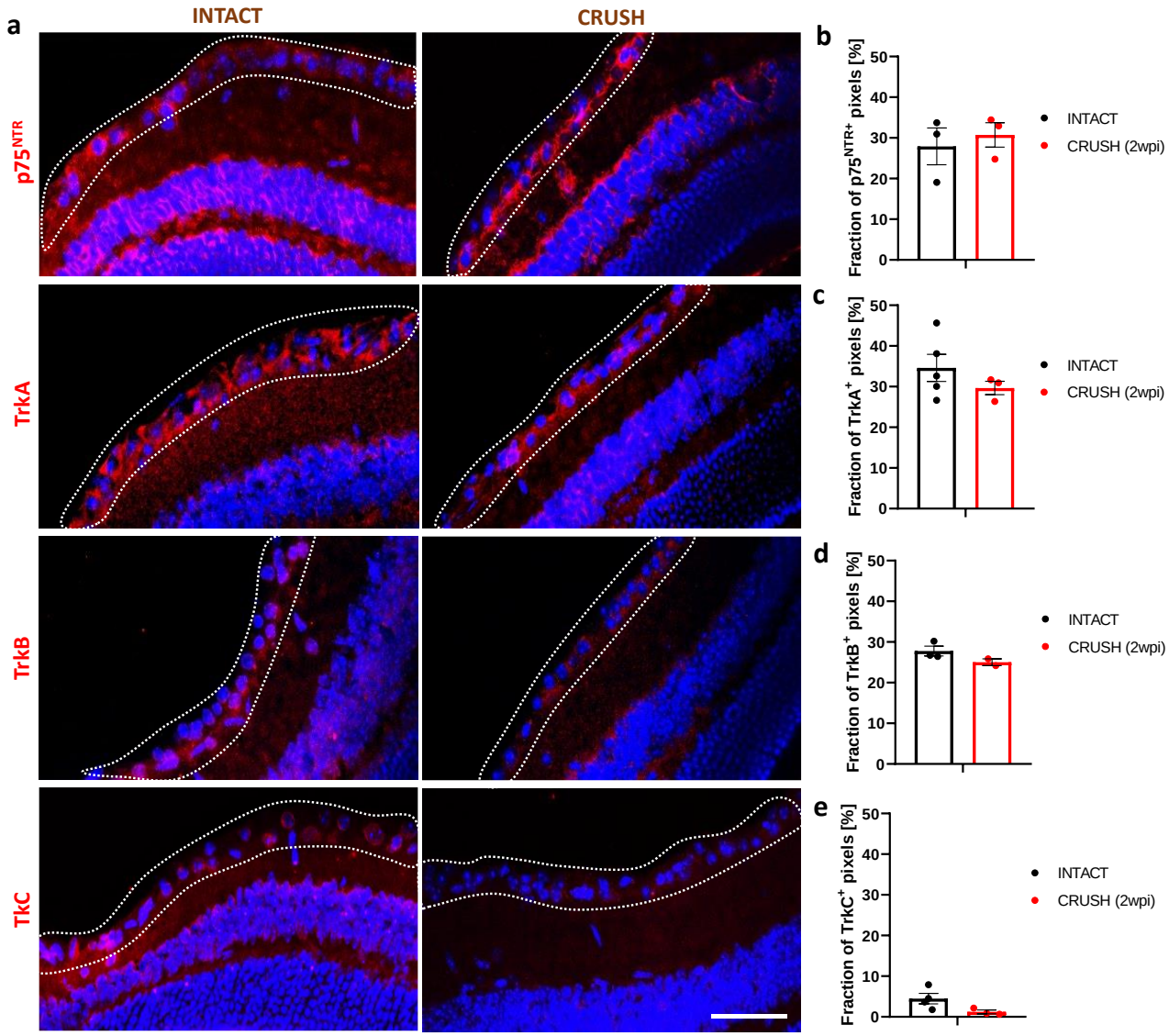

Fig. IV-3. ONC effects on NTR expression in the GCL at 2 wpi. (a) Representative fluorescence images of retina cross sections from intact and injured eyes at 2 wpi immunostained for $p75^{NTR}$, TrkA, TrkB and TrkC (red). GCL boundaries are denoted by dotted lines. Scale bar: 50 µm. **(b-e)** Quantification of the fraction of $p75^{NTR+}$, $TrkA^{+}$, $TrkB^{+}$ and $TrkC^{+}$ pixels in the GCL of intact and injured eyes at 2 wpi ("Intact": n=3-5, "Crush 2 wpi": n=2-3). Results are presented as mean ± SEM.

1.2. *In vivo* Design of BNN27 Delivery via Eye Drops in the Mouse Optic Nerve Crush Model

BNN27 delivery via eye drops was designed and evaluated in the ONC mouse model characterized in section IV-1.1. The advantages and disadvantages of eye drops as delivery method of therapeutic molecules were discussed in section I-5. Examples of NGF or BNN27 delivery via eye drops were described in sections I-5.1.2 and I-5.1.3. Since this is the first case of BNN27 delivery via eye drops in the ONC model, preliminary tests were performed in order to select the frequency and dose of BNN27 administration. In all tests, BNN27 administration started at 1 day post injury. The frequency of BNN27 administration varied from 1 eye drop per second day to 2 drops per day. BNN27 concentration in eye drops was selected based on limitations imposed by BNN27 solubility. Since MNTs have poor solubility in water (168), they need to be diluted in DMSO or ethanol. Here, 50 mM BNN27 was delivered in 5µl eye DMSO drops. The 5 µl volume was chosen

based on prior studies and the advice of experts. The 50 mM BNN27 concentration was chosen as the highest soluble concentration estimated by the reported solubility of DHEA in DMSO.

The toxicity of 5 µl 50 mM BNN27 drops in DMSO was evaluated in intact eyes. Specifically, RGC survival was evaluated after a 2-week administration in four animal groups: (a) intact eyes that received no treatment, (b) intact eyes treated with two 5 µl DMSO drops daily, (c) intact eyes treated with one 5 µl 50 mM BNN27 drop in DMSO daily, (d) intact eyes treated with two 5 µl 50 mM BNN27 drops in DMSO daily. As illustrated in **Fig. IV-4b**, the administration of DMSO eye drops (with or without BNN27) did not result in statistically significant effects in NeuN$^+$ cell linear density in the GCL among the 4 groups ("Intact": 10.4±0.5 cells/100µm, n=3; "Intact+DMSO 2 drops/day": 9.7±0.9 cells/100µm, n=3, P=0.78; "Intact+BNN27 1 drop/day": 8.4±0.6 cells/100µm, n=3, P=0.21; "Intact+BNN27 2 drops/day": 7.6±0.8 cells/100µm, n=3, P=0.06). Therefore, in the following results, the term "intact eye" refers to samples from contralateral eyes from all these 4 groups.

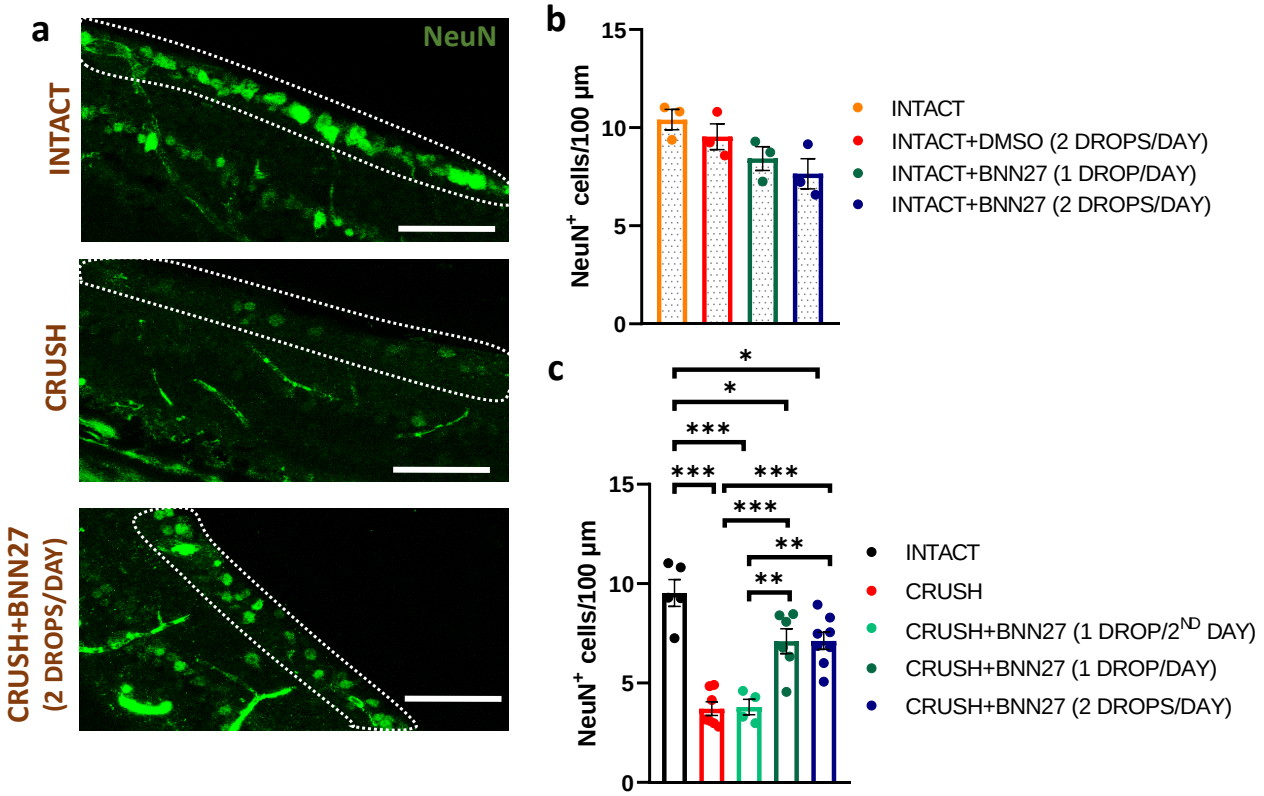

Fig. IV-4. Effects of BNN27 administration via eye drops on RGC survival following ONC at 2 wpi. (a) Representative fluorescence images of retina cross sections immunostained for NeuN (green). GCL boundaries are denoted by dotted lines. Scale bars: 50 µm. **(b)** Quantification of NeuN$^+$ cell linear density in the GCL of four groups of intact eyes at 2 wpi (n=3 for all groups). **(c)** Quantification of NeuN$^+$ cell linear density in the GCL of intact and injured (untreated or treated) eyes at 2 wpi ("Intact": n=5; "Crush": n=7; "Crush+BNN27 1 drop/2nd day": n=4; "Crush+BNN27 1 drop/day": n=6; "Crush+BNN27 2 drops/day": n=8). Results are presented as mean ± SEM. *P < 0.05, **P < 0.01, ***P < 0.001; Tukey's post-hoc pairwise test assuming $P_{1\text{-way-ANOVA}} < 0.05$.

Preliminary experiments on the effect of BNN27 eye drop administration in injured eyes showed that BNN27 (1 or 2 BNN27 50 mM drops/day) increased RGC survival at 2 wpi (**Fig. IV-4c**). Daily administration of BNN27 was required for efficient neuroprotection since the administration of 1 drop per second day did not result in statistically significant effects compared to "Crush" group ("Crush": 3.6±0.3 cells/100 µm, n=7; "Intact":

9.5±0.7 cells/100 µm, n=5, $P<10^{-4}$; "Crush+BNN27 1 drop/2nd day": 3.8±0.4 cells/100 µm, n=4, P>1.0; "Crush+BNN27 1 drop/day": 7.1±0.6 cells/100 µm, n=6, $P=4\cdot10^{-4}$; "Crush+BNN27 2 drops/day": 7.1±0.4 cells/100 µm, n=8, $P=10^{-4}$).

1.3. *In vivo* Design of BNN27 Delivery via CGS Grafts at the Mouse Optic Nerve Crush Injury Site

Due to the limitations of eye drops as delivery method of therapeutic molecules, discussed in section I-5, a more targeted way of delivery was developed. This study presents the first delivery of MNT via CGS grafts. CGS grafts were cut in 4x3x1.5 mm dimensions and placed at the injury site immediately after the ONC. In order to validate the correct placement of grafts, CGS grafts were fluorescently labeled using fluorescein isothiocynate (FITC). Imaging of harvested optic nerve tissues 10 days post-surgery via a fluorescent stereoscope verified that grafts were still located in the position they were initially placed 10 days ago **(Fig. IV-5)**.

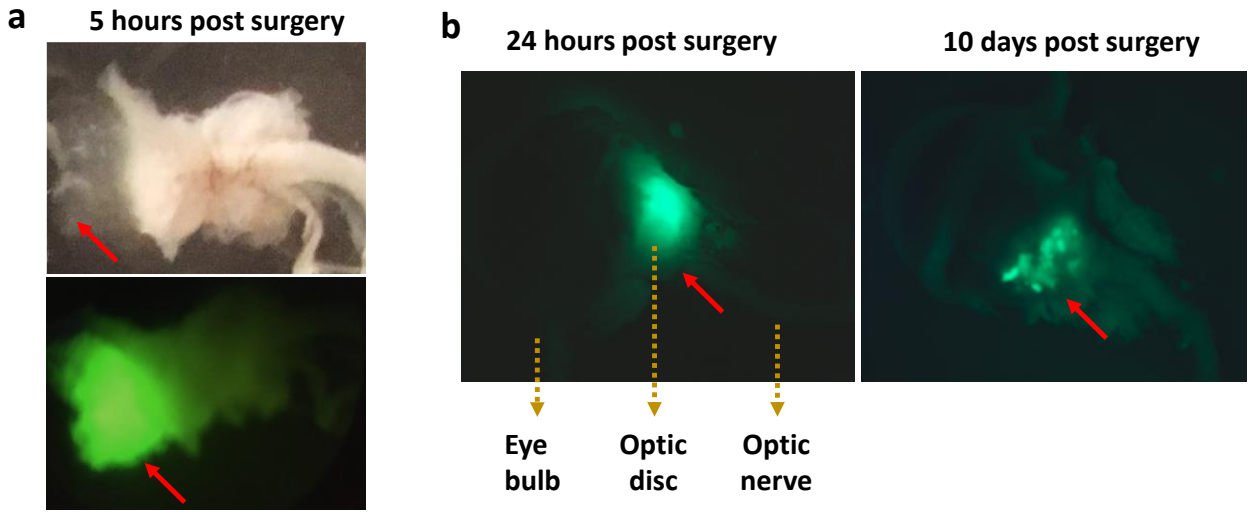

Fig. IV-5. CGS graft placed at the injury site of the optic nerve. (a) A FITC-labeled CGS graft (red arrows) located around the optic nerve as imaged by a regular and by a fluorescent microscope 5 hours post-surgery. **(b)** FITC-labeled CGS graft (red arrows) located around the optic nerve under fluorescent stereoscope 24 hours and 10 days post-surgery.

MNT delivery via a CGS graft placed around the injured optic nerve delivers MNT molecules in the proximity of the optic nerve lesion. Biomaterial-based delivery can be engineered to control the release rate of therapeutic molecules. Here, controlled MNT release was implemented via the entrapment of BNN27 in a FmocFF peptide hydrogel that was formed inside the CGS graft. Due to BNN27 solubility limitations and the hydrogel peptide preparation protocol, CGS grafts contained 6 µl 30 mM BNN27 in 25% ethanol aqueous solution. Once the graft was placed around the optic nerve, BNN27 release was defined by BNN27 diffusion through hydrogel pores.

1.4. Detection of Delivered BNN27 in Eye Tissues via Mass Spectrometry

A pilot study was conducted in order to validate the presence of BNN27 in target tissues (optic nerve, retina) when BNN27 was delivered via eye drops (one 5 µl 50 mM BNN27 in DMSO drop daily; drops were delivered

to both eyes) or via a CGS graft (30 mM BNN27) placed around the injured optic nerve. When BNN27 was delivered via drops, mice were sacrificed 1 wpi, 24 hours after the last drop administration. When BNN27 was delivered via a CGS graft, mice were sacrificed 2 wpi and graft implantation. Results showed (**Table IV-1**) that in both BNN27 delivery groups, BNN27 was detected (detection threshold: 0.7ng/ml) in some samples of retina, optic nerve and the rest parts of the eye. BNN27 was more frequently detected in the rest parts of the eye compared to retina or optic nerve. BNN27 was also detected in the rest parts of contralateral intact eyes without treatment.

Table IV-1. Validation of BNN27 delivery in retina, optic nerve and the rest eye parts via LC-MS.

Condition		Timepoint	Fraction of mice where BNN27 was detected in		
Eye	Delivery method		retina	optic Nerve	other eye parts
Intact	Eye drops	1 week	2/6	2/6	4/6
Injured	Eye drops	1 week	1/6	1/6	4/6
Intact	-	2 weeks	0/5	0/5	2/5
Injured	Graft	2 weeks	2/5	1/5	2/5

1.5. *In vivo* Evaluation of BNN27 Effects on the Mouse Optic Nerve Crush Model 2 weeks Following Injury

The therapeutic effects of BNN27 on the mouse ONC model were evaluated over a period of 2 weeks. BNN27 was delivered via two means:

1. via eye drops (50 mM BNN27 in 5 µl DMSO) delivered 1 or 2 times daily.
2. via the entrapment (30 mM BNN27 in 6 µl 25% ethanol aqueous solution) in a FmocFF peptide hydrogel formed inside a CGS graft, which was placed around the ONI site (details described in section III-10).

This experiment included 5 groups of injured mice: (a) mice that received no treatment ("Crush" group), (b) mice treated with a scaffold soaked with peptide that lacks BNN27 ("Crush (Scaffold)" group), (c) mice treated with one drop BNN27 per day ("Crush+BNN27 (1 drop/day)" group), (d) mice treated with 2 drops BNN27 per day ("Crush+BNN27 (2 drops/day)" group), (e) mice treated with a scaffold soaked with peptide and BNN27 ("Crush+BNN27 (Scaffold)" group). In each mouse, the optic nerve of the left eye was crushed, while the contralateral right eye was left intact. The right eye received the same drop treatment as the injured eye. Mice vision recovery was evaluated daily via the optomotor assay for 2 weeks. Then mice were sacrificed and tissues of interest (eye, optic nerve) were harvested for histological evaluation **(Fig. IV-6)**.

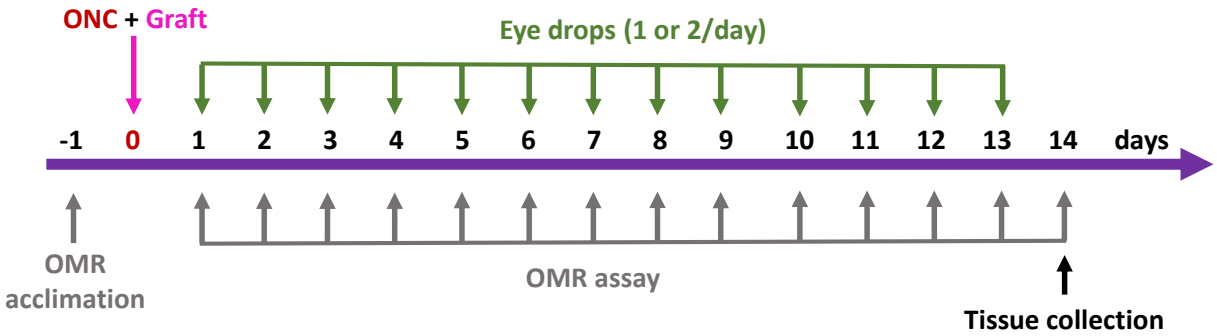

Fig. IV-6. Timeline of the 2-week ONC study.

1.5.1. BNN27 Effects on RGC Survival

The ability of BNN27 to protect RGCs from ONC-induced apoptosis was evaluated by immunostaining retina cross sections for NeuN and counting the linear density of NeuN$^+$ cells in the GCL. Results showed a significant loss of neurons and consequently RGCs in the GCL of injured eyes at 2 wpi compared to intact eyes ("Intact": 9.5±0.7 cells/100 µm, n=5; "Crush": 3.6±0.3 cells/100 µm, n=7, $P<10^{-4}$). Importantly, BNN27 delivered either via eye drops or via a CGS graft significantly increased RGC survival at 2 wpi compared to "Crush" group ("Crush": 3.6±0.3 cells/100µm, n=7; "Crush+BNN27 1 drop/day": 7.1±0.6 cells/100µm, n=6, $P<10^{-4}$; "Crush+BNN27 2 drops/day": 7.1±0.4 cells/100µm, n=8, $P<10^{-4}$; "Crush+BNN27 scaffold": 8.8±0.2 cells/100µm, n=9, $P<10^{-4}$). Interestingly, injured optic nerves treated with a CGS graft that contains a peptide hydrogel but lacks BNN27 also led to a statistically significant increase in RGC survival compared to "Crush" group ["Crush (scaffold)": 6.3±0.6 cells/100µm, n=4, P=0.01] **(Fig. IV-7)**.

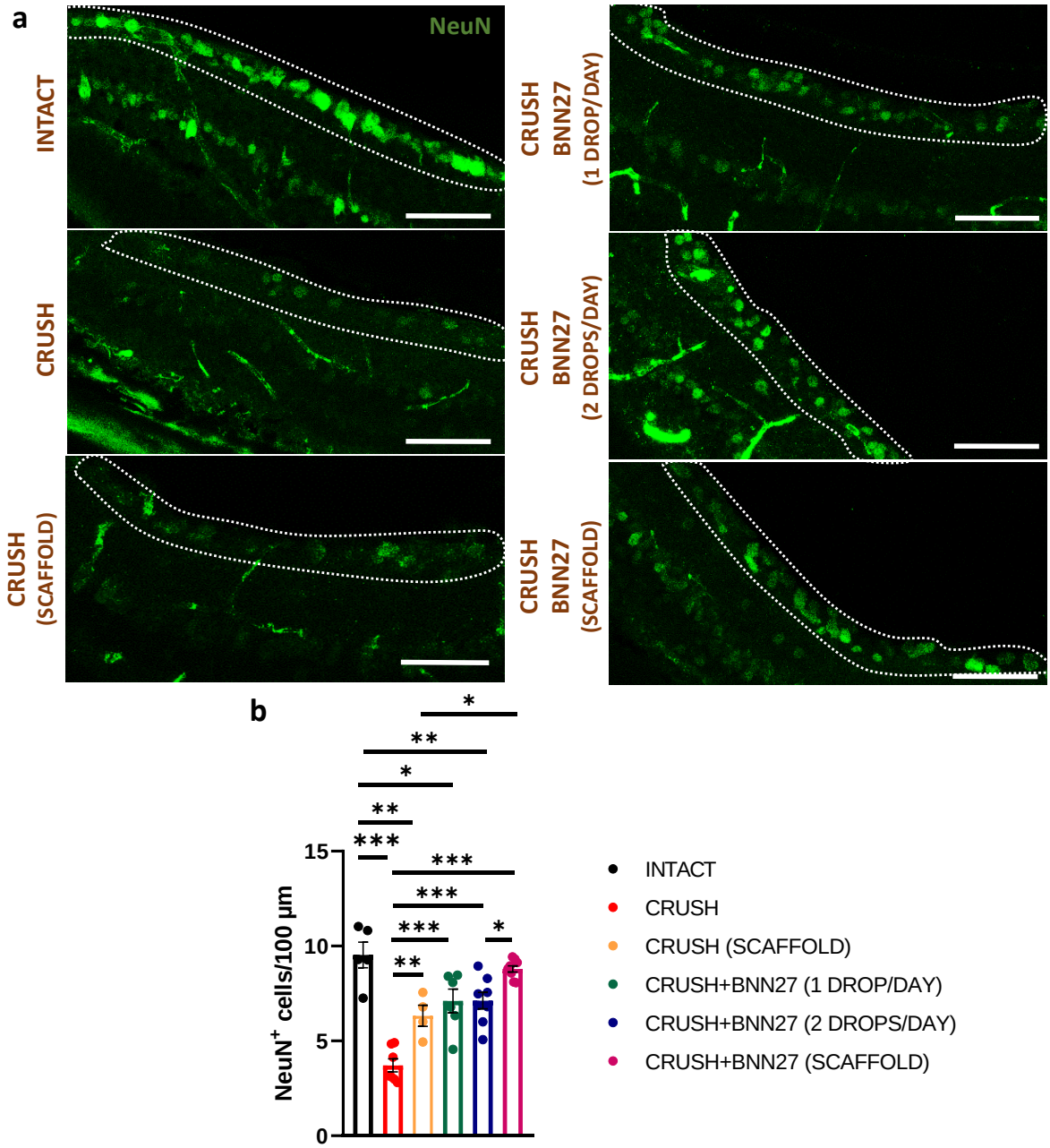

Fig. IV-7. BNN27 effects on RGC survival at 2 wpi. (a) Representative fluorescence images of retina cross sections from all groups of eyes immunostained for NeuN (green). GCL boundaries are denoted by

dotted lines. Scale bars: 50 µm. **(b)** Quantification of NeuN$^+$ cell linear density in the GCL of all mice groups at 2 wpi ("Intact": n=5; "Crush": n=7; "Crush+scaffold": n=4; "Crush+BNN27 1 drop/day": n=6; "Crush+BNN27 2 drops/day": n=8; "Crush+BNN27 scaffold": n=9). Results are presented as mean ± SEM. *P < 0.05, **P < 0.01, ***P < 0.001; Tukey's post-hoc pairwise test assuming $P_{1\text{-way-ANOVA}} < 0.05$.

Results showed that the number (one or two) of BNN27 drops administered per day did not affect RGC survival in a statistically significant way ("Crush+BNN27 1 drop/day" vs "Crush+BNN27 2 drops/day": P>0.99). Notably, targeted administration of BNN27 via a CGS graft ("Crush+BNN27 scaffold" group) resulted in larger and more consistent (less variation) RGC survival compared to BNN27 administration via eye drops. Finally, RGC survival in the "Crush+BNN27 scaffold" group was not statistically different than the one measured in intact eyes ("Crush+BNN27 2 drops/day" vs "Crush+BNN27 scaffold": P=0.04; "Intact" vs "Crush+BNN27 scaffold": P=0.84) **(Fig. IV-7)**.

1.5.2. BNN27 Effects on Gliosis in Retina

BNN27 effects on ONC-induced gliosis in retina were evaluated by immunostaining retina cross sections for GFAP and then calculating the linear density of GFAP$^+$ processes that cross the retinal layers **(Fig. IV-8a)**. Results showed that ONC led to a significant increase in the linear density of GFAP$^+$ processes at 2 wpi compared to intact eyes ("Intact": 1.5±0.4 processes/100µm, n=5; "Crush": 11.9±1.4 processes/100µm, n=7, $P<10^{-4}$). BNN27 administration (via drops or via a CGS graft) did not affect the linear density of GFAP$^+$ processes compared to "Crush" group ("Crush": 11.9±1.4 processes/100µm, n=7; "Crush+scaffold": 10.3±2.1 processes/100µm, n=4, P=0.94; "Crush+BNN27 1 drop/day": 9.1±0.8 processes/100µm, n=6, P=0.46; "Crush+BNN27 2 drops/day": 9.6±1.1 processes/100µm, n=8, P=0.59; "Crush+BNN27 scaffold": 10.6±0.7 processes/100µm, n=9, P=0.94) **(Fig. IV-8b)**.

1.5.3. BNN27 Effects on Axonal Elongation, Inflammation and OPC Recruitment

BNN27 effects on RGC axonal elongation in the optic nerve were evaluated by immunostaining longitudinal sections of crushed optic nerves for the L1 marker (**Fig. IV-9a**) and then counting the number of axons detected at various distances from the proximal end of the injury site. No significant effect of BNN27 was observed on axonal elongation at 2 wpi compared to "Crush" group (750 µm away from the proximal end: "Crush" 6.8±0.9 axons/100µm, n=4; "Crush+BNN27 2 drops/day" 7.6±2.3 axons/100µm, n=3, P=0.91; "Crush+BNN27 scaffold" 5.6±1.0 axons/100µm, n=5, P=0.77) **(Fig. IV-9b)**. While there was high accumulation of L1$^+$ axons just before the proximal end of the injury site, axons were almost absent after the injury site with or without BNN27 treatment.

BNN27 effects on microglia-mediated inflammation at the injury site following ONC were evaluated via immunostaining longitudinal optic nerve sections for Iba1 (microglia marker) and then counting the fraction of Iba1$^+$ pixels within the lesion **(Fig. IV-10a).** Results showed that BNN27 administration decreased microglia density at the injury site at 2 wpi compared to "Crush" group. Interestingly, this decrease was significant only when BNN27 was delivered via a CGS graft. On the other hand, when BNN27 was delivered via eye drops, measurements of Iba1$^+$ pixel fraction showed high variability ("Crush": 26.7±1.9%, n=4; "Crush+BNN27 2 drops/day": 18.1±5.2%, n=4, P=0.2; "Crush+BNN27 scaffold": 14.6±1.8%, n=5, P=0.04) **(Fig. IV-10b)**.

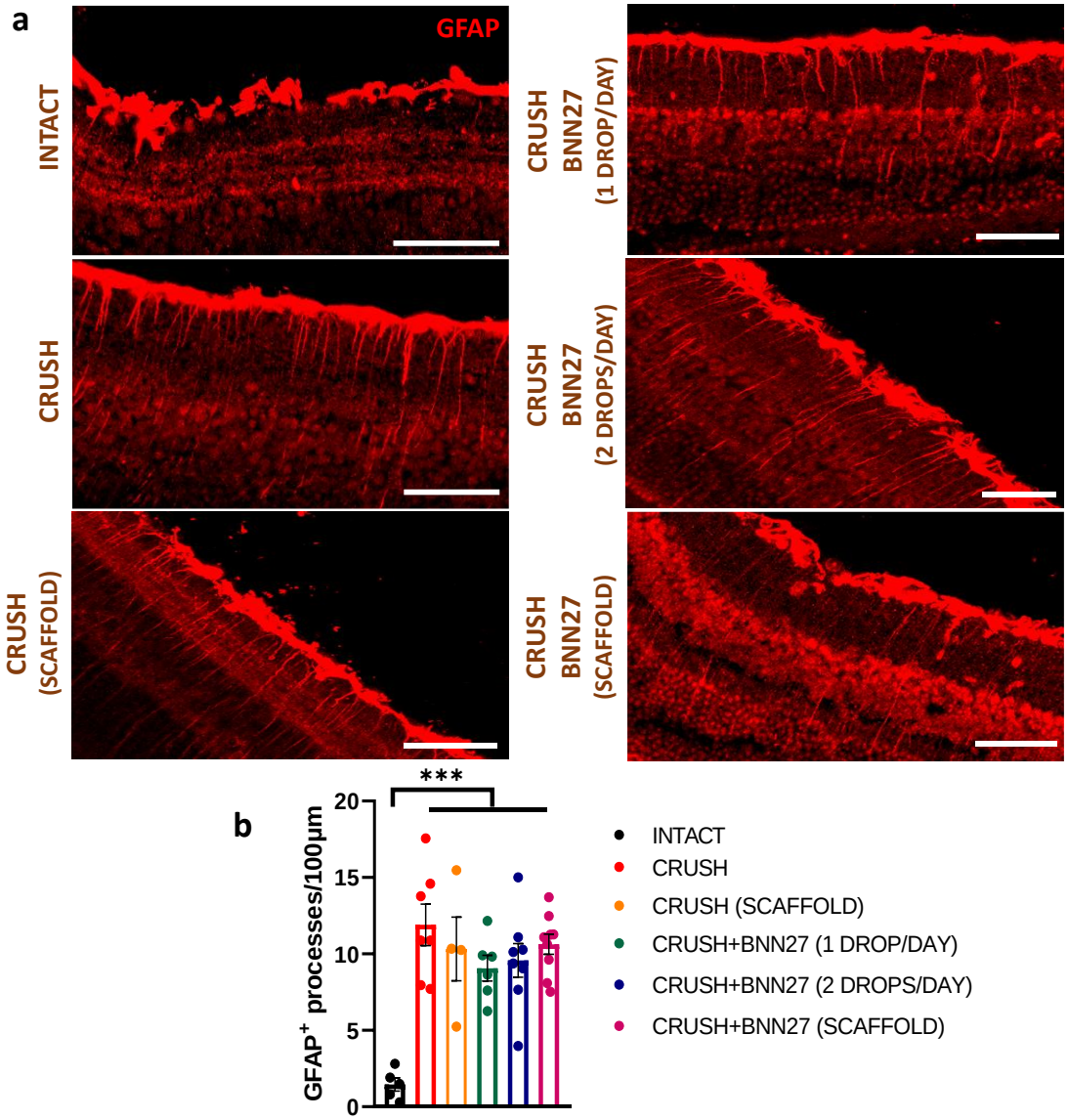

Fig. IV-8. BNN27 effects on gliosis in retina at 2 wpi. (a) Representative fluorescence images of retina cross sections from all groups of eyes immunostained for GFAP (red). Scale bars: 50 µm. **(b)** Quantification of GFAP⁺ processes linear density in the retina of all groups of eyes at 2 wpi ("Intact": n=5; "Crush": n=7; "Crush+scaffold": n=4; "Crush+BNN27 1 drop/day": n=6; "Crush+BNN27 2 drops/day": n=8; "Crush+BNN27 scaffold": n=9). Results are presented as mean ± SEM. ***P < 0.001; Tukey's post-hoc pairwise test assuming $P_{1\text{-}way\text{-}ANOVA} < 0.05$.

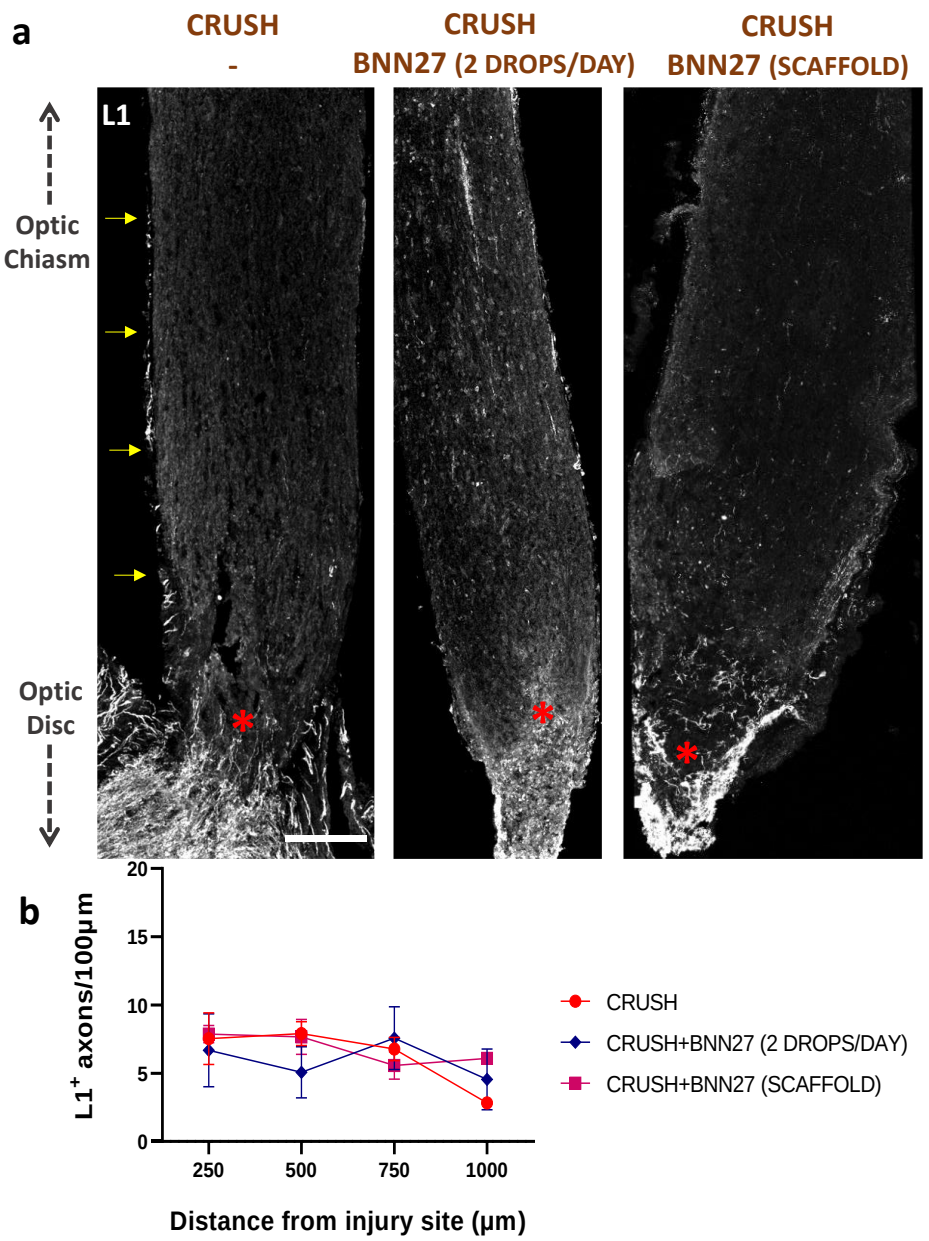

Fig. IV-9. BNN27 effects on axonal elongation in the optic nerve at 2 wpi. (a) Representative fluorescence images of longitudinal sections of crushed (untreated and treated) optic nerves immunostained for L1. The proximal end of the injury site is noted with a red asterisk. Distances of 250, 500, 750 and 1000 µm away from the proximal end of the injury site are noted with yellow arrows. Scale bar: 100 µm. **(b)** Quantification of the linear density of $L1^+$ axons per section at 250, 500, 750 and 1000 µm away from the proximal end of the injury site of crushed (untreated and treated) optic nerves at 2 wpi ("Crush": n=4; "Crush+BNN27 2 drops/day": n=3; "Crush+BNN27 scaffold": n=5). Results are presented as mean ± SEM.

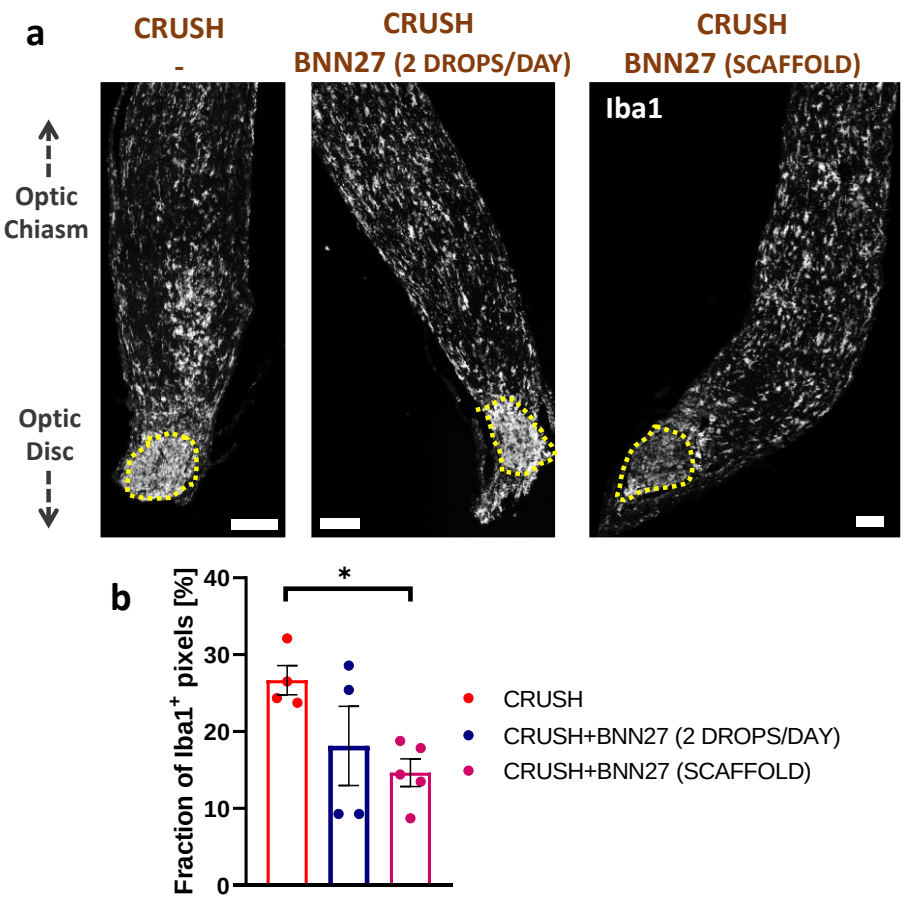

Fig. IV-10. BNN27 effects on microglia-mediated inflammation in ONI site at 2 wpi. (a) Representative fluorescence images of longitudinal sections of crushed (untreated and treated) optic nerves immunostained for Iba1. The injury site is defined by a dotted line. Scale bars: 100 µm. **(b)** Quantification of the fraction of Iba1$^+$ pixels within the injury site of crushed (untreated and treated) optic nerves at 2 wpi ("Crush": n=4; "Crush+BNN27 2 drops/day": n=4; "Crush+BNN27 scaffold": n=5). Results are presented as mean ± SEM. *P < 0.05; Tukey's post-hoc pairwise test assuming $P_{1\text{-way-ANOVA}} < 0.05$.

BNN27 effects on ONC-induced recruitment of OPCs were evaluated via immunostaining optic nerve longitudinal sections for PDFDRα (OPC marker) **(Fig. IV-11a)**. By counting the number of OPCs in different distances from the distal end of the injury site at 2 wpi, no difference was observed neither among the different groups nor among the different distances (750 µm from injury site: "Crush" 25.5±3.7 cells/mm^2, n=3; "Crush+BNN27 2 drops/day" 21.5±6.2 cells/mm^2, n=2, P=0.89; "Crush+BNN27 scaffold" 24.0±10.5 cells/mm^2, n=2, P=0.98) **(Fig. IV-11b)**. Additionally, BNN27 administration did not affect OPC density (assayed via the fraction of PDFDRα$^+$ pixels) within the lesion at 2 wpi ("Crush": 96.2±0.6%, n=3; "Crush+BNN27 2 drops/day": 96.3±0.6%, n=2, P=1.0; "Crush+BNN27 scaffold": 95.6±1.2%, n=2, P=0.84) **(Fig. IV-11c)**.

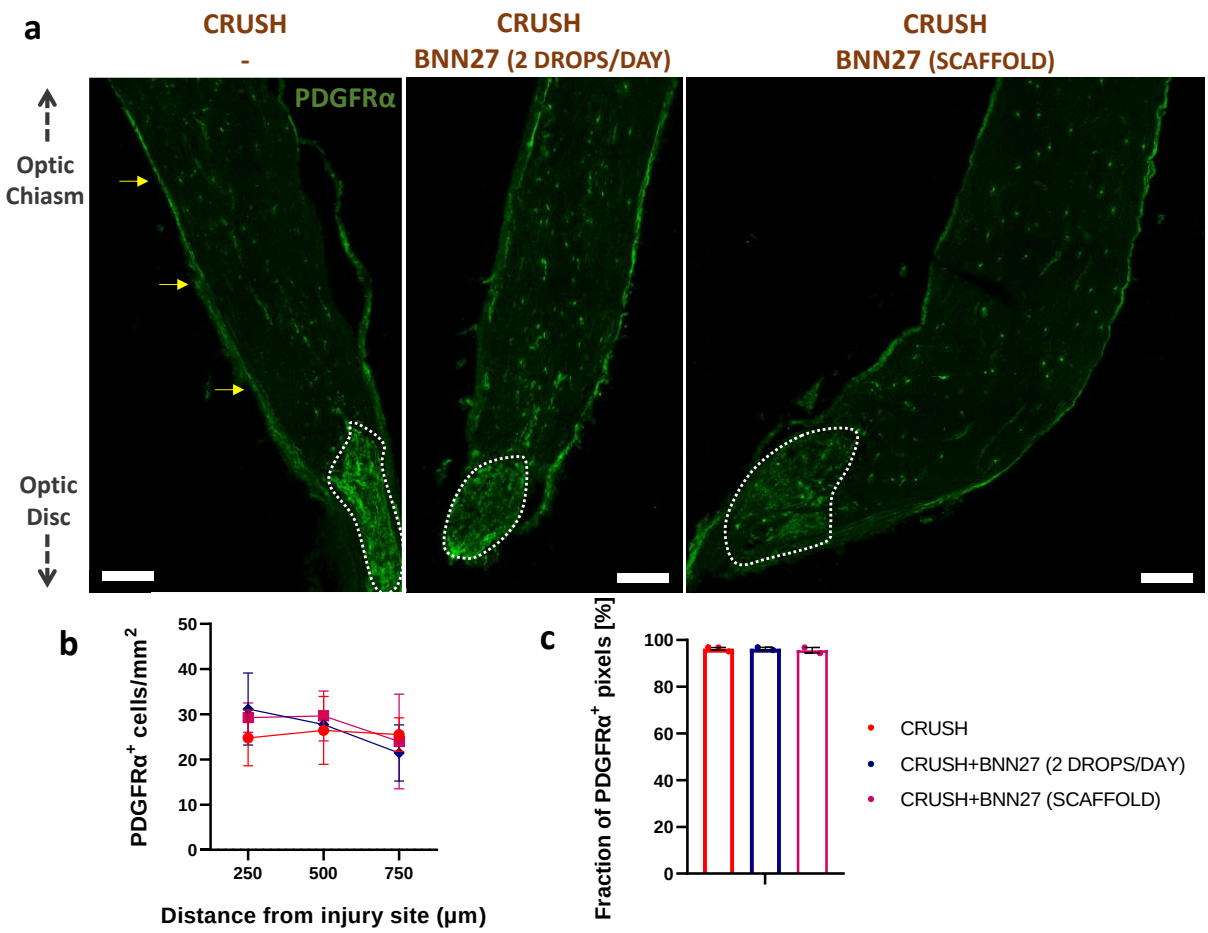

Fig. IV-11. BNN27 effects on OPC recruitment in ONI site at 2 wpi. (a) Representative fluorescence images of longitudinal sections of crushed (untreated and treated) optic nerves immunostained for PDGFRα. The injury site is defined by a yellow dotted line. Arrows denote distances of 250, 500 and 750 µm away from the distal end of the injury site. Scale bars: 100 µm. **(b)** Quantification of OPC density in sections located 250, 500 and 750 µm away from the injury site of crushed (untreated and treated) optic nerves at 2 wpi. **(c)** Quantification of the fraction of PDGFRα$^+$ pixels within the injury site of crushed (untreated and treated) optic nerves at 2 wpi. ("Crush": n=3; "Crush+BNN27 2 drops/day": n=2; "Crush+BNN27 scaffold": n=2). Results are presented as mean ± SEM.

1.5.4. BNN27 Effects on Vision Recovery

ONC led to vision impairment immediately, as detected 1 day post-injury via the OMR assay (**Fig. IV-12**). No OMR [no positive response of mice in any stripe pattern (0.01-0.5 cpd)] was observed during CW rotation of the drum with stripe patterns (examined the injured left eye). On the contrary, an OMR score of 0.4-0.5 cpd (the OMR score refers to the highest spatial frequency of the stripe pattern that induces a positive response in mice) was detected during CCW drum rotation (examined the intact right eye). Results showed that BNN27 administration did not enhance vision during the 2-week observation period, as it did not result in the detection of OMR in treated injured mice.

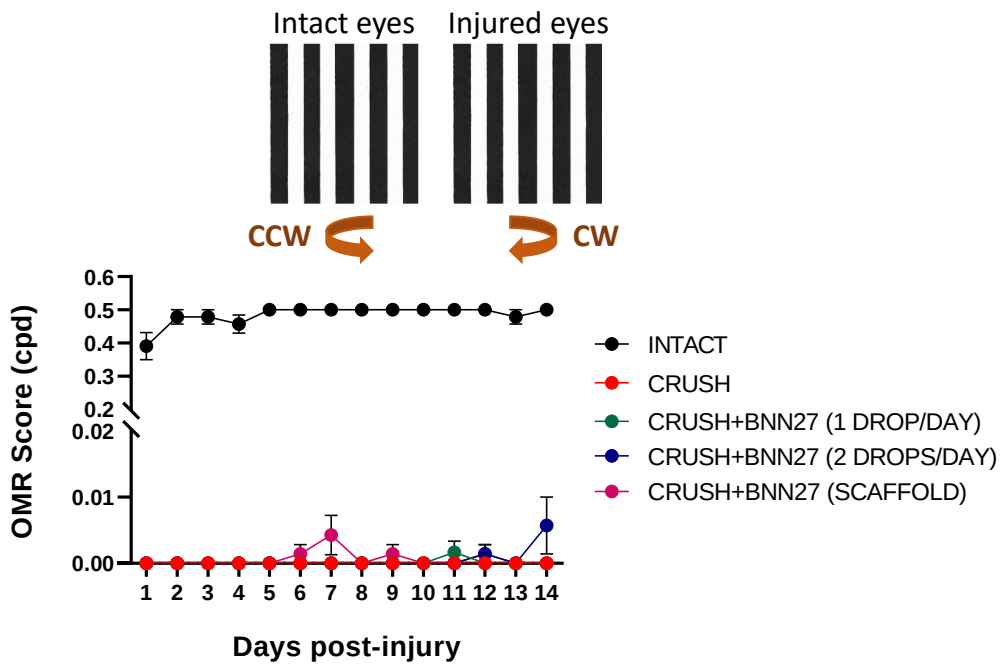

Fig. IV-12. BNN27 effects on OMR score over 2 weeks following ONC. Quantification of the OMR score observed when the drum was rotated CCW (examined the intact right eye) or CW (examined the injured left eye) at 2 wpi. ("Intact": n=8; "Crush": n=4 to 7; "Crush+BNN27 1 drop/day": n=6-12; "Crush+BNN27 2 drops/day": n=7; "Crush+BNN27 scaffold": n=7).

1.6. *In vivo* Evaluation of BNN27 Effects on the Mouse Optic Nerve Crush Model 10 weeks Following Injury

Following the results of the 2-week study (section IV-1.5), a longer study was conducted to probe if BNN27 effects observed at 2 wpi persist over time. The 10-week study contained the same 4 groups of injured mice as the 2-week study: (a) mice that received no treatment ("Crush" group), (b) mice treated with a scaffold soaked with peptide that lacks BNN27 ("Crush (Scaffold)" group), (c) mice treated with 2 drops BNN27 per day ("Crush+BNN27 (2 drops/day)" group), (d) mice treated with a scaffold soaked with peptide and BNN27 ("Crush+BNN27 (Scaffold)" group). In each mouse the optic nerve of the left eye was crushed. The contralateral right eye remained intact, yet it received the same drop treatment as the left eye. Mice vision recovery was evaluated via the optomotor assay for 10 weeks. Then mice were sacrificed for histological evaluation **(Fig. IV-13)**.

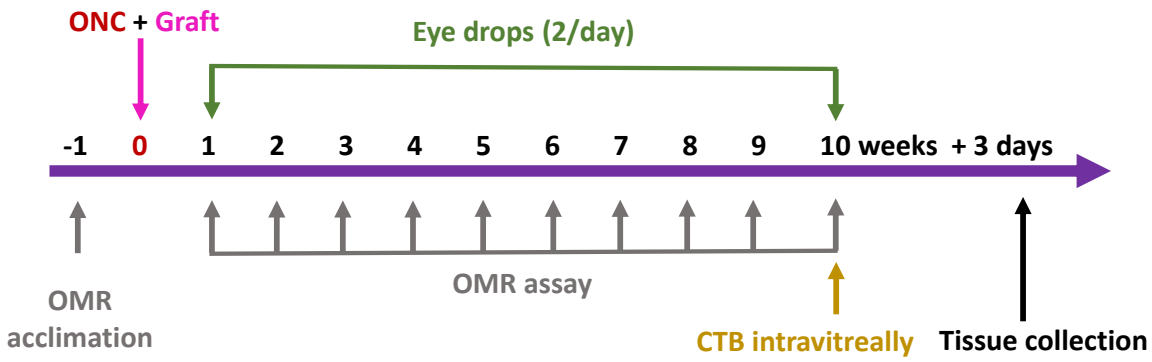

Fig. IV-13. Timeline of the 10-week ONC study.

1.6.1. BNN27 Effects on RGC Survival

BNN27 effects on RGC survival at 10 wpi were evaluated by immunostaining retina cross sections from all mice groups for NeuN. Results **(Fig. IV-14)** showed that, in contrast to 2 wpi, BNN27 administration did not increase RGC survival at 10 wpi compared to the untreated "Crush" group. In the untreated "Crush" group there was no decrease in the NeuN$^+$ cell linear density (increased RGC death) compared to 2 wpi ("Crush 2 wpi": 3.7±0.3 cells/100µm, n=7; "Crush 10 wpi": 4.5±0.3 cells/100µm, n=3, P=0.21). The linear density of NeuN$^+$ cells in the three treated groups did not differ significantly from the one of the untreated "Crush" group at 10 wpi ("Crush": 4.5±0.3 cells/100µm, n=3; "Crush+scaffold": 6.3±0.5 cells/100µm, n=5, P=0.09; "Crush+BNN27 2 drops/day": 5.8±0.5 cells/100µm, n=4, P=0.30; "Crush+BNN27 scaffold": 5.6±0.5 cells/100µm, n=4, P=0.41). Thus, the neuroprotective effects of BNN27 on ONC-induced RGC apoptosis observed at 2 wpi were abolished at 10 wpi.

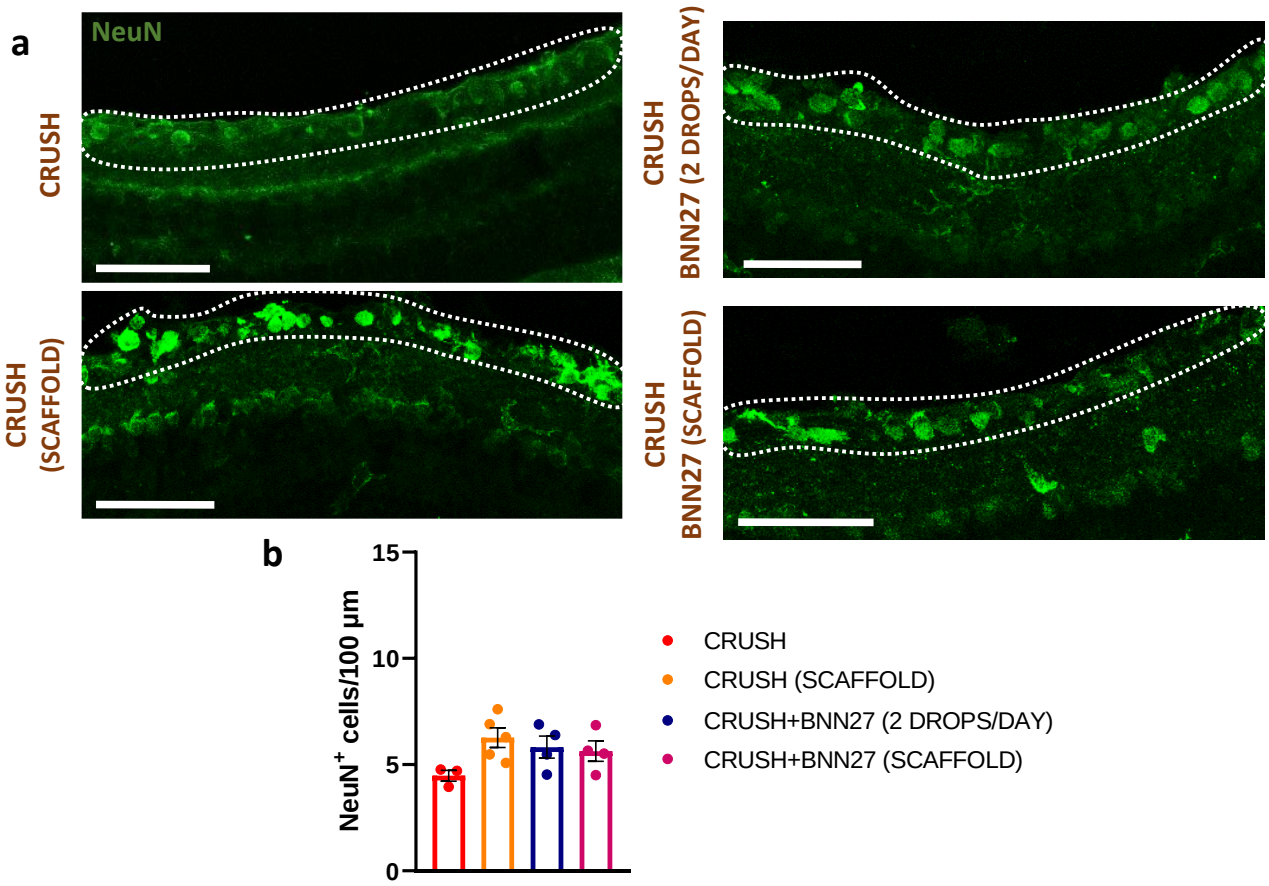

Fig. IV-14. BNN27 effects on RGC survival at 10 wpi. (a) Representative fluorescence images of retina cross sections of injured (untreated and treated) groups immunostained for NeuN (green). GCL boundaries are denoted by dotted lines. Scale bars: 50 µm. **(b)** Quantification of the linear density of NeuN$^+$ cells in the GCL for injured (untreated and treated) groups at 10 wpi ("Crush": n=3; "Crush+scaffold": n=5; "Crush+BNN27 2 drops/day": n=4; "Crush+BNN27 scaffold": n=4). Results are presented as mean ± SEM.

1.6.2. BNN27 Effects on Axonal Elongation

BNN27 effects on RGC axonal elongation in the optic nerve were evaluated by immunostaining longitudinal sections of crushed optic nerves for the L1 marker (**Fig. IV-15a**) and counting the number of L1$^+$ axons in optic nerve cross sections located various distances from the proximal end of the injury site. No significant effect of BNN27 was observed on the number of L1$^+$ axons at 10 wpi compared to "Crush" group (750 µm

from proximal end of the injury site: “Crush” 4.3±1.7 axons/100µm, n=3; “Crush+scaffold” 3.3±0.8 axons/100µm, n=4, P=0.91; “Crush+BNN27 2 drops/day” 5.1 axons/100µm, n=1, P=0.99; “Crush+BNN27 scaffold” 3.8±0.8 axons/100µm, n=5, P=0.84) **(Fig. IV-15b)**.

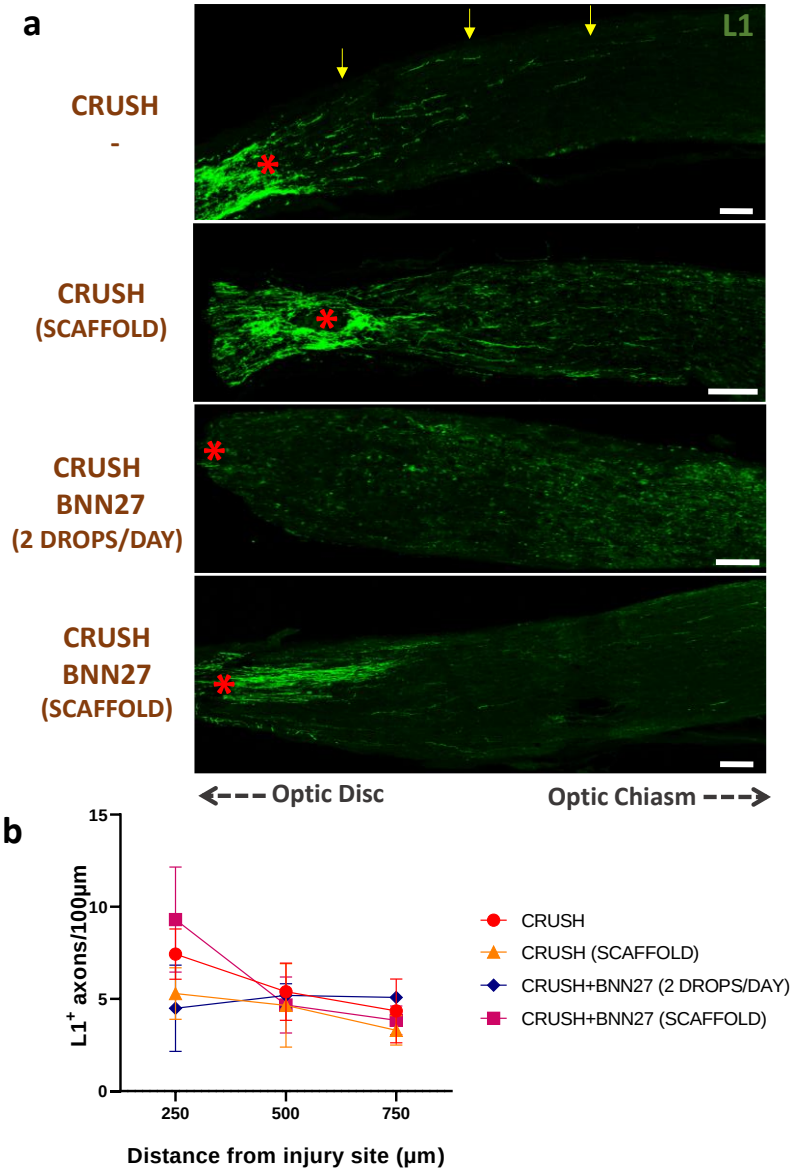

Fig. IV-15. BNN27 effects on axonal elongation in the optic nerve at 10 wpi. (a) Representative fluorescence images of longitudinal sections of the crushed (untreated and treated) optic nerve immunostained for L1. Red asterisks denote the proximal end of the injury site. Yellow arrows denote cross sections located 250, 500 and 750 µm away from the proximal end of the injury site. Scale bars: 100 µm. **(b)** Quantification of the density of $L1^+$ axons in cross sections located 250, 500 and 750 µm away from the proximal end of the injury site of crushed (untreated and treated) optic nerves at 10 wpi (“Crush”: n=3; “Crush+scaffold”: n=4; “Crush+BNN27 2 drops/day”: n=1; “Crush+BNN27 scaffold”: n=5). Results are presented as mean ± SEM.

1.6.3. BNN27 Effects on Vision Recovery

BNN27 effects on vision recovery following ONC were evaluated over a 10-week period following ONC using the optomotor assay. Similarly to the 2-week study, ONC led to vision impairment, as detected 1 day post

injury. No OMR events were observed during CW rotation of drum with stripes patterns (examined the injured left eyes). On the contrary, an OMR score of 0.4-0.5 cpd was detected during CCW drum rotation (examined the intact right eye). During the 10-week period following ONC, BNN27 administration did not enhance vision, as it could not lead to any OMR in mice even at 10 wpi **(Fig. IV-16)**.

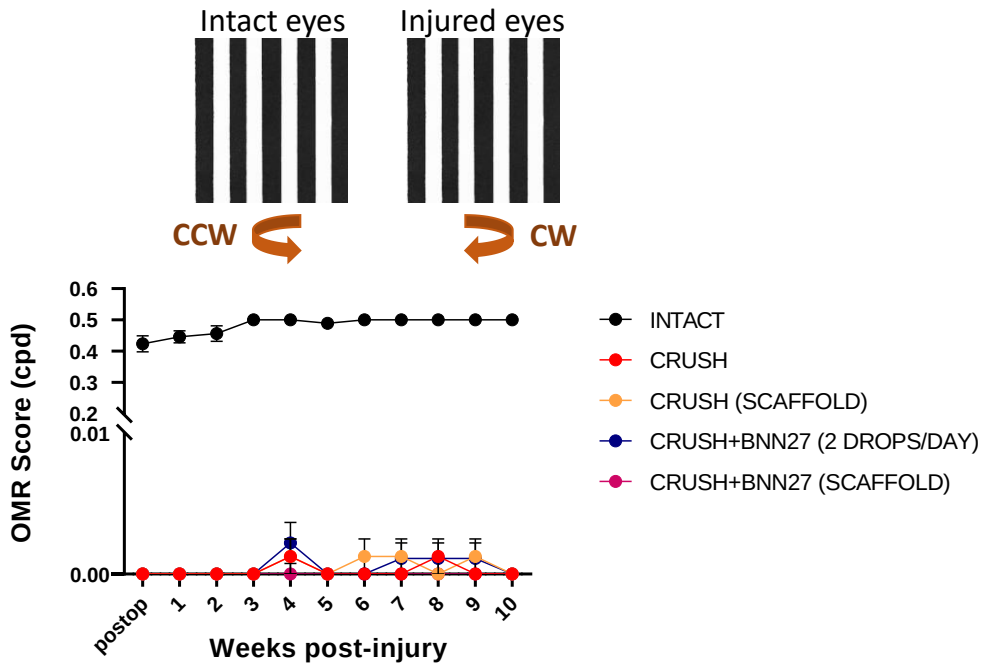

Fig. IV-16. BNN27 effects on OMR score over 10 weeks following ONC. Quantification of the OMR score observed when the drum is rotated CCW (examined the intact eye) or CW (examined the injured eye) at 10 wpi ("Intact": n=12; "Crush": n=8; "Crush+scaffold": n=8; "Crush+BNN27 2 drops/day": n=9; "Crush+BNN27 scaffold": n=9).

1.7. *Ex vivo* Evaluation of Microneurotrophin Effects on Mouse Adult Retina Explants

In order to further investigate MNT effects in retina, *ex vivo* adult retina explants were cultured in the presence of the NT NGF or MNTs over 2 weeks. Apart from BNN27, three more MNTs were tested: MNT10 (a TrkA-specific agonist), MNT11 (a TrkB-specific agonist) and MNT61 (a TrkB-specific agonist).

Axonal elongation of RGCs away from adult retina explants was quantified via immunostaining explants for Tuj1 (neuronal marker) and counting the number of outgoing Tuj1^{+} RGC neurites found at different distances from the explant's boundaries **(Fig. IV-17a)**. Preliminary analysis (from a small number of biological samples) revealed that none of the four tested MNTs managed to increase neurites extension compared to the untreated control ("DMSO" group) in a statistically significant way (200 µm from explant's boundaries: $P_{1\text{-way-ANOVA}}$=0.11, F=2.28). Results showed that NGF and BNN27 increased the number of neurites intersects compared to the "DMSO" group, yet in a non-statistically significant way. MNT10, a novel TrkA-specific agonist, had similar results to BNN27 and NGF (both can activate both TrkA and p75^{NTR} receptors) (DMSO: 26±8.7 neurites intersects at 200 µm (n=3); NGF: 53 ± 33 neurites intersects at 200 µm (n=2), P=0.63; BNN27: 43.7±5.2 neurites intersects at 200 µm (n=4) P=0.81; MNT10: 29.2±10.5 neurites intersects at 200µm, n=4, P=1.0) **(Fig. IV-17b,c)**. Furthermore, BNN27 and MNT10 resulted in longer neurites (up to 2mm) compared to other molecules **(Fig. IV-17b)**. In contrast, explant treatment with TrkB-specific agonists MNT11 and MNT61 decreased the number of neurites intersects compared to the "DMSO" group, yet in a non-

statistically significant way (MNT11: 8 neurites intersects at 200µm, n=1, P=0.96; MNT61: 9±1.6, n=4, P=0.84) **(Fig. IV-17b,c)**.

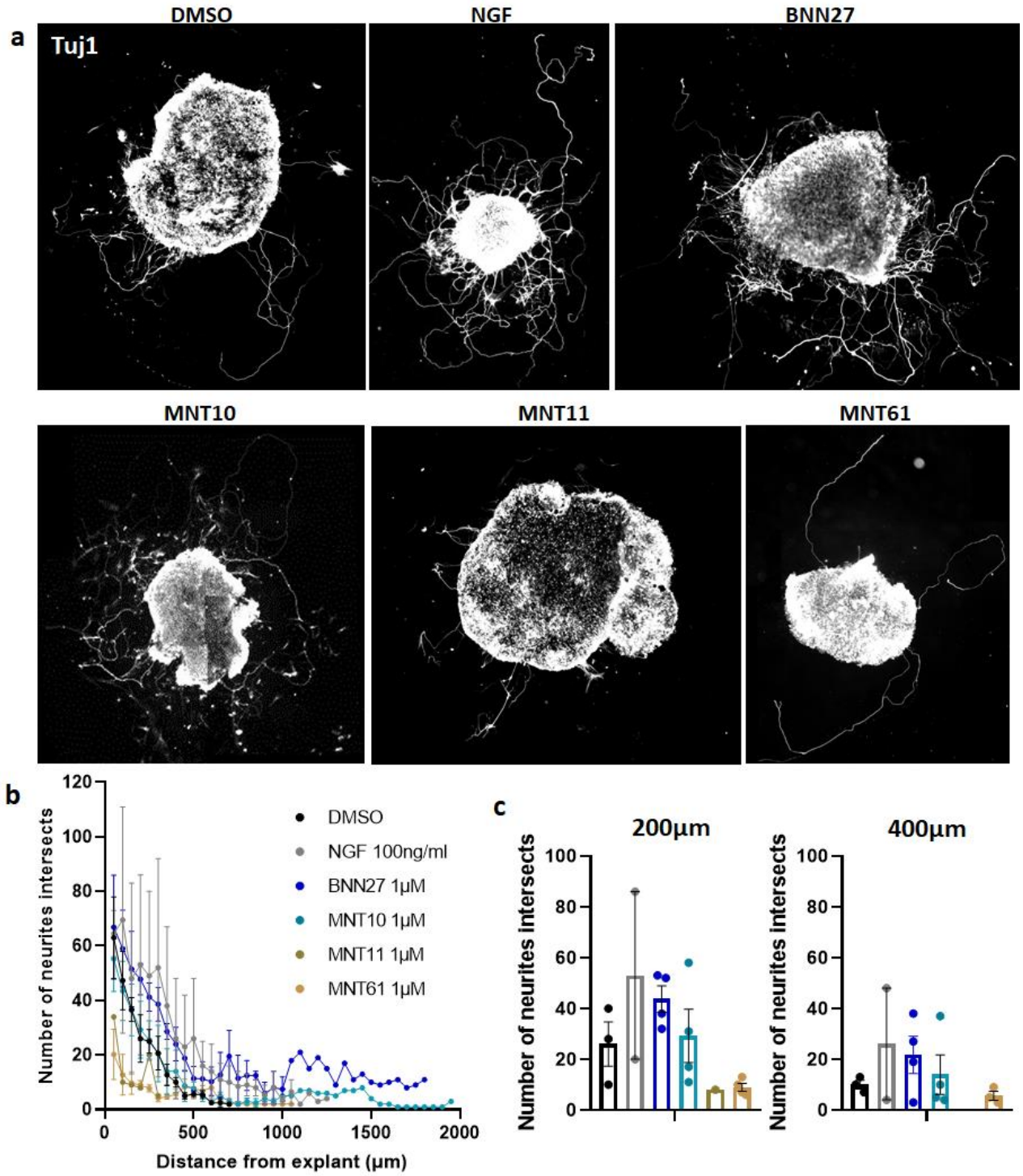

Fig. IV-17. MNT neurogenic effects on RGCs in mouse adult retina explants. (a) Representative images of adult retina explants treated with NGF or various MNTs, immunostained for Tuj1. **(b)** Quantification of the number of neurites in adult retina explants treated with NGF, BNN27, MNT10, MNT11 or MNT61 that intersect various distances from explant boundaries. **(c)** Quantification of the number of neurites of adult retina explants treated with NGF, BNN27, MNT10, MNT11 or MNT61 that intersect at 200 and 400 µm away from the explant boundaries ("DMSO": n=3, "NGF": n=2, "BNN27": n=4, "MNT10": n=4, "MNT11": n=1, "MNT61": n=4). Results are presented as mean ± SEM.

2. Evaluation of Combinatorial Treatments on Spinal Cord Injury

The second part of the thesis focuses on the evaluation of combinatorial treatments for SCI in the dorsal column crush mouse SCI model. Two experimental studies were conducted, named study A and B respectively. Study A studied the effects of NSC-seeded CS grafts. Study B focused on a treatment that combined NSC-seeded CS grafts with the systemic delivery of the seminal MNT BNN27. Details of the experimental design are described in section III-16.

2.1. *In vivo* Evaluation of the Effects of Mouse Embryonic NSC-seeded CS Grafts at the Injury Site on the Mouse Dorsal Column Crush Spinal Cord Injury Model (Study A)

The therapeutic effects of grafts consisting of porous CS seeded with mouse embryonic NSCs were evaluated in the dorsal column crush mouse SCI model **(Fig. IV-17)**. The crush results in the formation of a void (approximate volume 1 mm^3), appropriate for placing a biomaterial-based graft **(Fig. III-1,8)**. Experimental design included five injured animal groups: 1) In mice of the "Scaffold only" group, a cell-free porous CS graft was placed inside the injury site immediately after injury. 2) In mice of the "Scaffold+NSC" group, a porous CS graft seeded with mouse embryonic E13.5 NSCs was placed inside the injury site immediately after injury. 3) In mice of the "NSC injection" group a drop of mouse embryonic E13.5 NSC suspension was injected at the injury site immediately after injury. 4) In mice of the "Scaffold+NIH3T3" group a porous CS graft seeded with NIH3T3 cells (mouse fibroblasts) was placed inside the injury site immediately after injury. NIH3T3 fibroblasts were used as a non-NSC control group and were chosen due to their proliferative capacity, end-term differentiation state and robust adhesion to CS. 5) In mice of the "Crush only" group injured animals did not receive any treatment. Finally, the study included the "Uninjured Control" animal group, where, following laminectomy, the exposed spinal cord was not injured. The "Scaffold+NSC", "Scaffold+NIH3T3" and "NSC injection" groups utilized BrdU-pulsed cells to enable their detection via immunohistochemistry.

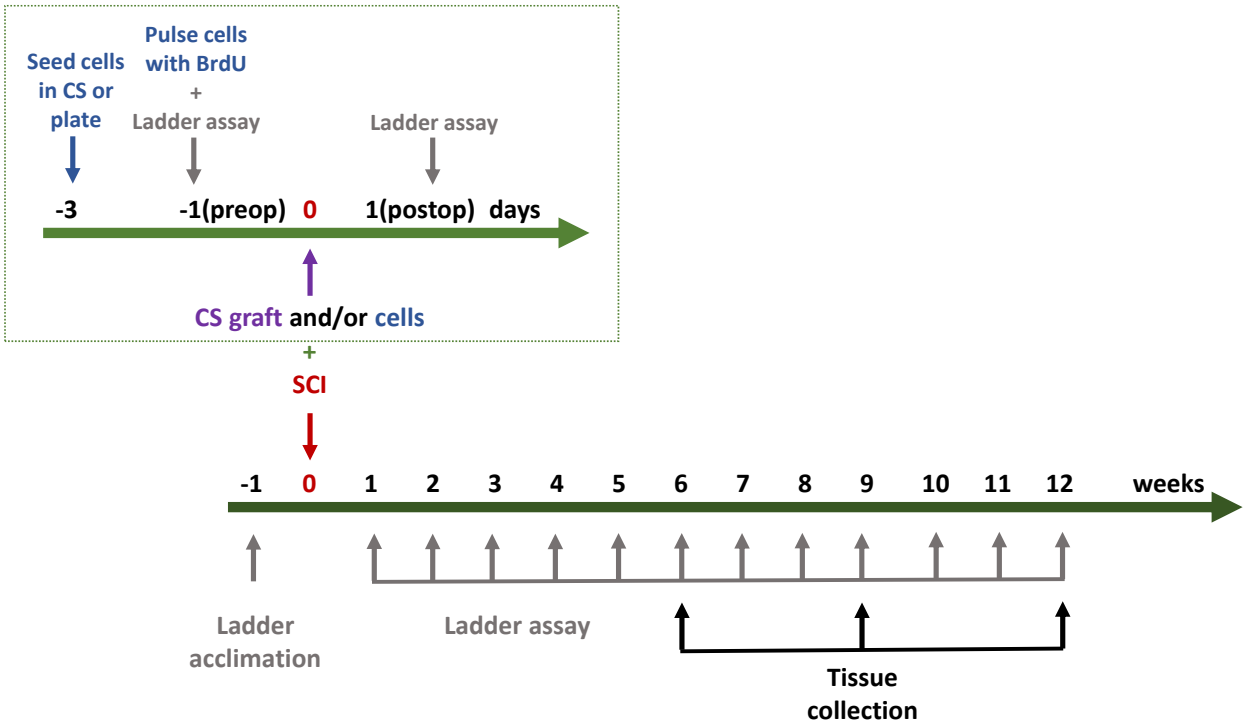

Fig. IV-17. Timeline of 12-week SCI study A.

2.1.1. Integration of Cell-seeded and Cell-free CS Grafts

Histological evaluation of spinal cord morphology in parasagittal sections at 6, 9, and 12 wpi via H&E staining **(Fig. IV-18)** revealed that NSC-seeded scaffolds integrated well with the surrounding tissue and no gaps were observed between the scaffold and the surrounding tissue. Contrarily, in the "Scaffold only" group, scaffolds drifted away from the injury site at 6 wpi. In the "Scaffold+NIH3T3" group, the scaffold was integrated with the surrounding tissue at 6 wpi, but there were extended areas of cavitation in the tissue surrounding the scaffold.

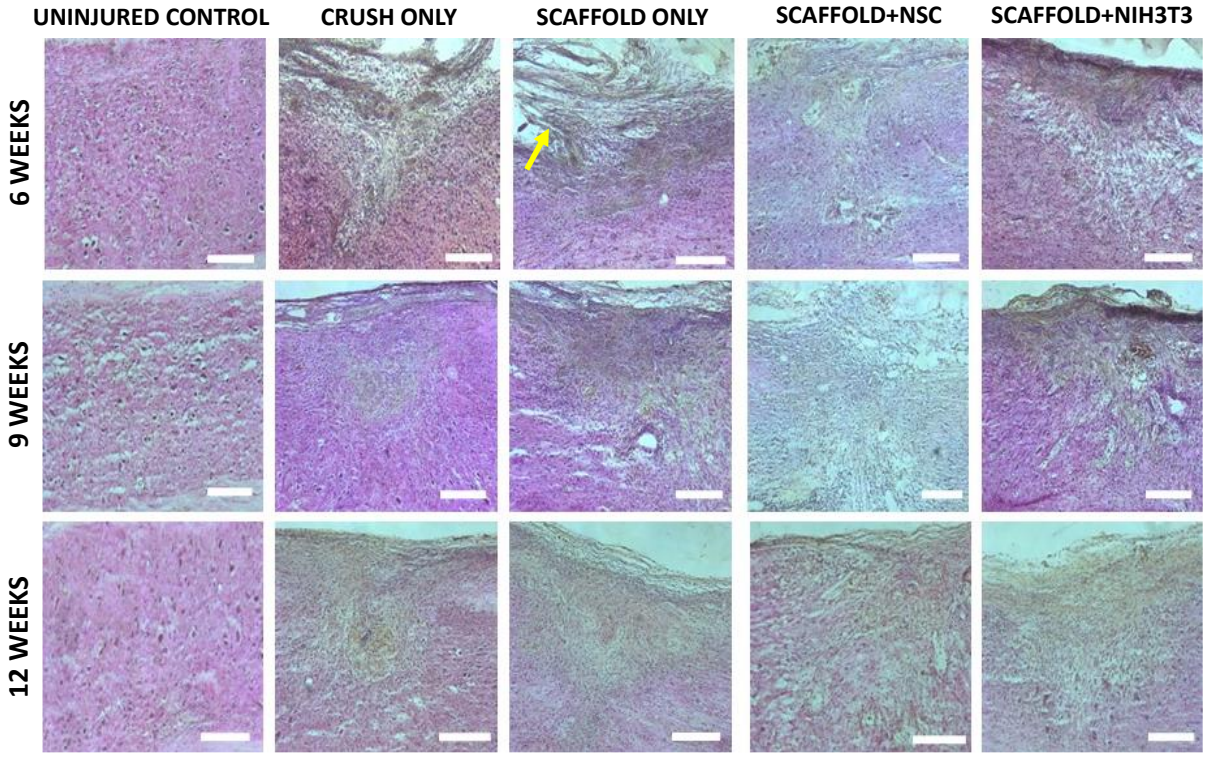

Fig. IV-18. Histological evaluation of CS Grafts Effects on Lesion Morphology at 6, 9 and 12 wpi. H&E staining of spinal cord parasagittal sections from the "Uninjured Control", "Crush only", "Scaffold only", "Scaffold+NSC" and "Scaffold+NIH3T3" mice groups at 6, 9 and 12 wpi. The yellow arrow in the "Scaffold only" group at 6 wpi indicates a drifted scaffold. Scale bars: 200µm.

In mice of the "Scaffold only" and "Scaffold+NSC" groups no further animals' health complications were observed. On the contrary, four out of eight animals of the "Scaffold+NIH3T3" group showed signs of poor health and distress (weight loss, back feet paralysis and heavy abdominal breathing) and were euthanized at 2 wpi. Histological evaluation of the euthanized animals showed extended damage of the tissue surrounding the lesion and inflammatory response **(Fig. IV-19)**. The remaining four animals of the "Scaffold+NIH3T3" group were monitored for locomotion recovery but were not included in further histological and statistical analysis, due to the complications observed in the group.

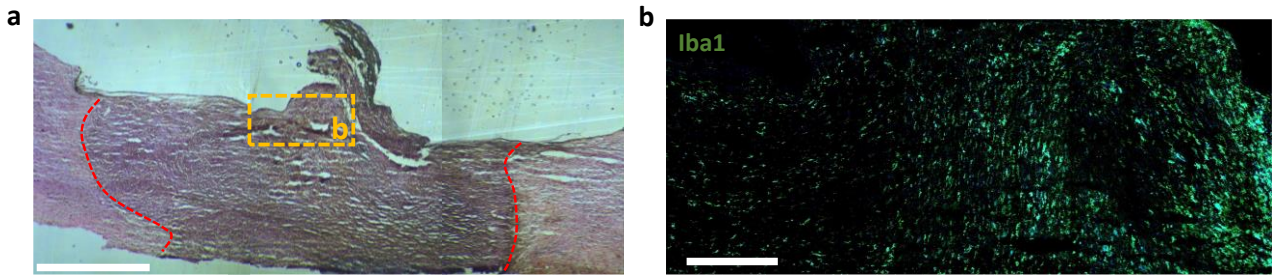

Fig. IV-19. Observations in euthanized mice treated with CS grafts seeded with NIH3T3. (a) H&E staining of a spinal cord parasagittal section from a mouse of the "Scaffold+NIH3T3" group that was euthanized 2 wpi due to signs of poor health and distress. Red dashed lines highlight the part of the spinal cord tissue that was severely damaged. The yellow marked ROI is presented in higher magnification immunostained with Iba1 **(b)**, indicating significant microglia-induced inflammation in the grafted region. Scale bars: 500 µm.

2.1.2. Effects of NSC-seeded CS Grafts on Locomotion Recovery Following Injury

Mice locomotion recovery over a period of 12 weeks following dorsal column SCI was evaluated by quantifying their step fault rate in the Horizontal Ladder Walking Assay **(Fig. IV-20a)**. During this 12-week period, mice of the "Uninjured Control" group had time-invariant fault rate (µ=7.5 %, σ= 3.2 %). No difference was observed among the five injured groups ("Crush only", "Scaffold only", "Scaffold+NSC", "NSC injection" and "Scaffold+NIH3T3") till the 1st wpi, confirming that injury was consistently performed in all animals (post-op: $P_{1\text{-way-ANOVA}}$=0.57, F=0.74; week 1: $P_{1\text{-way-ANOVA}}$=0.41, F=0.80).

Between 1 and 12 wpi, all injured groups showed some locomotion improvement. Eventually, differences in fault rate became statistically significant only in mice treated with NSC-seeded CS grafts compared to "Crush only" group at 10 wpi ("Crush only": 19.2±1.0%, n=6 vs. "Scaffold+NSC": 10.0±1.8%, n=8, P=0.02), 11 wpi ("Crush only": 16.9±2.1%, n=6 vs. "Scaffold+NSC": 9.6±0.9%, n=8, P=0.02) and 12 wpi ("Crush only": 16.6±1.6%, n=6 vs. "Scaffold+NSC": 8.4±0.8%, n=8, $P=4\cdot10^{-3}$). Interestingly, "Scaffold+NSC" group was the only injured group that did not differ statistically from the "Uninjured control" group (week 10: 7.1±0.9%, n=7, P=0.19; week 11: 6.6±1.2%, n=8, P=0.07; week 12: 7.1±0.8%, n=8, P=0.24) **(Fig. IV-20a,b)**. No improvement in locomotion recovery compared to "Crush only" group was observed in animals treated with NIH3T3-seeded CS grafts **(Fig. IV-20a)**. The "Scaffold+NIH3T3" group was not included in the statistical analysis of step fault rate of injured groups at 10, 11 and 12 wpi due to the major complications observed in mice of this group, as described in section IV-2.1.1.

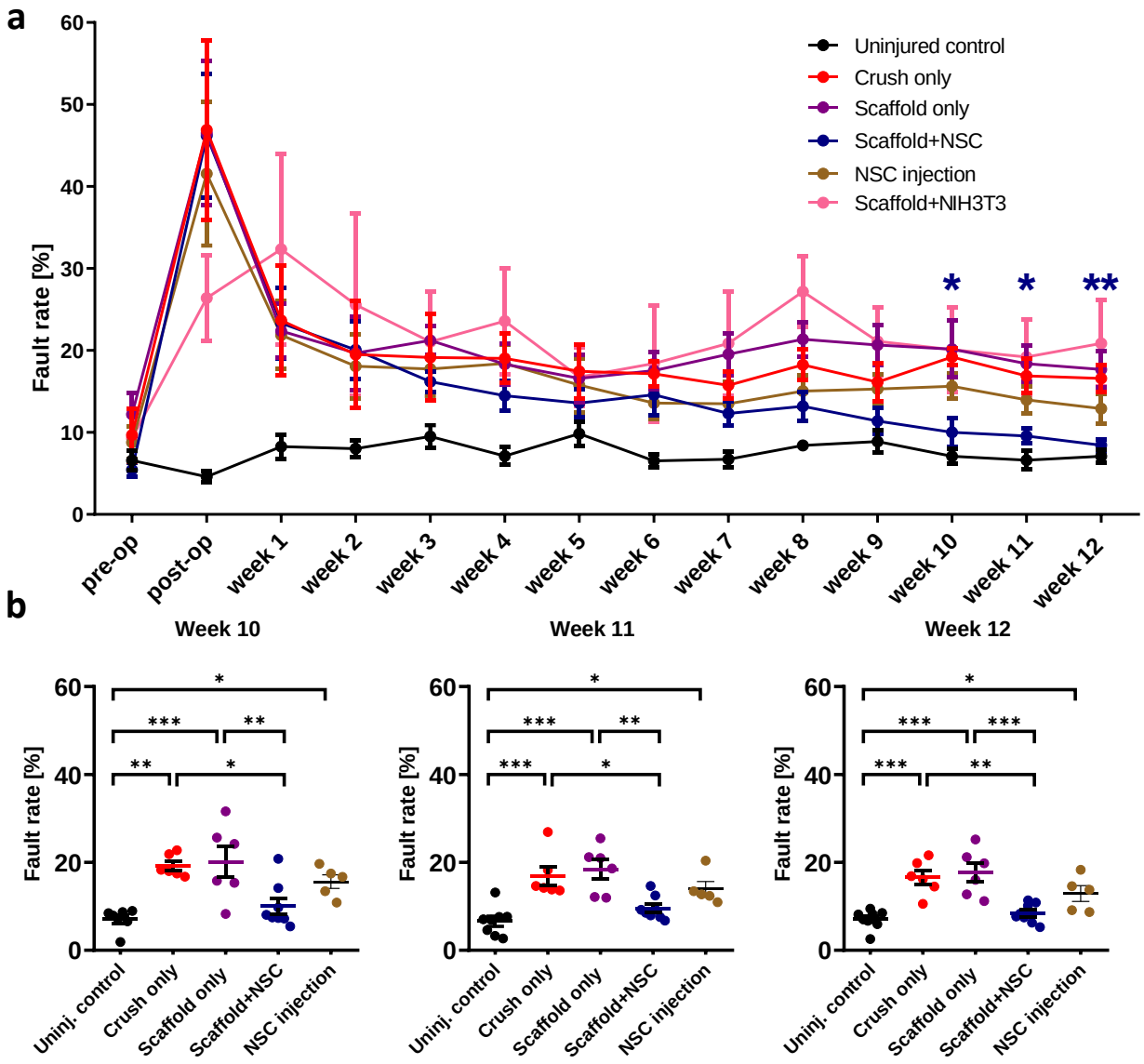

Fig. IV-20. Effects of NSC-seeded CS grafts on locomotion recovery in a mouse dorsal column crush SCI model over a 12-week period following injury. (a) Quantification of locomotion performance (fault rate) after SCI by the Horizontal Ladder Walking Assay ("Uninjured Control" and "Scaffold+NSC" groups: n=8, "Crush only" and "Scaffold only" groups: n=6, "NSC injection" group: n=5, "Scaffold+NIH3T3" group: n=3). Asterisks indicate the statistically significant difference between the "Crush only" group and the "Scaffold+NSC" group (blue) at 10, 11 and 12 wpi. **(b)** Dot plot of locomotion fault rate at 10, 11 and 12 wpi. Results are presented as mean ± SEM. *P < 0.05, **P < 0.01, ***P <0.001; Tukey's post-hoc pairwise test assuming $P_{1\text{-way-ANOVA}} < 0.05$.

A closer look on the type of misplacements (faults) detected in the Horizontal Ladder Walking Assay showed that severe foot misplacements were observed up to 2 wpi in injured groups **(Fig. IV-21)**. However, after 2 wpi the vast majority of detected misplacements were classified as "correction" and mainly as "partial placement". This finding suggests that dorsal column crush mainly affects fine motility.

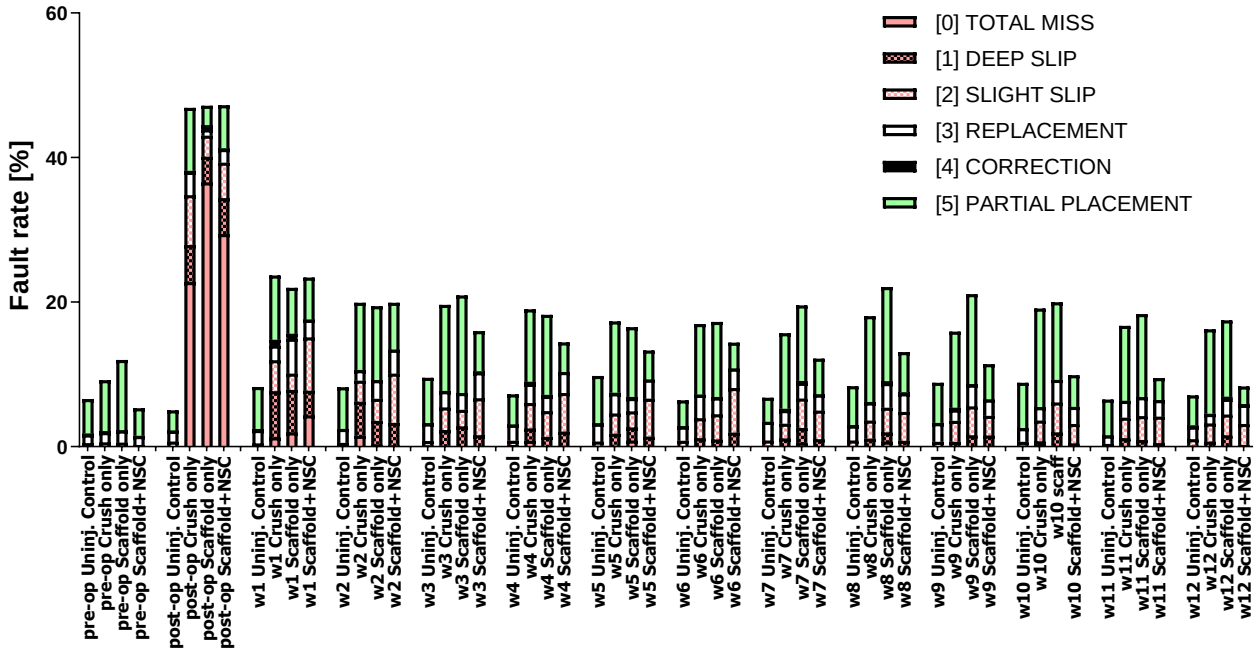

Fig. IV-21. Classification of misplaced steps (per group per time point) observed in the mouse dorsal column crush SCI model at 12 wpi.

2.1.3. Effects of NSC-seeded CS Grafts on Astrogliosis at 12 weeks Following Injury

Astrogliosis in the SCI lesion at 12 wpi was evaluated by immunostaining spinal cord parasagittal sections for GFAP and quantifying the fraction of $GFAP^+$ pixels in the lesion boundary region **(Fig. IV-22a)**. Compared to the "Crush only" group, a significant decrease in $GFAP^+$ pixel fraction was observed in the presence of NSC-seeded CS graft, but not in CS graft without cells ("Crush only": 2.1±0.2%, n=3; "Scaffold only": 1.9±0.3%, n=3, P=0.66; "Scaffold+NSC": 1.3±0.1%, n=3, P=0.04) **(Fig. IV-22b)**.

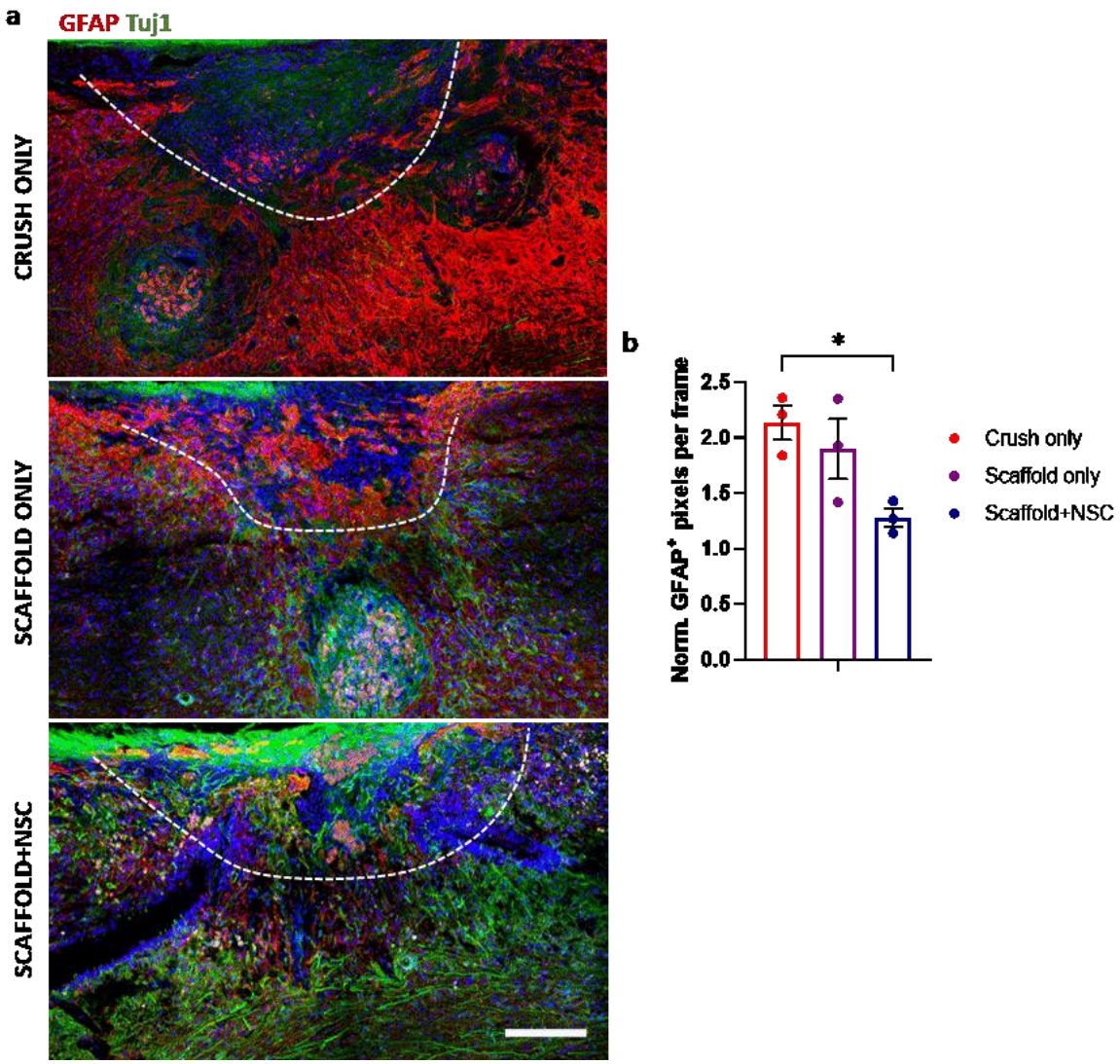

Fig. IV-22. Effects of NSC-seeded CS grafts on astrogliosis at 12 wpi. (a) Representative fluorescence images of spinal cord parasagittal sections from the three injured groups ("Crush only", "Scaffold only", "Scaffold+NSC") immunostained for Tuj1 (green) and GFAP (red). The boundaries of injury site are marked with a dotted line. Scale bar: 200 µm. **(b)** Quantification of the fraction of GFAP$^+$ pixels around the lesion boundary at 12 wpi in the three injured animal groups ("Crush only": n=3, "Scaffold only": n=3, "Scaffold+NSC": n=3). Results are presented as mean ± SEM. *P < 0.05; Tukey's post-hoc pairwise test assuming $P_{1\text{-way-ANOVA}} < 0.05$.

2.1.4. Effects of NSC-seeded CS Grafts on Neuron Density at the Injury Site at 12 weeks Following Injury

The presence of neurons at the injury site at 12 wpi was evaluated by immunostaining spinal cord parasagittal sections for the Tuj1 (neuronal marker) and calculating the density of Tuj1$^+$ cells within the injury site, which was denoted by the GFAP$^+$ boundary region **(Fig. IV-22a, 23a)**. Tuj1$^+$ cells and neurites were present at the injury site in all four injured groups ("Crush only", "Scaffold only", "Scaffold+NSC" and "NSC injection") **(Fig. IV-23a)**. Although there was a trend of increased Tuj1$^+$ density in the "Scaffold+NSC" group, statistical analysis showed no significant difference among the injured groups ($P_{1\text{-way-ANOVA}}$=0.62, F=0.61) **(Fig. IV-23b)**.

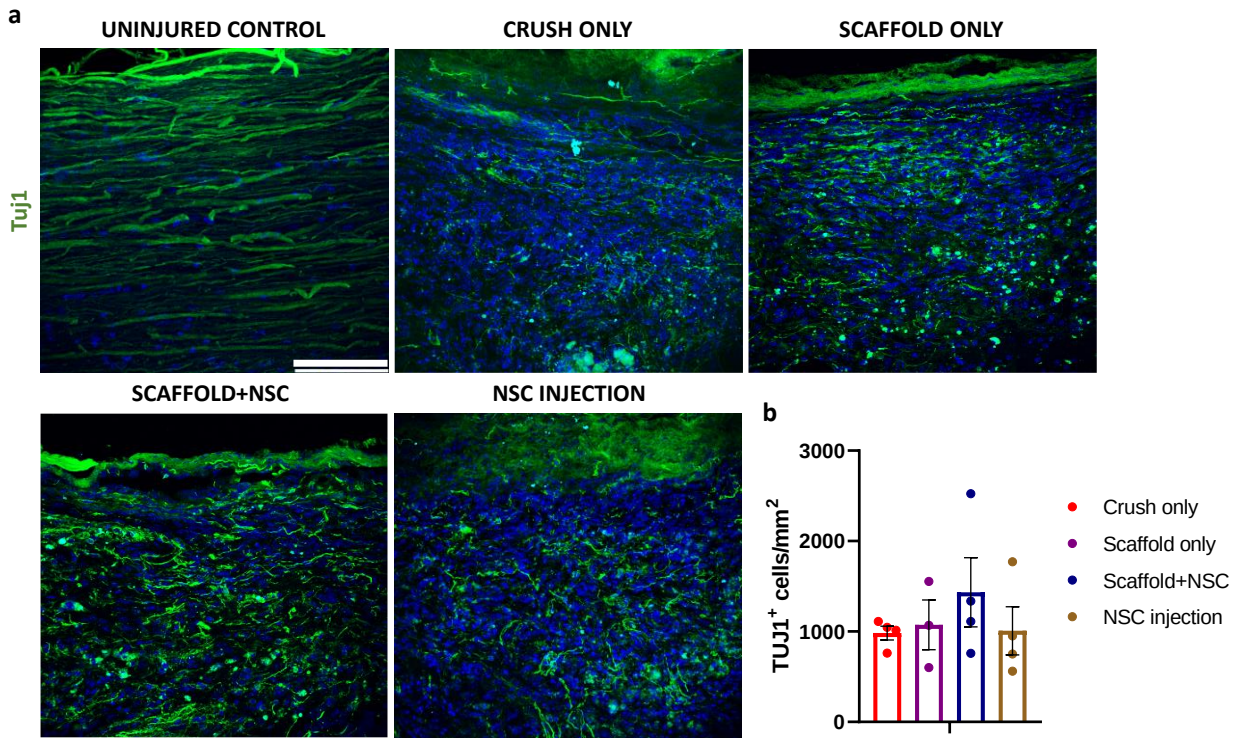

Fig. IV-23. Effects of NSC-seeded CS grafts on neuronal density at the injury site at 12 wpi. (a) Representative fluorescence images of spinal cord parasagittal sections from the uninjured control group and the four injured groups ("Crush only", "Scaffold only", "Scaffold+NSC" and "NSC injection") at the lesion epicenter visualizing Tuj1 immunostaining. Scale bar: 100 µm. **(b)** Quantification of the density of Tuj1$^+$ neurons within the lesion at 12 wpi in the four injured animal groups ("Crush only": n=4, "Scaffold only": n=3, "Scaffold+NSC": n=4, "NSC injection" n=4). Results are presented as mean ± SEM. *P < 0.05; Tukey's post-hoc pairwise test assuming $P_{1\text{-way-ANOVA}} < 0.05$.

2.1.5. Effects of NSC-seeded CS Grafts on Axonal Elongation at 12 weeks Following Injury

Ongoing axonal elongation at the injury site was evaluated by immunostaining spinal cord parasagittal sections for the L1 marker and quantifying the fraction of L1$^+$ pixels in the lesion epicenter and in the dorsal regions rostrally and caudally to the lesion **(Fig. IV-24a)**. No difference was observed among the four injured groups ("Crush only", "Scaffold only", "Scaffold+NSC" and "NSC injection") in the rostral region ($P_{1\text{-way-ANOVA}}$=0.90, F=0.19) and in the epicenter ($P_{1\text{-way-ANOVA}}$=0.47, F=0.91) **(Fig. IV-24b)**. Interestingly, treatment with NSC-seeded CS significantly increased the fraction of L1$^+$ pixels caudally to the lesion compared to the "Crush only" group (caudally: "Crush only": 11.6±2.1%, n=3; "Scaffold only": 19.4±2.5%, n=3, P=0.28; "Scaffold+NSC": 25.1±2.0%, n=3, P=0.04; "NSC injection": 15.1±3.3%, n=4, P=0.80) **(Fig. IV-24b)**.

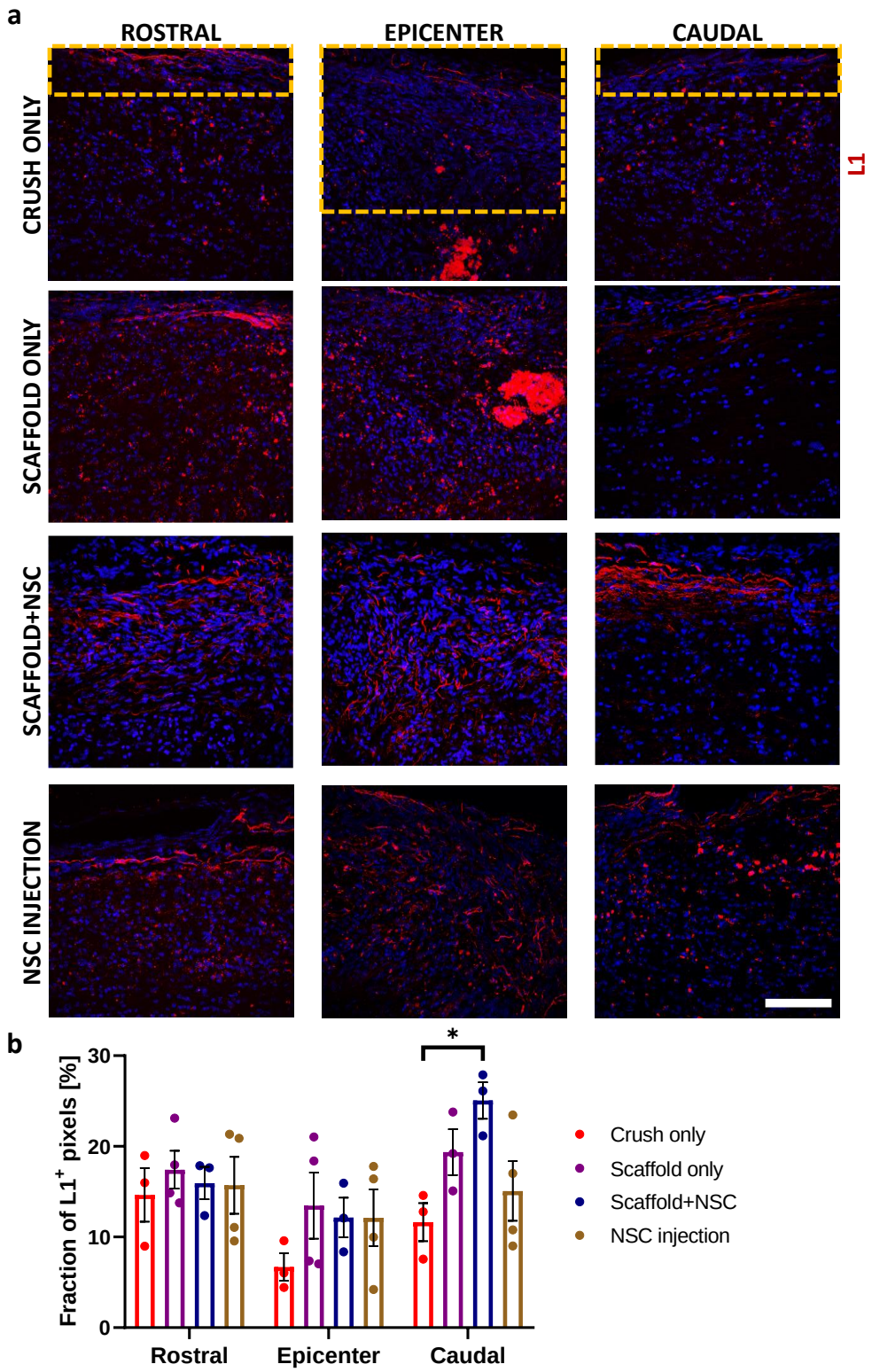

Fig. IV-24. Effects of NSC-seeded CS grafts on axonal elongation at 12 wpi. (a) Representative fluorescence images of spinal cord parasagittal sections from the four injured groups ("Crush only", "Scaffold only", "Scaffold+NSC" and "NSC injection") immunostained for L1 (red). The dotted squares show the regions that were quantified rostrally, in the epicenter and caudally to the lesion. Scale bar: 100µm **(b)** Quantification of the fraction of L1$^+$ pixels rostrally, in the epicenter and caudally to the lesion at 12 wpi in the four injured animal groups ("Crush only": n=3, "Scaffold only": n=3, "Scaffold+NSC": n=3,

"NSC injection": n=4). Results are presented as mean ± SEM. *P < 0.05; Tukey's post-hoc pairwise test assuming $P_{1\text{-way-ANOVA}} < 0.05$.

2.1.6. Effects of NSC-seeded CS Grafts on Synapse Formation at the Injury Site at 12 weeks Following Injury

The integration of neurons within the lesion area via the synapses formation at 12 wpi was evaluated by immunostaining spinal cord parasagittal sections for synaptophysin and quantifying the fraction of synaptophysin$^+$ pixels within the lesion **(Fig. IV-25a,b)**. Although there was a trend of increased fraction of synaptophysin$^+$ pixels in the lesion in "Scaffold+NSC" group, statistical analysis showed no significant difference among the four injured groups ("Crush only", "Scaffold only", "Scaffold+NSC" and "NSC injection") ($P_{1\text{-way-ANOVA}}$=0.19, F=2.04) **(Fig. IV-25c)**.

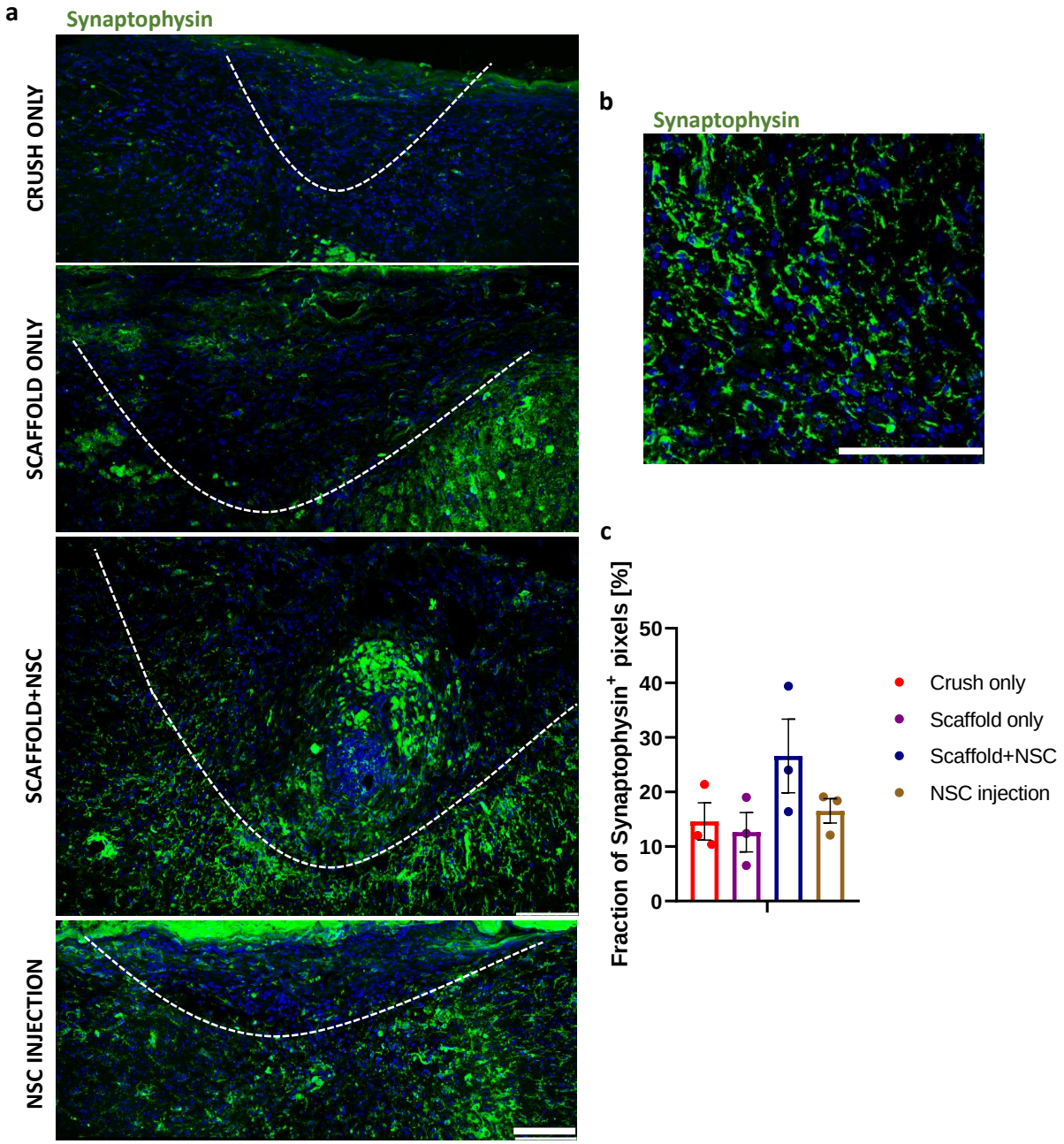

Fig. IV-25. Effects of NSC-seeded CS grafts on synapse formation at the injury site at 12 wpi. (a) Representative fluorescence images of spinal cord parasagittal sections at the injury site of the four

injured groups ("Crush only", "Scaffold only", "Scaffold+NSC" and "NSC injection") immunostained for synaptophysin (green). Scale bar: 100 µm. **(b)** A representative high-magnification fluorescence image at the lesion epicenter of "Scaffold+NSC" group immunostained for synaptophysin. Scale bar: 100 µm. **(c)** Quantification of synaptophysin$^+$ pixel fraction at the injury site in the four injured groups at 12 wpi (All groups: n=3). Results are presented as mean ± SEM. Tukey's post-hoc pairwise test assuming $P_{1\text{-way-ANOVA}} < 0.05$.

2.1.7. Effects of NSC-seeded CS Graft on Myelin Presence at the Injury Site at 12 weeks Following Injury

The myelin presence within the lesion area as indication of de- or re-myelination was evaluated by immunostaining spinal cord parasagittal sections for MBP marker **(Fig. IV-26a,b)** and quantifying the fraction of MBP$^+$ pixels in the lesion epicenter **(Fig. IV-26a)**. Although there was a trend of increased fraction of MBP$^+$ pixels in the lesion in "Scaffold+NSC" group, statistical analysis showed no significant difference among the three injured groups ("Crush only", "Scaffold only" and "Scaffold+NSC") at 12 wpi, considering though the small number of biological replicates of "Crush only" group ($P_{1\text{-way-ANOVA}}$=0.54, F=0.72) **(Fig. IV-26c)**.

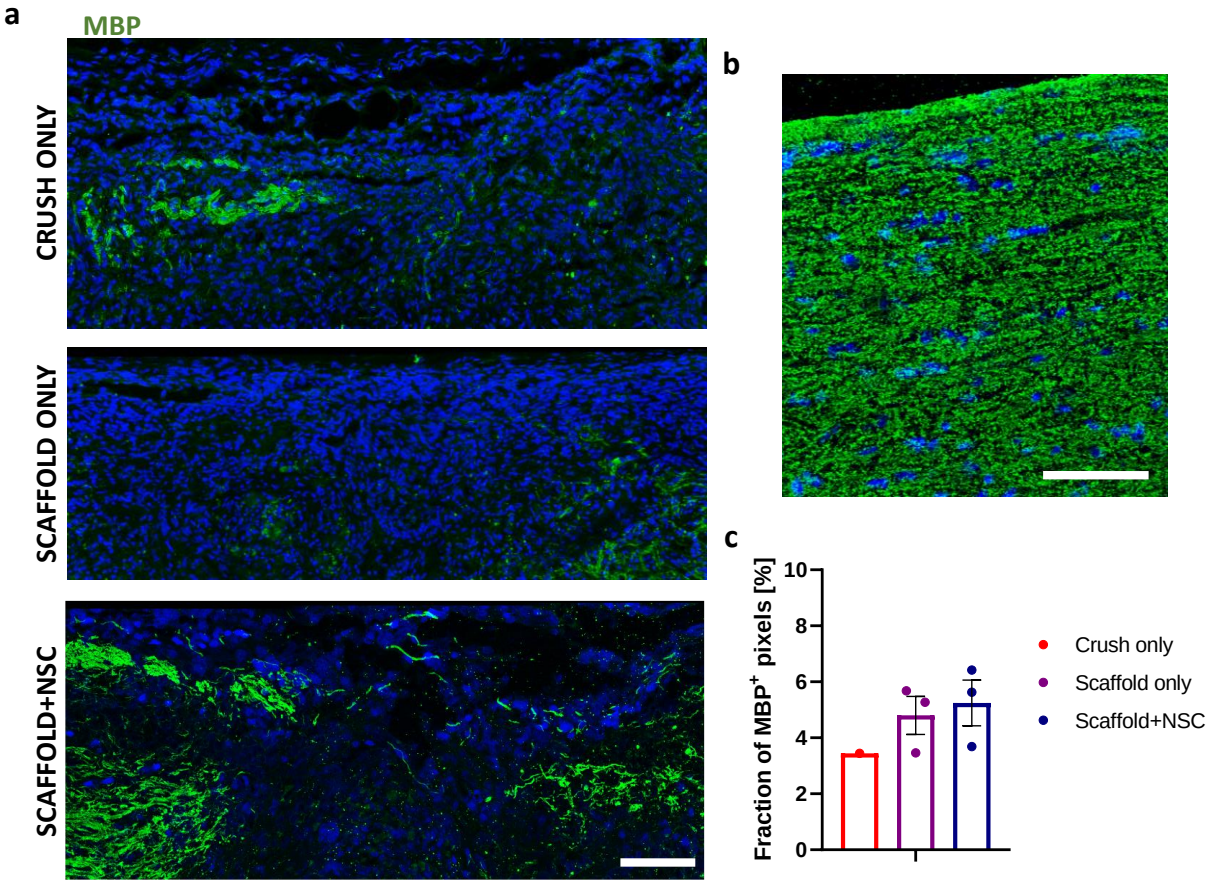

Fig. IV-26. Effects of NSC-seeded CS grafts on myelin presence at the injury site at 12 wpi. (a) Representative fluorescence images of spinal cord parasagittal sections at the injury site of the three injured groups ("Crush only", "Scaffold only" and "Scaffold+NSC") immunostained for MBP (green). Scale bar: 100µm. **(b)** Representative fluorescence image of spinal cord parasagittal sections of "Uninjured control" group immunostained for MBP (green). Scale bar: 100µm. **(c)** Quantification of MBP$^+$ pixel fraction at the injury site in the three injured groups at 12 wpi ("Crush only": n=1, "Scaffold only": n=3 and "Scaffold+NSC": n=3). Results are presented as mean ± SEM. *P < 0.05; Tukey's post-hoc pairwise test assuming $P_{1\text{-way-ANOVA}} < 0.05$.

2.1.8. Localization of NSCs Delivered at the Injury Site via Injection

The injection of cell suspensions is a commonly used method for the delivery of cellular therapies, including NSCs, into SCI sites (169,170). Indeed, this delivery method was included in the experimental design ("NSC injection" mice group) of study A. Nevertheless, literature highlights key limitations of NSC delivery in suspension, including limited control on NSC localization and the formation of NSC ectopic sites (171). In order to evaluate the localization of NSCs in the dorsal column crush lesion following NSC delivery in suspension (via a syringe), a separate pilot SCI study of 1- and 3-week duration was performed (n=2) **(Fig. IV-27a)**. In this study, BrdU-pulsed NSCs injected at the injury site were not found within the lesion in all animals as observed via immunostaining for BrdU **(Fig. IV-27b)**. Although this observation could be resulted by technical errors, it also demonstrates that NSC injection is not an accurate method for NSC delivery within the injury site. This delivery method can be characterized less effective, as well, since, contrary to "Scaffold+NSC" group, "NSC injection" group could not result in functional enhancement compared to "Crush only" group as described in section IV-2.1.2.

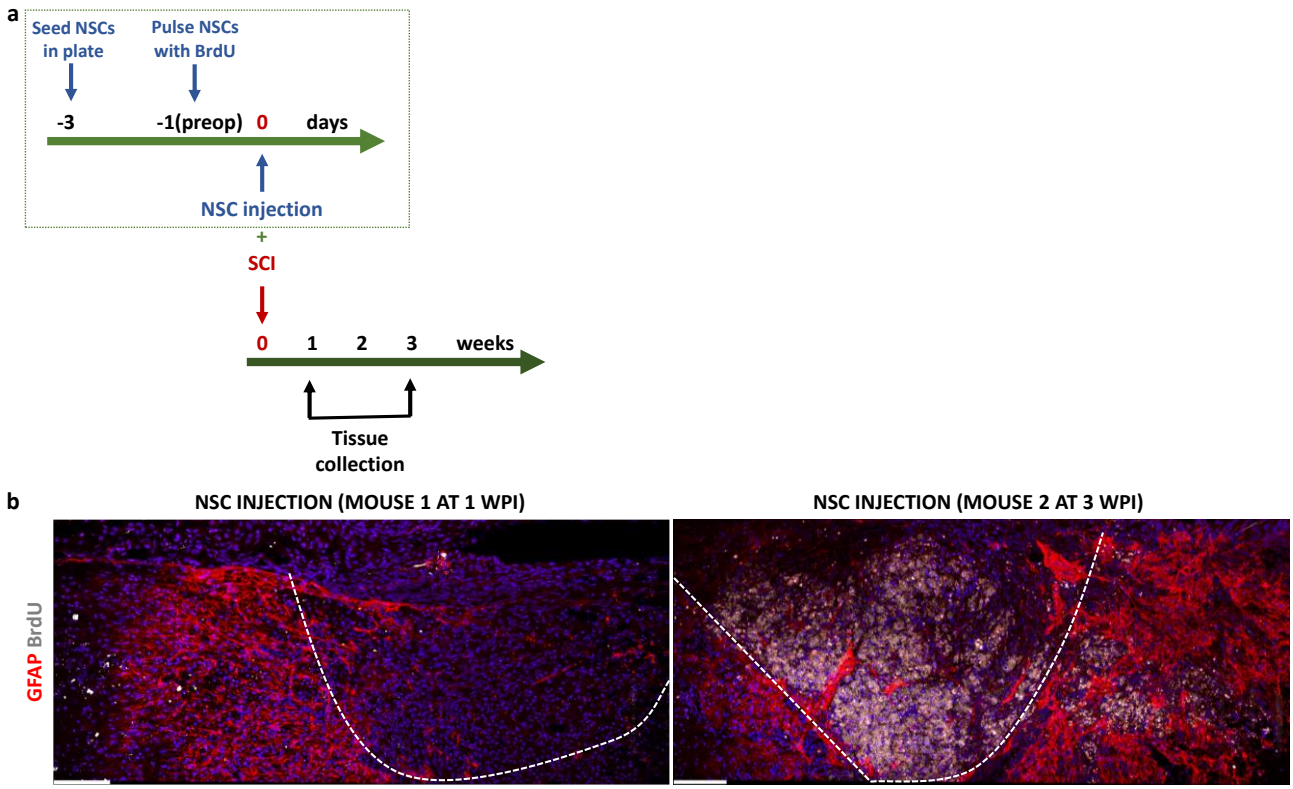

Fig. IV-27. Localization of NSCs delivered at the dorsal column crush injury site via an injection at 1 and 3 wpi. **(a)** Timeline of the study. **(b)** Fluorescence images of spinal cord parasagittal sections at the injury site of injured mice injected with BrdU-pulsed NSCs immunostained with BrdU (white) and GFAP (red) at 1 and 3 wpi. Dotted areas show the injury site. Scale bars: 100µm.

2.2. *In vivo* Evaluation of the Effects of Systemic Administration of BNN27 Combined with Mouse Embryonic NSC-seeded CS Grafts on the Mouse Dorsal Column Crush Spinal Cord Injury Model (Study B)

In SCI study B, therapeutic effects of BNN27 after SCI were evaluated using the same dorsal column crush mouse SCI model as in study A (section IV-2.1). Immediately after crush, three types of SCI treatments were tested: the first animal group was provided systemic administration of BNN27 via subcutaneous pellet ("BNN27" group; 18mg/pellet released over a 60-day period); the second animal group ("Scaffold NSC+BNN27") was treated with a combinatorial approach consisting of a CS implant seeded with mouse embryonic E13.5 NSCs grafted inside the injury site immediately after injury (same graft as the one described in section IV-2.1) concurrent with the systemic delivery of BNN27 via subcutaneous pellet; the third animal group ("Scaffold NSC+Placebo") was treated with NSC-seeded CS graft concurrent with subcutaneous pellet that lacked an active pharmaceutical ingredient. In addition, experimental design included the "Placebo" animal group (injured mice treated with subcutaneous pellets that lacked an active pharmaceutical ingredient) and the "Uninjured Control" animal group (where, following laminectomy, the exposed spinal cord was not injured) **(Fig. IV-28)**. In study B, grafts in the "Scaffold NSC" and "Scaffold NSC+BNN27" groups utilized NSCs isolated from mice obtained by crossing Rosa26-YFP mice containing a floxed YFP gene with CMV-Cre mice and keeping embryos whose NSCs express YFP, enabling their detection via live cell fluorescence imaging or immunocyto/histochemistry **(Fig. IV-29)**. Therefore, YFP-expressing NSCs could be detected in the host tissue in order to study their location, communication with the surrounding tissue and differentiation inside the graft. Contrarily, BrdU-pulsed NSCs that were used in grafts of study A (section IV-2.1) were not detected at 12 wpi.

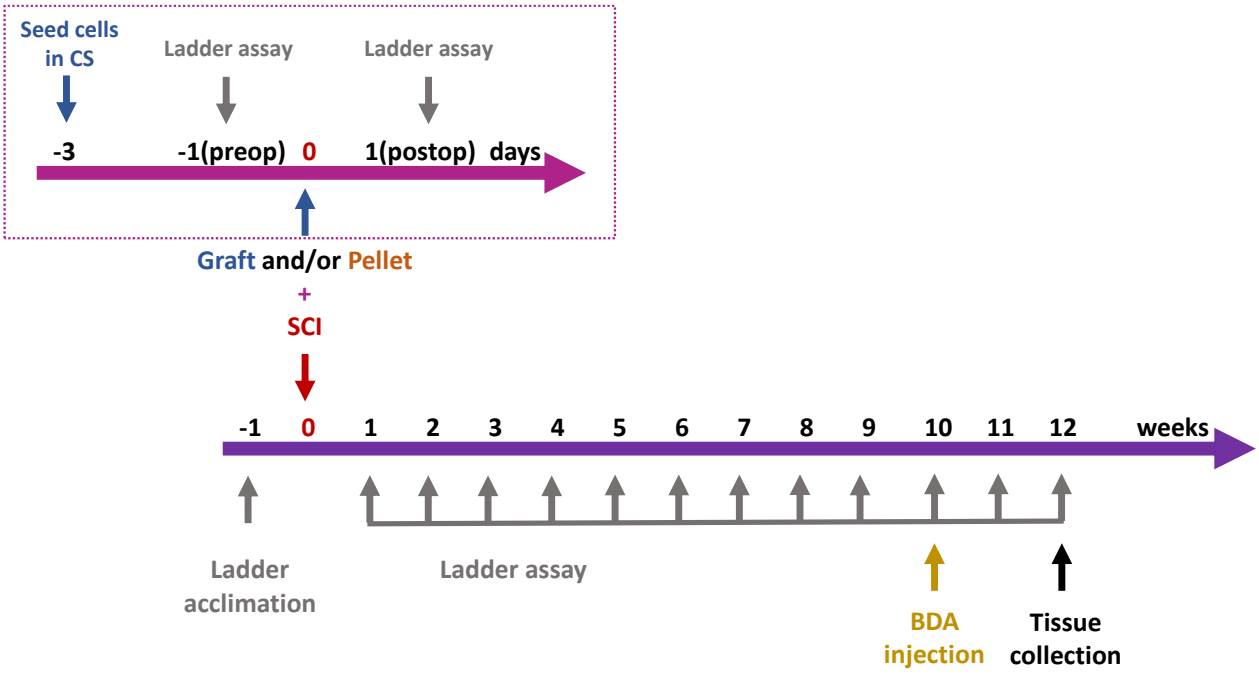

Fig. IV-28. Timeline of 12-week SCI study B.

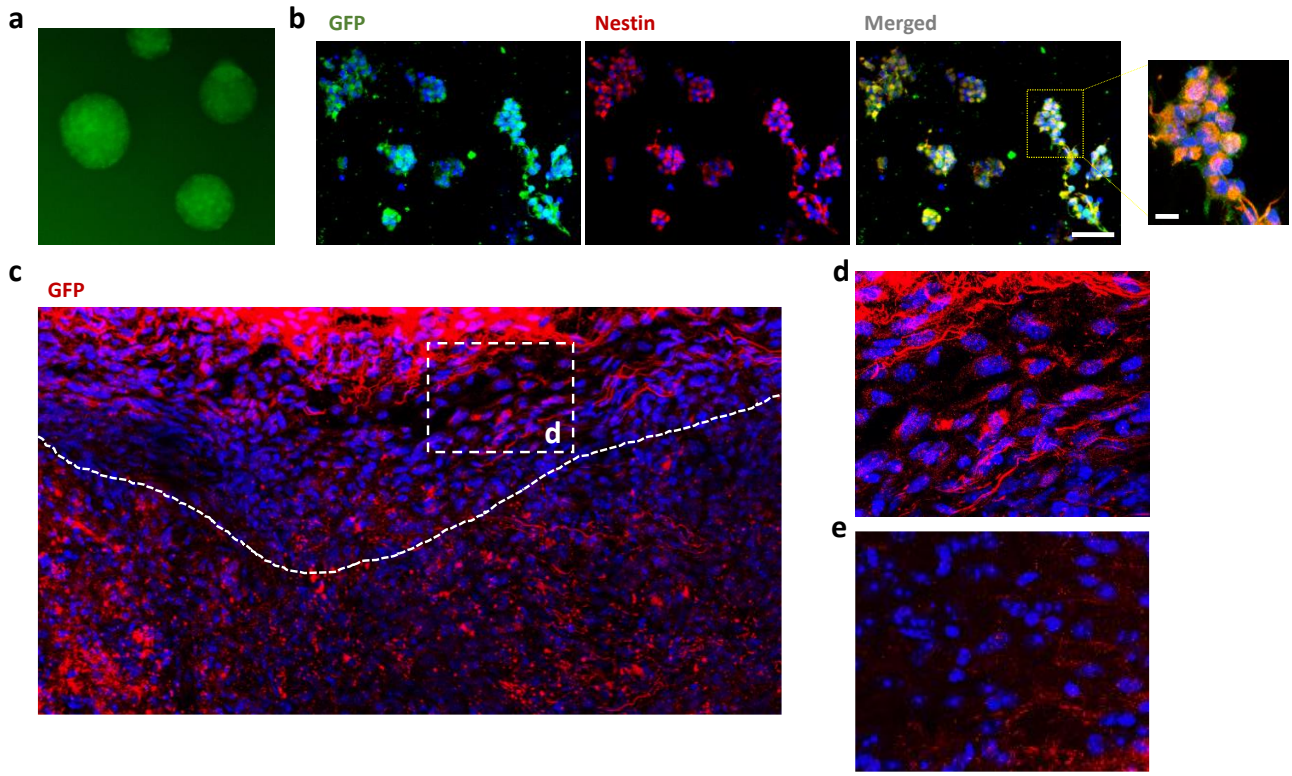

Fig. IV-29. Embryonic mouse YFP-expressing NSCs. (a) YFP-expressing NSCs in culture as neurospheres. **(b)** YFP-expressing NSCs seeded in CS for 3 days and immunostained for GFP (green) and Nestin (red). Scale bars: 50 µm and 10 µm. **(c)** Representative fluorescence image of spinal cord parasagittal sections at the injury site of injured mouse implanted with YFP-expressing NSCs and immunostained for GFP (red) at 6 wpi. **(d)** Magnification of (c) within the lesion in the presence of YFP-expressing NSCs. **(e)** Magnification far from the lesion in the absence of YFP-expressing NSCs.

2.2.1. *In vitro* evaluation of BNN27 Effects on Mouse Embryonic NSCs

BNN27 effects on mouse embryonic E13.5 YFP-expressing NSCs were evaluated *in vitro* regarding their proliferation and differentiation. Adding BNN27 in NSC medium that lacked EGF and FGF2 did not affect NSC proliferation as quantified by the fraction of $BrdU^+$ cells after a 4h BrdU pulse ("No factors": 7.3±2.2%, n=4; "DMSO": 7.8±2.5%, n=4; "0.1 µM BNN27": 8.4±1.5%, n=4; "1 µM BNN27": 8.5±2.3%, n=4) **(Fig. IV-30a,b)**. BNN27 supplementation also did not affect the differentiation of NSCs grown inside CS towards neuron and astrocyte fates after 5-day culture in medium free of EGF and FGF2. NSC differentiation was evaluated by quantifying the fraction of $Tuj1^+$ ("No factors": 6.9±1.3%, n=5; "0.1 µM BNN27": 7.3±1.7%, n=5; "1 µM BNN27": 9.8±1.9%, n=5) and $GFAP^+$ ("No factors": 24.3±2.8%, n=5; "0.1 µM BNN27": 23.9±2.6%, n=3; "1 µM BNN27": 22.7±1.8%, n=5) cells, respectively (**Fig. IV-30c-e**). Combined, these *in vitro* experiments suggest that BNN27 does not directly affect the proliferation and differentiation of mouse E13.5 NSCs.

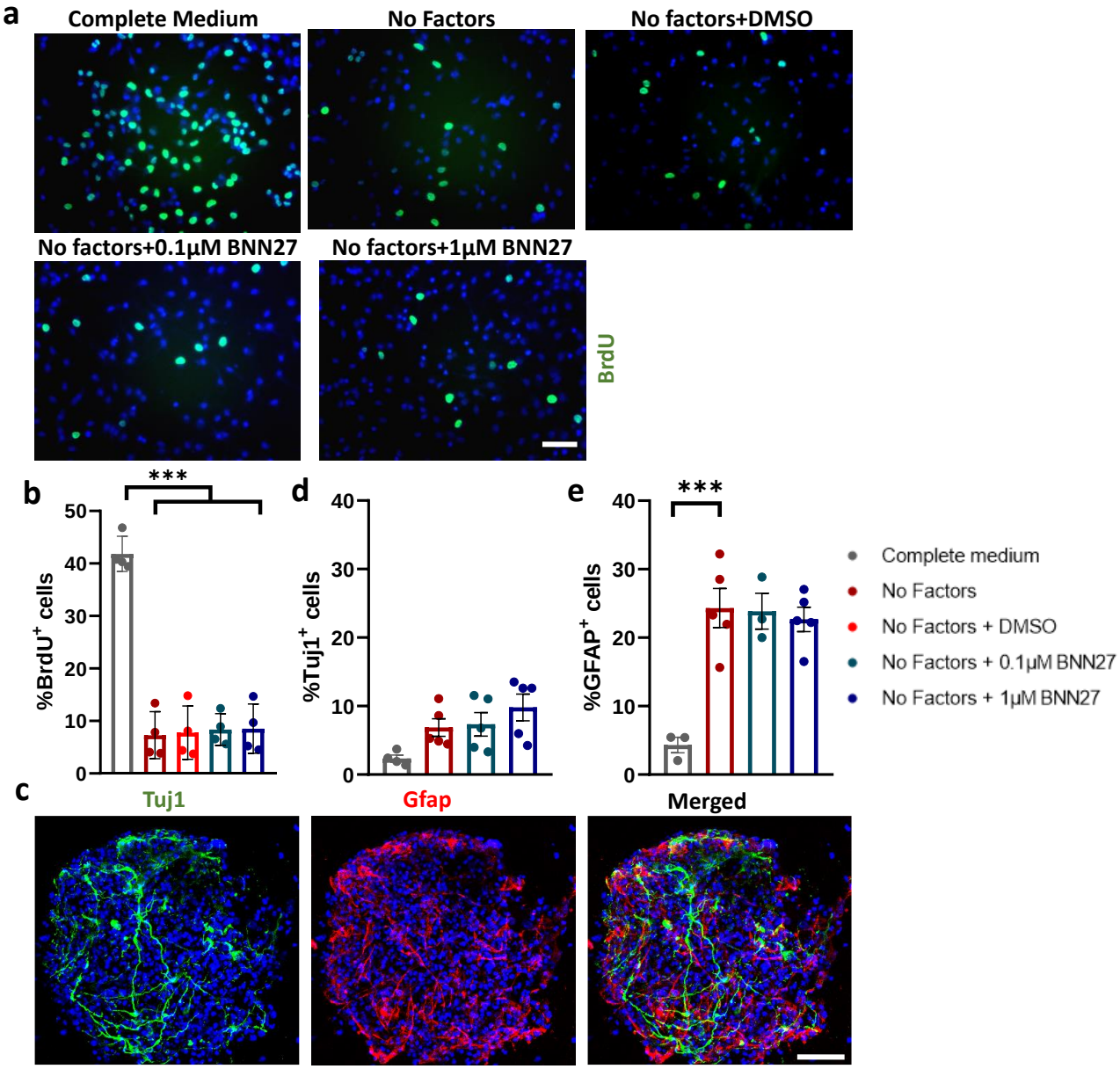

Figure IV-30. BNN27 effects on mouse embryonic NSC proliferation and differentiation *in vitro*. (a) Representative fluorescence images of proliferating NSCs immunostained for BrdU (green) and grown in complete NSC medium or EGF/FGF2-deprived medium in the absence or presence of BNN27. **(b)** Quantification of the fraction of BrdU$^+$ cells grown in medium free of EGF and FGF2 for 24 hours in the absence or presence of BNN27. (All groups: n=4.) Results are presented as mean ± SEM. Tukey's post-hoc pairwise test assuming $P_{1\text{-way-ANOVA}} < 0.05$. **(c)** Representative confocal fluorescence images of NSCs grown inside a CS in medium free of EGF and FGF2 for 5 days. The sample was immunostained for Tuj1 (neurons; green) and GFAP (astrocytes; red). Quantification of the fraction of Tuj1$^+$ neurons **(d)** and Gfap$^+$ astrocytes **(e)** in NSCs grown inside CS in medium free of FGF2 and EGF for 5 days in the absence or presence of BNN27. ("Control": n=4, "No factors": n=5, "BNN27 0.1 µM": n=5, "BNN27 1 µM": n=5.) Results are presented as mean ± SEM. ***P < 0.001; Dunnett post-hoc test assuming $P_{1\text{-way-ANOVA}} < 0.05$. Scale bars: 50µm.

2.2.2. Effects of Systemic Administration of BNN27 Combined with NSC-seeded CS Grafts on Locomotion Recovery Following Injury

Mice locomotion recovery over a period of 10 weeks following dorsal column crush was evaluated by quantifying their step fault rate in the Horizontal Ladder Walking Assay **(Fig. IV-31).** During the 10-week period, mice of the "Uninjured Control" group had time-invariant fault rate (μ =6.9%, $\sigma = 2.4\%$). No difference was observed among the four injured groups till the 1st wpi, confirming that injury was consistently performed in all animals (post-op: $P_{1\text{-way-ANOVA}}$=0.94, F=0.12; week 1: $P_{1\text{-way-ANOVA}}$=0.57, F=0.69). Between 1 and 10 wpi, all injured groups showed some locomotion improvement. Eventually, differences in fault rate became statistically significant only in mice treated with NSC-seeded CS grafts compared to the untreated injured group at 9 wpi ("Placebo": 20.9±0.5%, n=4 vs. "Scaffold NSC+Placebo": 13.6±1.7%, n=5, P=0.01; "Placebo" vs "Scaffold NSC+BNN27": 14.8±0.7%, n=5, P=0.04) and 10 wpi ("Placebo": 22.8±1.5%, n=4 vs "Scaffold NSC+Placebo": 15.6±1.2%, n=5, P=0.04; "Placebo" vs. "Scaffold NSC+BNN27": 14.8±2%, n=5, P=0.02), replicating the findings of the study in section IV-2.1. While grafting mice with NSC-seeded CS statistically improved locomotion recovery after 8 weeks (week 9: $P_{2\text{-way-ANOVA}}=10^{-3}$; week 10: $P_{2\text{-way-ANOVA}}=10^{-3}$), BNN27 administration did not (week 9: $P_{2\text{-way-ANOVA}}$=0.89; week 10: $P_{2\text{-way-ANOVA}}$=0.45). The fault rate in the "BNN27" group was not statistically different than the one of the untreated "Placebo" group (9 weeks: "BNN27": 19.3±2%, n=4, P=0.86; 10 weeks: "BNN27": 21.1±1.7%, n=4, P=0.9). Similarly, BNN27 administration did not further improve locomotion recovery when combined with NSC-seeded PCS grafts since the fault rate in the two mice groups treated with NSC-seeded CS grafts ("Scaffold NSC+Placebo", "Scaffold NSC+BNN27") was not statistically different over the 10-week period (week 9: P=0.91; week 10: P=0.98). Worth noting that although locomotion evaluation was performed till the 12th week, results after 10th week are not valuable and, consequently, are not presented due to effects of BDA injection performed on 10th week on animal's behavior.

2.2.3. Effects of Systemic Administration of BNN27 Combined with NSC-seeded CS Grafts on Astrogliosis at 12 weeks Following Injury

Astrogliosis in the SCI injury site at 12 wpi was evaluated by immunostaining spinal cord parasagittal sections for GFAP and quantifying the fraction of $GFAP^+$ pixels at the lesion boundary region (**Fig. IV-32a,b**). 2-way ANOVA revealed that both NSC-seeded CS ($P_{2\text{-way-ANOVA}}=4\cdot10^{-3}$) and BNN27 ($P_{2\text{-way-ANOVA}}$=0.04) had a statistically significant effect on the fraction of $GFAP^+$ pixels at the lesion boundary at 12 wpi. Compared to the untreated "Placebo" group, a significant decrease in $GFAP^+$ pixel fraction was observed in the presence of BNN27 administration or NSC-seeded CS grafts with or without BNN27 ("Placebo": 21.1±2.8%, n=4; "BNN27": 12.6±1.5%, n=4, P=0.05; "Scaffold NSC": 10.0±0.6%, n=3, P=0.02; "Scaffold NSC+BNN27": 8.7±2.0%, n=4, $P=5\cdot10^{-3}$) (**Fig. IV-32c**). BNN27 administration did not lead to synergistic effects when combined with NSC-seeded CS grafts ("Scaffold NSC+Placebo" vs "Scaffold NSC+BNN27": P=0.97).

2.2.4. Effects of Systemic Administration of BNN27 Combined with NSC-seeded CS Grafts on Neuron Presence at the Injury Site at 12 weeks Following Injury

The presence of neurons at the injury site at 12 wpi was evaluated by immunostaining spinal cord parasagittal sections for Tuj1 and calculating the density of $Tuj1^+$ cells within the injury site, which was denoted by a $GFAP^+$ boundary region **(Fig. IV-32a)**. While $Tuj1^+$ cells and neurites were present in all four injured groups **(Fig. IV-33a)**, statistical analysis revealed that both NSC-seeded CS ($P_{2\text{-way-ANOVA}}=5\cdot10^{-4}$) and BNN27 ($P_{2\text{-way-ANOVA}}$=0.01) had statistically significant effect on the density of $Tuj1^+$ cells within the injury site at 12 wpi. A significant increase in $Tuj1^+$ cell density was observed in the presence of BNN27 administration

or NSC-seeded CS grafts with or without BNN27 compared to the untreated "Placebo" group ("Placebo": 397.1±53.2 cells/mm^2, n=4; "BNN27": 683.8±44.8 cells/mm^2, n=3, P=0.01; "Scaffold NSC": 776.6±47.2 cells/mm^2, n=5, P=6·10^{-4}; "Scaffold NSC+BNN27": 789.2±50.6 cells/mm^2, n=4, P=7·10^{-4}) **(Fig. IV-33b)**. Simultaneous treatment with BNN27 and NSC-seeded CS grafts did not have statistically significant synergistic effects in the density of Tuj1$^+$ cells compared to treatment only with NSC-seeded CS grafts.

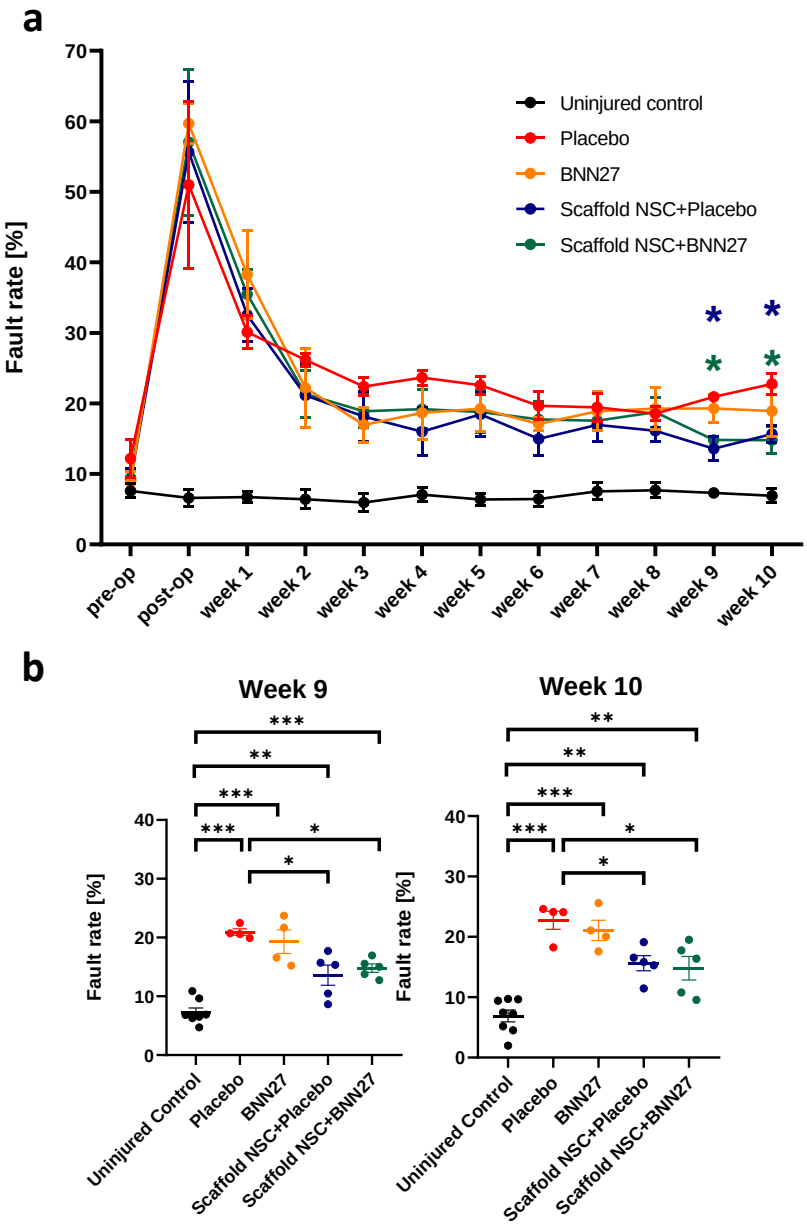

Fig. IV-31. Effects of systemic administration of BNN27 combined with NSC-seeded CS grafts on locomotion recovery in a mouse dorsal column crush SCI model over a 10-week period following injury. (a) Quantification of locomotion performance (fault rate) after SCI by the Horizontal Ladder Walking Assay over a period of 10 wpi ("Uninjured Control" group: n = 8, "Placebo" and "BNN27" groups: n = 4, "Scaffold NSC" and "Scaffold NSC+BNN27" groups: n = 5). Asterisks indicate the statistically significant difference between the "Placebo" group and the "Scaffold NSC+Placebo" group (blue) or the "Scaffold NSC+BNN27" groups (green) at 9 and 10 wpi. **(b)** Dot plot of locomotion fault rate at 9 and 10 wpi. Results are presented as mean ± SEM. *P < 0.05, **P < 0.01, ***P <0.001; Tukey's post-hoc pairwise test assuming $P_{1\text{-way-ANOVA}} < 0.05$.

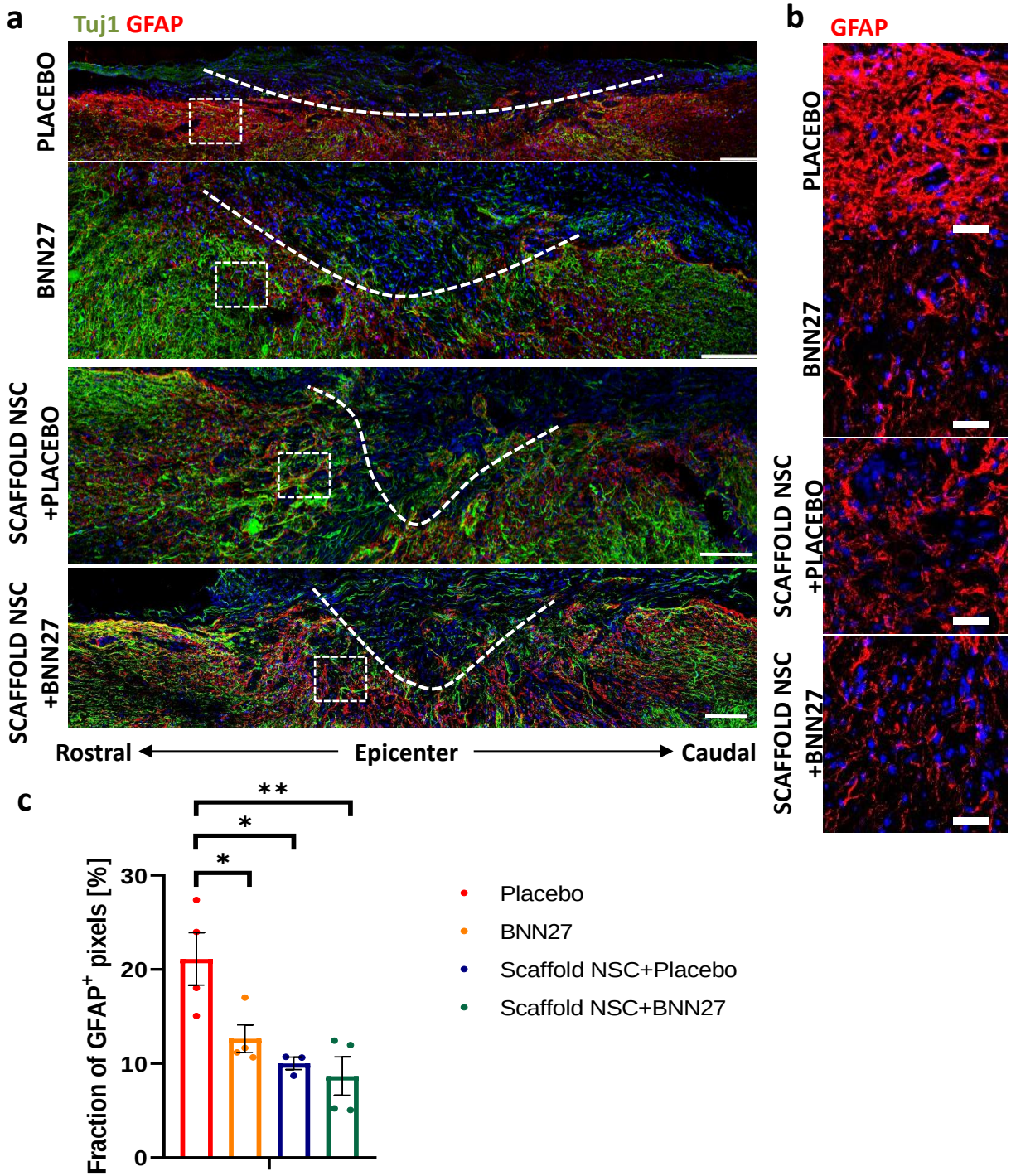

Fig. IV-32. Effects of systemic administration of BNN27 combined with NSC-seeded CS grafts on astrogliosis at 12 wpi. (a) Representative fluorescence images of spinal cord parasagittal sections from all four injured groups immunostained for Tuj1 (green) and GFAP (red). The boundaries of injury site are marked with a dotted line. Scale bars: 100 µm. **(b)** High magnification fluorescence images of the rectangular inserts of image (a) showing GFAP immunostaining at the lesion boundary region. Scale bars: 30 µm. **(c)** Quantification of the fraction of $GFAP^+$ pixels around the lesion boundary at 12 wpi in the four injured animal groups ("Placebo": n=4, "BNN27": n=4, "Scaffold NSC+Placebo": n=3, "Scaffold NSC+BNN27" n=4). Results are presented as mean ± SEM. *P < 0.05, **P < 0.01, ***P < 0.001; Tukey's post-hoc pairwise test assuming $P_{2\text{-}way\text{-}ANOVA} < 0.05$.

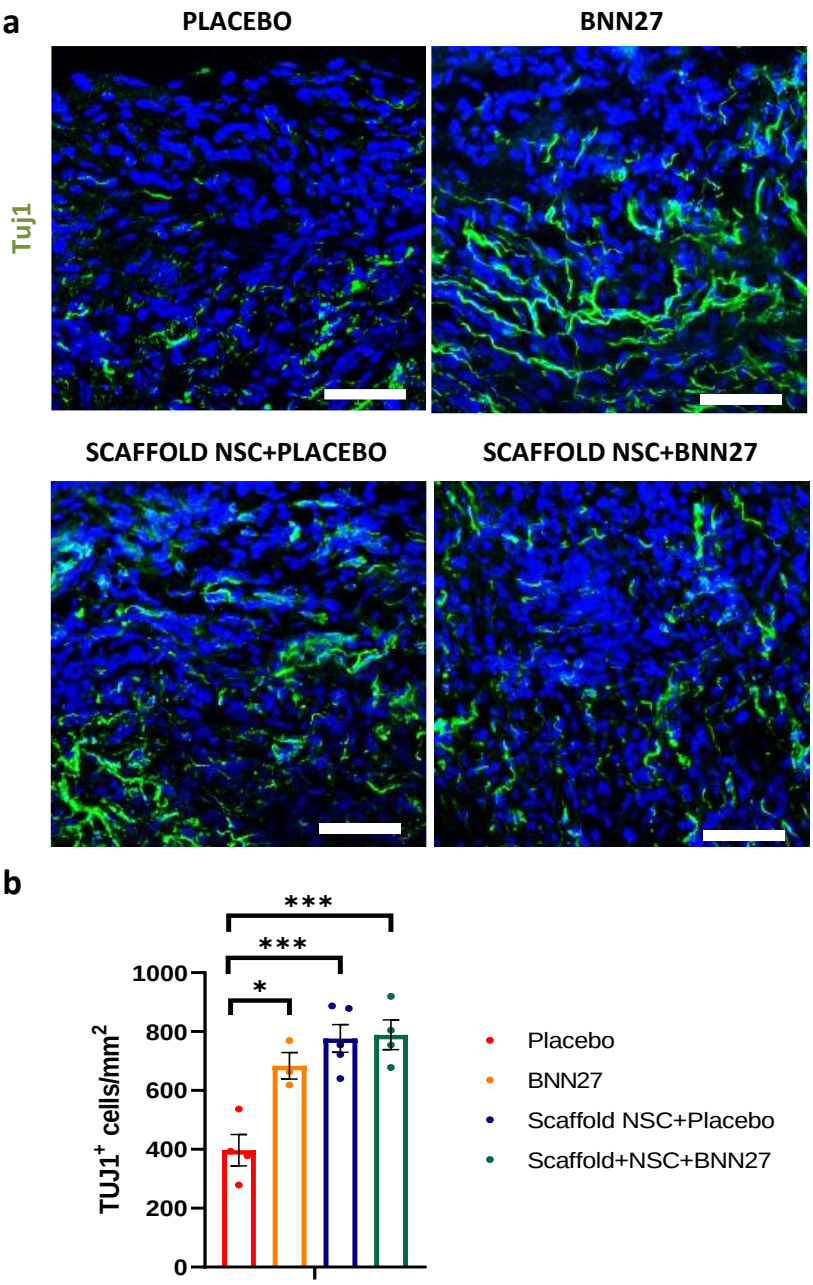

Fig. IV-33. Effects of systemic administration of BNN27 combined with NSC-seeded CS grafts on neuronal density at the injury site at 12 wpi. (a) Representative fluorescence images of spinal cord parasagittal sections at the injury site of the four injured groups immunostained for Tuj1. Scale bars: 30 µm. **(b)** Quantification of the density of Tuj1$^+$ neurons within the lesion at 12 wpi in the four injured animal groups ("Placebo": n=4, "BNN27": n=3, "Scaffold NSC+Placebo": n=5, "Scaffold NSC+BNN27" n=4). Results are presented as mean ± SEM. *P < 0.05, **P < 0.01, ***P < 0.001; Tukey's post-hoc pairwise test assuming $P_{2\text{-}way\text{-}ANOVA} < 0.05$.

2.2.5. Effects of Systemic Administration of BNN27 Combined with NSC-seeded CS Grafts on Axonal Elongation at 12 weeks Following Injury

Ongoing axonal elongation at the injury site was evaluated by immunostaining spinal cord parasagittal sections for the L1 marker and quantifying the fraction of L1$^+$ pixels at the lesion epicenter and at the dorsal regions rostrally and caudally to the lesion **(Fig. IV-34a)**. No difference was observed among the four injured

groups in the rostral region and in the epicenter. Interestingly, treatment with NSC-seeded CS had statistically significant effect ($P_{2\text{-}way\text{-}ANOVA}<10^{-4}$) on the fraction of $L1^+$ pixels caudally to the lesion at 12 wpi **(Fig. IV-34b)**, replicating the findings of the study in section IV-2.1. The two CS graft-treated groups showed increased axonal elongation in the caudal region compared to the untreated "Placebo" group (caudally: "Placebo": 7.1±0.8%, n=5; "Scaffold NSC+Placebo": 11.8±0.7%, n=4, $P<10^{-3}$; "Scaffold NSC+BNN27": 11±0.4%, n=5, $P=2\cdot10^{-3}$). BNN27 administration did not affect axonal elongation ($P_{2\text{-}way\text{-}ANOVA}=0.99$). The fraction of $L1^+$ pixels was not different in the "BNN27" group compared to the untreated "Placebo" group ("BNN27": 7.9±0.5%, n=4, P=0.83). Similarly, combinatorial treatment with NSC-seeded CS grafts and BNN27 did not increase the fraction of $L1^+$ pixels compared to animals treated only with grafts ("Scaffold NSC+Placebo" vs "Scaffold NSC+BNN27" P=0.83) **(Fig. IV-34b)**.

2.2.6. Effects of Systemic Administration of BNN27 Combined with NSC-seeded CS Grafts on Synapse Formation at the injury Site at 12 weeks Following Injury

The integration of neurons within the lesion area via the synapse formation at 12 wpi was evaluated by immunostaining spinal cord parasagittal sections for synaptophysin and quantifying the fraction of synaptophysin$^+$ pixels within the injury site (**Fig. IV-35a, b**). Overall, treatment with NSC-seeded CS had statistically significant effect ($P_{2\text{-}way\text{-}ANOVA}<10^{-4}$) on the fraction of synaptophysin$^+$ pixels in the lesion. Both graft-treated groups contained larger fraction of synaptophysin$^+$ pixels than the untreated "Placebo" group ("Placebo": 4.1±0.7%, n=3; "Scaffold NSC+Placebo": 8.4±0.7%, n=3, $P=2\cdot10^{-3}$; "Scaffold NSC+BNN27": 8.7±0.4%, n=3, $P=10^{-3}$). On the other hand, BNN27 administration did not increase the fraction of synaptophysin$^+$ pixels ($P_{2\text{-}way\text{-}ANOVA}=0.37$; "Placebo" vs "BNN27": 4.8±0.2%, n=3, P=0.79; "Scaffold NSC+Placebo" vs "Scaffold NSC+BNN27": P=0.98) (**Fig. IV-35c**).

2.2.7. Effects of Systemic Administration of BNN27 Combined with NSC-seeded CS Grafts on Angiogenesis at the injury Site at 12 weeks Following Injury

The presence of blood vessels within the injury site was evaluated by immunostaining spinal cord parasagittal sections for αSMA (a marker of vessel-associated pericytes) and quantifying the number of αSMA$^+$ vessels within the injury site (**Fig. IV-36a,b**). Treatment with NSC-seeded CS ($P_{2\text{-}way\text{-}ANOVA}=3\cdot10^{-3}$) but not BNN27 administration ($P_{2\text{-}way\text{-}ANOVA}=0.44$) had statistically significant effect on the number of αSMA$^+$ vessels at 12 wpi. The two CS graft-treated groups contained increased number of αSMA$^+$ vessels within the injury site compared to the untreated "Placebo" group ("Placebo": 2.7±0.6%, n=4; "Scaffold NSC+Placebo": 7.2±1.0%, n=4, P=0.03; "Scaffold NSC+BNN27": 7.7±0.9%, n=3, P=0.03). The number of αSMA$^+$ vessels was not different in the "BNN27" group compared to the untreated "Placebo" group ("BNN27": 4.0±1.5%, n=3, P=0.82). Similarly, combinatorial treatment with NSC-seeded CS grafts and BNN27 did not increase the number of αSMA$^+$ vessels compared to animals treated only with grafts ("Scaffold NSC+Placebo" vs "Scaffold NSC+BNN27" P=0.99) (**Fig. IV-36c**).

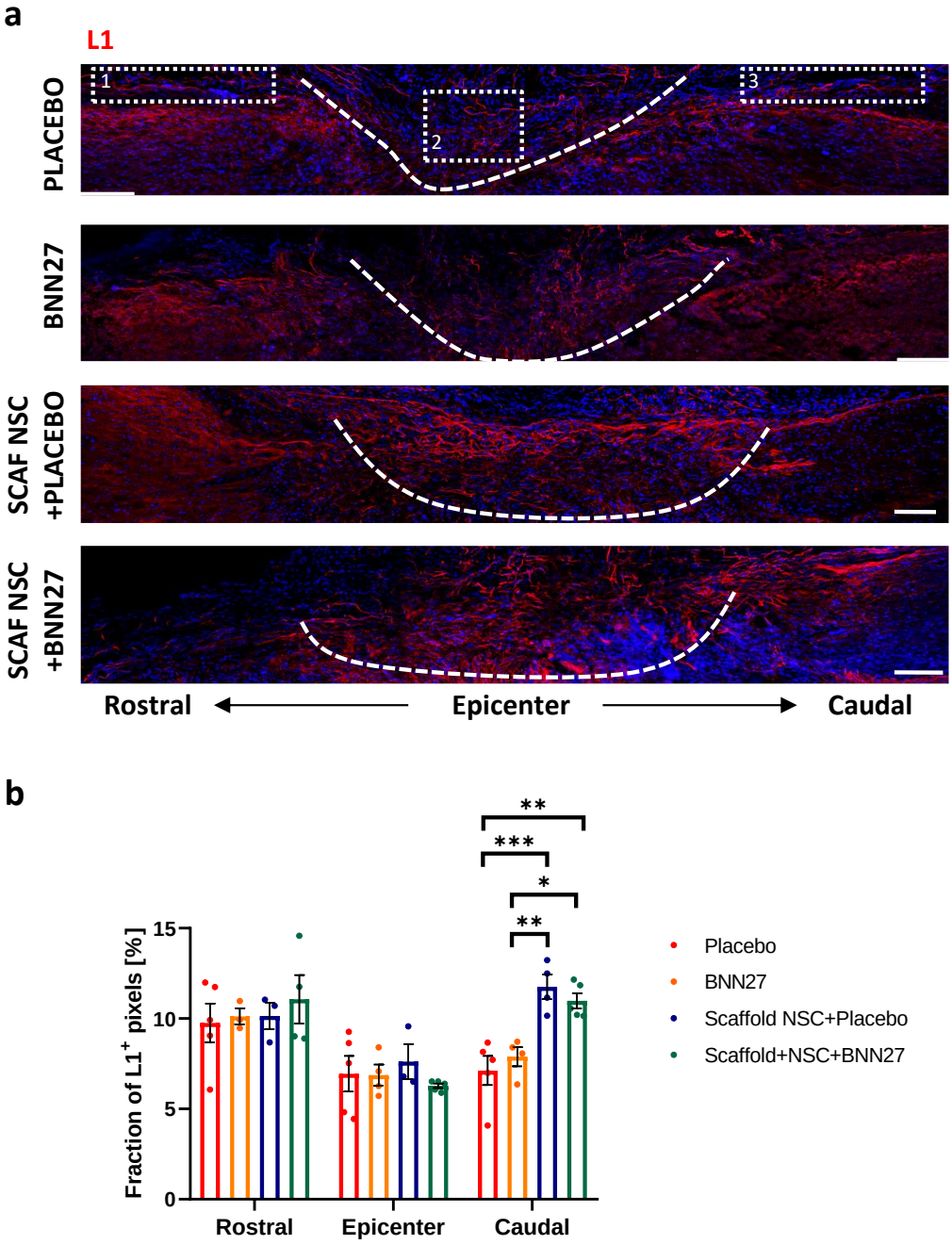

Fig. IV-34. Effects of systemic administration of BNN27 combined with NSC-seeded CS grafts on axonal elongation at 12 wpi. (a) Representative fluorescence images of spinal cord parasagittal sections at the injury site from all four injured groups immunostained for L1 (red). The boundaries of injury site are marked with the dotted line. The dotted rectagulars show the regions that were quantified rostrally (1), in the epicenter (2) and caudally (3) to the lesion. Scale bars: 100 µm. **(b)** Quantification of the fraction of $L1^+$ pixels rostrally, in the epicenter and caudally to the lesion at 12 wpi in the four injured animal groups ("Placebo": n=5, "BNN27": n=4, "Scaffold NSC+Placebo": n=4, "Scaffold NSC+BNN27" n=5). Results are presented as mean ± SEM. *P<0.05, **P<0.01, ***P<0.001; Tukey's post-hoc pairwise test assuming $P_{2\text{-way-ANOVA}}<0.05$.

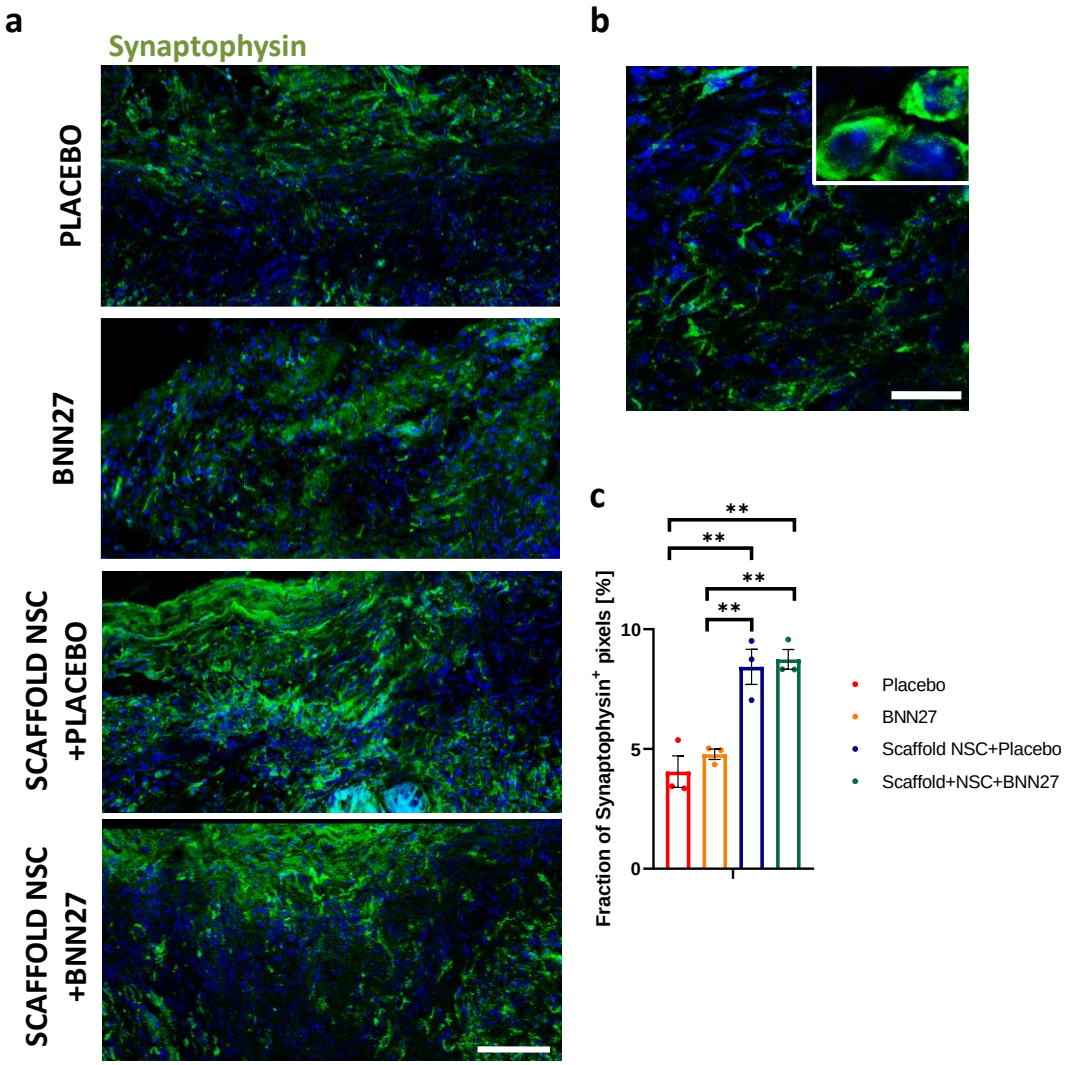

Fig. IV-35. Effects of systemic administration of BNN27 combined with NSC-seeded CS grafts on synapse formation at the injury site at 12 wpi. (a) Representative fluorescence images of spinal cord parasagittal sections at the injury site of the four injured groups immunostained for synaptophysin (green). Scale bars: 100 µm. **(b)** A representative high-magnification fluorescence image at the lesion epicenter ("Scaffold NSC+Placebo" group) immunostained for synaptophysin. Scale bar: 30 µm. **(c)** Quantification of synaptophysin$^+$ pixel fraction at the injury site in the four injured groups at 12 wpi (All groups: n=3). Results are presented as mean ± SEM. *P<0.05, **P<0.01, ***P<0.001; Tukey's post-hoc pairwise test assuming $P_{2\text{-}way\text{-}ANOVA} < 0.05$.

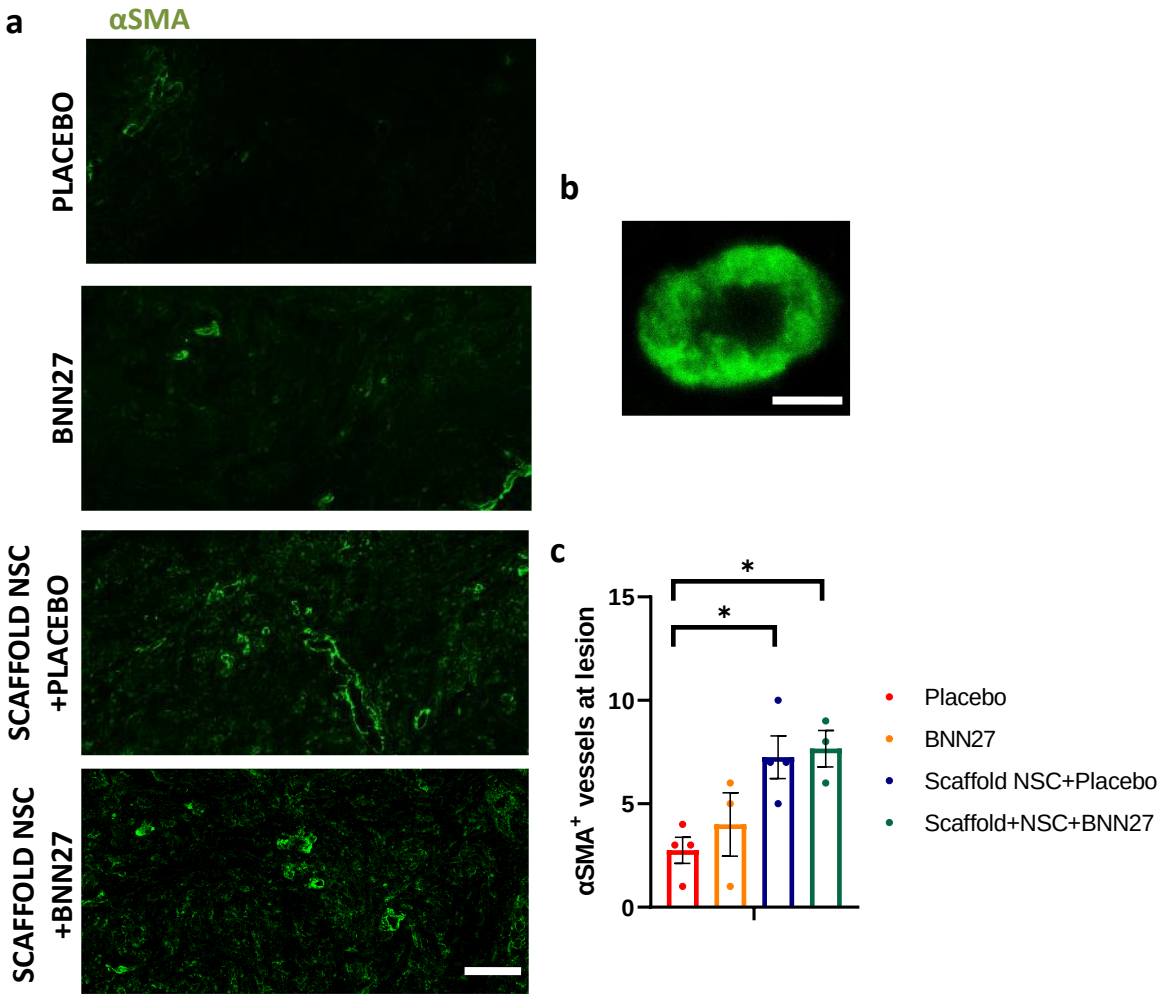

Fig. IV-36. Effects of systemic administration of BNN27 combined with NSC-seeded CS grafts on angiogenesis at the injury site at 12 wpi. (a) Representative fluorescence images of spinal cord parasagittal sections at the injury site of the four injured groups immunostained for αSMA (green). Scale bar: 50 µm. **(b)** A representative high-magnification fluorescence image of a vessel immunostained for αSMA. Scale bar: 5 µm. **(c)** Quantification of the number of αSMA$^+$ vessels within the lesion in the four injured animal groups at 12 wpi ("Placebo": n=4, "BNN27": n=3, "Scaffold NSC+Placebo": n=4, "Scaffold NSC+BNN27": n=3). Results are presented as mean ± SEM. *P<0.05, **P<0.01, ***P<0.001; Tukey's post-hoc pairwise test assuming $P_{2\text{-}way\text{-}ANOVA} < 0.05$.

2.2.8. Fate of Implanted NSCs

Implanted YFP-expressing NSCs could be distinguished from endogenous cells by immunostaining for GFP (**Fig. IV-37a**). Immunostaining of spinal cord parasagittal sections for GFP (implanted NSC-derived cells), Tuj1 (neurons) and GFAP (astrocytes) revealed an interesting specific spatial pattern on the fate of implanted NSC-derived cells. Tuj1$^+$GFP$^+$ (NSC-derived neurons) remained mostly within the lesion (**Fig. IV-37a**). On the other hand, GFAP$^+$GFP$^+$ (NSC-derived astrocytes) were localized in the lesion boundaries where they contributed to the formation of glial scar (**Fig. IV-37a,b**). Double immunostaining for GFP and various neuronal markers revealed that neurons derived from implanted NSCs included inhibitory GAD67$^+$ GABAergic neurons, 3TH$^+$ dopaminergic neurons and VGLUT$^+$ excitatory glutamatergic neurons (**Fig. IV-37c**). Interestingly, many GFP$^+$ cells were detected approximately 250 µm outside the lesion, having penetrated the surrounding glial scar (**Fig. IV-37d**).

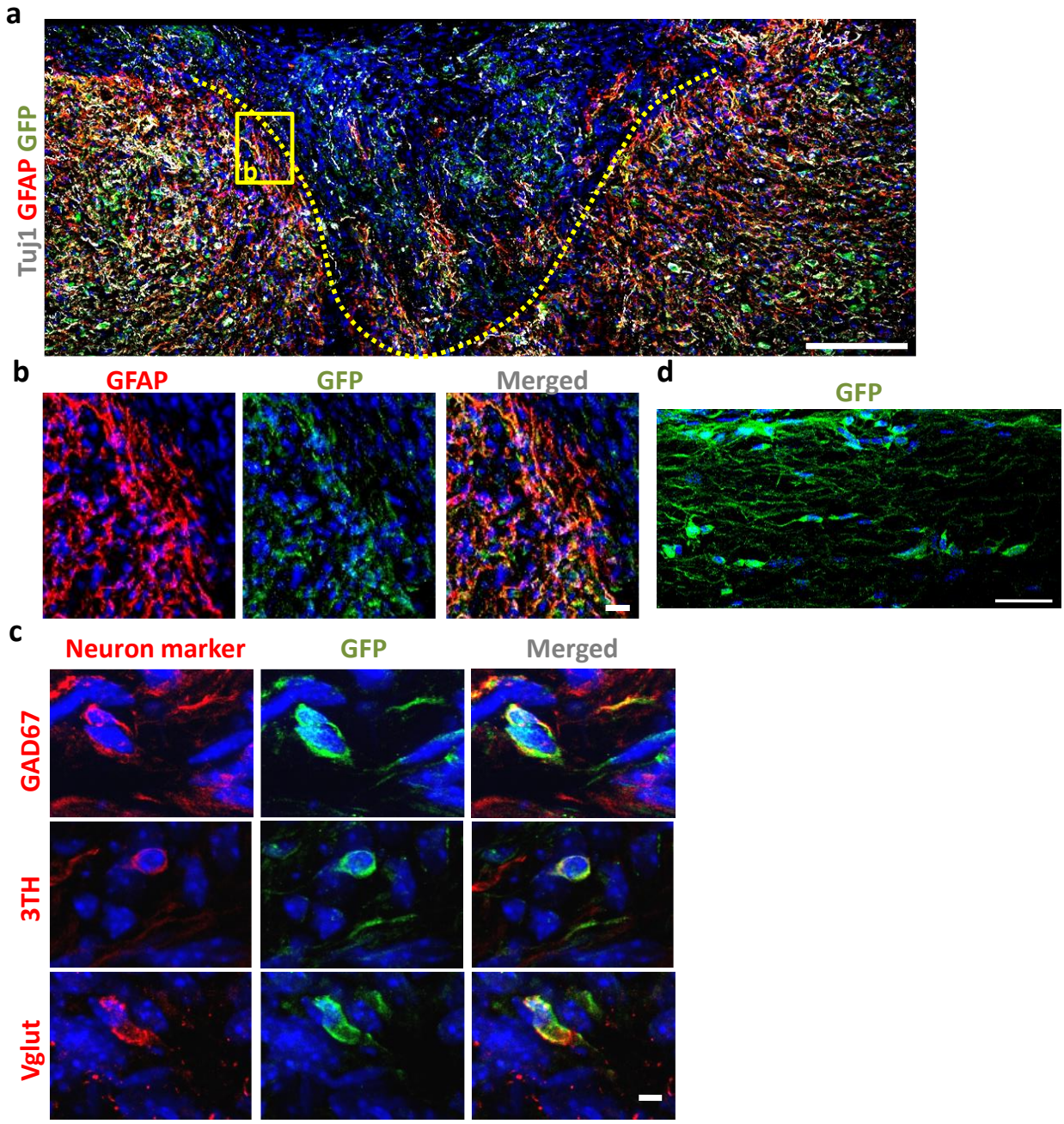

Fig. IV-37. Spatial patterning of implanted NSC fate at the SCI site. (a) A representative fluorescence image of a parasagittal section of a SCI lesion immunostained for Tuj1$^+$ neurons (white), GFAP$^+$ astrocytes (red) and GFP$^+$ implanted NSC-derived cells (green). Scale bar: 100µm. **(b)** High-magnification fluorescence image of the rectangular insert of image (a) showing GFP$^+$GFAP$^+$ implanted NSC-derived astrocytes at the lesion boundaries. Scale bar: 30 µm. **(c)** Representative high-magnification fluorescence images of GFP$^+$ implanted NSC-derived cells double-immunostained with markers of different neuron types: GAD67 (inhibitory GABAergic neurons; upper row), 3TH (dopaminergic neurons; middle row) and VGLUT (excitatory glutamatergic neurons; lower row) (red). Scale bar: 3µm. **(d)** Representative fluorescence image of a spinal cord parasagittal section showing GFP$^+$ implanted NSC-derived cells located in the dorsal column, approximately 250 µm caudally to the lesion. Scale bar: 30 µm.

2.2.9. Effects of Systemic Administration of BNN27 on Implanted NSC Survival and Differentiation at 12 weeks Following Injury

BNN27 effects on the density of implanted NSC-derived cells at the injury site at 12 wpi were evaluated by counting the number of GFP$^+$ cells (derived from implanted NSCs) in the two graft-treated groups. Results showed that BNN27 administration increased the density of GFP$^+$ cells at the injury site ("Scaffold NSC+Placebo": $7.51 \cdot 10^5 \pm 1.25 \cdot 10^5$ cells/mm^3, n=5 vs "Scaffold NSC+BNN27": $15.24 \cdot 10^5 \pm 2.57 \cdot 10^5$ cells/mm^3, n=3, P=0.02) (**Fig. IV-38a,b**). In order to evaluate the effects of BNN27 administration on the neuronal fate of implanted NSCs, the Tuj1$^+$GFP$^+$ cells were counted at the injury site (**Fig. IV-38c**). BNN27 did not affect the fraction of GFP$^+$ cells that had differentiated to Tuj1$^+$ neurons ("Scaffold NSC+Placebo": 22.6±5.4%, n=4 vs "Scaffold NSC+BNN27": 22.0±1.7%, n=3, P=0.93) (**Fig. IV-38d**). However, BNN27 administration increased the fraction of Tuj1$^+$ neurons that originated from implanted NSCs ("Scaffold NSC+Placebo": 13.1±3.3%, n=4 vs "Scaffold NSC+BNN27": 24.4±1.6%, n=3, P=0.04) (**Fig. IV-38e**).

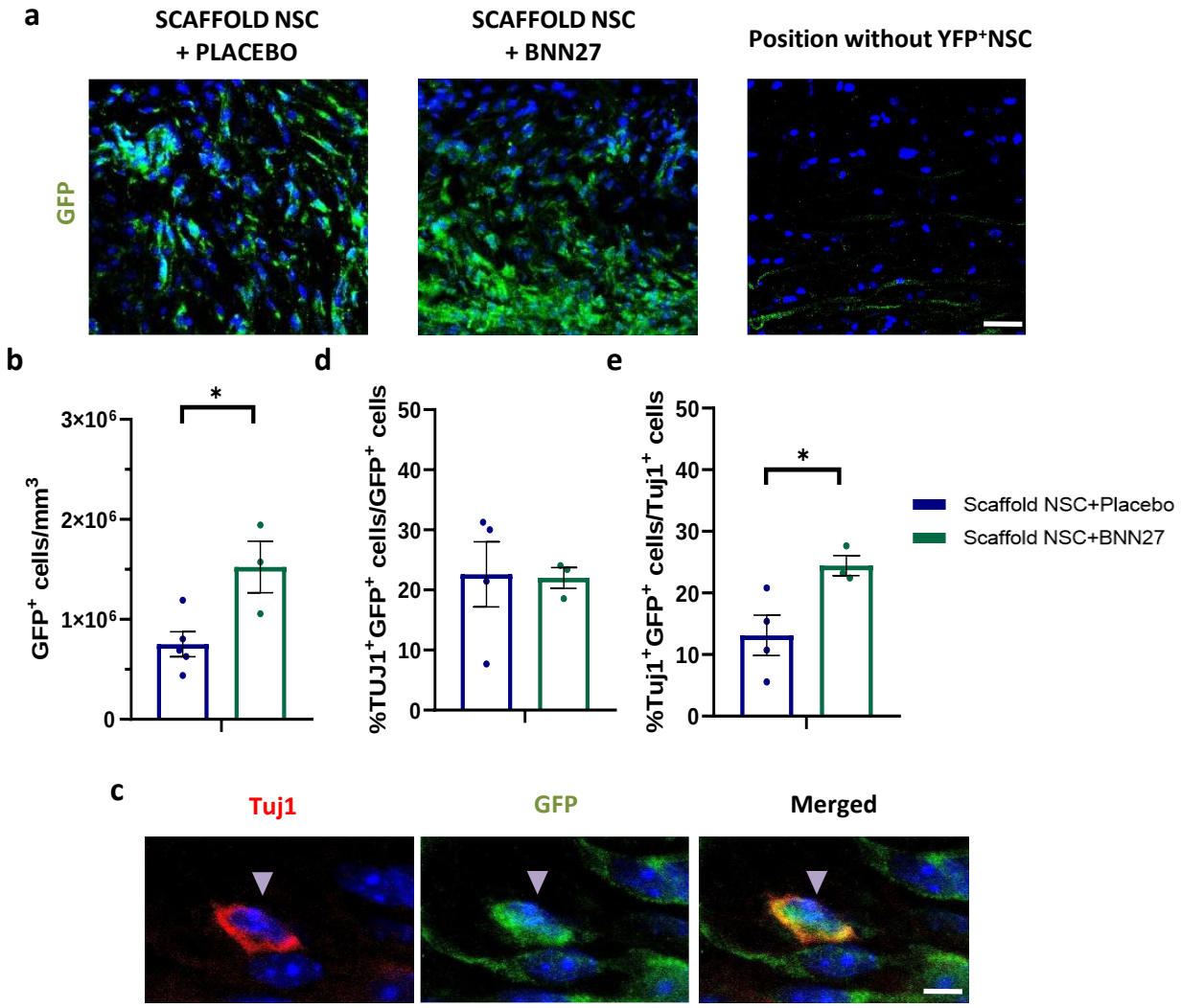

Fig. IV-38. Effects of systemic administration of BNN27 on the density and neuronal fate of implanted NSCs at the injury site at 12 wpi. (a) Representative high-magnification fluorescence images of GFP$^+$ implanted NSC-derived cells from the two animal groups ("Scaffold NSC+Placebo", "Scaffold NSC+BNN27") treated with NSC-seeded CS. Scale bar: 30 µm. **(b)** Quantification of the density of GFP$^+$ cells at the injury site at 12 wpi. **(c)** High magnification fluorescence images of cells within the injury site double-stained for GFP (green; implanted NSC-derived cells) and Tuj1 (red; neurons). Scale bar: 5 µm. **(d)**

Quantification of the fraction of GFP^+ cells that also stain for the Tuj1 at the injury site at 12 wpi. **(e)** Quantification of the fraction of $Tuj1^+$ neurons that also stain for GFP at the injury site at 12 wpi ("Scaffold NSC+Placebo": n=4, "Scaffold NSC+BNN27": n=3). Results are presented as mean ± SEM. *P < 0.05; unpaired two-tailed Student's t-test.

2.3. Comparison of the Horizontal Ladder Walking Assay and the Rotarod Assay in the Evaluation of Locomotion Recovery in the Mouse Dorsal Column Crush Spinal Cord Injury Model

Evaluating the effects of a SCI treatment relies heavily on behavioral assays that can quantify mice function. Appropriate behavioral assays need to match the specifics of the particular SCI model chosen, detect and quantify with adequate sensitivity and repeatability SCI-induced effects. Accordingly, experiments presented in sections IV-2.1,2.2 utilized the Horizontal Ladder Walking assay to quantify locomotion performance, thereby probe the effects of injury and treated treatments. While the Horizontal Ladder Walking assay was able to detect the effects of dorsal column crush SCI and treatments in statistically meaningful ways **(Fig. IV-20)**, it suffers from three major disadvantages: 1) its quantification is not automatic and it requires a trained person to inspect videos and assign a score to each mouse step, 2) scoring by a human rather than an algorithm introduces subjectivity, 3) watching and analyzing videos of walking mice is a very labor intensive procedure. In contrast, the Rotarod assay (167) is an automated assay that could be utilized to quantify the wound healing response following SCI. The Rotarod assay offers several advantages compared to the Horizontal Ladder Walking Assay: 1) easier and faster implementation, since multiple mice can be tested simultaneously, and 2) automated objective quantifications, as results are not based on observations of an expert user.

In order to evaluate the ability of the Rotarod assay to quantify the wound healing response and the effects of candidate treatments following dorsal column crush SCI in mice, a small pilot study was designed and implemented. The pilot study repeated part (monitored mice over 6 wpi) of the bigger study described in section IV-2.1 (monitored animals over 12 wpi) and focused on comparing the locomotion recovery quantification provided by the Horizontal Ladder Walking assay and the Rotarod assay **(Fig. IV-39a)**.

The results of locomotion recovery quantification over 6 wpi provided by the Horizontal Ladder Walking assay **(Fig. IV-39b)** agree with the results shown in **Fig. IV-20**. In "Uninjured control" mice, the measured fault rate remained invariant over time (μ = 11.8 %, σ = 3.4 %). In both injured groups, the fault rate measured at 1 day as well as 1- and 2- weeks post injury showed consistency of the injury (according to the exclusion criteria of section III-17). Moreover, in both injured groups, 1 day post injury, the fault rate increased significantly ("Crush only": 38.2$\pm$6.9 %; "Scaffold+NSC": 47.3$\pm$8.5 %). In addition, in both injured groups, the fault rate at 1 wpi was indistinguishable ("Crush only" vs "Scaffold +NSC" 1 wpi: P=0.81) and statistically different from the "Uninjured control" group ("Uninjured control" vs "Crush only" 1 wpi: P=0.01; "Uninjured control" vs "Scaffold +NSC" 1 wpi: P=0.01). Last but not least, the response of the injured untreated ("Crush only") and the injured treated ("Scaffold+NSC") group was indistinguishable over 6 wpi ("Crush only" vs "Scaffold +NSC" 6wpi: P=0.49), in agreement with previous observations (Section IV-2.1.2).

The corresponding quantification of locomotion recovery via the Rotarod assay over 6 wpi is shown in **Fig. IV-39c**. In "Uninjured control" mice, the measured latency was not stable over time (μ = 199.9 sec, σ = 49.2 sec). Interestingly, in both injured groups, 1 day post injury, the latency decreased significantly (preop: "Crush only": 132.5$\pm$36.7 sec, "Scaffold+NSC": 184.0$\pm$20.9 sec; postop: "Crush only": 60.5$\pm$20.1 sec,

"Scaffold+NSC": 56.0±26.8 sec). Then, during the 6-week recovery, in both injured groups latency progressively increased, a sign of locomotion recovery. Nevertheless, the samples in "Scaffold+NSC" group showed high variability and the response of all groups saturated at 240 sec (4 min), the maximum allowable duration of each Rotarod assay. This saturation precludes the comparison of latencies measured in different animal groups. Thus, results possibly indicate that the chosen Rotarod parameters (angular speed, maximum duration) were not optimally selected. Indeed, the Rotarod apparatus offers a great variety of parameters that could be tuned to optimize the level of task difficulty, which were not rigorously studied here. Therefore, although the Rotarod assay data of **Fig. IV-39c** are inappropriate for the quantification of this specific mouse SCI model, the Rotarod assay sensitivity could be altered in order to capture the delicate differences that exist between injured and uninjured animals.

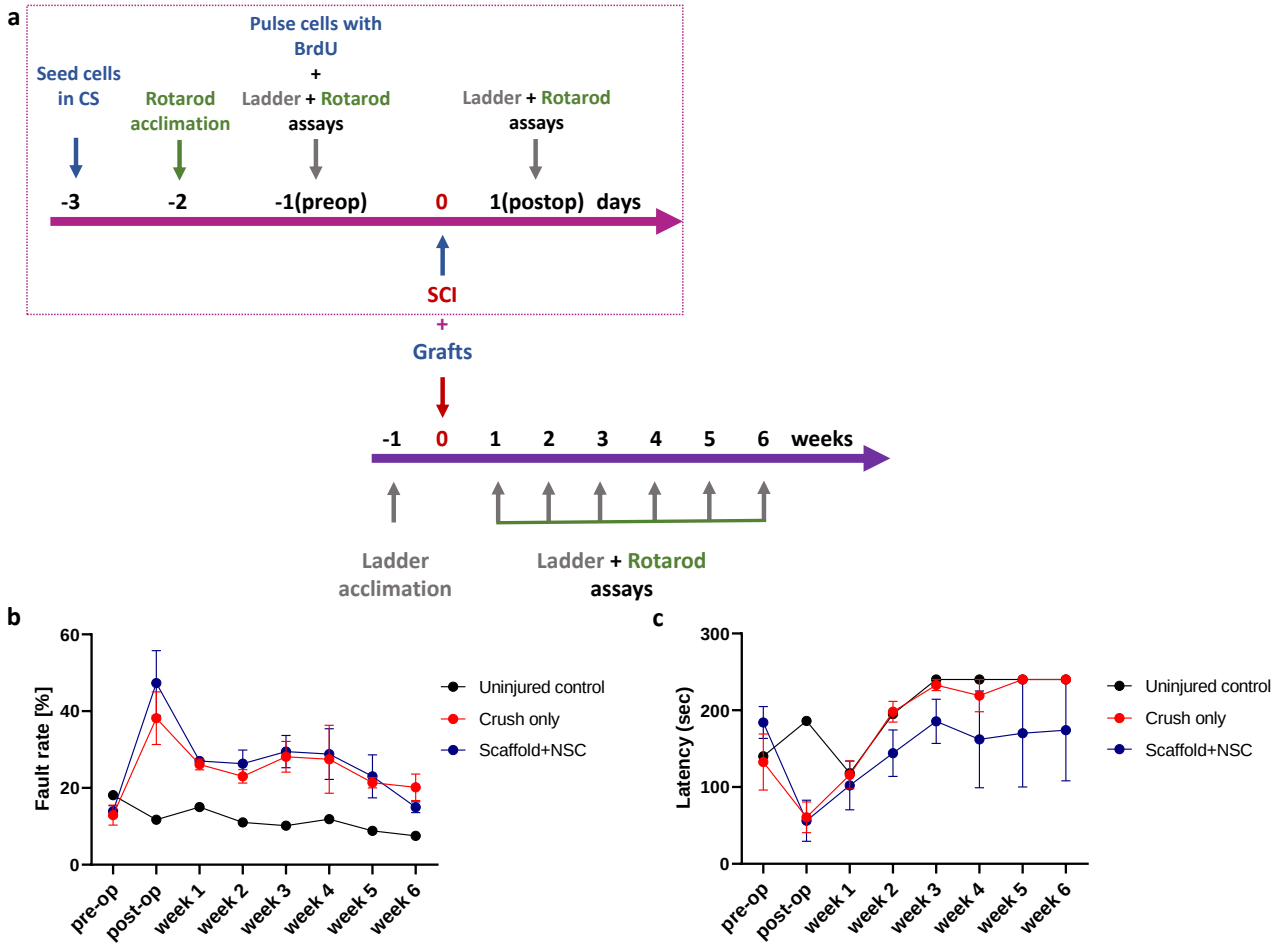

Fig. IV-39. Comparison of quantification of locomotion recovery after SCI via the Horizontal Ladder Walking assay and via the Rotarod assay. (a) Experimental timeline. **(b)** Quantification of locomotion performance (fault rate) after SCI by the Horizontal Ladder Walking assay over a period of 6 weeks following injury. **(c)** Quantification of locomotion performance (latency) after SCI by the Rotarod assay over a period of 6 weeks following injury ("Uninjured control" n=1, "Crush only" n=4, "Scaffold+NSC" n=4). Results are presented as mean ± SEM.

IV. Discussion

This thesis evaluates novel combinatorial treatments for CNS injuries that contain three "components": 1) porous collagen-based scaffolds (PCS), 2) Neural Stem Cells (NSC), multipotent cells that can replace neural cells lost by CNS injuries, 3) Microneurotrophins (MNT), small-molecule analogs of neurotrophins (NT).

Significant research focuses on developing combinatorial treatments for CNS injuries that integrate the complementary actions of biomaterials, cell therapies and therapeutic molecules (43). In such treatments, biomaterials contribute structural support, inflammation regulation, delivery, protection and orientation of cells, a substrate for cellular migration and axonal elongation, and localized delivery of diffusible therapeutic molecules at the lesion (37). PCS are biomaterials with established clinical applications in regenerative medicine. Although optimized PCS (CS and CGS) have been approved by FDA and are utilized in the clinical treatment of injured skin and transected peripheral nerves, much research remains in order to develop PCS-based grafts for CNS injuries. In order to address the complex nature of wound healing following a CNS injury, research (including the one presented in this thesis) focuses on i) characterizing the effects of PCS on wound healing response and ii) optimizing PCS as carriers of cellular therapies or bioactive soluble molecules.

The cellular part of combinatorial treatments usually focuses on replacing neural cells lost during injury and re-establishing connectivity at the injury site (98). Among the various kinds of stem cells tested in experimental SCI treatments, NSCs have shown promising results in animal models, including the extension of a high number of axons caudally to the lesion and synapse creation with CST axons (113,172). Although NSC-based treatments are slowly progressing in human clinical evaluation (119), much work remains to enhance their efficacy. Along this direction, much research focuses on implanting cells via biomaterial grafts and complementing grafted cells with therapeutic molecules. Herein, NSC-seeded PCS were tested in a SCI model.

MNTs are considered candidate therapeutic treatments for various neurologic diseases, since they mimic the effects of endogenous NTs, do not cause hyperalgesia and are BBB-permeable, in contrast to endogenous NTs (85). Despite promising results in several rodent neurodegeneration models, the therapeutic activity of MNTs had not been evaluated in any CNS injury model. Herein, for the first time, MNTs were tested in two CNS injury models: ONI and SCI.

1. Treatments for Optic Nerve Injury based on Microneurotrophins and PCS Grafts

The first part of the thesis focused on evaluating the effects of BNN27, the seminal and best-described MNT, in a mouse ONC model. The mouse ONC model is widely utilized and is considered a simpler and surgically less invasive CNS injury model compared to SCI. The simplicity of ONC model is based on the direct effects of ONI in RGCs leading to direct and simple obervation of key events, such as RGC death and axonal elongation.

Of particular interest to this thesis is the previously reported Neurotrophic hypothesis that supports that obstruction of retrograde transport in RGC axons in the optic nerve leads to RGC neurotrophic support deprivation and, consequently, to RGC apoptotic cell death (73). Regarding NTRs, $p75^{NTR}$ and TrkA are expressed in RGCs (71), but published reports about ONI-induced NTR expression alterations are contradictory depending on the time and method of quantification (74). Of interest is not only NTR expression alteration, but mainly the balance between proNGF/NGF and TrkA/$p75^{NTR}$, since NGF/TrkA signaling favors survival, while proNGF/$p75^{NTR}$ can induce apoptosis (74). Herein, no clear result was acquired about the alteration of NTRs expression following ONC, as well. Although there was a trend of $p75^{NTR}$ upregulation and TrkA downregulation at 2 wpi **(Fig. IV-3)**, these results were not statistically significant.

However, the expression of all NTRs in GCL was indeed verified in **Fig. IV-3**, suggesting that cells in GCL can respond to NTs and MNTs, including BNN27.

BNN27 was delivered via eye drops or via a CGS-based graft on an ONC mouse model and the effects were evaluated via behavioral observations as well as histological analysis at 2 and 10 wpi. The delivery of BNN27 in target tissues (retina, optic nerve) via eye drops (24 hours after the last administration) or CGS grafts (2 weeks after graft placement) was evaluated via LC-MS. LC-MS results **(Table IV-1)** detected small amounts of BNN27 both in retina and optic nerve of treated eyes via both delivery methods. Small amounts of BNN27 detected in intact contralateral eyes where no treatments were applied were attributed to BNN27 delivered in the injured eye and transferred via systemic circulation. A recent pharmacokinetic study about the permeability of BNN27 in rodent CNS though revealed the presence of BNN27 in rodent retina 30 min after i.p. injection and its rapid elimination that made it undetectable in retina 6 h after injection (91). Thus, the abovementioned results might suggest that tissues should be harvested earlier (e.g. a few minutes to hours after BNN27 delivery). However, since there is no previous report on the pharmacokinetics of BNN27 delivery via eye drops or CGS grafts, the detection of even small amounts of BNN27 at 24 hours after the last eye drop administration or 2 weeks after CGS graft placement can be a preliminary proof of efficient BNN27 delivery via both methods.

BNN27 release from the CGS graft was evaluated in an *in vitro* experiment that quantified the release kinetics of fluorescein (instead of BNN27) entrapped in a CGS graft. Fluorescein release kinetics from CGS grafts were measured in the presence and absence of the FmocFF peptide hydrogel (Master's Thesis of Papagiannaki 2022). Results showed that 99% of fluorescein entrapped in FmocFF peptide hydrogel inside the CGS graft was released within 6.72 ± 1.12 hours. No difference in release was observed when fluorescein was released from a CGS graft that lacked the peptide (6.04 ± 0.28 hours). However, the findings of Papagiannaki's thesis cannot be directly applied to infer the *in vivo* release of BNN27 from CGS grafts placed around injured optic nerves for 2 reasons: (a) Papagiannaki's thesis quantified the diffusion of fluorescein instead of BNN27. Although fluorescein and BNN27 have similar molecular weights, the study did not consider differences in other physicochemical properties, such as lipophilicity, which may affect the interactions of BNN27 with the scaffold or the FmocFF peptide. (b) Papagiannaki's thesis utilized fluorescein sodium salt, a compound that has excellent solubility in water, while in contrast the solubility of BNN27 in water is poor (< 0.1 mg/mL). Thus, 30 mM BNN27 (the concentration of BNN27 diluted in 70% ethanol solution) utilized *in vivo* is expected to be released more slowly since BNN27 is expected to precipitate as it meets aqueous solutions around the graft.

Following ONC, results indicated that ≈40% of RGCs were lost at 1 wpi, while 60-70% of RGCs were lost at 2 wpi **(Fig. IV-2b)**. These results replicate previous experimental findings. Following ONC, it is reported that 85-90% of RGCs die within 2-3 wpi (35). Differences in RGC survival reported in the literature indicate the variability of ONC model due to the elegant nature of the crush operation, which means that different users probably induce crush of variable severity. Herein, results on RGC survival following ONC were consistent, highlighting the accuracy and repeatability of the operator.

A main finding of the ONC studies was that BNN27, delivered via eye drops or via a CGS graft, significantly decreased ONC-induced **RGC apoptosis** at 2 wpi. Initially, the non-toxicity of BNN27 and its diluent DMSO was confirmed in intact eyes **(Fig. IV-4b)** and was in accordance with previous study that evaluated DMSO drop effects to retina (95). Then, when BNN27 was delivered via eye drops (1 or 2 per day), increased (double) RGC survival was observed at 2 wpi compared to non-treated injured eyes **(Fig. IV-4c)**. These results agree with previous reports on the ability of NGF administration to reduce RGC loss *in vivo* (76,77). A major

limitation of utilizing eye drops for the delivery of therapeutic molecules to retina (discussed in section I-5) is the high percentage of therapeutic molecule loss till reaching retina; less than 3% of therapeutic molecule delivery via eye drops reaches the posterior segment (42,173). This explains the high frequency of BNN27 administration required for neuroprotective effects; unlike daily BNN27 administration, administration every second day did not increase RGC survival 2 wpi (**Fig. IV-4c**). On the other hand, BNN27 administration via a CGS graft placed around the injured optic nerve resulted in improved and approximately 3 times more RGC survival compared to non-treated injured eyes **(Fig. IV-7)**. This finding highlights the advantages of targeted delivery of therapeutic molecules in the proximity of a CNS lesion and at controlled released rate. This effect was also demonstrated in a recent study, where a combination of two compounds (the corticosteroid triamcinolone acetonide and the neuroprotective agent Fasudil), delivered locally in the optic nerve lesion via a PLGA-collagen graft placed at the optic nerve, promoted RGC survival (174). Interestingly, this thesis is one of the few studies that directly compares the effects in retina of a compound delivered via eye drops or via a biomaterial graft placed around the optic nerve.

Experimental results showed that placing a CGS graft that included a FmocFF hydrogel but lacked BNN27 around the ONC lesion also led to significant increase (approximately double) in RGC survival compared to non-treated injured eyes **(Fig. IV-7)**. Although there is a lot of literature on PCS-based conduits on peripheral nerve regeneration, there are no previous reports on the effects of PCS grafts (like the CGS graft utilized in this study) on wound healing in the optic nerve following ONI. In general, biomaterials have been used to guide axons into the CNS lesion and improve the lesion environment (103). For instance, a study utilized self-assembling peptide nanofiber scaffold grafts to provide the appropriate environment in injured optic nerve resulting in axonal regeneration (133). Apart from the biomaterial itself, the CGS graft contains the FmocFF peptide that could also affect RGC survival. For instance, FmocFF piezoelectric properties have been associated with axonal regeneration and consequently with neuroprotection (175).

Despite promising neuroprotective effects at 2 wpi, the neuroprotective effects of BNN27 on ONC-induced RGC apoptosis were abolished at 10 wpi. RGC survival in BNN27-treated injured eyes either via eye drops or via grafts did not differ from the one in untreated injured eyes at 10 wpi **(Fig. IV-14)**. This result agrees with previous studies that state that following ONI, RGCs not only receive less trophic factors due to decreased retrograde transport, but they also lose their responsiveness to trophic factors, even during long-term delivery of trophic factors. Elevation of cAMP intracellular levels in RGCs has been shown able to restore ONI-induced lost responsiveness (176). Another explanation could lie in the ability of BNN27 to bind and activate both $p75^{NTR}$ and TrkA, since $p75^{NTR}$ has been associated to apoptosis via activation of JNK (52). Administration of mutant NGF that activates only TrkA or a compound that prevents the binding of endogenous NGF and pro-NGF to $p75^{NTR}$ has resulted in neuroprotection effects after ONT, in contrary to administration of normal NGF that has not resulted in any neuroprotection effects. In the same study, a NGF mutant-selective $p75^{NTR}$ agonist induced RGC death both in normal and transected eyes (177). Thus, TrkA-specific agonists, such as MNT ENT-A010 or ENT-A013, could probably enhance and prolong RGC neuroprotection compared to BNN27 (178,179).

Activation of astrocytes and Müller cells is a key response of retina to ONI. GFAP is not physiologically expressed by Müller cells, however it is induced in activated Müller cells (180). In this study $GFAP^+$ processes of activated Müller cells were quantified as a means to probe ONC-induced gliosis in retina. Results showed a significant increase in the density of $GFAP^+$ radial processes in retina at 1 and 2 wpi **(Fig. IV-8)**. Despite various studies on the detrimental and beneficial roles of reactive gliosis on SCI, its effect on retina has not been clear yet. Recently, research has focused on the beneficial role of astrocytes and Müller cells in supporting RGCs by providing them with neurotrophic factors. For instance, both astrocytes and Müller cells

increase CNTF release after lens injury promoting RGC axonal regeneration. Moreover, Müller cells have been characterized unique due to their ability to dedifferentiate into retinal progenitor-like cells (181). Therefore, the fact that no effect of BNN27 administration either via eye drops or via graft was observed in this study on reactive gliosis in retina may be beneficial. Although several studies have demonstrated the ability of BNN27 to reduce astrogliosis by decreasing GFAP expression in other animal models of CNS degeneration such as cuprizone-induced demyelination (96), the 5xFAD Alzheimer's disease mouse model (Karali et al. in preparation) and diabetes-induced retinal damage (94), these results should not be considered contradictory to the ones of the present study due to differences in pathophysiology. Furthermore, these studies quantify astrogliosis via different means; in this study the evaluation was performed in retina by quantifying the density of Müller cell processes and not in a glial scar formed around a CNS injury lesion where astrogliosis is usually quantified via GFAP expression.

Another key response to ONI is **inflammation** (section I-2), which is activated within the first minutes to hours following injury and involves many cell types, such as microglia. Apart from some reported beneficial effects, inflammation can lead to further tissue damage and neuronal death. Interestingly, in the present study, BNN27 administration significantly decreased ONC-induced microglia-mediated inflammation at the injury site at 2 wpi. Specifically, the fraction of $Iba1^+$ pixels within the ONC lesion was almost half after BNN27 administration via scaffolds compared to untreated eyes **(Fig. IV-10)**. This finding is in agreement with the reported activation of anti-inflammatory TrkA-mediated pathways (PI3K-Akt1/Akt2-CREB) by NGF and DHEA (88,182). Moreover, BNN27 administration in a diabetic-induced retinal damage rat model led to reduced secretion of pro-inflammatory cytokines and increased secretion of anti-inflammatory cytokines (94). Herein, BNN27 effects on microglia-mediated inflammation were statistically significant only when BNN27 was delivered via a CGS graft around the ONI site. On the contrary, administration of BNN27 via eye drops resulted in highly variable $Iba1^+$ staining results, highlighting again the importance of targeted delivery.

Axonal degeneration starts the first few hours after ONC and is associated with cytoskeleton alterations and autophagy linked to increased intra-axonal Ca^{+2} levels (183). Herein, ONC resulted in high axonal degeneration and loss of axon myelin integrity at 2 wpi. Released MAG from damaged myelin observed in crushed optic nerves **(Fig. IV-2f)** is one of the main inhibitors of axon regeneration, as described in chapter I.

Limited spontaneous **regeneration** in short distances has been observed up to 10 days post-injury. Literature reports that just 0.2% of optic nerve axons reach the optic chiasm at 1 month post-injury (35). Axonal bi-directional transport of molecules and organelles is of high importance for RGC survival (discussed in section IV-5.1.2). Since axonal dysfunction precedes RGC death, it is important for a treatment to promote RGCs to regenerate their axons before they die (184). Unfortunately, the results of this thesis showed that BNN27 administration did not prevent axonal degeneration and did not promote axonal regeneration at 2 or 10 wpi, since the number of $L1^+$ axons measured in optic nerve cross sections at various distances from the proximal end of the injury site in treated injured eyes did not differ from the one measured in untreated ones **(Fig. IV-9,15)**. These results are in agreement with published results on the inability of BNN27 alone to promote neurite extension (93). Additionally, none of the MNTs tested *ex vivo* in retina explants promoted axonal elongation at 2 weeks post-dissection. Consequently, BNN27 administration did not lead to vision recovery at 2 or 10 wpi, since no positive OMR was observed when the injured eyes of mice were tested **(Fig. IV-12,16).** Previous studies that achieved axonal regeneration and OMR by 10 wpi used combination of treatments in order to both decrease inhibitory signaling and increase mechanisms supportive of axon regrowth and guidance. For instance, the i.v. administration of the pro-inflammatory agent zymosan and the i.v. administration of the cAMP have been used to increase the neuronal sensitivity to trophic factors, lead RGCs to an active growth state and decrease sensitivity to inhibitory signals from the CNS myelin and the

glial scar. In these studies, oncomodulin (ocm) was the key factor as it binds to RGC receptors with high affinity in a cAMP dependent manner. Ocm was produced by macrophages in the zymosan-induced inflammatory cells influx. Consequently, ocm led to inflammation-induced axon regeneration via binding to RGC receptors (162,185,186). Similarly, a treatment that combined neural activity enhancement and mTOR signaling activation in RGCs resulted in target-specific axonal regeneration and partial function recovery (187).

Last but not least, it has been suggested that **OPC response** to demyelination in the optic nerve is very limited compared to other CNS lesions (188). Herein, BNN27 did not increase OPC recruitment in the injury site at 2 wpi, as measured by counting the density of OPCs at the injury site and at various distances (up to 750 μm) from the distal end of the injury site **(Fig. IV-11)**. The same method of quantification was also described in Mendoca et al., who achieved increased OPC recruitment 1.5 mm away from the injury site at 12 wpi by i.v. injection of zymosan and cAMP in pten-null mice (189).

2. Treatments for Spinal Cord Injury based on NSC-seeded PCS Grafts and Microneurotrophins

The second part of this thesis focused on evaluating various combinatorial treatments for SCI in the dorsal column crush mouse SCI model. More specifically, CS-based grafts seeded with NSCs were firstly tested in this SCI model, whereas afterwards, the treatment was further boosted with the addition of a therapeutic molecule, the MNT BNN27. As mentioned in section I-5.1.2, low levels of NGF are observed following SCI, whereas both NGF receptors (TrkA, $p75^{NTR}$) are expressed in spinal cord under normal conditions (64–66). BNN27 was delivered systemically using subcutaneous pellets over a period of approximately 60 days. Subcutaneous systemic administration is expected to provide a relatively steady BNN27 dose with no animal distraction, appropriate for minimizing artifacts in locomotion evaluation. The permeability of BNN27 in rodent CNS was demonstrated by a previous pharmacokinetic study that demonstrated the presence of BNN27 in rodent brain and retina 30 min after i.p. injection (90,91).

Although contusion models described in section I-4.2 are closer to clinical cases, dorsal column crush mouse SCI model was chosen in this thesis, because it provides a lesion volume where a graft can be implanted, giving the opportunity to further evaluate the effects of CS-based grafts on SCI (190). In addition, dorsal column crush model is known to irreversibly affect both ascending and descending pathways (including the CST) (191), representing a well-described model for evaluating axonal regeneration following SCI (190). Transection SCI models, which are more widely used, are even less clinically related. Interestingly, dorsal column crush model has also been used for evaluating therapeutic molecules, such as NTs (192,193), as well as NSC implantation at the injury site (194). Functional evaluation in the dorsal column crush model though can be challenging, because the deficit is mild and shows a spontaneous recovery in the beginning (190).

Biomaterials are a key component of regenerative medicine treatments providing structural support, inflammation regulation and a substrate for cellular migration and axonal elongation. The present thesis focuses on porous CS, a particular type of sponge-like biomaterial, that has been shown to induce regeneration following trauma and has received FDA approval for PNS injuries (146,147). Prior to this thesis, CS grafts had been tested only once in a transected SCI model. In that study, cell-free CS or CS seeded with adult NSCs decreased lesion cavity at 6 wpi, but did not improve functional recovery (148). Herein, H&E histology revealed that grafted cell-free CS grafts drifted away from the injury site at 6 wpi, while cell-seeded CS grafts (seeded either with NSCs or with NIH3T3) integrated well with the surrounding tissue **(Fig. IV-18)**.

Part of the CS graft remained non-degraded at the injury site at 6 wpi, in agreement with the reported 3-week *in vivo* degradation half-life of CS measured in peripheral nerves (146). The role of CS grafts in the delivery system of cells into injury sites was highlighted, since contrary to the inaccurate and ineffective method of injecting NSCs directly in SCI sites **(Fig. IV-27)**, the 3D structure of CS provided a physical support and enhanced cell integration within the lesion. Cells were grown inside the CS leading to their accurate and targeted placement in the lesion without any losses that could occur via the injection method.

Among other cell therapies described in section I-5.2, NSCs were chosen for the implants in this thesis as multipotent cells that can replace neural cells lost by SCI (103). Interestingly, as further discussed in the following paragraphs, NSC implantation has been widely used and enhanced crucial events following SCI, such as neuron density, axonal elongation and synaptogenesis. However, the appropriate origin and differentiation stage of NSCs have not been well-characterized, yet. Regarding the choice of NSC origin, many SCI studies use spinal cord isolated NSCs, in order to be implanted in the same tissue they are isolated from (195). Nevertheless, it is important to take into consideration that NSCs differentiate according to the provided environmental cues. For instance, adult spinal cord NSCs implanted in the neurogenic region of hippocampus differentiated into neurons, while their transplantation into the non-neurogenic spinal cord resulted in glial cells (121). Herein, cortical NSCs were chosen, which have also been used previously in SCI implants (151). Regarding NSC differentiation stage, two studies reported that both developing and fully mature unicellular NSCs or neurospheres resulted in CST regeneration, indicating that various differentiation stages enhance regeneration (118,170). However, this result in the second study occurs only under the condition that cells are derived from the same region (NPCs isolated from spinal cord) (118). Herein, E13.5 NSCs were chosen and transplanted in 3 DIV. E13.5 NSCs seeded in CS grafts have been studied previously *in vitro* in Kourgiantaki's PhD thesis (2017), where they showed highly elongated dendrites under differentiation conditions in 7 DIV compared to 2D cultured NSCs. Herein, cell type was critical for the graft, since NIH3T3-seeded CS grafts caused severe complications in animal's health (even mortality), while tissue damage and inflammation were visible in lesion histology. Contrarily, NSC-seeded grafts integrated well without having gaps with the surrounding tissue and did not result in other complications **(Fig. IV-18,19)**.

Evaluation of **locomotion recovery** via the Horizontal Ladder Walking assay in both studies A and B showed that grafting SCI lesions with NSC-seeded CS grafts led to statistically significant locomotion improvement after dorsal column crush in mice starting at 9-10 wpi **(Fig. IV-20,31)**. These reproducible findings highlight the central role of NSC-based cell therapies in SCI treatments and are in agreement with a recent study where transplantation of NSC-seeded CS grafts in a transected SCI model resulted in functional recovery (BB&B score over a period of 8 wpi), as well (118). Interestingly, the "Scaffold+NSC" group (and not "NSC injection" group) was the only mice group whose locomotion performance was not statistically different from the one of the "Uninjured control" group at 12 wpi.

On the other hand, results indicated that the systemic administration of BNN27 did not improve locomotion recovery. This finding agrees with a previous study where local delivery of NGF in rat SCI lesions via genetically modified fibroblasts did not lead to functional improvement at 3 months post-injury evaluated via 3 conditioned locomotion tasks (over a mesh for sensorimotor modalities, over a wide platform with footprint analysis and over an elevated platform for the ability to climb) (56). Nevertheless, our histological data provide evidence that BNN27 affected several processes related to SCI wound healing, discussed in detail below.

Following SCI, the formation of **glial scar** acts as a physical barrier that isolates the injury site to prevent damage spread, yet obstructs axonal elongation through it (120). Previous research approaches mainly

targeted the growth inhibitory components of glial scar. For instance, local administration of ChABC in the injury site of a dorsal column crush model removed chondroitin sulfate chains in CNS lesions and thereby enhanced axonal growth (193). However, the clinical application of ChABC is limited by safety concerns and inefficient delivery (need for repetitive injections of ChABC at the injury site) (196). Another approach to target glial scar is by targeting astrogliosis and thus preventing the activation of astrocytes that synthesize glial scar following SCI. Herein, NSC-seeded grafts were shown (in both studies A and B) to significantly decrease astrogliosis at 12 wpi **(Fig. IV-22,32)**. This finding agrees with previous reports that NSC-seeded scaffold grafts (e.g. PGA or collagen/silk fibroin) can decrease glial scar in hemi- or complete transected SCI models (142,151).

Furthermore, systemic administration of BNN27 significantly decreased astrogliosis at 12 wpi **(Fig. IV-32)**. Several studies have demonstrated the ability of BNN27 to reduce astrogliosis in various animal models of CNS degeneration such as cuprizone-induced demyelination (96), the 5xFAD Alzheimer's disease mouse model (Karali et al. in preparation) and diabetes-induced retinal damage (94). Herein, this study confirmed for the first time the anti-astrogliotic effect of BNN27 in a CNS injury model. This finding also agrees with the report that local delivery of NGF in rat contusive SCI lesions via genetically modified NSCs can reduce astrogliosis (70).

Emerging SCI treatments aim to replace or reduce the **loss of neural tissue** induced by injury. Along this direction, in this thesis, both NSC-seeded CS grafts and BNN27 administration increased neuron density in the injury site at 12 wpi **(Fig. IV-33)**. The ability of NSC-seeded CS grafts to increase neuron density within SCI sites has also been reported previously (118). The ability of BNN27 to significantly increase neuron density in SCI lesions is in agreement with the reported neuroprotective activity of BNN27 in various neuron types (92,93). It also agrees with published reports on the ability of NGF administration to decrease neuron loss after SCI via contusion (67,68). Like previously reported for NGF (45,83), BNN27 effects on neurons following SCI could be mediated either directly (via NGF receptors) or indirectly via effects to other cell types.

Furthermore, the present studies highlight the ability of NSC-seeded CS grafts to enhance important SCI processes, where BNN27 showed no significant effect. Specifically, NSC-seeded CS grafts enhanced **neuronal communication** between the newly formed tissue at the lesion epicenter and the surrounding spared tissue, as they increased **synapse** density in the epicenter **(Fig. IV-35)** and **axonal elongation** caudally to the epicenter **(Fig. IV-24,34)** at 12 wpi, key events to support functional recovery (21). Several studies in complete transected SCI models have shown that implantation of neural stem/progenitor cells (NSPC) into the lesion cavity can lead to extensive axonal regeneration of both host axons into the graft and axons of NSPC-derived neurons caudally to the lesion over long distances (113,169). NSPC grafts have been shown able to organize, become synaptically active and interact with host axons in a dorsal column crush SCI model (195). Interestingly, study B showed that GFP^+ implanted NSC-derived cells were able to cross the astrogliotic boundary and migrate a few hundred micrometers caudally to the lesion, but not much further to create ectopic colonies, indicating that the porous nature of CS could facilitate the integration of implanted NSC with the surrounding tissue.

Another process related to enhanced functional recovery after SCI is **angiogenesis**. Previous studies report that endogenous angiogenesis following SCI is not sufficient to replace lost blood vessels (197,198). Herein, the study showed that NSC-seeded CS grafts increased the number of αSMA^+ vessels within the injury site **(Fig. IV-36)**, in agreement with the reported ability of transplanted embryonic stem cell-derived neural progenitors to enhance angiogenesis in mouse contusive SCI lesions (199,200).

A major motivation of emerging NSC therapies for SCI is to deliver a significant population of neural cell precursors at the lesion in order to complement the limited number of endogenous neural precursor cells. However, previous studies have highlighted low **NSC survival** post-implantation at SCI sites as a major challenge that impedes the long-term efficacy of such NSC-based SCI treatments. For instance, one study reported that just 4.6% of transplanted NSCs survived at 9 wpi (201). Additionally, implanted NSCs had low proliferation rate *in situ* (202). Overall, NSC survival has been shown to depend strongly on the methodology and timepoint of delivery. NSC survival was lower when NSCs were transplanted in the acute phase of injury (1%) compared to the subacute one (6%), whereas fewer NSCs were present in the epicenter (203,204). This deficiency could be caused by inflammatory pathways and early immunoreaction events at the injury site, which are toxic to implanted cells (205,206). Strategies for protecting implanted NSCs from the harsh SCI environment include delivering NSCs inside biomaterials (such as the CS grafts utilized in this study) and providing anti-apoptotic support via therapeutic molecules (such as the MNTs utilized in this study). Indeed, herein robust survival of implanted NSCs at 12 wpi ($7.5 \cdot 10^5$ cells/mm^3) was reported when NSCs were delivered via CS. Importantly, BNN27 administration further protected implanted NSCs, doubling the density of survived implanted NSC-derived cells ($15 \cdot 10^5$ cells/mm^3) **(Fig. IV-38a,b)**.

Another major challenge of NSC-based SCI treatments is that **NSCs differentiate** mostly into glial cells and poorly towards neurons, because of the unfavorable environment of lesion for neuronal differentiation (100,204,206–208). Significant research aims to regulate the fate of implanted NSCs using biomaterials and growth factors that enhance neuronal survival and differentiation (208). Herein, although BNN27 did not affect the differentiation of implanted NSCs, approximately 20% of implanted NSCs had differentiated towards the neuronal fate by 12 wpi **(Fig. IV-38d)**. Additionally, an interesting spatial organization pattern for implanted NSC-derived cells was shown **(Fig. IV-37a,b)**. Implanted NSCs that differentiated into astrocytes became part of the glial scar and were localized at the SCI lesion boundaries. On the other hand, implanted NSCs that differentiated towards neurons were localized within the lesion, replenishing lost neurons. This spatial pattern has also been described by Lien et al. (209). Importantly, it is demonstrated here that implanted NSCs differentiated to various types of neurons **(Fig. IV-37c)**, including GABAergic neurons, dopaminergic neurons and glutamatergic neurons in the presence or absence of BNN27.

The observed BNN27 effects on the density and fate of implanted NSC-derived cells could originate in various mechanisms, including direct BNN27 effects on NSCs, NSC-derived neural cells and intermediate precursors or indirect effects via other cells that participate in SCI wound healing. Regarding BNN27 effects on NSCs, various types of embryonic rodent NSCs have been reported to express both $p75^{NTR}$ and TrkA NGF receptors (125,210). Moreover, there are reports that NGF can increase proliferation in NSCs isolated from embryonic E14 rat brain or adult rat spinal cord (127,128). BNN27 has demonstrated neuroprotective effects on various types of neurons mediated via NGF receptors (92,93). However, our *in vitro* results showed that supplementing EGF/FGF2-free medium with BNN27 did not affect NSC proliferation and differentiation into neurons and astrocytes **(Fig. IV-30)**. Although this finding is in contrast to previous *in vitro* reports and present *in vivo* results, this discrepancy could be explained by the fact that BNN27 neuroprotective effects can also be mediated by indirectly affecting glial cells in the SCI lesion. For instance, the ability of BNN27 to decrease astrogliosis, described above, could facilitate NSC survival and interaction, as well as their newly formed neuronal integration, due to less blockade by the presence of glial scar as barrier as well as the secretion of inhibitory molecules by scar components. Moreover, it has been supported that environmental conditions in cell culture can affect NT expression and signaling. For example, $p75^{NTR}$ expression was increased *in vitro* under cell stress due to changes in serum, temperature or cell density (52).

V. Conclusions

This thesis probes the effects of combinatorial treatments consisting of PCS grafts, NSCs and/or BNN27 in two mouse CNS injury models, the mouse ONC model (first part) and the mouse dorsal column crush SCI model (second part).

While several studies have demonstrated therapeutic effects of MNTs on various mouse models of neurologic diseases, the **first part** of this thesis demonstrates the first evidence on the effects of BNN27, the seminal MNT, in animal models of ONI. More particularly, in the mouse ONC model, BNN27 had significant effects on the survival of RGCs and microglia-mediated inflammation at 2 weeks following ONC **(Fig. IV-7,10)**.

Given that BNN27 neuroprotection was not observed at 10 wpi as well as there was no effect on axonal elongation, more investigation is needed. Firstly, there is need of a new pharmacokinetic study of BNN27 delivered either via eye drops or via CGS grafts with more and shorter timepoints of tissue collection (e.g. approximately 30 min to hours after BNN27 delivery) **(section IV-1.4)**. Secondly, RGC death and axonal elongation could also be measured in more timepoints between 2 and 10 wpi. Further insight about the effects of MNTs on RGC survival and axonal elongation can unravel the mechanisms and timepoints of MNT action leading to a better design of their administration. Regarding axonal elongation, the *ex vivo* assay of various MNTs in adult retina explants should be repeated in order to be statistically correct, since there is a trend of increased axonal elongation by TrkA-specific MNTs **(Fig. IV-17)**. Furthermore, CTB labeling of RGC axons via i.v. injection could be utilized for more precise quantification of regenerated axons. Yet, even if MNT effects are indeed only neuroprotective and not neurogenic, the result is still very important. As Zheng et al. support, enhanced survival does not always lead to enhanced regeneration (21). The observed neuroprotective effects can be utilized to develop novel treatments for ONI, complemented by other therapeutic molecules that can prolong the neuroprotection and enhance the elongation of surviving axons towards their targets.

The first part of this thesis also presents the first administration of MNTs via a biomaterial graft. Delivery of small molecule compounds via implanted grafts promises to provide targeted delivery at injury sites. Indeed, herein, BNN27 delivery via CGS graft around the ONC lesion resulted in higher and more consistent neuroprotection of RGCs compared to eye drop delivery method **(Fig. IV-7)**.

Thus, BNN27 release should be studied more into detail. For instance, fluorescein assay **(section V-1)** could be repeated by using fluorescently labeled BNN27. In addition, different methods of compound entrapment or conjugation inside the CGS graft could be tested, such as non-covalently conjugation on CGS, in order to control BNN27 release rate. Furthermore, since CGS graft that included a FmocFF hydrogel but lacked BNN27 showed some neuroprotective effects as well, more investigation should be performed on collagen and FmocFF effects on neuroprotection via *in vitro* viability assays on primary RGC or other neurons cultured inside CGS and/or in the absence or presence of FmocFF.

The **second part** of the thesis presents novel combinatorial treatments for SCI that are based on porous CS grafts, similar to FDA-approved grafts used clinically for skin and PNS regeneration. This study probes CS effects in CNS injury, as a promising delivery method of cell therapies into the lesion of SCI in order to replace the lost neuronal tissue. Along this direction, NSCs delivered via CS grafts in SCI lesions could get well integrated with the surrounding tissue via the supportive environment provided by CS, contrary to methods of syringe injection of NSC suspension **(section IV-2.1.8)**. This thesis demonstrates that NSC-seeded CS grafts decreased glial scar and enhanced crucial events of wound healing following SCI, such as neuron density, synaptogenesis, axonal elongation and angiogenesis at 12 wpi **(Fig. IV-22,32-36)**. Interestingly, NSC-seeded CS grafts led to a remarkable locomotion recovery starting at 9-10 wpi **(Fig. IV-20,31)**.

Taking it one step further, the same experiment could be designed with the use of iPSCs or somatic cells instead of mouse embryonic NSCs in order to get closer to the clinical translation. The use of iPSC-derived NSCs lacks ethical concerns of embryonic NSCs. Alternatively, somatic cells could be directly reprogrammed into NSCs or neurons before transplantation, avoiding iPSC concerns, such as teratoma formation.

The second part of this thesis also presents the first demonstration of therapeutic effects of MNTs in an animal model of SCI. Systemic administration of BNN27 decreased astrogliosis and neuronal loss following SCI **(Fig. IV-32,33)**. Furthermore, when BNN27 administration was combined with the implantation of NSC-seeded CS grafts, BNN27 significantly increased the density of implanted NSC-derived cells **(Fig. IV-38)**, possibly addressing a major challenge of emerging NSC-based cell therapies. Considering a wider perspective, this thesis suggests that MNTs can contribute to combinatorial treatments for CNS injuries by simultaneously enhancing cell therapies and modulating the loss of neuronal tissue.

Despite the promising findings in two mouse CNS injury models, the mechanisms of BNN27 effects in ONC and SCI were not elucidated in detail in this thesis. More *in vitro* assays are needed in order to elucidate candidate mechanisms, including whether BNN27 acts directly via the NGF receptors of neurons or indirectly via glial cells. MNT contribution in combinatorial treatments could also be further enhanced by optimizing MNT dosing, exploiting novel MNTs designs that target specific NT receptors (178,179) or utilizing targeted methods to control their spatiotemporal delivery within CNS lesions.

In addition, considering the importance of synaptic circuits in functional recovery, another approaches that are not discussed in this thesis but should be taken into consideration in translational studies are the electrical stimulation and rehabilitative training (21). In particular, one of the most important publications of 2022 in the field of SCI applied spatiotemporal epidural electrical stimulation of the lumbar spinal cord during neurorehabilitation and notably led to walking restoration in patients with chronic SCI (211).

Overall, the complexity of CNS injury demands combinatorial treatments with specific design, dose as well as time and frequency of administration. Such treatments also need combination of knowledge and effort from various fields including biology, chemistry, materials science, bioengineering and neurosurgery. The findings of this thesis could hopefully add new tools in regenerative medicine that would be clinically translated to “give light and motion” to humans that need it.

References

1. Salazar, J. J. , Ramírez, A. I. , De Hoz, R. , Salobrar-Garcia, E. , Rojas, P. , Fernández-Albarral, J. A. , López-Cuenca, I. , Blanca Rojas, B. , Triviño, A. , Ramírez JM. Anatomy of the Human Optic Nerve: Structure and Function. Intech [Internet]. 2018; Available from: https://www.intechopen.com/books/advanced-biometric-technologies/liveness-detection-in-biometrics

2. Webvision. Moran Eye Center. Gross Anatomy of the Eye [Internet]. Available from: http://webvision.med.utah.edu/book/part-i-foundations/gross-anatomy-of-the-ey/

3. Gray, H; Williams PBL. Gray's anatomy : the anatomical basis of medicine and surgery. 38th ed. Churchill Livingstone; 1999.

4. Lukowski SW, Lo CY, Sharov AA, Nguyen Q, Fang L, Hung SS, et al. A single-cell transcriptome atlas of the adult human retina. EMBO J. 2019;38(18):1–15.

5. Chapot CA, Euler T, Schubert T. How do horizontal cells 'talk' to cone photoreceptors? Different levels of complexity at the cone–horizontal cell synapse. J Physiol. 2017;595(16):5495–506.

6. Visual System [Internet]. Available from: http://what-when-how.com/neuroscience/visual-system-sensory-system-part-1

7. Kandel ER; Schwartz JH; Jessell TM; Siegelbaum SA; Hudspeth AJ. Principles of neural science. 5th ed. McGraw-Hill Professional Pub; 2012.

8. Silva NA, Sousa N, Reis RL, Salgado AJ. From basics to clinical: A comprehensive review on spinal cord injury. Prog Neurobiol. 2014;114:25–57.

9. Spinal cord [Internet]. Available from: https://www.pharmacy180.com/article/spinal-cord-3554/

10. Mladinic M, Nistri A, Dekanic A. How the discovery of neuronal stem cells have changed neuroscience and perspective for the therapy for central nervous system illnesses. Period Biol. 2015;117(1):185–92.

11. Shechter R, Schwartz M. CNS sterile injury: Just another wound healing? Trends Mol Med [Internet]. 2013;19(3):135–43. Available from: http://dx.doi.org/10.1016/j.molmed.2012.11.007

12. Jacobs WB, Fehlings MG, Grossman RG, Hodge CJ, Liu CY. The molecular basis of neural regeneration. Neurosurgery. 2003;53(4):943–9.

13. Mothe AJ, Tator CH. Advances in stem cell therapy for spinal cord injury. J Clin Invest. 2012;122(11):3824–34.

14. Alizadeh A, Dyck SM, Karimi-Abdolrezaee S. Traumatic spinal cord injury: An overview of pathophysiology, models and acute injury mechanisms. Front Neurol. 2019;10(March).

15. Krucoff MO, Rahimpour S, Slutzky MW, Edgerton VR, Turner DA. Enhancing nervous system recovery through neurobiologics, neural interface training, and neurorehabilitation. Front Neurosci. 2016;10(DEC).

16. Abe N, Nishihara T, Yorozuya T, Tanaka J. Microglia and Macrophages in the Pathological Central and Peripheral Nervous Systems. Cells. 2020;9(9):1–21.

17. Tsujioka H, Yamashita T. Neural circuit repair after central nervous system injury. Int Immunol. 2021;33(6):301–9.

18. Jerry Silver, Martin E. Schwab and PGP. Central Nervous System Regenerative Failure : Cold Spring Harb Perspect Biol. 2015;7:a020602.

19. Schwab JM, Kleinschnitz C. Overcoming trivialization: The neuroimmune response after acute central nervous system injury. J Neuroimmunol. 2019;330(December 2018):28–30.

20. Pekny M, Pekna M. Reactive gliosis in the pathogenesis of CNS diseases. Biochim Biophys Acta - Mol Basis Dis [Internet]. 2016;1862(3):483–91. Available from:

http://dx.doi.org/10.1016/j.bbadis.2015.11.014

21. Zheng B, Tuszynski MH. Regulation of axonal regeneration after mammalian spinal cord injury. Nat Rev Mol Cell Biol. 2023;

22. Cajal R. Degeneration & regeneration of the nervous system. Hafner Publishing Company, New York; 1959.

23. Van Niekerk EA, Tuszynski MH, Lu P, Dulin JN. Molecular and cellular mechanisms of axonal regeneration after spinal cord injury. Mol Cell Proteomics. 2016;15(2):394–408.

24. Nicholls JG, Frs, Adams WB, Eugenin J, Geiser R, Lepre M, et al. Does central nervous system not regenerate after injury? Surv Ophthalmol. 1999;43(6 SUPPL.):8–9.

25. Modrak M, Talukder MAH, Gurgenashvili K, Noble M, Elfar JC. Peripheral nerve injury and myelination: Potential therapeutic strategies. J Neurosci Res. 2020;98(5):780–95.

26. Brosius Lutz A, Barres BA. Contrasting the Glial Response to Axon Injury in the Central and Peripheral Nervous Systems. Dev Cell [Internet]. 2014;28(1):7–17. Available from: http://dx.doi.org/10.1016/j.devcel.2013.12.002

27. Sarkies N. Traumatic optic neuropathy. Eye [Internet]. 2004;18(11):1122–5. Available from: http://www.nature.com/articles/6701571

28. Pirouzmand F. Epidemiological trends of traumatic optic nerve injuries in the largest canadian adult trauma center. J Craniofac Surg. 2012;23(2):516–20.

29. Yu-Wai-Man P. Traumatic optic neuropathy-Clinical features and management issues. Taiwan J Ophthalmol. 2015;5(1):3–8.

30. Levkovitch-Verbin H. Animal models of optic nerve diseases. Eye. 2004;18(11):1066–74.

31. Leinonen H, Tanila H. Vision in laboratory rodents—Tools to measure it and implications for behavioral research. Behav Brain Res. 2018;352:172–82.

32. Bastakis GG, Ktena N, Karagogeos D, Savvaki M. Models and treatments for traumatic optic neuropathy and demyelinating optic neuritis. Dev Neurobiol. 2019;79(8):819–36.

33. Herrera E, Agudo-Barriuso M, Murcia-Belmonte V. Cranial Pair II: The Optic Nerves. Anat Rec. 2019;302(3):428–45.

34. Lima S De, Koriyama Y, Kurimoto T, Oliveira T, Yin Y, Li Y, et al. Correction for de Lima et al., Full-length axon regeneration in the adult mouse optic nerve and partial recovery of simple visual behaviors. Proc Natl Acad Sci [Internet]. 2012;109(33):13465–13465. Available from: http://www.pnas.org/cgi/doi/10.1073/pnas.1211885109

35. Li H-J, Sun Z-L, Yang X-T, Zhu L, Feng D-F. Exploring Optic Nerve Axon Regeneration. Curr Neuropharmacol [Internet]. 2017;15(6):861–73. Available from: http://www.eurekaselect.com/148741/article

36. Barbiellini Amidei C, Salmaso L, Bellio S, Saia M. Epidemiology of traumatic spinal cord injury: a large population-based study. Spinal Cord. 2022;60(9):812–9.

37. Zimmermann R, Vieira Alves Y, Sperling LE, Pranke P. Nanotechnology for the Treatment of Spinal Cord Injury. Tissue Eng - Part B Rev. 2021;27(4):353–65.

38. Sribnick EA, Popovich PG, Hall MW. Central nervous system injury-induced immune suppression. Neurosurg Focus. 2022;52(2):1–8.

39. Hamers FPT, Koopmans GC, Joosten EAJ. CatWalk-assisted gait analysis in the assessment of spinal cord injury. J Neurotrauma. 2006;23(3–4):537–48.

40. Zhang R, Zhang H, Xu L, Ma K, Wallrapp C, Jonas JB. Neuroprotective effect of intravitreal cell-based

glucagon-like peptide-1 production in the optic nerve crush model. Acta Ophthalmol. 2011;89(4):320–6.

41. Nayak K, Misra M. A review on recent drug delivery systems for posterior segment of eye. Biomed Pharmacother [Internet]. 2018;107(February):1564–82. Available from: https://doi.org/10.1016/j.biopha.2018.08.138

42. Subrizi A, del Amo EM, Korzhikov-Vlakh V, Tennikova T, Ruponen M, Urtti A. Design principles of ocular drug delivery systems: importance of drug payload, release rate, and material properties. Drug Discov Today [Internet]. 2019;24(8):1446–57. Available from: https://doi.org/10.1016/j.drudis.2019.02.001

43. Gomes E, Silva N, Salgado A. Combinatorial therapies for spinal cord injury: Strategies to induce regeneration. Neural Regen Res. 2019;14(1):69–71.

44. Kabu S, Gao Y, Kwon BK, Labhasetwar V. Drug delivery, cell-based therapies, and tissue engineering approaches for spinal cord injury. J Control Release [Internet]. 2015;219:141–54. Available from: https://doi.org/10.1016/j.jconrel.2015.08.060

45. Widenfalk J, Lundströmer K, Jubran M, Brené S, Olson L. Neurotrophic factors and receptors in the immature and adult spinal cord after mechanical injury or kainic acid. J Neurosci. 2001;21(10):3457–75.

46. Griffin JM, Bradke F. Therapeutic repair for spinal cord injury: combinatory approaches to address a multifaceted problem. EMBO Mol Med. 2020;12(3):1–29.

47. Srinivas S, Wali AR, Pham MH. Efficacy of riluzole in the treatment of spinal cord injury: A systematic review of the literature. Neurosurg Focus. 2019;46(3):1–18.

48. Barros Ribeiro Da Silva V, Porcionatto M, Toledo Ribas V. The Rise of Molecules Able to Regenerate the Central Nervous System. J Med Chem. 2020;63(2):490–511.

49. Casha S, Zygun D, McGowan MD, Bains I, Yong VW, John Hurlbert R. Results of a phase II placebo-controlled randomized trial of minocycline in acute spinal cord injury. Brain. 2012;135(4):1224–36.

50. Ferraro G, Alabed Y, Fournier A. Molecular Targets to Promote Central Nervous System Regeneration. Curr Neurovasc Res. 2005;1(1):61–75.

51. Anjum A, Yazid MD, Daud MF, Idris J, Hwei Ng AM, Naicker AS, et al. Spinal cord injury: Pathophysiology, multimolecular interactions, and underlying recovery mechanisms. Int J Mol Sci. 2020;21(20):1–35.

52. Chao M V. Neurotrophins and their receptors: A convergence point for many signalling pathways. Nat Rev Neurosci. 2003;4(4):299–309.

53. Bothwell M. Recent advances in understanding neurotrophin signaling [version 1; referees: 2 approved]. F1000Research. 2016;5(0):1–9.

54. Reichardt LF. Neurotrophin-regulated signalling pathways. Philos Trans R Soc B Biol Sci. 2006;361(1473):1545–64.

55. Josephy-Hernandez S, Jmaeff S, Pirvulescu I, Aboulkassim T, Saragovi HU. Neurotrophin receptor agonists and antagonists as therapeutic agents: An evolving paradigm. Neurobiol Dis. 2017;97:139–55.

56. Tuszynski MH, Murai K, Blesch A, Grill R, Miller I. Functional characterization of NGF-secreting cell grafts to the acutely injured spinal cord. Cell Transplant. 1997;6(3):361–8.

57. Grill RJ, Blesch A, Tuszynski MH. Robust growth of chronically injured spinal cord axons induced by grafts of genetically modified NGF-secreting cells. Exp Neurol. 1997;148(2):444–52.

58. Houlton J, Abumaria N, Hinkley SFR, Clarkson AN. Therapeutic potential of neurotrophins for repair after brain injury: A helping hand from biomaterials. Front Genet. 2019;10(JUL).

59. Meeker RB, Williams KS. The p75 neurotrophin receptor: At the crossroad of neural repair and death. Neural Regen Res. 2015;10(5):721–5.

60. Yamashita N. Retrograde signaling via axonal transport through signaling endosomes. J Pharmacol Sci [Internet]. 2019;141(2):91–6. Available from: https://doi.org/10.1016/j.jphs.2019.10.001

61. Zweifel LS, Kuruvilla R, Ginty DD. Functions and mechanisms of retrograde neurotrophin signalling. Nat Rev Neurosci. 2005;6(8):615–25.

62. Tasdemir-Yilmaz OE, Segal RA. There and back again: Coordinated transcription, translation and transport in axonal survival and regeneration. Curr Opin Neurobiol. 2016;39:62–8.

63. Miller FD, Kaplan DR. Neurotrophin signalling pathways regulating neuronal apoptosis. Cell Mol Life Sci. 2001;58(8):1045–53.

64. Krenz NR, Weaver LC. Nerve growth factor in glia and inflammatory cells of the injured rat spinal cord. J Neurochem. 2000;74(2):730–9.

65. Davis-López De Carrizosa MA, Morado-Díaz CJ, Morcuende S, De La Cruz RR, Pastor ÁM. Nerve growth factor regulates the firing patterns and synaptic composition of motoneurons. J Neurosci. 2010;30(24):8308–19.

66. Aloe L, Bianchi P, De Bellis A, Soligo M, Rocco ML. Intranasal nerve growth factor bypasses the bloodbrain barrier and affects spinal cord neurons in spinal cord injury. Neural Regen Res. 2014;9(10):1025–30.

67. Zhang H, Wu F, Kong X, Yang J, Chen H, Deng L, et al. Nerve growth factor improves functional recovery by inhibiting endoplasmic reticulum stress-induced neuronal apoptosis in rats with spinal cord injury. J Transl Med. 2014;12(1):1–15.

68. Song Z, Wang Z, Shen J, Xu S, Hu Z. Nerve growth factor delivery by ultrasound-mediated nanobubble destruction as a treatment for acute spinal cord injury in rats. Int J Nanomedicine. 2017;12:1717–29.

69. Wu Q, Xiang Z, Ying Y, Huang Z, Tu Y, Chen M, et al. Nerve growth factor (NGF) with hypoxia response elements loaded by adeno-associated virus (AAV) combined with neural stem cells improve the spinal cord injury recovery. Cell Death Discov. 2021;7(1):1–9.

70. Wang L, Gu S, Gan J, Tian Y, Zhang F, Zhao H, et al. Neural Stem Cells Overexpressing Nerve Growth Factor Improve Functional Recovery in Rats Following Spinal Cord Injury via Modulating Microenvironment and Enhancing Endogenous Neurogenesis. Front Cell Neurosci. 2021;15:1–15.

71. Parmhans N, Sajgo S, Niu J, Luo W, Badea TC. Characterization of retinal ganglion cell, horizontal cell, and amacrine cell types expressing the neurotrophic receptor tyrosine kinase Ret. J Comp Neurol. 2018;526(4):742–66.

72. Mysona BA, Zhao J, Bollinger KE. Role of BDNF/TrkB pathway in the visual system: therapeutic implications for glaucoma. Expert Rev Ophthalmol [Internet]. 2017;12(1):69–81. Available from: http://dx.doi.org/10.1080/17469899.2017.1259566

73. Johnson EC, Guo Y, Cepurna WO, Morrison JC. Neurotrophin roles in retinal ganglion cell survival: Lessons from rat glaucoma models. Exp Eye Res. 2009;88(4):808–15.

74. Garcia TB, Hollborn M, Bringmann A. Expression and signaling of NGF in the healthy and injured retina. Cytokine Growth Factor Rev. 2017;34:43–57.

75. Candeo P, Carmignoto G, Maffei L, Canella R, Comelli C. NGF effects on the survival of rat retinal ganglion cells following optic nerve section. Pharmacol Res Commun. 1988;20(SUPPL. 2):65.

76. Mesentier-Louro LA, Rosso P, Carito V, Mendez-Otero R, Santiago MF, Rama P, et al. Nerve Growth Factor Role on Retinal Ganglion Cell Survival and Axon Regrowth: Effects of Ocular Administration in Experimental Model of Optic Nerve Injury. Mol Neurobiol. 2019;56(2):1056–69.

77. Guo L, Davis BM, Ravindran N, Galvao J, Kapoor N, Haamedi N, et al. Topical recombinant human Nerve growth factor (rh-NGF) is neuroprotective to retinal ganglion cells by targeting secondary degeneration. Sci Rep [Internet]. 2020;10(1):3375. Available from: http://dx.doi.org/10.1038/s41598-020-60427-2

78. Lebrun-Julien F, Bertrand MJ, De Backer O, Stellwagen D, Morales CR, Di Polo A, et al. ProNGF induces TNF -dependent death of retinal ganglion cells through a p75NTR non-cell-autonomous signaling pathway. Proc Natl Acad Sci [Internet]. 2010;107(8):3817–22. Available from: http://www.pnas.org/cgi/doi/10.1073/pnas.0909276107

79. Harada C, Azuchi Y, Noro T, Guo X, Kimura A, Namekata K, et al. TrkB Signaling in Retinal Glia Stimulates Neuroprotection after Optic Nerve Injury. Am J Pathol [Internet]. 2015;185(12):3238–47. Available from: http://dx.doi.org/10.1016/j.ajpath.2015.08.005

80. Keefe KM, Sheikh IS, Smith GM. Targeting neurotrophins to specific populations of neurons: NGF, BDNF, and NT-3 and their relevance for treatment of spinal cord injury. Int J Mol Sci. 2017;18(3):1–17.

81. Faustino C, Rijo P, Reis CP. Nanotechnological strategies for nerve growth factor delivery: Therapeutic implications in Alzheimer's disease. Pharmacol Res [Internet]. 2017;120:68–87. Available from: http://dx.doi.org/10.1016/j.phrs.2017.03.020

82. Tuszynski, Mark H., Peterson, Daniel A., Jasodhara, Ray, Baird, Andriew, Nakahara, Yasushi, and Gage FH. Fibroblasts genetically modified to produce Nerve Growth Factor Induce Robust Neuritic Ingrowth after Grafting to the Spinal Cord. Exp Neurol. 1994;1–14.

83. Tuszynski MH, Gabriel K, Gage FH, Suhr S, Meyer S, Rosetti A. Nerve growth factor delivery by gene transfer induces differential outgrowth of sensory, motor, and noradrenergic neurites after adult spinal cord injury. Exp Neurol. 1996;137(1):157–73.

84. Feng S qing, Kong X hong, Liu Y, Ban D xiang, Ning G zhi, Chen J tong, et al. Regeneration of spinal cord with cell and gene therapy. Orthop Surg. 2009;1(2):153–63.

85. Gravanis A, Pediaditakis I, Charalampopoulos I. Synthetic microneurotrophins in therapeutics of neurodegeneration. Oncotarget. 2017;8(6):9005–6.

86. Charalampopoulos I, Remboutsika E, Margioris AN, Gravanis A. Neurosteroids as modulators of neurogenesis and neuronal survival. Trends Endocrinol Metab. 2008;19(8):300–7.

87. Kokona D, Charalampopoulos I, Pediaditakis I, Gravanis A, Thermos K. The neurosteroid dehydroepiandrosterone (DHEA) protects the retina from AMPA-induced excitotoxicity: NGF TrkA receptor involvement. Neuropharmacology [Internet]. 2012;62(5–6):2106–17. Available from: http://dx.doi.org/10.1016/j.neuropharm.2012.01.006

88. Alexaki VI, Fodelianaki G, Neuwirth A, Mund C, Kourgiantaki A, Ieronimaki E, et al. DHEA inhibits acute microglia-mediated inflammation through activation of the TrkA-Akt1/2-CREB-Jmjd3 pathway. Mol Psychiatry [Internet]. 2018;23(6):1410–20. Available from: http://dx.doi.org/10.1038/mp.2017.167

89. Calogeropoulou T, Avlonitis N, Minas V, Alexi X, Pantzou A, Charalampopoulos I, et al. Novel dehydroepiandrosterone derivatives with antiapoptotic, neuroprotective activity. J Med Chem. 2009;52(21):6569–87.

90. Bennett JP, O'Brien LC, Brohawn DG. Pharmacological properties of microneurotrophin drugs developed for treatment of amyotrophic lateral sclerosis. Biochem Pharmacol [Internet]. 2016;117:68–77. Available from: http://dx.doi.org/10.1016/j.bcp.2016.08.001

91. Tsika C, Tzatzarakis MN, Antimisiaris SG, Tsoka P, Efstathopoulos P, Charalampopoulos I, et al.

Quantification of BNN27, a novel neuroprotective 17-spiroepoxy dehydroepiandrosterone derivative in the blood and retina of rodents, after single intraperitoneal administration. Pharmacol Res Perspect. 2021;9(2):1–8.

92. Pediaditakis I, Kourgiantaki A, Prousis KC, Potamitis C, Xanthopoulos KP, Zervou M, et al. BNN27, a 17-spiroepoxy steroid derivative, interacts with and activates p75 neurotrophin receptor, rescuing cerebellar granule neurons from apoptosis. Front Pharmacol. 2016;7(DEC):1–14.

93. Pediaditakis I, Efstathopoulos P, Prousis KC, Zervou M, Arévalo JC, Alexaki VI, et al. Selective and differential interactions of BNN27, a novel C17-spiroepoxy steroid derivative, with TrkA receptors, regulating neuronal survival and differentiation. Neuropharmacology. 2016;111:266–82.

94. Ibán-Arias R, Lisa S, Mastrodimou N, Kokona D, Koulakis E, Iordanidou P, et al. The synthetic microneurotrophin BNN27 affects retinal function in rats with streptozotocin-induced diabetes. Diabetes. 2018;67(2):321–33.

95. Ibán-Arias R, Lisa S, Poulaki S, Mastrodimou N, Charalampopoulos I, Gravanis A, et al. Effect of topical administration of the microneurotrophin BNN27 in the diabetic rat retina. Graefe's Arch Clin Exp Ophthalmol. 2019;257(11):2429–36.

96. Bonetto G, Charalampopoulos I, Gravanis A, Karagogeos D. The novel synthetic microneurotrophin BNN27 protects mature oligodendrocytes against cuprizone-induced death, through the NGF receptor TrkA. Glia. 2017;65(8):1376–94.

97. Poulaki S, Rassouli O, Liapakis G, Gravanis A, Venihaki M. Analgesic and anti-inflammatory effects of the synthetic neurosteroid analogue bnn27 during cfa-induced hyperalgesia. Biomedicines. 2021;9(9):1–21.

98. Assinck P, Duncan GJ, Hilton BJ, Plemel JR, Tetzlaff W. Cell transplantation therapy for spinal cord injury. Nat Neurosci. 2017;20(5):637–47.

99. Mothe AJ, Tator CH, Mothe AJ, Tator CH. Advances in stem cell therapy for spinal cord injury Find the latest version : Science in medicine Advances in stem cell therapy for spinal cord injury. Thew J Clin Investig. 2012;122(11):3824–34.

100. Zhu Y, Uezono N, Yasui T, Nakashima K. Neural stem cell therapy aiming at better functional recovery after spinal cord injury. Dev Dyn. 2018;247(1):75–84.

101. Mukhamedshina YO, Akhmetzyanova ER, Kostennikov AA, Zakirova EY, Galieva LR, Garanina EE, et al. Adipose-derived mesenchymal stem cell application combined with fibrin matrix promotes structural and functional recovery following spinal cord injury in rats. Front Pharmacol. 2018;9(APR):1–13.

102. de Araújo LT, Macêdo CT, Damasceno PKF, Das Neves ÍGC, de Lima CS, Santos GC, et al. Clinical Trials Using Mesenchymal Stem Cells for Spinal Cord Injury: Challenges in Generating Evidence. Cells. 2022;11(6).

103. Katoh H, Yokota K, Fehlings MG. Regeneration of spinal cord connectivity through stem cell transplantation and biomaterial scaffolds. Front Cell Neurosci. 2019;13(January 2020).

104. Mead B, Berry M, Logan A, Scott RAH, Leadbeater W, Scheven BA. Stem cell treatment of degenerative eye disease. Stem Cell Res [Internet]. 2015;14(3):243–57. Available from: http://dx.doi.org/10.1016/j.scr.2015.02.003

105. Mead B, Logan A, Berry M, Leadbeater W, Scheven BA. Intravitreally transplanted dental pulp stem cells promote neuroprotection and axon regeneration of retinal ganglion cells after optic nerve injury. Investig Ophthalmol Vis Sci. 2013;54(12):7544–56.

106. Mesentier-Louro LA, Teixeira-Pinheiro LC, Gubert F, Vasques JF, Silva-Junior AJ, Chimeli-Ormonde L, et al. Long-term neuronal survival, regeneration, and transient target reconnection after optic nerve crush and mesenchymal stem cell transplantation. Stem Cell Res Ther. 2019;10(1):1–12.

107. Gao H, Zhang HL, Shou J, Chen L, Shen Y, Tang Q, et al. Towards retinal ganglion cell regeneration. Regen Med [Internet]. 2012;7(6):865–75. Available from: http://www.ncbi.nlm.nih.gov/pubmed/23164085

108. Boia R, Ruzafa N, Aires ID, Pereiro X, Ambrósio AF, Vecino E, et al. Neuroprotective strategies for retinal ganglion cell degeneration: Current status and challenges ahead. Int J Mol Sci. 2020;21(7):1–39.

109. Lindvall O, Kokaia Z. Stem cells in human neurodegenerative disorders - Time for clinical translation? J Clin Invest. 2010;120(1):29–40.

110. Tang Y, Yu P, Cheng L. Current progress in the derivation & therapeutic application of neural stem cells. Cell Death Dis. 2017;8(10).

111. Meletis K, Barnabé-Heider F, Carlén M, Evergren E, Tomilin N, Shupliakov O, et al. Spinal cord injury reveals multilineage differentiation of ependymal cells. PLoS Biol. 2008;6(7):1494–507.

112. Lu P, Wang Y, Graham L, McHale K, Gao M, Wu D, et al. Long-distance growth and connectivity of neural stem cells after severe spinal cord injury. Cell. 2012;150(6):1264–73.

113. Kadoya K, Lu P, Nguyen K, Lee-Kubli C, Kumamaru H, Yao L, et al. Spinal cord reconstitution with homologous neural grafts enables robust corticospinal regeneration. Nat Med [Internet]. 2016;22(5):479–87. Available from: http://dx.doi.org/10.1038/nm.4066

114. Lu P, Woodruff G, Wang Y, Graham L, Hunt M, Wu D, et al. Long-Distance Axonal Growth from Human Induced Pluripotent Stem Cells after Spinal Cord Injury. Neuron. 2014;83(4):789–96.

115. Chan HH, Wathen CA, Ni M, Zhuo S. Stem cell therapies for ischemic stroke: current animal models, clinical trials and biomaterials. RSC Adv [Internet]. 2017;7(30):18668–80. Available from: http://dx.doi.org/10.1039/C7RA00336F

116. Rosenzweig ES, Brock JH, Lu P, Kumamaru H, Salegio EA, Kadoya K, et al. Restorative effects of human neural stem cell grafts on the primate spinal cord. Nat Med. 2018;24(4):484–90.

117. Lu P, Ceto S, Wang Y, Graham L, Wu D, Kumamaru H, et al. Prolonged human neural stem cell maturation supports recovery in injured rodent CNS. J Clin Invest. 2017;127(9):3287–99.

118. Liu S, Fan C, Xie Y, Wang L, Cui Y, Wang B. Collagen scaffold loaded allogeneic neural stem cells promoted locomotion recovery of spinal cord injury mainly through secreting neurotrophic factors. Mater Des [Internet]. 2022;219:110804. Available from: https://doi.org/10.1016/j.matdes.2022.110804

119. Curtis E, Martin JR, Gabel B, Sidhu N, Rzesiewicz TK, Mandeville R, et al. A First-in-Human, Phase I Study of Neural Stem Cell Transplantation for Chronic Spinal Cord Injury. Cell Stem Cell [Internet]. 2018;22(6):941-950.e6. Available from: https://doi.org/10.1016/j.stem.2018.05.014

120. Silva NA, Sousa N, Reis RL, Salgado AJ. From basics to clinical: A comprehensive review on spinal cord injury. Prog Neurobiol. 2014;114:25–57.

121. Cao Q, Benton RL, Whittemore SR. Stem cell repair of central nervous system injury. J Neurosci Res. 2002;68(5):501–10.

122. Zhang C, Egiazaryan KA, Ratyev AP, Feniksov VM, Wu H, Chekhonin VP. Progress in the study of stem cell transplantation for the repair of spinal cord injury. Russ Open Med J. 2017;6(3):1–5.

123. Cao Q, Benton RL, Whittemore SR. Stem cell repair of central nervous system injury. J Neurosci Res. 2002;68(5):501–10.

124. Karimi-Abdolrezaee S, Eftekharpour E, Wang J, Schut D, Fehlings MG. Synergistic effects of transplanted adult neural stem/progenitor cells, chondroitinase, and growth factors promote functional repair and plasticity of the chronically injured spinal cord. J Neurosci. 2010;30(5):1657–76.

125. Lachyankar MB, Condon PJ, Quesenberry PJ, Litofsky NS, Recht LD, Ross AH. Embryonic precursor cells that express Trk receptors: Induction of different cell fates by NGF, BDNF, NT-3, and CNTF. Exp Neurol. 1997;144(2):350–60.

126. Kumar V, Gupta AK, Shukla RK, Tripathi VK, Jahan S, Pandey A, et al. Molecular mechanism of switching of TrkA/p75 NTR signaling in monocrotophos induced neurotoxicity. Sci Rep [Internet]. 2015;5:1–17. Available from: http://dx.doi.org/10.1038/srep14038

127. Oliveira SLB, Trujillo CA, Negraes PD, Ulrich H. Effects of ATP and NGF on Proliferation and Migration of Neural Precursor Cells. Neurochem Res. 2015;40(9):1849–57.

128. Han Y, Kim KT. Neural growth factor stimulates proliferation of spinal cord derived-neural precursor/stem cells. J Korean Neurosurg Soc. 2016;59(5):437–41.

129. Ziemba AM, Gilbert RJ. Biomaterials for local, controlled drug delivery to the injured spinal cord. Front Pharmacol. 2017;8(MAY):1–20.

130. Crapo PM, Tottey S, Slivka PF, Badylak SF. Effects of biologic scaffolds on human stem cells and implications for CNS tissue engineering. Tissue Eng - Part A. 2014;20(1–2):313–23.

131. Geissler S, Sabin A, Besser R, Gooden O, Shirk B, Nguyen Q, et al. Biomimetic hydrogels direct spinal progenitor cell differentiation and promote functional recovery after spinal cord injury. J Neural Eng. 2018;15(2):025004.

132. Elliott Donaghue I, Tam R, Sefton M V., Shoichet MS. Cell and biomolecule delivery for tissue repair and regeneration in the central nervous system. J Control Release [Internet]. 2014;190:219–27. Available from: http://dx.doi.org/10.1016/j.jconrel.2014.05.040

133. Ellis-Behnke RG, Liang YX, You SW, Tay DKC, Zhang S, So KF, et al. Nano neuro knitting: Peptide nanofiber scaffold for brain repair and axon regeneration with functional return of vision. Proc Natl Acad Sci U S A. 2006;103(13):5054–9.

134. Gao Y, Yang Z, Li X. Regeneration strategies after the adult mammalian central nervous system injury-biomaterials. Regen Biomater. 2016;3(2):115–22.

135. Kaji H, Nagai N, Nishizawa M, Abe T. Drug delivery devices for retinal diseases. Adv Drug Deliv Rev [Internet]. 2018;128:148–57. Available from: https://doi.org/10.1016/j.addr.2017.07.002

136. Oudega M, Hao P, Shang J, Haggerty AE, Wang Z, Sun J, et al. Validation study of neurotrophin-3-releasing chitosan facilitation of neural tissue generation in the severely injured adult rat spinal cord. Exp Neurol [Internet]. 2019;312(December):51–62. Available from: https://doi.org/10.1016/j.expneurol.2018.11.003

137. Xu G, Nie DY, Wang WZ, Zhang PH, Shen J, Ang BT, et al. Optic nerve regeneration in polyglycolic acid-chitosan conduits coated with recombinant L1-Fc. Neuroreport. 2004;15(14):2167–72.

138. Giannaccini M, Usai A, Chiellini F, Guadagni V, Andreazzoli M, Ori M, et al. Neurotrophin-conjugated nanoparticles prevent retina damage induced by oxidative stress. Cell Mol Life Sci. 2018;75(7):1255–67.

139. Tam RY, Fuehrmann T, Mitrousis N, Shoichet MS. Regenerative therapies for central nervous system diseases: A biomaterials approach. Neuropsychopharmacology [Internet]. 2014;39(1):169–88. Available from: http://dx.doi.org/10.1038/npp.2013.237

140. Ren T, van der Merwe Y, Steketee MB. Developing Extracellular Matrix Technology to Treat Retinal or Optic Nerve Injury. eNeuro [Internet]. 2015;2(5). Available from: http://eneuro.sfn.org/cgi/doi/10.1523/ENEURO.0077-15.2015

141. Teixeira AI, Duckworth JK, Hermanson O. Getting the right stuff: Controlling neural stem cell state and fate in vivo and in vitro with biomaterials. Cell Res. 2007;17(1):56–61.

142. Shin JE, Jung K, Kim M, Hwang K, Lee H, Kim IS, et al. Brain and spinal cord injury repair by implantation of human neural progenitor cells seeded onto polymer scaffolds. Exp Mol Med [Internet]. 2018;50(4). Available from: http://dx.doi.org/10.1038/s12276-018-0054-9

143. Bai YR, Lai BQ, Han WT, Sun JH, Li G, DIng Y, et al. Decellularized optic nerve functional scaffold transplant facilitates directional axon regeneration and remyelination in the injured white matter of the rat spinal cord. Neural Regen Res. 2021;16(11):2276–83.

144. Negishi H, Dezawa M, Oshitari T, Adachi-Usami E. Optic nerve regeneration within artificial Schwann cell graft in the adult rat. Brain Res Bull. 2001;55(3):409–19.

145. Mneimneh AT, Mehanna MM. Collagen-based scaffolds: An auspicious tool to support repair, recovery, and regeneration post spinal cord injury. Int J Pharm. 2021;601(February).

146. Yannas I V., Tzeranis DS, Harley BA, So PTC. Biologically active collagen-based scaffolds: Advances in processing and characterization. Philos Trans R Soc A Math Phys Eng Sci. 2010;368(1917):2123–39.

147. Soller EC, Tzeranis DS, Miu K, So PTC, Yannas I V. Common features of optimal collagen scaffolds that disrupt wound contraction and enhance regeneration both in peripheral nerves and in skin. Biomaterials [Internet]. 2012;33(19):4783–91. Available from: http://dx.doi.org/10.1016/j.biomaterials.2012.03.068

148. Cholas RH, Hsu HP, Spector M. The reparative response to cross-linked collagen-based scaffolds in a rat spinal cord gap model. Biomaterials [Internet]. 2012;33(7):2050–9. Available from: http://dx.doi.org/10.1016/j.biomaterials.2011.11.028

149. Yeh JZ, Wang DH, Cherng JH, Wang YW, Fan GY, Liou NH, et al. A collagen-based scaffold for promoting neural plasticity in a rat model of spinal cord injury. Polymers (Basel). 2020;12(10):1–12.

150. Zhong Y, Bellamkonda R V. Biomaterials for the central nervous system. J R Soc Interface. 2008;5(26):957–75.

151. Jiang JP, Liu XY, Zhao F, Zhu X, Li XY, Niu XG, et al. Three-dimensional bioprinting collagen/silk fibroin scaffold combined with neural stem cells promotes nerve regeneration after spinal cord injury. Neural Regen Res. 2020;15(5):959–68.

152. Deng WS, Ma K, Liang B, Liu XY, Xu HY, Zhang J, et al. Collagen scaffold combined with human umbilical cord-mesenchymal stem cells transplantation for acute complete spinal cord injury. Neural Regen Res. 2020;15(9):1686–700.

153. Madl CM, Heilshorn SC, Blau HM. Bioengineering strategies to accelerate stem cell therapeutics. Nature. 2018;557(7705):335–42.

154. The Jackson Laboratory. C57BL/6J. [Internet]. [cited 2022 Nov 18]. Available from: https://www.jax.org/strain/000664

155. Mouse Genome Informatics. 129X1/SvJ. [Internet]. [cited 2022 Nov 18]. Available from: http://www.informatics.jax.org/strain/MGI:3044210

156. The Jackson Laboratory. B6.C-Tg(CMV-cre)1Cgn/Je. [Internet]. [cited 2022 Nov 18]. Available from: https://www.jax.org/strain/006054

157. O'Brien F, Harley BA, Yannas I V., Gibson L. Influence of freezing rate on pore structure in freeze-dried collagen-GAG scaffolds. Biomaterials. 2004;25(6):1077–86.

158. Azari H, Sharififar S, Rahman M, Ansari S, Reynolds BA. Establishing embryonic mouse neural stem cell culture using the neurosphere assay. J Vis Exp. 2010;(47):1–4.

159. Sun D, Zhou X, Yu HL, He XX, Guo WX, Xiong WC, et al. Regulation of neural stem cell proliferation and differentiation by Kinesin family member 2a. PLoS One. 2017;12(6):1–17.

160. Schaeffer J, Delpech C, Albert F, Belin S. Adult Mouse Retina Explants : From ex vivo to in vivo Model of Central Nervous System Injuries. 2020;13(November):1–19.

161. Tehrani S, Delf RK, Cepurna WO, Davis L, Johnson EC, Morrison JC. In Vivo Small Molecule Delivery to the Optic Nerve in a Rodent Model. Sci Rep [Internet]. 2018;8(1):1–9. Available from: http://dx.doi.org/10.1038/s41598-018-22737-4

162. de Lima S, Habboub G, Benowitz LI. Combinatorial Therapy Stimulates Long-Distance Regeneration, Target Reinnervation, and Partial Recovery of Vision After Optic Nerve Injury in Mice. Int Rev Neurobiol. 2012;106:153–72.

163. Savvaki M, Kafetzis G, Kaplanis SI, Ktena N, Theodorakis K, Karagogeos D. Neuronal, but not glial, Contactin 2 negatively regulates axon regeneration in the injured adult optic nerve. Eur J Neurosci. 2021;53(6):1705–21.

164. Jiang D, Feng H, Zhang Z, Yan B, Chen L, Ma C, et al. Mesenchymal stem cells protect retinal ganglion cells from degeneration via mitochondrial donation. bioRxiv. 2018;

165. Harrison M, O'Brien A, Adams L, Cowin G, Ruitenberg MJ, Sengul G, et al. Vertebral landmarks for the identification of spinal cord segments in the mouse. Neuroimage. 2013;68:22–9.

166. Farr TD, Liu L, Colwell KL, Whishaw IQ, Metz GA. Bilateral alteration in stepping pattern after unilateral motor cortex injury: A new test strategy for analysis of skilled limb movements in neurological mouse models. J Neurosci Methods. 2006;153(1):104–13.

167. Shiotsuki H, Yoshimi K, Shimo Y, Funayama M, Takamatsu Y, Ikeda K, et al. A rotarod test for evaluation of motor skill learning. J Neurosci Methods [Internet]. 2010;189(2):180–5. Available from: http://dx.doi.org/10.1016/j.jneumeth.2010.03.026

168. Bennett JP, O'Brien LC, Brohawn DG. Pharmacological properties of microneurotrophin drugs developed for treatment of amyotrophic lateral sclerosis. Biochem Pharmacol. 2016;117:68–77.

169. Lu P, Wang Y, Graham L, McHale K, Gao M, Wu D, et al. Long-distance growth and connectivity of neural stem cells after severe spinal cord injury. Cell. 2012;150(6):1264–73.

170. Kadoya K, Lu P, Nguyen K, Lee-kubli C, Kumamaru H, Knackert J, et al. Spinal cord reconstitution with homologous neural grafts enables. Nat Med. 2016;22(5):479–87.

171. Steward O, Sharp KG, Yee KM, Hatch MN, Bonner JF. Characterization of ectopic colonies that form in widespread areas of the nervous system with neural stem cell transplants into the site of a severe spinal cord injury. J Neurosci. 2014;34(42):14013–21.

172. Lu P, Gomes-Leal W, Anil S, Dobkins G, Huie JR, Ferguson AR, et al. Origins of Neural Progenitor Cell-Derived Axons Projecting Caudally after Spinal Cord Injury. Stem Cell Reports [Internet]. 2019;13(1):105–14. Available from: https://doi.org/10.1016/j.stemcr.2019.05.011

173. Rodrigues G, Lutz D, Shen J, Yuan X, Shen H, Cunningham J, et al. Topical Drug Delivery to the Posterior Segment of the Eye: Addressing the Challenge of Preclinical to Clinical Translation. Pharm Res. 2018;35:245.

174. Li L, Deng F, Qiu H, Li Y, Gong Z, Wang L, et al. An adherent drug depot for retinal ganglion cell protection and regeneration in rat traumatic optic neuropathy models. RSC Adv. 2021;11(37):22761–72.

175. Ryan K, Beirne J, Redmond G, Kilpatrick JI, Guyonnet J, Buchete NV, et al. Nanoscale Piezoelectric Properties of Self-Assembled Fmoc-FF Peptide Fibrous Networks. ACS Appl Mater Interfaces. 2015;7(23):12702–7.

176. Shen S, Wiemelt AP, McMorris FA, Barres BA. Retinal ganglion cells lose trophic responsiveness after axotomy. Neuron. 1999;23(2):285–95.

177. Bai Y, Dergham P, Nedev H, Xu J, Galan A, Rivera JC, et al. Chronic and acute models of retinal neurodegeneration TrkA activity are neuroprotective whereas p75NTR activity is neurotoxic through a paracrine mechanism. J Biol Chem. 2010;285(50):39392–400.

178. Rogdakis T, Charou D, Latorrata A, Papadimitriou E, Tsengenes A, Athanasiou C, et al. Development and Biological Characterization of a Novel Selective TrkA Agonist with Neuroprotective Properties against Amyloid Toxicity. Biomedicines. 2022;10(3).

179. Yilmaz C, Rogdakis T, Latorrata A, Thanou E, Karadima E, Papadimitriou E, et al. ENT-A010, a Novel Steroid Derivative, Displays Neuroprotective Functions and Modulates Microglial Responses. Biomolecules. 2022;12(3).

180. Jünemann AGM, Rejdak R, Huchzermeyer C, Maciejewski R, Grieb P, Kruse FE, et al. Elevated vitreous body glial fibrillary acidic protein in retinal diseases. Graefe's Arch Clin Exp Ophthalmol [Internet]. 2015;253(12):2181–6. Available from: http://dx.doi.org/10.1007/s00417-015-3127-7

181. Yoo HS, Shanmugalingam U, Smith PD. Harnessing astrocytes and müller glial cells in the retina for survival and regeneration of retinal ganglion cells. Cells. 2021;10(6).

182. Minnone G, De Benedetti F, Bracci-Laudiero L. NGF and its receptors in the regulation of inflammatory response. Int J Mol Sci. 2017;18(5).

183. Knoferle J, Koch JC, Ostendorf T, Michel U, Planchamp V, Vutova P, et al. Mechanisms of acute axonal degeneration in the optic nerve in vivo. Proc Natl Acad Sci [Internet]. 2010;107(13):6064–9. Available from: http://www.pnas.org/cgi/doi/10.1073/pnas.0909794107

184. Benowitz LI, He Z, Goldberg JL. Reaching the brain: Advances in optic nerve regeneration. Exp Neurol [Internet]. 2017;287:365–73. Available from: http://dx.doi.org/10.1016/j.expneurol.2015.12.015

185. Yin Y, Cui Q, Gilbert HY, Yang Y, Yang Z, Berlinicke C, et al. Oncomodulin links inflammation to optic nerve regeneration. Proc Natl Acad Sci U S A. 2009;106(46):19587–92.

186. De Lima S, Koriyama Y, Kurimoto T, Oliveira JT, Yin Y, Li Y, et al. Erratum: Full-length axon regeneration in the adult mouse optic nerve and partial recovery of simple visual behaviors (Proceedings of the National Academy of Sciences of the United States of America (2012) 109, 23, (9149-9154) doi:10.1073/pnas.1119449109). Proc Natl Acad Sci U S A. 2012;109(33):13465.

187. Lim JHA, Stafford BK, Nguyen PL, Lien B V., Wang C, Zukor K, et al. Neural activity promotes long-distance, target-specific regeneration of adult retinal axons. Nat Neurosci. 2016;19(8):1073–84.

188. Pajoohesh-Ganji A, Miller RH. Targeted Oligodendrocyte Apoptosis in Optic Nerve Leads to Persistent Demyelination. Neurochem Res [Internet]. 2019;0(0):0. Available from: http://dx.doi.org/10.1007/s11064-019-02754-z

189. Mendonça HR, Villas Boas COG, Heringer L dos S, Oliveira JT, Martinez AMB. Myelination of regenerating optic nerve axons occurs in conjunction with an increase of the oligodendrocyte precursor cell population in the adult mice. Brain Res Bull [Internet]. 2021;166(July 2020):150–60. Available from: https://doi.org/10.1016/j.brainresbull.2020.11.012

190. Attwell CL, van Zwieten M, Verhaagen J, Mason MRJ. The Dorsal Column Lesion Model of Spinal Cord Injury and Its Use in Deciphering the Neuron-Intrinsic Injury Response. Dev Neurobiol. 2018;78(10):926–51.

191. Vogelaar C, Estrada V. Experimental Spinal Cord Injury Models in Rodents: Anatomical Correlations and Assessment of Motor Recovery. Intech [Internet]. 2016;225–40. Available from: https://www.intechopen.com/books/advanced-biometric-technologies/liveness-detection-in-biometrics

192. Bradbury EJ, Khemani S, King VR, Priestley J V., McMahon SB. NT-3 promotes growth of lesioned adult rat sensory axons ascending in the dorsal columns of the spinal cord. Eur J Neurosci.

1999;11(11):3873–83.

193. Bradbury EJ, Moon LDF, Popat RJ, King VR, Bennett GS, Patel PN, et al. Chondroitinase ABC promotes functional recovery after spinal cord injury. Nature. 2002;416(6881):636–40.

194. Lu P, Jones LL, Snyder EY, Tuszynski MH. Neural stem cells constitutively secrete neurotrophic factors and promote extensive host axonal growth after spinal cord injury. Exp Neurol. 2003;181(2):115–29.

195. Ceto S, Sekiguchi KJ, Takashima Y, Nimmerjahn A, Tuszynski MH. Neural Stem Cell Grafts Form Extensive Synaptic Networks that Integrate with Host Circuits after Spinal Cord Injury. Cell Stem Cell [Internet]. 2020;27(3):430-440.e5. Available from: https://doi.org/10.1016/j.stem.2020.07.007

196. Gaudet AD, Fonken LK. Glial Cells Shape Pathology and Repair After Spinal Cord Injury. Neurotherapeutics. 2018;15(3):554–77.

197. Yao C, Cao X, Yu B. Revascularization After Traumatic Spinal Cord Injury. Front Physiol. 2021;12(April):1–9.

198. Tsivelekas KK, Evangelopoulos DS, Pallis D, Benetos IS, Papadakis SA, Vlamis J, et al. Angiogenesis in Spinal Cord Injury: Progress and Treatment. Cureus. 2022;14(5).

199. Kumagai G, Okada Y, Yamane J, Nagoshi N, Kitamura K, Mukaino M, et al. Roles of ES cell-derived gliogenic neural stem/progenitor cells in functional recovery after spinal cord injury. PLoS One. 2009;4(11).

200. Nori S, Okada Y, Yasuda A, Tsuji O, Takahashi Y, Kobayashi Y, et al. Grafted human-induced pluripotent stem-cell-derived neurospheres promote motor functional recovery after spinal cord injury in mice. Proc Natl Acad Sci U S A. 2011;108(40):16825–30.

201. Hwang DH, Shin HY, Kwon MJ, Choi JY, Ryu BY, Kim BG. Survival of neural stem cell grafts in the lesioned spinal cord is enhanced by a combination of treadmill locomotor training via insulin-like growth factor-1 signaling. J Neurosci. 2014;34(38):12788–800.

202. Karimi-Abdolrezaee S, Eftekharpour E, Wang J, Morshead CM, Fehlings MG. Delayed transplantation of adult neural precursor cells promotes remyelination and functional neurological recovery after spinal cord injury. J Neurosci. 2006;26(13):3377–89.

203. Parr AM, Kulbatski I, Tator CH. Transplantation of adult rat spinal cord stem/progenitor cells for spinal cord injury. J Neurotrauma. 2007;24(5):835–45.

204. Liu S, Chen Z. Employing endogenous NSCs to promote recovery of spinal cord injury. Stem Cells Int. 2019;2019.

205. Wilcox, J. T., Satkunendrarajah, K., Zuccato, J. A., Nassiri, F., & Fehlings MG. Neural Precursor Cell Transplantation Enhances Functional Recovery and Reduces Astrogliosis in Bilateral Compressive/Contusive Cervical Spinal Cord Injury. Stem Cells Transl Med. 2014;3:1148–59.

206. Younsi A, Zheng G, Riemann L, Scherer M, Zhang H, Tail M, et al. Long-term effects of neural precursor cell transplantation on secondary injury processes and functional recovery after severe cervical contusion-compression spinal cord injury. Int J Mol Sci. 2021;22(23):1–23.

207. Cao Q lin, Zhang YP, Howard RM, Walters WM, Tsoulfas P, Whittemore SR. Pluripotent stem cells engrafted into the normal or lesioned adult rat spinal cord are restricted to a glial lineage. Exp Neurol. 2001;167(1):48–58.

208. Xue W, Fan C, Chen B, Zhao Y, Xiao Z, Dai J. Direct neuronal differentiation of neural stem cells for spinal cord injury repair. Stem Cells. 2021;39(8):1025–32.

209. Lien B V., Tuszynski MH, Lu P. Astrocytes migrate from human neural stem cell grafts and functionally integrate into the injured rat spinal cord. Exp Neurol. 2019;314(December 2018):46–57.

210. Kumar V, Gupta AK, Shukla RK, Tripathi VK, Jahan S, Pandey A, et al. Molecular mechanism of switching of TrkA/p75 NTR signaling in monocrotophos induced neurotoxicity. Sci Rep [Internet]. 2015;5(January):1–17. Available from: http://dx.doi.org/10.1038/srep14038

211. Kathe C, Skinnider MA, Hutson TH, Regazzi N, Gautier M, Demesmaeker R, et al. The neurons that restore walking after paralysis. Nature. 2022;611(November).

Appendix

biomedicines

MDPI

Article

Microneurotrophin BNN27 Reduces Astrogliosis and Increases Density of Neurons and Implanted Neural Stem Cell-Derived Cells after Spinal Cord Injury

Konstantina Georgelou [1,2], Erasmia-Angeliki Saridaki [1], Kanelina Karali [1,2], Argyri Papagiannaki [1], Ioannis Charalampopoulos [1,2], Achille Gravanis [1,2,†] and Dimitrios S. Tzeranis [2,3,*,†]

1 Department of Pharmacology, School of Medicine, University of Crete, 71003 Heraklion, Greece
2 Institute of Molecular Biology and Biotechnology, Foundation for Research and Technology-Hellas, 71003 Heraklion, Greece
3 Department of Mechanical and Manufacturing Engineering, University of Cyprus, Nicosia 2109, Cyprus
* Correspondence: tzeranis.dimitrios@ucy.ac.cy
† These authors contributed equally to this work.

Abstract: Microneurotrophins, small-molecule mimetics of endogenous neurotrophins, have demonstrated significant therapeutic effects on various animal models of neurological diseases. Nevertheless, their effects on central nervous system injuries remain unknown. Herein, we evaluate the effects of microneurotrophin BNN27, an NGF analog, in the mouse dorsal column crush spinal cord injury (SCI) model. BNN27 was delivered systemically either by itself or combined with neural stem cell (NSC)-seeded collagen-based scaffold grafts, demonstrated recently to improve locomotion performance in the same SCI model. Data validate the ability of NSC-seeded grafts to enhance locomotion recovery, neuronal cell integration with surrounding tissues, axonal elongation and angiogenesis. Our findings also show that systemic administration of BNN27 significantly reduced astrogliosis and increased neuron density in mice SCI lesion sites at 12 weeks post injury. Furthermore, when BNN27 administration was combined with NSC-seeded PCS grafts, BNN27 increased the density of survived implanted NSC-derived cells, possibly addressing a major challenge of NSC-based SCI treatments. In conclusion, this study provides evidence that small-molecule mimetics of endogenous neurotrophins can contribute to effective combinatorial treatments for SCI, by simultaneously regulating key events of SCI and supporting grafted cell therapies in the lesion site.

Keywords: spinal cord injury; neurotrophins; astrogliosis; neuroprotection; neural stem cells; biomaterials

check for updates

Citation: Georgelou, K.; Saridaki, E.-A.; Karali, K.; Papagiannaki, A.; Charalampopoulos, I.; Gravanis, A.; Tzeranis, D.S. Microneurotrophin BNN27 Reduces Astrogliosis and Increases Density of Neurons and Implanted Neural Stem Cell-Derived Cells after Spinal Cord Injury. *Biomedicines* **2023**, *11*, 1170. https://doi.org/10.3390/biomedicines11041170

Academic Editor: Nicolas Guerout

Received: 4 March 2023
Revised: 2 April 2023
Accepted: 12 April 2023
Published: 13 April 2023

Copyright: © 2023 by the authors. Licensee MDPI, Basel, Switzerland. This article is an open access article distributed under the terms and conditions of the Creative Commons Attribution (CC BY) license (https://creativecommons.org/licenses/by/4.0/).

1. Introduction

Spinal cord injury (SCI) leads to partial or complete loss of sensory and/or motor functions. According to the World Health Organization, approximately 400,000 individuals around the world suffer a SCI each year. Despite significant efforts, existing clinical treatments are limited to surgical intervention for spinal cord decompression and the controversial administration of methylprednisolone, a corticosteroid that has serious adverse effects and poor efficacy [1]. The development of effective SCI treatments remains an unmet clinical need.

SCI triggers a complex cascade of interrelated events. Acute primary injury (cell death, hemorrhage, edema and ischemia) proceeds to secondary injury (inflammatory and cytotoxic events) within the next few hours to weeks and leads to chronic injury over the next months to years [2]. The multifactorial nature of SCI calls for the development of combinatorial therapies that will combine the complementary effects of multiple components to simultaneously regulate multiple events.

Significant research focuses on developing combinatorial treatments for SCI that integrate the complementary actions of biomaterials, cell therapies and diffusible growth

factors [3]. In such combinatorial treatments, biomaterials contribute structural support, inflammation regulation, delivery, protection and orientation of cells, a substrate for cellular migration and axonal elongation, and localized delivery of diffusible therapeutic molecules (small molecules, biologics) at the lesion [1]. The cellular part of combinatorial treatments usually focuses on replacing neural cells lost during injury and re-establishing connectivity in the lesion site [4]. Among the various kinds of stem cells tested in experimental SCI treatments, neural stem cells (NSCs) have shown promising results in animal models, including the extension of a large number of axons caudally to the lesion and synapse creation with corticospinal tract axons [5,6]. Despite effort to translate NSC-based treatments towards human clinical evaluation [7], much work remains to enhance their efficacy. In this direction, much research focuses on optimizing the biomaterial part of SCI treatments and complementing grafted cells with soluble factors. Recently, we demonstrated that porous collagen scaffold (PCS) grafts can safely deliver NSCs in SCI lesions, enabling their differentiation into neurons and glia. Such NSC-seeded PCS grafts significantly improved locomotion recovery over a period of 12 weeks in a mouse dorsal column crush SCI model [8]. This work focuses on the third part of combinatorial SCI treatments, the supplementation of cell therapies with soluble therapeutic molecules, emphasizing neurotrophic factors.

Much research on SCI treatments has focused on trophic factors' support, due to their role in neuronal survival, axonal guidance and synapse formation [9,10]. Among trophic factors, NGF, the prototypic member of the neurotrophin family, has received significant attention. NGF and its receptors (TrkA, $p75^{NTR}$) are expressed in the spinal cord [11–13]. The poor regenerative capacity of the CNS compared to the peripheral nervous system (PNS) has been partly attributed to inadequate trophic support, including low levels of NGF following injury. Indeed, following SCI, NGF expression in the spinal cord was detected just in meningeal cells and Schwann cells in nerve roots [9]. SCI does not induce NGF expression in spinal cord oligodendrocytes, in contrast to the PNS axotomy that induces robust NGF expression in Schwann cells. These observations suggest trophic factor supplementation as a potential therapeutic strategy for SCI. Following SCI, NGF administration induced tract-specific neurite growth [14,15], reduced neuronal death [16–18], inhibited SCI-induced autophagy [18], and led to behavioral improvement [16–19]. Significant research has focused on developing means of NGF administration that bypass the poor penetration of NGF via the blood–brain barrier (BBB) [20], including intranasal delivery [13], local BBB disruption using ultrasound [17] and the delivery of NGF-expressing genetically modified cells, such as fibroblasts [14,21,22], Schwann cells [23] or NSCs [18,19], in the lesion site. Overall, despite some promising results, the utilization of NGF in combinatorial research treatments for SCI has been limited, due to unfavorable pharmacokinetics and side effects, including hyperalgesia [24].

Key limitations of endogenous neurotrophins regarding therapeutic applications can be bypassed by microneurotrophins (MNT), 17-carbon small-molecule derivatives of dehydroepiandrosterone that specifically activate neurotrophin receptors and can pass the BBB [25]. BNN27, the seminal MNT, is an NGF analog that can activate both its receptors (TrkA, $p75^{NTR}$) and lacks the hyperalgesia effects of NGF. BNN27 has demonstrated various effects related to wound healing: BNN27 demonstrated neuroprotective effects on various kinds of neurons (superior cervical ganglion cells, dorsal root ganglion cells, cerebellar granule neurons) mediated via both NGF receptors and downstream pro-survival pathways [26,27], decreased apoptosis of $TrkA^{+}$ sensory neurons in E13.5 NGF null mice embryos [26], decreased retina cell apoptosis and astrogliosis in a rat model of diabetes-induced retinal damage [28,29], and reduced microgliosis in a mouse cuprizone-induced demyelination model [30]. Nevertheless, the effects of BNN27 have not been evaluated yet in any CNS injury model, either in the form of a monotherapy or as a part of a combinatorial therapy.

The present study evaluates the effects of BNN27 in the mouse dorsal column crush SCI model. BNN27 was delivered systemically either by itself or combined with NSC-seeded PCS grafts demonstrated recently to improve locomotion performance in the same SCI

model [8]. Our findings highlight the central role of NSC-seeded PCS grafts in locomotion improvement, the replenishment of neural cells lost due to SCI and the integration of neuronal cells with surrounding CNS tissue 12 weeks post injury (wpi). While systemic administration of BNN27 did not improve locomotion recovery over a 10-week period following SCI, BNN27 significantly reduced astrogliosis and increased neuron density in the lesion site at 12 wpi. Furthermore, BNN27 increased the density of implanted NSC-derived cells in the lesion. Our study provides evidence that small-molecule mimetics of endogenous neurotrophins can contribute to effective combinatorial SCI treatments by regulating key events of SCI and supporting grafted cell therapies in the lesion site.

2. Materials and Methods

2.1. Animals

Animal care and experimentation protocols were performed according to the approval of the Veterinary Directorate of the region of Crete in compliance with Greek Government guidelines, EU guidelines 2010/63/EU, FORTH ethics committee guidelines and in accordance with approved protocols from the Federation of European Laboratory Animal Science Associations (FELASA) on use of laboratory animals. Facility License number: EL91-BIOexp-02; Project title: "Investigating the effects of neurotrophins and their synthetic analogues on the mechanisms of neurodegeneration and neurogenesis in Alzheimer's disease and the effect of neuroimplants based on porous collagen scaffolds in the central nervous system trauma"; approval numbers: 262,272 and 360,667; date of initial approval: 29 October 2018; date of reapproval: 29 November 2021. C57/BL6 [31] and Rosa26-YFP mice (containing a floxed yellow fluorescent protein (YFP) gene) [32] were maintained in climate-controlled conditions (30–50% humidity, 21 $\pm$ 2 °C, 12:12 h light/dark cycle) on a 12 h light/dark cycle with ad libitum access to food and water. Rosa26-YFP mice were crossed with CMV-Cre transgenic mice [33] to obtain mice that expressed YFP in all tissues.

2.2. Scaffold Fabrication

PCS sheets were fabricated by lyophilizing a 5 mg/mL microfibrillar collagen I suspension in 50 mM acetic acid as described previously [8]. The resulting 2.5 mm-thick dry sheets were cross-linked via dehydro-thermal treatment (105 °C, 50 mTorr, 24 h). Scaffold structure was verified by scanning electron microscopy.

2.3. Primary Neural Stem Cell Isolation and Culture

NSC isolation was performed from brain tissue (cortex) of mouse embryos (E13.5) of Rosa26-YFP mice crossed with CMV-Cre transgenic mice via the enzymatic digestion of the cortex. Specifically, pregnant mice (gestational day 13.5) were sacrificed via cervical dislocation and embryos were carefully removed. Embryos' cortical hemispheres were washed gently in Hanks' balanced salt solution (Thermo scientific) with 5% penicillin/streptomycin and were mechanically dissociated for NSC isolation in complete NSC medium (Dulbecco's modified Eagle's medium/F12 (Thermo scientific), B27 supplement minus vitamin A (Thermo scientific), 0.6% D-glucose, 50 mg/mL primocin (InvivoGen), 20 μg/mL fibroblast growth factor 2 (R&D), 20 μg/mL epidermal growth factor (R&D)). Then, $2.5 \cdot 10^5$ NSCs were seeded in T25 flasks in 5 mL complete NSC medium and 1 mL of fresh medium was added every other day. Neurospheres formed within 2 days and were dissociated by Accutase (Sigma) at day 4 or 5. Dissociated NSCs were either passaged or used for experiments (passage 3–8). Care was taken in the first passage to pick and keep neurospheres of YFP-expressing embryos.

2.4. Spinal Cord Injury Animal Model

Procedures for SCI and graft implantation followed previously published protocols [8]. Specifically, 3 days prior to injury, $3 \cdot 10^4$ YFP-expressing NSCs were seeded into 1 × 1 × 1.5 mm PCS samples and cultured in complete NSC medium. Prior to implantation, grafts were washed for 30 min in phosphate-buffered saline (PBS). All surfaces,

tools, and instruments utilized had been sterilized carefully. C57/BL6 male mice approximately 4 weeks old were anesthetized by 2.5:1 isoflurane:oxygen mix inhalation for 5 min in a scavenger box until breathing slowed down. Before anesthesia, a drop of meloxicam (Metacam) was introduced per os. After verifying the absence of paw reflexes, each mouse was shaved in the level of the humpback and the exposed skin was disinfected. Each mouse was then transferred onto a heat pad, where ophthalmic ointment was applied to avoid eye dryness and 2:1 isoflurane:oxygen mix was applied to maintain deep anesthesia via a mask. In all animal groups ("Uninjured control", "Placebo", "BNN27", "Scaffold NSC + Placebo", "Scaffold NSC + BNN27") a skin incision was made from the base of the humpback until the higher point of the rib cage and exposed muscles were carefully torn. After removing surrounding ligaments, the bone of T10 vertebra was removed and an incision was made in the dura matter above the T13 segment [34]. In four injured animal groups ("Placebo", "BNN27", "Scaffold NSC + Placebo", "Scaffold NSC + BNN27") the dorsal column was crushed by inserting Dumont #5 fine forceps 1 mm deep into the white matter and keeping them closed for 10 sec. This step was repeated once to create a $\approx$1 mm^3 pocket (lesion). In two animal groups ("Scaffold NSC + Placebo", "Scaffold NSC + BNN27") a NSC-seeded graft was placed in the pocket immediately following injury. In all animal groups, the exposed spinal cord tissue was covered by a Geistlich membrane (Geistlich Bio-Gide) and then a hemostatic agent (Lyostypt, B. Braun Company), the muscles and skin were sutured and the skin was disinfected. Then, in animals of the "BNN27" and "Scaffold NSC + BNN27" groups, a small incision was made close to the shoulder and a pellet that contained 18 mg BNN27 (60 day release period; Innovative Research of America #SX999) was implanted under the skin. After inserting the pellet, the skin was sutured and disinfected. Similarly, in animals of the "Placebo" and "Scaffold NSC + Placebo" groups, mice were implanted with a pellet that lacked an active pharmaceutical ingredient (Innovative Research of America #SC111). All animal groups were provided with meloxicam for the next 3 days for analgesia.

2.5. Horizontal Ladder Walking Assay

Locomotion performance of mice over a 10-week period following SCI was assessed via the horizontal ladder walking assay [35], as described previously [8]. Briefly, animals crossed a 1 m-long horizontal ladder consisted of sidewalls made of clear plexiglass connected by aluminum rods (ø2 mm diameter) spaced approximately 1 cm from each other. The ladder was elevated above the ground at the height of two cages. Animals were trained to cross the ladder from a neutral cage to their home cage and always in the same direction.

For handling and acclimation, the week prior to surgeries, mice settled down in the animal facility to become familiarized. For 6 consecutive days prior to testing, animals were handled for 5 min by the examiner and walked through the ladder for 5 min in order to reduce their stress during the testing procedure. Each animal was tested five times per session. Before each session, mice crossed the ladder twice for habituation. For locomotion analysis, each trial was video recorded. Videos of walking mice were analyzed frame-by-frame by two researchers blind to the condition (group, week) of the animal analyzed to identify locomotion errors, defined as steps where a hind limb missed or slipped off or was misplaced on a rod. Each fault was classified using a 7-category scale (0: total miss, 1: deep slip, 2: slight slip, 3: replacement, 4: correction, 5: partial placement, 6: correct placement) as described previously [35]. Locomotion performance was described via the fault rate (fraction of steps classified in categories 0 to 5). The last step before and the first step after a stop were excluded; only consecutive steps were included in the analysis.

While initially each animal group consisted of 9–10 mice, some of them were excluded from our final results in order to ensure consistent injury in all animals. Exclusion criteria were based on mice locomotion performance. Mice of the "Uninjured Control" group were excluded when their mean fault rate over the 10-week monitoring period exceeded 10%. Mice of the remaining four injured groups were excluded when there were strong indications of insufficient injury (e.g., fault rate <20% the day following injury or <15% at

1 wpi) or excessive injury (e.g., fault rate >90% the day following injury or >45% at 1 wpi or >35% at 2 wpi). Mice exclusions were confirmed by histology based on the magnitude of the observed lesion in mice spinal cord sections.

2.6. Histological Evaluation

At 12 wpi, mice were deeply anesthetized using 2.5:1 isoflurane:oxygen mix and transcardially perfused with ice-cold heparinized (10 U/mL) saline followed by 4% paraformaldehyde (PFA) in PBS. Spinal cords were dissected, post-fixed in 4% PFA at 4 °C for 1 h, washed in PBS, and immersed in 30% sucrose solution in 0.1 M phosphate buffer at 4 °C for 24 h. The 1 cm-long part of the spinal cord tissue centered around the lesion was frozen in isopentane at −70 °C and 20 µm-thick parasagittal sections were cut in super-frost slides.

For histological analysis, slides were placed in ice-cold acetone for 5 min, air-dried for 10 min in laminar flow, washed twice in PBS, once in 0.1% Triton X-100 in PBS (PBST) and once in 0.3% PBST, then blocked in 0.1% PBST supplemented with 0.1% bovine serum albumin (BSA) and 10% goat or horse serum at room temperature for 1 h, incubated in primary antibodies (L1: 1:000 rabbit polyclonal antibody (obtained by Dr. Fritz G. Rathjen)); tubulin β3 (Tubb3): 1:1000 Biolegend #801201 (clone Tuj1); glial fibrillary acidic protein (GFAP): 1:2000 Millipore #AB5541; synaptophysin: 1:200 Millipore #MAB368; green fluorescent protein (GFP): 1:200 Minotech #701-1; vesicular glutamate transporter 1 (VGLUT1): 1:400 Synaptic systems #135304; tyrosine hydroxylase (3TH): 1:40 Thermo #MA1-24654; glutamic acid decarboxylase 67 (GAD67): 1:1000 Sigma #MAB5406; α-smooth muscle actin (αSMA): 1:200 Sigma #A5228) diluted in blocking solution at 4 °C overnight, washed twice in 0.1% PBST, incubated with fluorophore-conjugated secondary antibodies (Thermo) diluted 1:1000 in PBS at room temperature for 1 h, washed twice in PBS, counterstained with Hoechst 33,342 and mounted.

Immunostained sections were imaged in a TCS SP8 inverted confocal microscope (Leica Microsystems, Wetzlar, Germany) using a 40× or a 63× oil-immersion objective lens. Images were taken at the epicenter, caudally and rostrally to the lesion. The presence of neurons was quantified by counting the density of Tuj1$^+$ cells in the lesion epicenter. Astrogliosis was quantified by calculating the fraction of pixels that stained positively for GFAP immediately around the lesion boundary, by selecting up to 5 regions (approximately 0.025 mm^2 each) per section. The presence of implanted cells was quantified by counting the density of GFP$^+$ cells in the lesion epicenter, expressed per volume, using images acquired by a 63× objective lens. Synapse formation was quantified by calculating the fraction of pixels that stained positively for synaptophysin in the lesion epicenter. Axonal elongation was quantified by calculating the fraction of pixels that stained positively for L1 in the lesion epicenter as well as in dorsal region rostrally and caudally to the lesion. Angiogenesis was quantified by counting the number of αSMA$^+$ vessels in the lesion epicenter. All imaging analysis was performed in Fiji software. In thresholding operations, care was taken to avoid counting the background of each staining and define positive staining using a common value chosen by an expert user.

2.7. Statistical Analysis

Experimental data are expressed as mean ± standard error of the mean (SEM). Statistical analysis was performed using the Prism software (Graphpad, La Jolla, CA, USA). Statistically significant effects on locomotion fault rate were assessed by 1-way analysis of variance (ANOVA; for evaluating the overall effects of injury among the groups at postop and 1 wpi) and by 2-way ANOVA (for evaluating the overall effects of BNN27 and NSC-seeded PCS graft treatments) followed by Tukey's post hoc test (for pairwise comparisons between groups at 2–10 wpi). Statistically significant effects in the quantification of GFAP$^+$, synaptophysin$^+$, L1$^+$ pixel fractions, Tuj1$^+$ cell density and αSMA$^+$ vessel number were assessed by 2-way ANOVA (for evaluating the effects of BNN27 and NSC-seeded PCS graft treatments) followed by Tukey's post hoc test (for pairwise comparisons between groups). Statistically significant effects of BNN27 administration on the density and neuronal fate of

implanted NSCs were assessed by unpaired two-tailed Student's *t*-tests. All statistical tests assumed a statistical significance level of 0.05.

3. Results

Therapeutic effects of BNN27 after SCI were evaluated using the well-described mouse dorsal column crush SCI model [8]. Immediately after crush, three types of SCI treatments were tested: the first animal group was provided systemic administration of BNN27 via subcutaneous pellet ("BNN27" group; 18mg/pellet released over a 60-day period); the second animal group ("Scaffold NSC + BNN27") was treated with a combinatorial approach consisting of a PCS implant seeded with mouse embryonic E13.5 NSCs grafted inside the lesion site immediately after injury (same graft as the one described in [8]) concurrent with the systemic delivery of BNN27 via subcutaneous pellet; the third animal group ("Scaffold NSC + Placebo") was treated with NSC-seeded PCS implant concurrent with subcutaneous pellet that lacked an active pharmaceutical ingredient. In addition, experimental design included the "Placebo" animal group (injured mice treated with a subcutaneous pellet that lacked an active pharmaceutical ingredient) and the "Uninjured Control" animal group (where, following laminectomy, the exposed spinal cord was not injured). Grafts in the "Scaffold NSC" and "Scaffold NSC + BNN27" groups utilized NSCs isolated from mice obtained by crossing Rosa26-YFP mice containing a floxed YFP gene with CMV-Cre mice and keeping embryos whose NSCs express YFP, enabling their detection via live cell fluorescence imaging or immunocyto/histochemistry (Supplementary Materials: Figure S1).

3.1. BNN27 and NSC Graft Treatment Effects on Locomotion Recovery after SCI

Mice locomotion recovery over a period of 10 weeks following dorsal column crush was evaluated by quantifying their step fault rate in the horizontal ladder walking assay (Figure 1 and Supplementary Materials: Figure S2). During the 10-week period, mice of the "Uninjured Control" group had a time-invariant fault rate (μ = 6.9%, σ = 2.4%). No difference was observed among the four injured groups till the 1st wpi, confirming that injury was consistently performed in all animals (post-op: $P_{1\text{-way-ANOVA}} = 0.94$, F = 0.12; week 1: $P_{1\text{-way-ANOVA}} = 0.57$, F = 0.69). Between 1 and 10 wpi, all injured groups showed some locomotion improvement. Eventually, differences in fault rate became statistically significant only in mice treated with NSC-seeded PCS grafts compared to the untreated injured group at 9 wpi ("Placebo": 20.9 ± 0.5%, n = 4 vs. "Scaffold NSC + Placebo": 13.6 ± 1.7%, n = 5, $p = 0.01$; "Placebo" vs. "Scaffold NSC + BNN27": 14.8 ± 0.7%, n = 5, $p = 0.04$) and 10 wpi ("Placebo": 22.8 ± 1.5%, n = 4 vs. "Scaffold NSC + Placebo": 15.6 ± 1.2%, n = 5, $p = 0.04$; "Placebo" vs. "Scaffold NSC + BNN27": 14.8 ± 2%, n = 5, $p = 0.02$), replicating the findings of our previous study [8]. While grafting mice with NSC-seeded PCS statistically improved locomotion recovery after 8 weeks (week 9: $P_{2\text{-way-ANOVA}} = 10^{-3}$; week 10: $P_{2\text{-way-ANOVA}} = 10^{-3}$), BNN27 administration did not (week 9: $P_{2\text{-way-ANOVA}} = 0.89$; week 10: $P_{2\text{-way-ANOVA}} = 0.45$). The fault rate in the "BNN27" group was not statistically different from the one of the untreated "Placebo" group (9 weeks: "BNN27": 19.3 ± 2%, n = 4, $p = 0.86$; 10 weeks: "BNN27": 21.1 ± 1.7%, n = 4, $p = 0.9$). Similarly, BNN27 administration did not further improve locomotion recovery when combined with NSC-seeded PCS grafts since the fault rate in the two mice groups treated with NSC-seeded PCS grafts ("Scaffold NSC + Placebo", "Scaffold NSC + BNN27") was not statistically different over the 10-week period (week 9: $p = 0.91$; week 10: $p = 0.98$).

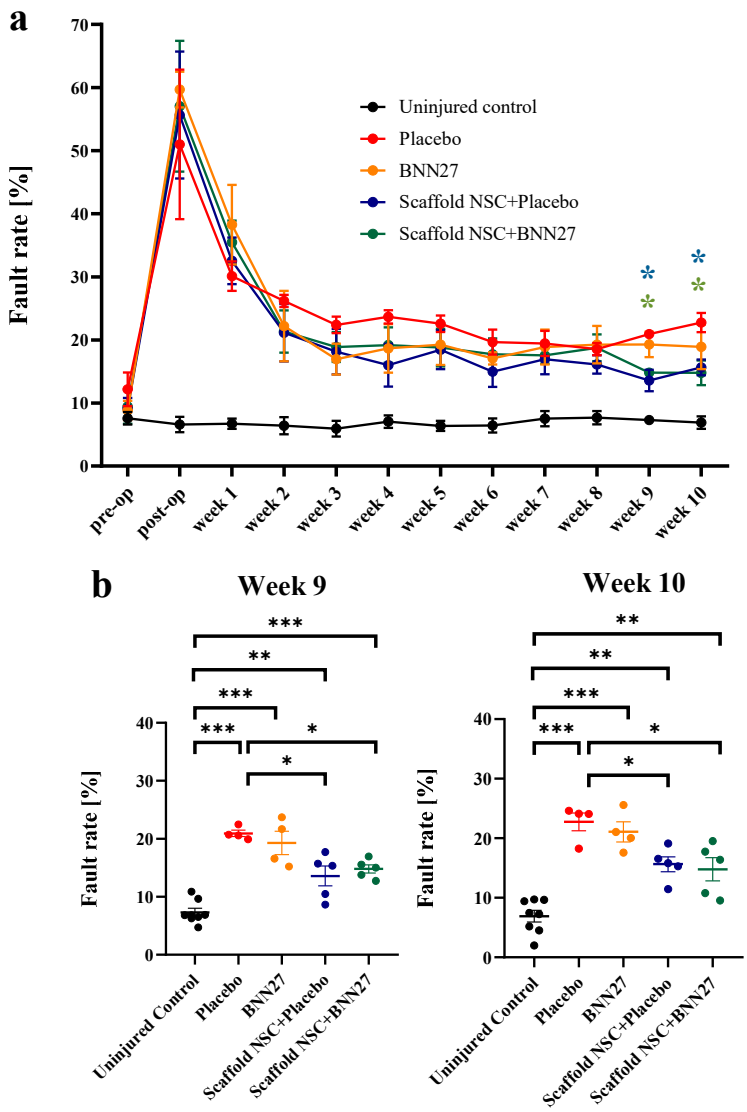

Figure 1. Effects of NSC-seeded PCS grafts and systemic administration of BNN27 on locomotion recovery. (**a**) Quantification of locomotion performance (fault rate) after SCI by the horizontal ladder walking assay over a period of 10 wpi ("Uninjured Control" group: n = 8, "Placebo" and "BNN27" groups: n = 4, "Scaffold NSC" and "Scaffold NSC + BNN27" groups: n = 5). The complete dataset is available in Supplementary Materials: Figure S2. Asterisks indicate the statistically significant difference between the "Placebo" group and the "Scaffold NSC + Placebo" group (blue) or the "Scaffold NSC + BNN27" group (green) at 9 and 10 wpi. (**b**) Dot plot of locomotion fault rate at 9 and 10 wpi. Results are presented as mean ± SEM. * $p < 0.05$, ** $p < 0.01$, *** $p < 0.001$; Tukey's post hoc pairwise test assuming $P_{1\text{-way-ANOVA}} < 0.05$.

3.2. BNN27 and NSC Graft Treatment Effects on Neuron Presence and Astrogliosis at the Lesion Site

The presence of neurons in the lesion epicenter at 12 wpi was evaluated by immunostaining spinal cord parasagittal sections for the Tuj1 neuronal marker and calculating the density of Tuj1$^+$ cells within the lesion epicenter, which was denoted by a GFAP$^+$ boundary region (Figure 2a). While Tuj1$^+$ cells and neurites were present in all four injured groups (Figure 2b), statistical analysis revealed that both NSC-seeded PCS ($P_{2\text{-way-ANOVA}} = 5{\cdot}10^{-4}$) and BNN27 ($P_{2\text{-way-ANOVA}} = 0.01$) had a statistically significant effect on the density of Tuj1$^+$ cells in the lesion epicenter at 12 wpi. A significant increase in Tuj1$^+$ cell density was observed in the presence of BNN27 administration or NSC-seeded PCS grafts with or without BNN27 compared to the untreated "Placebo"

group ("Placebo": 397.1 ± 53.2 cells/mm^2, n = 4; "BNN27": 683.8 ± 44.8 cells/mm^2, n = 3, p = 0.01; "Scaffold NSC": 776.6 ± 47.2 cells/mm^2, n = 5, $p = 6{\cdot}10^{-4}$; "Scaffold NSC + BNN27": 789.2 ± 50.6 cells/mm^2, n = 4, $p = 7{\cdot}10^{-4}$) (Figure 2d). Simultaneous treatment with BNN27 and NSC-seeded PCS grafts did not have statistically significant synergistic effects on the density of Tuj1$^+$ cells compared to treatment only with NSC-seeded PCS grafts.

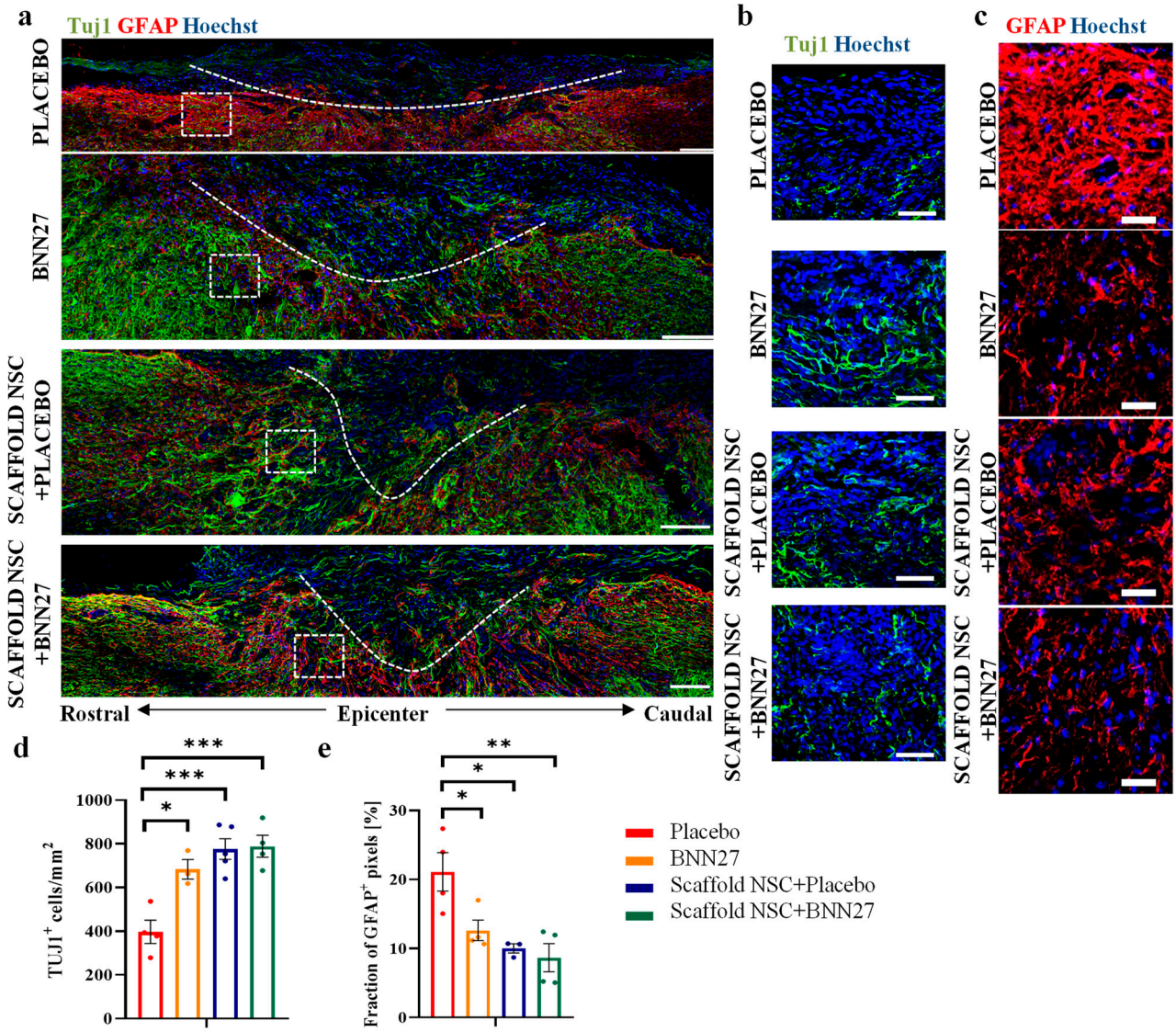

Figure 2. Effects of NSC-seeded PCS grafts and BNN27 administration on neuronal density and astrogliosis. (**a**) Representative fluorescence images of spinal cord parasagittal sections from all four injured groups immunostained for Tuj1 (green) and GFAP (red). The boundaries of lesion site (epicenter) are marked with a dotted line. Scale bars: 100 µm. (**b**) High-magnification fluorescence images in the lesion epicenter of image (**a**) visualizing Tuj1 immunostaining. Scale bars: 30 µm. (**c**) High-magnification fluorescence images of the rectangular ROI of image (**a**) showing GFAP immunostaining at the lesion boundary region. Scale bars: 30 µm. (**d**) Quantification of the density of Tuj1$^+$ cells within the lesion epicenter at 12 wpi in the four injured animal groups ("Placebo": n = 4, "BNN27": n = 3, "Scaffold NSC + Placebo": n = 5, "Scaffold NSC + BNN27" n = 4). (**e**) Quantification of the fraction of GFAP$^+$ pixels (marker of astrogliosis) in the lesion boundary region at 12 wpi in the four injured animal groups ("Placebo": n = 4, "BNN27": n = 4, "Scaffold NSC + Placebo": n = 3, "Scaffold NSC + BNN27" n = 4). Results are presented as mean ± SEM. * $p < 0.05$, ** $p < 0.01$, *** $p < 0.001$; Tukey's post hoc pairwise test assuming $P_{2\text{-way-ANOVA}} < 0.05$.

Astrogliosis in the SCI lesion site at 12 wpi was evaluated by immunostaining spinal cord parasagittal sections for GFAP (marker of astrocytes) and quantifying the fraction of $GFAP^+$ pixels in the lesion boundary region (Figure 2a,c). Two-way ANOVA revealed that both NSC-seeded PCS ($P_{2\text{-way-ANOVA}} = 4{\cdot}10^{-3}$) and BNN27 ($P_{2\text{-way-ANOVA}} = 0.04$) had a statistically significant effect on the fraction of $GFAP^+$ pixels in the lesion boundary region at 12 wpi. Compared to the untreated "Placebo" group, a significant decrease in $GFAP^+$ pixel fraction was observed in the presence of BNN27 administration or NSC-seeded PCS grafts with or without BNN27 ("Placebo": 21.1 ± 2.8%, n = 4; "BNN27": 12.6 ± 1.5%, n = 4, $p = 0.05$; "Scaffold NSC": 10.0 ± 0.6%, n = 3, $p = 0.02$; "Scaffold NSC + BNN27": 8.7 ± 2.0%, n = 4, $p = 5{\cdot}10^{-3}$) (Figure 2e). BNN27 administration did not lead to statistically significant synergistic effects when combined with NSC-seeded PCS grafts ("Scaffold NSC + Placebo" vs. "Scaffold NSC + BNN27": $p = 0.97$).

3.3. Treatment Effects on Synapse Formation, Axonal Elongation and Angiogenesis at the Lesion Site

The integration of neurons within the lesion area via synapse formation at 12 wpi was evaluated by immunostaining spinal cord parasagittal sections for synaptophysin and then quantifying the fraction of synaptophysin$^+$ pixels within the lesion epicenter (Figure 3a–c). Overall, treatment with NSC-seeded PCS had a statistically significant effect ($P_{2\text{-way-ANOVA}} < 10^{-4}$) on the fraction of synaptophysin$^+$ pixels in the lesion. Both graft-treated groups contained a larger fraction of synaptophysin$^+$ pixels than the untreated "Placebo" group ("Placebo": 4.1 ± 0.7%, n = 3; "Scaffold NSC + Placebo": 8.4 ± 0.7%, n = 3, $p = 2{\cdot}10^{-3}$; "Scaffold NSC + BNN27": 8.7 ± 0.4%, n = 3, $p = 10^{-3}$). On the other hand, BNN27 administration did not increase the fraction of synaptophysin$^+$ pixels ($P_{2\text{-way-ANOVA}} = 0.37$; "Placebo" vs. "BNN27": 4.8 ± 0.2%, n = 3, $p = 0.79$; "Scaffold NSC + Placebo" vs. "Scaffold NSC + BNN27": $p = 0.98$) (Figure 3d).

Ongoing axonal elongation in the lesion site was evaluated by immunostaining spinal cord parasagittal sections for the L1 cell adhesion molecule that is upregulated in elongating axons [36] and quantifying the fraction of $L1^+$ pixels in the lesion epicenter and in the dorsal regions rostrally and caudally to the lesion (Supplementary Materials: Figure S3a). No difference was observed among the four injured groups in the rostral region and in the lesion epicenter. Treatment with NSC-seeded PCS grafts had a statistically significant effect ($P_{2\text{-way-ANOVA}} < 10^{-4}$) on the fraction of $L1^+$ pixels caudally to the lesion (Supplementary Materials: Figure S3b). The two PCS graft-treated groups showed increased axonal elongation in the caudal region compared to the untreated "Placebo" group (caudally: "Placebo": 7.1 ± 0.8%, n = 5; "Scaffold NSC + Placebo": 11.8 ± 0.7%, n = 4, $p < 10^{-3}$; "Scaffold NSC + BNN27": 11 ± 0.4%, n = 5, $p = 2{\cdot}10^{-3}$). BNN27 administration did not affect axonal elongation (caudally: $P_{2\text{-way-ANOVA}} = 0.99$). The fraction of $L1^+$ pixels was not different in the "BNN27" group compared to the untreated "Placebo" group (caudally: "BNN27": 7.9 ± 0.5%, n = 4, $p = 0.83$). Similarly, the combinatorial treatment with NSC-seeded PCS grafts and BNN27 administration did not increase the fraction of $L1^+$ pixels compared to animals treated only with grafts (caudally: "Scaffold NSC + Placebo" vs. "Scaffold NSC + BNN27" $p = 0.83$) (Supplementary Materials: Figure S3b).

The presence of blood vessels within the lesion site was evaluated by immunostaining spinal cord parasagittal sections for αSMA, a marker of vessel-associated pericytes, and quantifying the number of αSMA^+ vessels within the lesion epicenter (Figure 3e,f). The results show that treatment with NSC-seeded PCS grafts ($P_{2\text{-way-ANOVA}} = 3{\cdot}10^{-3}$) but not BNN27 administration ($P_{2\text{-way-ANOVA}} = 0.44$) had a statistically significant effect on the number of αSMA^+ vessels. The two PCS graft-treated groups contained an increased number of vessels within the lesion epicenter compared to the untreated "Placebo" group ("Placebo": 2.7 ± 0.6%, n = 4; "Scaffold NSC + Placebo": 7.2 ± 1.0%, n = 4, $p = 0.03$; "Scaffold NSC + BNN27": 7.7 ± 0.9%, n = 3, $p = 0.03$). The number of αSMA^+ vessels was not different in the "BNN27" group compared to the untreated "Placebo" group ("BNN27": 4.0 ± 1.5%, n = 3, $p = 0.82$). Similarly, combinatorial treatment with NSC-seeded PCS

grafts and BNN27 did not increase the number of αSMA$^+$ vessels compared to animals treated only with grafts ("Scaffold NSC + Placebo" vs. "Scaffold NSC + BNN27" $p = 0.99$) (Figure 3g).

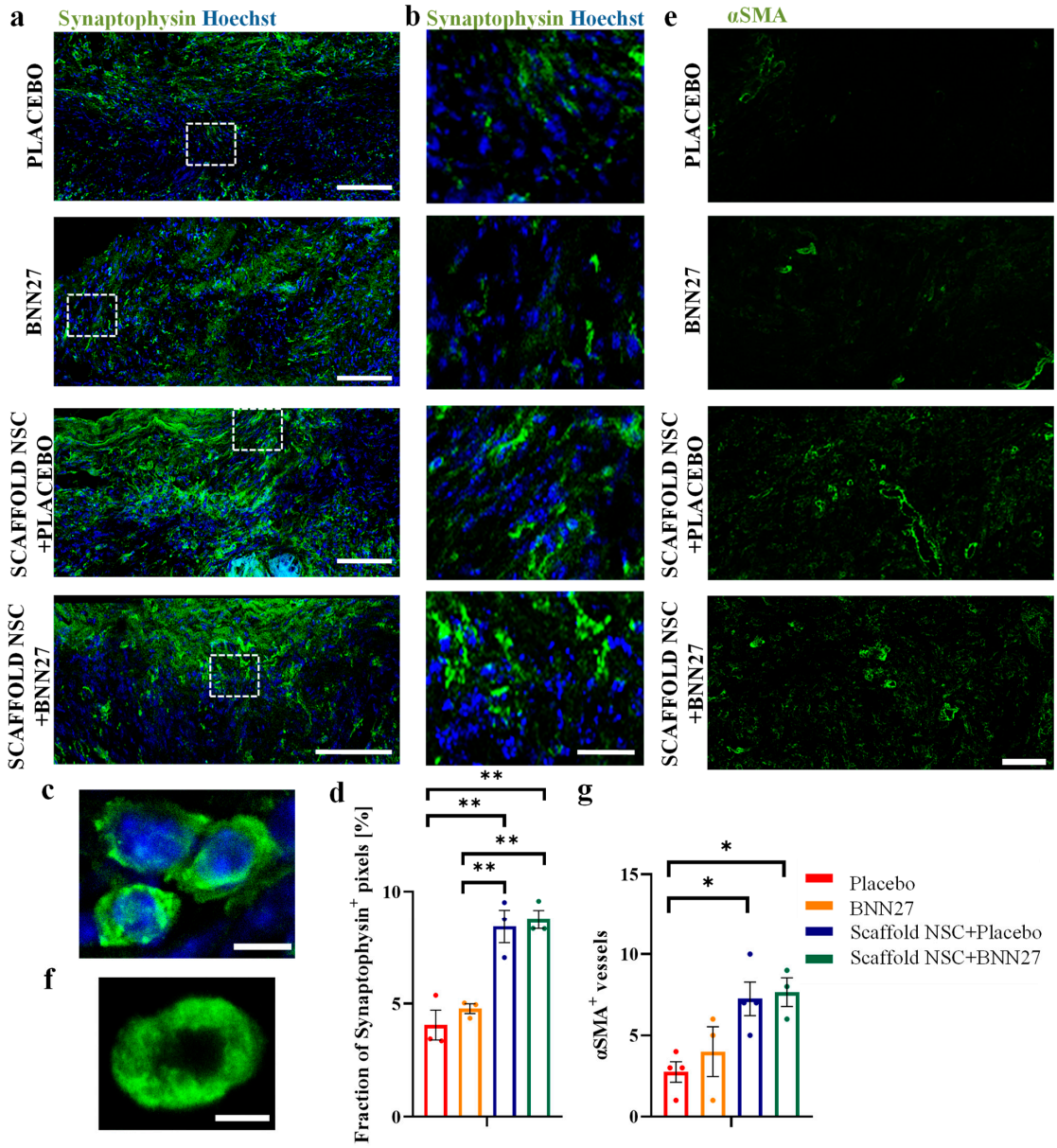

Figure 3. Effects of NSC-seeded PCS grafts on synapse density and angiogenesis. (**a**) Representative fluorescence images of spinal cord parasagittal sections in the lesion epicenter from all four injured groups immunostained for synaptophysin (green). Scale bars: 100 µm. (**b**) High-magnification fluorescence images of the rectangular ROIs of image (**a**) showing synaptophysin immunostaining in the lesion epicenter. Scale bars: 50 µm. (**c**) A representative high-magnification fluorescence image immunostained for synaptophysin. Scale bar: 5 µm. (**d**) Quantification of synaptophysin$^+$ pixel fraction within the lesion epicenter in the four injured groups at 12 wpi (All groups: n = 3). (**e**) Representative fluorescence images of spinal cord parasagittal sections in the lesion epicenter from all four injured groups immunostained for αSMA (green). Scale bar: 50 µm. (**f**) A representative high-magnification fluorescence image of a vessel in the lesion epicenter immunostained for αSMA. Scale bar: 5 µm (**g**) Quantification of the number of αSMA$^+$ vessels within the lesion epicenter in the four injured animal groups at 12 wpi ("Placebo": n = 4, "BNN27": n = 3, "Scaffold NSC + Placebo": n = 4, "Scaffold NSC + BNN27": n = 3). Results are presented as mean ± SEM. * $p < 0.05$, ** $p < 0.01$; Tukey's post hoc pairwise test assuming $P_{2\text{-way-ANOVA}} < 0.05$.

3.4. BNN27 Effects on Implanted NSCs

In our NSC-seeded PCS grafts, we utilized YFP-expressing NSCs so that they could be distinguished from endogenous cells by immunostaining for GFP (Figures 4 and 5a). Immunostaining spinal cord parasagittal sections for GFP (implanted NSC-derived cells), Tuj1 (neurons) and GFAP (astrocytes) revealed an interesting specific spatial pattern on the fate of implanted NSC-derived cells. While Tuj1$^+$GFP$^+$ cells (NSC-derived neurons) remained mostly within the lesion epicenter (Figure 4a), GFAP$^+$GFP$^+$ cells (NSC-derived astrocytes) were localized in the lesion boundary region where they contributed to the formation of glial scar (Figure 4a,b). Double immunostaining for GFP and various neuronal markers revealed that neurons derived from implanted NSCs included inhibitory GAD67$^+$ GABAergic neurons, 3TH$^+$ dopaminergic neurons and VGLUT1$^+$ excitatory glutamatergic neurons (Figure 4c). Interestingly, some GFP$^+$ cells were detected approximately 250 µm outside the lesion, having penetrated the surrounding glial scar (Figure 4d).

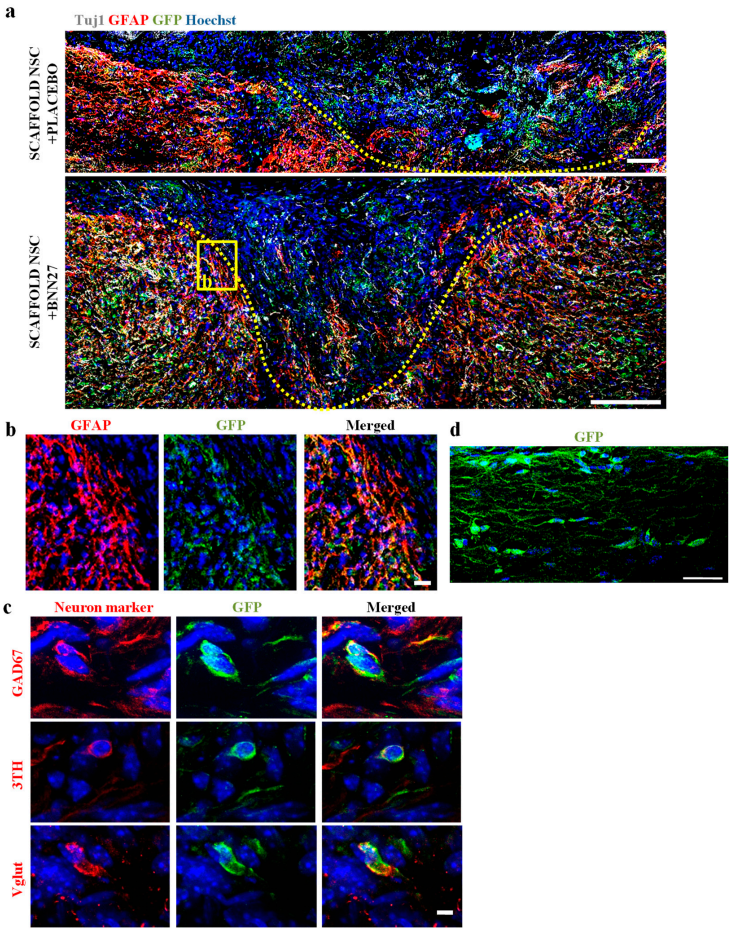

Figure 4. Spatial patterning of implanted NSC fate at the spinal cord lesion site. (**a**) Representative fluorescence images of spinal cord parasagittal sections of SCI lesion immunostained for Tuj1$^+$ neurons (gray), GFAP$^+$ astrocytes (red) and GFP$^+$ implanted NSC-derived cells (green). The boundaries of lesion sites are marked with a dotted line. Scale bars: 100 µm. (**b**) High-magnification fluorescence image of the rectangular insert of image (**a**) showing GFP$^+$GFAP$^+$ implanted NSC-derived astrocytes at the lesion boundary region. Scale bar: 30 µm. (**c**) Representative high-magnification fluorescence images of GFP$^+$ implanted NSC-derived cells double-immunostained with markers of different neuron types: GAD67 (inhibitory GABAergic neurons; upper row), 3TH (dopaminergic neurons; middle row) and VGLUT1 (excitatory glutamatergic neurons; lower row) (red). Scale bar: 3µm. (**d**) Representative fluorescence image of a spinal cord parasagittal section showing GFP$^+$ implanted NSC-derived cells located in the dorsal column, approximately 250 µm caudally to the lesion. Scale bar: 30 µm.

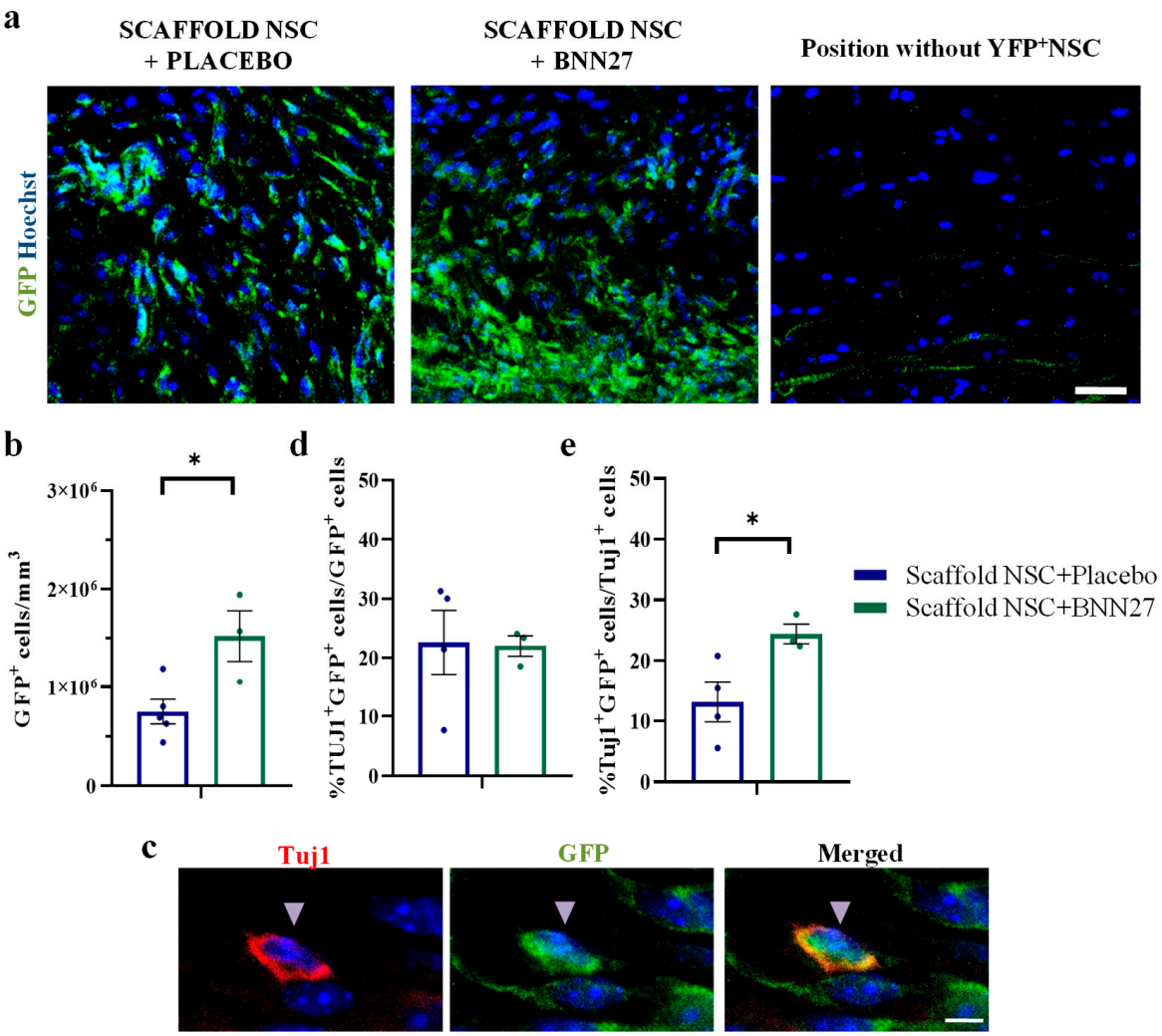

Figure 5. Effects of BNN27 administration on the density and neuronal fate of implanted NSCs. (**a**) Representative high-magnification fluorescence images of GFP$^+$ implanted NSC-derived cells from the two animal groups ("Scaffold NSC + Placebo", "Scaffold NSC + BNN27") treated with NSC-seeded PCS and a region without implanted NSCs. Scale bar: 30 µm. (**b**) Quantification of the density of GFP$^+$ cells in the lesion epicenter at 12 wpi. (**c**) High magnification fluorescence images of cells within the lesion epicenter double-stained for GFP (green; implanted NSC-derived cells) and Tuj1 (red; neurons). Scale bars: 5 µm. (**d**) Quantification of the fraction of GFP$^+$ cells that also stain for the Tuj1 in the lesion epicenter at 12 wpi. (**e**) Quantification of the fraction of Tuj1$^+$ neurons that also stain for GFP in the lesion epicenter at 12 wpi ("Scaffold NSC + Placebo": n = 4, "Scaffold NSC + BNN27": n = 3). Results are presented as mean ± SEM. * $p < 0.05$; unpaired two-tailed Student's *t*-test.

BNN27 effects on the density of implanted NSC-derived cells in the lesion epicenter at 12 wpi were evaluated by counting the number of GFP$^+$ cells (derived from implanted NSCs) in the two animal groups grafted with NSC-seeded PCS grafts. The results show that BNN27 administration increased the density of GFP$^+$ cells in the lesion epicenter ("Scaffold NSC + Placebo": $7.51 \cdot 10^5 \pm 1.25 \cdot 10^5$ cells/mm^3, n = 5 vs. "Scaffold NSC + BNN27": $15.24 \cdot 10^5 \pm 2.57 \cdot 10^5$ cells/mm^3, n = 3, $p = 0.02$) (Figure 5a,b). In order to evaluate the effects of BNN27 administration on the neuronal fate of implanted NSCs, we counted Tuj1$^+$ GFP$^+$ cells in the lesion epicenter (Figure 5c). BNN27 did not affect the fraction of GFP$^+$ cells that had differentiated to Tuj1$^+$ neurons ("Scaffold NSC + Placebo": 22.6 ± 5.4%, n = 4 vs. "Scaffold NSC + BNN27": 22.0 ± 1.7%, n = 3, $p = 0.93$) (Figure 5d). However, BNN27 administration increased the fraction of Tuj1$^+$ neurons that originated from implanted NSCs

("Scaffold NSC + Placebo": 13.1 ± 3.3%, n = 4 vs. "Scaffold NSC + BNN27": 24.4 ± 1.6%, n = 3, p = 0.04) (Figure 5e).

4. Discussion

MNTs are considered candidate therapeutic treatments for various neurologic diseases, since they mimic the effects of endogenous neurotrophins, do not cause hyperalgesia and are BBB-permeable, in contrast to endogenous neurotrophins [25]. Despite promising results in several mice neurodegeneration models, so far the therapeutic activity of MNTs had not been evaluated in any CNS injury model. Herein, we build upon our recent work on the effects of NSC-seeded PCS grafts on the dorsal column crush SCI in mice [8] and focus on the effects of BNN27 in SCI either as monotherapy or combined with NSC-seeded PCS grafts. BNN27 was delivered systemically using subcutaneous pellets over a period of approximately 60 days. Subcutaneous systemic administration is expected to provide a relatively steady BNN27 dose with no animal distraction, appropriate for minimizing artifacts in locomotion evaluation. The permeability of BNN27 in rodent CNS was demonstrated in pharmacokinetic studies where BNN27 was detected in rodent brain and retina 30 min after intraperitoneal injection [37,38].

Evaluation of locomotion recovery via the horizontal ladder walking assay showed that grafting SCI lesions with NSC-seeded PCS grafts led to statistically significant locomotion improvement after dorsal column crush in mice starting on week 9, replicating the results of our previous study [8] and highlighting the central role of NSC-based cell therapies in SCI treatments. On the other hand, systemic administration of BNN27 did not improve locomotion recovery, in agreement with a previous study where local delivery of NGF in rat SCI lesions via genetically modified fibroblasts did not lead to functional improvement 3 months post-injury [15]. Nevertheless, our histological data provide evidence that BNN27 affected several processes related to SCI wound healing, which are discussed in the following paragraphs.

Following SCI, the formation of glial scar isolates the lesion site to prevent damage spread, yet acts as a major physical barrier that obstructs axonal elongation through the lesion [2]. One way to block the inhibitory effects of a glial scar is to target its extracellular growth inhibitory components. For instance, local administration of chondroitinase ABC (ChABC), a bacterial enzyme, enhances axonal growth in CNS lesion sites by removing inhibitory chondroitin sulfate chains [39,40]. However, the clinical use of ChABC is limited by the safety of its local administration in the lesion site [41]. An alternative approach is to target astrogliosis, the accumulation and activation of astrocytes, thus impeding the major cellular component of the glial scar. Grafting SCI lesions with appropriate biomaterials, such as the PCS utilized in this study, have been reported able to reduce astrogliosis [42,43]. Here, we show that the systemic administration of BNN27 also significantly decreased astrogliosis 12 weeks following SCI (Figure 2a,c,e). This finding agrees with the report that local delivery of NGF (via genetically modified NSCs) in rat SCI lesions reduced astrogliosis [19]. While several studies have demonstrated the ability of BNN27 to reduce astrogliosis in animal models of CNS degeneration (including cuprizone-induced demyelination in mice [30], the 5xFAD Alzheimer's disease mouse model (Karali et al. in preparation), diabetes-induced retinal damage in rats [28]), here we demonstrate for the first time the anti-astrogliotic effects of BNN27 in an animal model of CNS injury. Combinatory treatment with NSC-seeded grafts and systemic BNN27 administration further decreased the fraction of $GFAP^+$ pixels compared to the animal groups that received each treatment separately, yet in a non-statistically significant manner (Figure 2e).

Emerging treatments for SCI aim to replace or reduce the loss of neural tissue induced by primary or secondary injury. In this direction, we report that grafting the SCI site with NSC-seeded PCS grafts increased neuron density in the lesion epicenter 12 weeks post SCI (Figure 2a,b,d). In the two groups where mice were grafted with NSC-seeded PCS, the increased neuron density compared to the untreated control could be attributed to multiple possible mechanisms, including the secretion of neurotrophic factors by NSCs [44] and the

partial differentiation of NSCs into neurons. Quantification of Tuj1$^+$ neurons in the lesion epicenter shows that 13–25% of neurons were derived from implanted NSCs (Figure 5e), suggesting that neuronal NSC differentiation cannot solely explain the increased neuronal density in the two graft-treated groups. Furthermore, we report that systemic administration of BNN27 increased neuron density in the lesion epicenter at 12 wpi (Figure 2a,b,d). This observation agrees with BNN27 neuroprotection effects reported in various neuron types in several in vitro and in vivo studies [26,27]. It also agrees with published reports on the ability of NGF administration to decrease neuron loss after SCI [16,17]. As previously reported for NGF [9,22], BNN27 effects on neurons following SCI could be mediated either directly (via NGF receptors) or indirectly via effects on other cell types. The combinatorial treatment of NSC-seeded PCS grafts and systemic BNN27 administration did not statistically increase neuronal density compared to the one in the two animal groups that received each treatment separately (Figure 2d), although BNN27 administration increased the fraction of Tuj1$^+$ neurons in the lesion epicenter that originated from NSCs (Figure 5e).

A major motivation of emerging NSC-based therapies for SCI is to deliver a significant population of neural cell precursors in the lesion in order to complement the limited number of endogenous precursor cells and enhance the synthesis of new neural tissue and its connection with the surrounding spared tissue. However, previous studies have highlighted the low post-implantation survival of NSCs in SCI lesions as a major challenge that impedes the long-term efficacy of such NSC-based SCI treatments [45]. For instance, a study showed that just 4.6% of transplanted NSCs survived at 9 wpi [46]. Additionally, implanted NSCs had a low proliferation rate in situ [47]. Overall, NSC survival has been shown to depend strongly on the methodology and timepoint of delivery. NSC survival was lower when NSCs were transplanted in the acute phase of injury (1%) compared to the subacute one (6%) [48,49]. This deficiency could be caused by early immunoreaction events at the lesion site, which are toxic to implanted cells [50,51]. Strategies for protecting implanted NSCs from the harsh SCI lesion environment include delivering NSCs inside biomaterials (such as the PCS utilized in this study) and providing anti-apoptotic support via small molecule compounds or biologics. Indeed, herein we report that BNN27 administration doubled the density of implanted NSC-derived cells within the grafted lesion at 12 wpi from $7.51 \times 10^5 \pm 1.25 \times 10^5$ cells/mm^3 (when injured animals were treated only with NSC-seeded grafts) to $15.24 \times 10^5 \pm 2.57 \times 10^5$ cells/mm^3 (animals treated with both NSC-seeded scaffold grafts and systemic BNN27 administration) (Figure 5a,b). Comparison of these cell density measurements with data from previous studies is usually not straightforward because they utilized different experimental protocols (injury, cell seeding). Furthermore, very few published studies have quantified the number or density of cells derived from implanted NSC grafts within the lesion site. Nevertheless, our measurements on the density of implanted NSC-derived cells in the lesion are of the same order of magnitude as the ones reported in a study that grafted human neural stem/progenitor cells (NSPCs) within a fibrin–thrombin hydrogel [52].

Another major challenge of NSC-based SCI treatments is that NSCs differentiate mostly into glial cells and poorly towards neurons, as the lesion environment is unfavorable for neuronal differentiation [49,51,53–55]. Significant research has attempted to guide the fate of implanted NSCs using biomaterials and growth factors that enhance neuronal survival and differentiation [55]. Herein, our data show that, although BNN27 did not affect the differentiation of implanted NSCs, approximately 20% of implanted NSCs differentiated towards the neuronal fate by 12 wpi (Figure 5d), in agreement with our previous findings [8]. Furthermore, our data show an interesting spatial organization pattern for implanted NSC-derived cells in the presence or absence of BNN27 (Figure 4a). Implanted NSCs that differentiated into astrocytes became part of the glial scar and were localized in the lesion boundary region (Figure 4a,b). On the other hand, implanted NSCs that differentiated towards neurons were localized within the lesion epicenter, replenishing lost neurons. This spatial pattern has also been described by Lien et al. [56]. Finally, we demonstrate that implanted NSCs differentiated to various types of neurons (Figure 4c), including

GABAergic neurons, dopaminergic neurons and glutamatergic neurons in the presence or absence of BNN27. The presence of implanted NSC-derived GAD67$^+$ GABAergic neurons, VGLUT1$^+$ glutamatergic and 3TH$^+$ dopaminergic neurons has been reported in rat SCI models [43,57].

The observed BNN27 effects on the density and fate of implanted NSC-derived cells could originate in various mechanisms, including direct BNN27 effects on NSCs, NSC-derived neural cells and intermediate precursors or indirect effects via other cells that participate in SCI wound healing. Regarding BNN27 effects on NSCs, various types of embryonic rodent NSCs have been reported to express both p75^{NTR} and TrkA NGF receptors [58,59]. Moreover, there are reports that NGF can increase proliferation in NSCs isolated from embryonic E14 rat brain or adult rat spinal cord [60,61]. BNN27 has demonstrated neuroprotective effects on various types of neurons mediated via NGF receptors [26,27], although no prior study has demonstrated direct effects on spinal cord neurons or NSC-derived neurons. Finally, BNN27 neuroprotective effects could also be mediated by indirect effects in SCI lesions. For instance, the ability of BNN27 to decrease astrogliosis, described above, could facilitate NSC survival and enhance the integration of NSC-derived neurons.

Apart from quantifying the effects of BNN27 in SCI, the present study further highlights the ability of NSC-seeded PCS grafts to enhance important SCI processes, which were not affected by BNN27 administration. First, grafting SCI lesions with NSC-seeded PCS grafts resulted in significantly larger fraction of synaptophysin$^+$ pixels (Figure 3a–d), suggesting enhanced neuronal integration and communication in the lesion epicenter. Indeed, specific NSPC grafts have been shown able to organize, become synaptically active and interact with host axons [62]. Second, grafting SCI lesions with NSC-seeded PCS enhanced axonal elongation caudally to the epicenter (Supplementary Materials: Figure S3), in agreement with previous measurements of axonal elongation at 6 and 9 wpi [8]. Several studies have shown that NSPC implantation can lead to extensive axonal regeneration of both host axons into the graft and axons of NSPC-derived neurons caudally to the lesion over long distances [5,57]. Third, our work shows that GFP$^+$ implanted NSC-derived cells crossed the astrogliotic boundary and migrated a few hundred micrometers caudally to the lesion, but not much further to create ectopic colonies, a key limitation of NSC delivery in suspension [8]. Finally, our data show that NSC-seeded PCS enhanced angiogenesis, a critical process related to enhanced functional recovery, since endogenous angiogenesis following SCI is not sufficient to replace lost blood vessels [63,64]. Herein, we show that NSC-seeded PCS grafts increased the number of αSMA$^+$ vessels within the lesion site (Figure 3e–g), in agreement with the reported ability of transplanted embryonic stem cell-derived neural progenitors to enhance angiogenesis in mouse SCI lesions [65,66].

5. Conclusions

This study presents the first demonstration of therapeutic effects of MNTs in an animal model of CNS injury. It shows that systemic administration of BNN27 had significant effects on astrogliosis and neuronal density following dorsal column SCI in mice. BNN27 administration also significantly increased the density of cells derived from implanted NSCs, possibly addressing a major challenge of emerging NSC-based cell therapies. Considering a wider perspective, our study suggests that MNTs can contribute to combinatorial treatments for CNS injuries by simultaneously enhancing cell therapies and modulating the loss of neuronal tissue. MNT contribution in such treatments could be further enhanced by optimizing MNT dosing, exploiting novel MNT designs that target specific neurotrophin receptors [67,68] or utilizing targeted methods to control their spatiotemporal delivery within CNS lesions.

Supplementary Materials: The following supporting information can be downloaded at: https://www.mdpi.com/article/10.3390/biomedicines11041170/s1, Figure S1: YFP-expressing NSCs; Figure S2: Raw data of the fault rate response in the horizontal ladder walking assay per experimental group; Figure S3: Effects of NSC-seeded PCS on axonal elongation.

Author Contributions: Conceptualization, D.S.T., A.G., I.C. and K.G.; methodology, K.G., D.S.T., A.G., I.C. and K.K.; validation, K.G., D.S.T. and K.K.; formal analysis, K.G., D.S.T., E.-A.S. and A.P.; investigation, K.G. and E.-A.S.; resources, D.S.T., A.G., I.C. and K.K.; data curation, K.G. and D.S.T.; writing—original draft preparation, K.G. and D.S.T.; writing—review and editing, K.G., D.S.T., A.G., I.C. and K.K.; visualization, K.G. and D.S.T.; supervision, D.S.T., A.G. and I.C.; project administration, D.S.T., A.G., I.C. and K.K; funding acquisition, D.S.T., K.K. and K.G. All authors have read and agreed to the published version of the manuscript.

Funding: This research was funded by the Hellenic Foundation for Research and Innovation (HFRI) and the General Secretariat for Research and Technology (GSRT) under grant agreement No 1635 to D.T. and K.K., and a State Scholarships Foundation (IKY) scholarship to K.G.

Institutional Review Board Statement: Animal care and experimentation protocols were performed according to the approval of the Veterinary Directorate of the region of Crete in compliance with Greek Government guidelines, EU guidelines 2010/63/EU, FORTH ethics committee guidelines and in accordance with approved protocols from the Federation of European Laboratory Animal Science Associations (FELASA) on use of laboratory animals. Facility License number: EL91-BIOexp-02, Project title: "Investigating the effects of neurotrophins and their synthetic analogues on the mechanisms of neurodegeneration and neurogenesis in Alzheimer's disease and the effect of neuroimplants based on porous collagen scaffolds in the central nervous system trauma", Approval numbers: 262272 and 360667, date of initial approval: 29 October 2018. Date of reapproval: 29 November 2021.

Informed Consent Statement: Not applicable.

Data Availability Statement: Data are available within the article or in Supplementary Materials. Raw data are available upon reasonable request.

Acknowledgments: We thank D. Karagogeos (University of Crete) for the kind gift of L1 antibody and F. Moschogiannaki for assistance in scaffold fabrication.

Conflicts of Interest: The authors declare no conflict of interest.

Abbreviations

ANOVA: analysis of variance, BBB: blood–brain barrier, BSA: bovine serum albumin, ChABC: chondroitinase ABC, CNS: central nervous system, GAD67: glutamic acid decarboxylase 67, GFAP: glial fibrillary acidic protein, GFP: green fluorescent protein, MNT: microneurotrophin, NSC: neural stem cell, NSPC: neural stem/progenitor cell, PBS: phosphate-buffered saline, PBST: Triton X-100 in PBS, PCS: porous collagen scaffold, PFA: paraformaldehyde, PNS: peripheral nervous system, ROI: region of interest, SCI: spinal cord injury, SEM: standard error of the mean, VGLUT1: vesicular glutamate transporter 1, wpi: week post injury, YFP: yellow fluorescent protein, αSMA: α-smooth muscle actin, 3TH: tyrosine hydroxylase.

References

1. Zimmermann, R.; Alves, Y.V.; Sperling, L.E.; Pranke, P. Nanotechnology for the Treatment of Spinal Cord Injury. *Tissue Eng. Part B Rev.* **2021**, *27*, 353–365. [CrossRef]
2. Silva, N.A.; Sousa, N.; Reis, R.L.; Salgado, A.J. From basics to clinical: A comprehensive review on spinal cord injury. *Prog. Neurobiol.* **2014**, *114*, 25–57. [CrossRef] [PubMed]
3. Salgado, A.J.; Gomes, E.D.; Silva, N.A. Combinatorial therapies for spinal cord injury: Strategies to induce regeneration. *Neural Regen. Res.* **2019**, *14*, 69–71. [CrossRef] [PubMed]
4. Assinck, P.; Duncan, G.J.; Hilton, B.J.; Plemel, J.R.; Tetzlaff, W. Cell transplantation therapy for spinal cord injury. *Nat. Neurosci.* **2017**, *20*, 637–647. [CrossRef] [PubMed]

5. Kadoya, K.; Lu, P.; Nguyen, K.; Lee-Kubli, C.; Kumamaru, H.; Yao, L.; Knackert, J.; Poplawski, G.; Dulin, J.N.; Strobl, H.; et al. Spinal cord reconstitution with homologous neural grafts enables robust corticospinal regeneration. *Nat. Med.* **2016**, *22*, 479–487. [CrossRef]
6. Lu, P.; Gomes-Leal, W.; Anil, S.; Dobkins, G.; Huie, J.R.; Ferguson, A.; Graham, L.; Tuszynski, M. Origins of Neural Progenitor Cell-Derived Axons Projecting Caudally after Spinal Cord Injury. *Stem Cell Rep.* **2019**, *13*, 105–114. [CrossRef] [PubMed]
7. Curtis, E.; Martin, J.R.; Gabel, B.; Sidhu, N.; Rzesiewicz, T.K.; Mandeville, R.; Van Gorp, S.; Leerink, M.; Tadokoro, T.; Marsala, S.; et al. A First-in-Human, Phase I Study of Neural Stem Cell Transplantation for Chronic Spinal Cord Injury. *Cell Stem Cell* **2018**, *22*, 941–950.e6. [CrossRef] [PubMed]
8. Kourgiantaki, A.; Tzeranis, D.S.; Karali, K.; Georgelou, K.; Bampoula, E.; Psilodimitrakopoulos, S.; Yannas, I.V.; Stratakis, E.; Sidiropoulou, K.; Charalampopoulos, I.; et al. Neural stem cell delivery via porous collagen scaffolds promotes neuronal differentiation and locomotion recovery in spinal cord injury. *NPJ Regen. Med.* **2020**, *5*, 12. [CrossRef]
9. Widenfalk, J.; Lundströmer, K.; Jubran, M.; Brené, S.; Olson, L. Neurotrophic factors and receptors in the immature and adult spinal cord after mechanical injury or kainic acid. *J. Neurosci.* **2001**, *21*, 3457–3475. [CrossRef]
10. Griffin, J.M.; Bradke, F. Therapeutic repair for spinal cord injury: Combinatory approaches to address a multifaceted problem. *EMBO Mol. Med.* **2020**, *12*, e11505. [CrossRef]
11. Krenz, N.R.; Weaver, L.C. Nerve Growth Factor in Glia and Inflammatory Cells of the Injured Rat Spinal Cord. *J. Neurochem.* **2001**, *74*, 730–739. [CrossRef] [PubMed]
12. Davis-López De Carrizosa, M.A.; Morado-Díaz, C.J.; Morcuende, S.; De La Cruz, R.R.; Pastor, Á.M. Nerve growth factor regulates the firing patterns and synaptic composition of motoneurons. *J. Neurosci.* **2010**, *30*, 8308–8319. [CrossRef]
13. Aloe, L.; Bianchi, P.; De Bellis, A.; Soligo, M.; Rocco, M.L. Intranasal nerve growth factor bypasses the blood-brain barrier and affects spinal cord neurons in spinal cord injury. *Neural Regen. Res.* **2014**, *9*, 1025–1030. [CrossRef] [PubMed]
14. Grill, R.; Blesch, A.; Tuszynski, M. Robust Growth of Chronically Injured Spinal Cord Axons Induced by Grafts of Genetically Modified NGF-Secreting Cells. *Exp. Neurol.* **1997**, *148*, 444–452. [CrossRef] [PubMed]
15. Tuszynski, M.H.; Murai, K.; Blesch, A.; Grill, R.; Miller, I. Functional Characterization of Ngf-Secreting Cell Grafts to the Acutely Injured Spinal Cord. *Cell Transplant.* **1997**, *6*, 361–368. [CrossRef] [PubMed]
16. Zhang, H.; Wu, F.; Kong, X.; Yang, J.; Chen, H.; Deng, L.; Cheng, Y.; Ye, L.; Zhu, S.; Zhang, X.; et al. Nerve growth factor improves functional recovery by inhibiting endoplasmic reticulum stress-induced neuronal apoptosis in rats with spinal cord injury. *J. Transl. Med.* **2014**, *12*, 130. [CrossRef]
17. Song, Z.; Wang, Z.; Shen, J.; Xu, S.; Hu, Z. Nerve growth factor delivery by ultrasound-mediated nanobubble destruction as a treatment for acute spinal cord injury in rats. *Int. J. Nanomed.* **2017**, *12*, 1717–1729. [CrossRef] [PubMed]
18. Wu, Q.; Xiang, Z.; Ying, Y.; Huang, Z.; Tu, Y.; Chen, M.; Ye, J.; Dou, H.; Sheng, S.; Li, X.; et al. Nerve growth factor (NGF) with hypoxia response elements loaded by adeno-associated virus (AAV) combined with neural stem cells improve the spinal cord injury recovery. *Cell Death Discov.* **2021**, *7*, 301. [CrossRef]
19. Wang, L.; Gu, S.; Gan, J.; Tian, Y.; Zhang, F.; Zhao, H.; Lei, D. Neural Stem Cells Overexpressing Nerve Growth Factor Improve Functional Recovery in Rats Following Spinal Cord Injury via Modulating Microenvironment and Enhancing Endogenous Neurogenesis. *Front. Cell. Neurosci.* **2021**, *15*, 773375. [CrossRef]
20. Faustino, C.; Rijo, P.; Reis, C.P. Nanotechnological strategies for nerve growth factor delivery: Therapeutic implications in Alzheimer's disease. *Pharmacol. Res.* **2017**, *120*, 68–87. [CrossRef]
21. Tuszynski, M.H.; Peterson, D.A.; Ray, J.; Baird, A.; Nakahara, Y.; Gages, F.H. Fibroblasts genetically modified to produce Nerve Growth Factor Induce Robust Neuritic Ingrowth after Grafting to the Spinal Cord. *Exp. Neurol.* **1994**, *126*, 1–14. [CrossRef]
22. Tuszynski, M.H.; Gabriel, K.; Gage, F.H.; Suhr, S.; Meyer, S.; Rosetti, A. Nerve growth factor delivery by gene transfer induces dif-ferential outgrowth of sensory, motor, and noradrenergic neurites after adult spinal cord injury. *Exp. Neurol.* **1996**, *137*, 157–173. [CrossRef] [PubMed]
23. Feng, S.-Q.; Kong, X.-H.; Liu, Y.; Ban, D.-X.; Ning, G.-Z.; Chen, J.-T.; Guo, S.-F.; Wang, P. Regeneration of spinal cord with cell and gene therapy. *Orthop Surg.* **2009**, *1*, 153–163. [CrossRef] [PubMed]
24. Keefe, K.M.; Sheikh, I.S.; Smith, G.M. Targeting Neurotrophins to Specific Populations of Neurons: NGF, BDNF, and NT-3 and Their Relevance for Treatment of Spinal Cord Injury. *Int. J. Mol. Sci.* **2017**, *18*, 548. [CrossRef]
25. Gravanis, A.; Pediaditakis, I.; Charalampopoulos, I. Synthetic microneurotrophins in therapeutics of neurodegeneration. *Oncotarget* **2017**, *8*, 9005–9006. [CrossRef]
26. Pediaditakis, I.; Efstathopoulos, P.; Prousis, K.C.; Zervou, M.; Arévalo, J.C.; Alexaki, V.I.; Nikoletopoulou, V.; Karagianni, E.; Potamitis, C.; Tavernarakis, N.; et al. Selective and differential interactions of BNN27, a novel C17-spiroepoxy steroid derivative, with TrkA receptors, regulating neuronal survival and differentiation. *Neuropharmacology* **2016**, *111*, 266–282. [CrossRef] [PubMed]
27. Pediaditakis, I.; Kourgiantaki, A.; Prousis, K.C.; Potamitis, C.; Xanthopoulos, K.P.; Zervou, M.; Calogeropoulou, T.; Charalampopoulos, I.; Gravanis, A. BNN27, a 17-Spiroepoxy Steroid Derivative, Interacts With and Activates p75 Neurotrophin Receptor, Rescuing Cerebellar Granule Neurons from Apoptosis. *Front. Pharmacol.* **2016**, *7*, 512. [CrossRef]
28. Ibán-Arias, R.; Lisa, S.; Mastrodimou, N.; Kokona, D.; Koulakis, E.; Iordanidou, P.; Kouvarakis, A.; Fothiadaki, M.; Papadogkonaki, S.; Sotiriou, A.; et al. The Synthetic Microneurotrophin BNN27 Affects Retinal Function in Rats With Streptozotocin-Induced Diabetes. *Diabetes* **2017**, *67*, 321–333. [CrossRef]

29. Ibán-Arias, R.; Lisa, S.; Poulaki, S.; Mastrodimou, N.; Charalampopoulos, I.; Gravanis, A.; Thermos, K. Effect of topical administration of the microneurotrophin BNN27 in the diabetic rat retina. *Graefe's Arch. Clin. Exp. Ophthalmol.* **2019**, *257*, 2429–2436. [CrossRef] [PubMed]
30. Bonetto, G.; Charalampopoulos, I.; Gravanis, A.; Karagogeos, D. The novel synthetic microneurotrophin BNN27 protects mature oligodendrocytes against cuprizone-induced death, through the NGF receptor TrkA. *Glia* **2017**, *65*, 1376–1394. [CrossRef]
31. The Jackson Laboratory. C57BL/6J. Available online: https://www.jax.org/strain/000664 (accessed on 18 November 2022).
32. Mouse Genome Informatics. 129X1/SvJ. Available online: http://www.informatics.jax.org/strain/MGI:3044210 (accessed on 18 November 2022).
33. The Jackson Laboratory. B6.C-Tg(CMV-cre)1Cgn/Je. Available online: https://www.jax.org/strain/0060543044210 (accessed on 18 November 2022).
34. Harrison, M.; O'Brien, A.; Adams, L.; Cowin, G.; Ruitenberg, M.J.; Sengul, G.; Watson, C. Vertebral landmarks for the identification of spinal cord segments in the mouse. *Neuroimage* **2013**, *68*, 22–29. [CrossRef]
35. Farr, T.D.; Liu, L.; Colwell, K.L.; Whishaw, I.Q.; Metz, G.A. Bilateral alteration in stepping pattern after unilateral motor cortex injury: A new test strategy for analysis of skilled limb movements in neurological mouse models. *J. Neurosci. Methods* **2006**, *153*, 104–113. [CrossRef] [PubMed]
36. Savvaki, M.; Kafetzis, G.; Kaplanis, S.; Ktena, N.; Theodorakis, K.; Karagogeos, D. Neuronal, but not glial, Contactin 2 negatively regulates axon regeneration in the injured adult optic nerve. *Eur. J. Neurosci.* **2021**, *53*, 1705–1721. [CrossRef]
37. Bennett, J.P.; O'Brien, L.C.; Brohawn, D.G. Pharmacological properties of microneurotrophin drugs developed for treatment of amyotrophic lateral sclerosis. *Biochem. Pharmacol.* **2016**, *117*, 68–77. [CrossRef] [PubMed]
38. Tsika, C.; Tzatzarakis, M.N.; Antimisiaris, S.G.; Tsoka, P.; Efstathopoulos, P.; Charalampopoulos, I.; Gravanis, A.; Tsilimbaris, M.K. Quantification of BNN27, a novel neuroprotective 17-spiroepoxy dehydroepiandrosterone derivative in the blood and retina of rodents, after single intraperitoneal administration. *Pharmacol. Res. Perspect.* **2021**, *9*, e00724. [CrossRef]
39. Bradbury, E.J.; Moon, L.D.F.; Popat, R.J.; King, V.R.; Bennett, G.S.; Patel, P.N.; Fawcett, J.W.; McMahon, S.B. Chondroitinase ABC promotes functional recovery after spinal cord injury. *Nature* **2002**, *416*, 636–640. [CrossRef] [PubMed]
40. Ferraro, G.B.; Alabed, Y.; Fournier, A. Molecular Targets to Promote Central Nervous System Regeneration. *Curr. Neurovascular Res.* **2004**, *1*, 61–75. [CrossRef]
41. Gaudet, A.D.; Fonken, L.K. Glial Cells Shape Pathology and Repair After Spinal Cord Injury. *Neurotherapeutics* **2018**, *15*, 554–577. [CrossRef]
42. Spilker, M.H.; Yannas, I.V.; Kostyk, S.K.; Norregaard, T.V.; Hsu, H.P.; Spector, M. The Effects of Tubulation on Healing and Scar Formation after Transection of the Adult Rat Spinal Cord. *Restor. Neurol. Neurosci.* **2021**, *18*, 23–38.
43. Li, X.; Liu, S.; Zhao, Y.; Li, J.; Ding, W.; Han, S.; Chen, B.; Xiao, Z.; Dai, J. Training Neural Stem Cells on Functional Collagen Scaffolds for Severe Spinal Cord Injury Repair. *Adv. Funct. Mater.* **2016**, *26*, 5835–5847. [CrossRef]
44. Lu, P.; Jones, L.; Snyder, E.; Tuszynski, M. Neural stem cells constitutively secrete neurotrophic factors and promote extensive host axonal growth after spinal cord injury. *Exp. Neurol.* **2003**, *181*, 115–129. [CrossRef]
45. Lepore, A.; Fischer, I. Lineage-restricted neural precursors survive, migrate, and differentiate following transplantation into the injured adult spinal cord. *Exp. Neurol.* **2005**, *194*, 230–242. [CrossRef]
46. Hwang, D.H.; Shin, H.Y.; Kwon, M.J.; Choi, J.Y.; Ryu, B.-Y.; Kim, B.G. Survival of Neural Stem Cell Grafts in the Lesioned Spinal Cord Is Enhanced by a Combination of Treadmill Locomotor Training via Insulin-Like Growth Factor-1 Signaling. *J. Neurosci.* **2014**, *34*, 12788–12800. [CrossRef] [PubMed]
47. Karimi-Abdolrezaee, S.; Eftekharpour, E.; Wang, J.; Morshead, C.M.; Fehlings, M.G. Delayed Transplantation of Adult Neural Precursor Cells Promotes Remyelination and Functional Neurological Recovery after Spinal Cord Injury. *J. Neurosci.* **2006**, *26*, 3377–3389. [CrossRef] [PubMed]
48. Parr, A.M.; Kulbatski, I.; Tator, C.H. Transplantation of Adult Rat Spinal Cord Stem/Progenitor Cells for Spinal Cord Injury. *J. Neurotrauma* **2007**, *24*, 835–845. [CrossRef] [PubMed]
49. Liu, S.; Chen, Z. Employing Endogenous NSCs to Promote Recovery of Spinal Cord Injury. *Stem Cells Int.* **2019**, *2019*, 1958631. [CrossRef] [PubMed]
50. Wilcox, J.T.; Satkunendrarajah, K.; Zuccato, J.A.; Nassiri, F.; Fehlings, M.G. Neural Precursor Cell Transplantation Enhances Functional Recovery and Reduces Astrogliosis in Bilateral Compressive/Contusive Cervical Spinal Cord Injury. *STEM CELLS Transl. Med.* **2014**, *3*, 1148–1159. [CrossRef]
51. Younsi, A.; Zheng, G.; Riemann, L.; Scherer, M.; Zhang, H.; Tail, M.; Hatami, M.; Skutella, T.; Unterberg, A.; Zweckberger, K. Long-Term Effects of Neural Precursor Cell Transplantation on Secondary Injury Processes and Functional Recovery after Severe Cervical Contusion-Compression Spinal Cord Injury. *Int. J. Mol. Sci.* **2021**, *22*, 13106. [CrossRef]
52. Rosenzweig, E.S.; Brock, J.H.; Lu, P.; Kumamaru, H.; Salegio, E.A.; Kadoya, K.; Weber, J.L.; Liang, J.J.; Moseanko, R.; Hawbecker, S.; et al. Restorative effects of human neural stem cell grafts on the primate spinal cord. *Nat. Med.* **2018**, *24*, 484–490. [CrossRef]
53. Cao, Q.L.; Zhang, Y.P.; Howard, R.M.; Walters, W.M.; Tsoulfas, P.; Whittemore, S.R. Pluripotent stem cells engrafted into the normal or lesioned adult rat spinal cord are restricted to a glial lineage. *Exp. Neurol.* **2001**, *167*, 48–58. [CrossRef]
54. Zhu, Y.; Uezono, N.; Yasui, T.; Nakashima, K. Neural stem cell therapy aiming at better functional recovery after spinal cord injury. *Dev. Dyn.* **2017**, *247*, 75–84. [CrossRef] [PubMed]

55. Xue, W.; Fan, C.; Chen, B.; Zhao, Y.; Xiao, Z.; Dai, J. Direct neuronal differentiation of neural stem cells for spinal cord injury repair. *STEM CELLS* **2021**, *39*, 1025–1032. [CrossRef] [PubMed]
56. Lien, B.V.; Tuszynski, M.H.; Lu, P. Astrocytes migrate from human neural stem cell grafts and functionally integrate into the injured rat spinal cord. *Exp. Neurol.* **2019**, *314*, 46–57. [CrossRef] [PubMed]
57. Lu, P.; Wang, Y.; Graham, L.; McHale, K.; Gao, M.; Wu, D.; Brock, J.; Blesch, A.; Rosenzweig, E.S.; Havton, L.A.; et al. Long-Distance Growth and Connectivity of Neural Stem Cells after Severe Spinal Cord Injury. *Cell* **2012**, *150*, 1264–1273. [CrossRef] [PubMed]
58. Lachyankar, M.B.; Condon, P.J.; Quesenberry, P.J.; Litofsky, N.; Recht, L.D.; Ross, A.H. Embryonic Precursor Cells That Express Trk Receptors: Induction of Different Cell Fates by NGF, BDNF, NT-3, and CNTF. *Exp. Neurol.* **1997**, *144*, 350–360. [CrossRef]
59. Kumar, V.; Gupta, A.K.; Shukla, R.K.; Tripathi, V.K.; Jahan, S.; Pandey, A.; Srivastava, A.; Agrawal, M.; Yadav, S.; Khanna, V.K.; et al. Molecular Mechanism of Switching of TrkA/p75NTR Signaling in Monocrotophos Induced Neurotoxicity. *Sci. Rep.* **2015**, *5*, srep14038. [CrossRef]
60. Oliveira, S.L.; Trujillo, C.A.; Negraes, P.D.; Ulrich, H. Effects of ATP and NGF on Proliferation and Migration of Neural Precursor Cells. *Neurochem. Res.* **2015**, *40*, 1849–1857. [CrossRef] [PubMed]
61. Han, Y.; Kim, K.T. Neural growth factor stimulates proliferation of spinal cord derived-neural precursor/stem cells. *J. Korean Neurosurg. Soc.* **2016**, *59*, 437–441. [CrossRef]
62. Ceto, S.; Sekiguchi, K.J.; Takashima, Y.; Nimmerjahn, A.; Tuszynski, M.H. Neural Stem Cell Grafts Form Extensive Synaptic Networks that Integrate with Host Circuits after Spinal Cord Injury. *Cell Stem Cell* **2020**, *27*, 430–440.e5. [CrossRef] [PubMed]
63. Yao, C.; Cao, X.; Yu, B. Revascularization After Traumatic Spinal Cord Injury. *Front. Physiol.* **2021**, *12*, 631500. [CrossRef] [PubMed]
64. Tsivelekas, K.K.; Evangelopoulos, D.S.; Pallis, D.; Benetos, I.S.; Papadakis, S.A.; Vlamis, J.; Pneumaticos, S.G. Angiogenesis in Spinal Cord Injury: Progress and Treatment. *Cureus* **2022**, *14*, e25475. [CrossRef]
65. Kumagai, G.; Okada, Y.; Yamane, J.; Nagoshi, N.; Kitamura, K.; Mukaino, M.; Tsuji, O.; Fujiyoshi, K.; Katoh, H.; Okada, S.; et al. Roles of ES Cell-Derived Gliogenic Neural Stem/Progenitor Cells in Functional Recovery after Spinal Cord Injury. *PLoS ONE* **2009**, *4*, e7706. [CrossRef] [PubMed]
66. Nori, S.; Okada, Y.; Yasuda, A.; Tsuji, O.; Takahashi, Y.; Kobayashi, Y.; Fujiyoshi, K.; Koike, M.; Uchiyama, Y.; Ikeda, E.; et al. Grafted human-induced pluripotent stem-cell-derived neurospheres promote motor functional recovery after spinal cord injury in mice. *Proc. Natl. Acad. Sci. USA* **2011**, *108*, 16825–16830. [CrossRef] [PubMed]
67. Rogdakis, T.; Charou, D.; Latorrata, A.; Papadimitriou, E.; Tsengenes, A.; Athanasiou, C.; Papadopoulou, M.; Chalikiopoulou, C.; Katsila, T.; Ramos, I.; et al. Development and Biological Characterization of a Novel Selective TrkA Agonist with Neuroprotective Properties against Amyloid Toxicity. *Biomedicines* **2022**, *10*, 614. [CrossRef] [PubMed]
68. Yilmaz, C.; Rogdakis, T.; Latorrata, A.; Thanou, E.; Karadima, E.; Papadimitriou, E.; Siapi, E.; Li, K.W.; Katsila, T.; Calogeropoulou, T.; et al. ENT-A010, a Novel Steroid Derivative, Displays Neuroprotective Functions and Modulates Microglial Responses. *Biomolecules* **2022**, *12*, 424. [CrossRef] [PubMed]

Disclaimer/Publisher's Note: The statements, opinions and data contained in all publications are solely those of the individual author(s) and contributor(s) and not of MDPI and/or the editor(s). MDPI and/or the editor(s) disclaim responsibility for any injury to people or property resulting from any ideas, methods, instructions or products referred to in the content.

npj | Regenerative Medicine

www.nature.com/npjregenmed

ARTICLE OPEN

Neural stem cell delivery via porous collagen scaffolds promotes neuronal differentiation and locomotion recovery in spinal cord injury

Alexandra Kourgiantaki[1,2,6], Dimitrios S. Tzeranis[2,3,6], Kanelina Karali[1,2,6], Konstantina Georgelou[1,2], Efstathia Bampoula[4], Sotirios Psilodimitrakopoulos[5], Ioannis V. Yannas[3], Emmanuel Stratakis[5], Kyriaki Sidiropoulou[2,4], Ioannis Charalampopoulos[1,2] and Achille Gravanis[1,2]✉

Neural stem cell (NSC) grafts have demonstrated significant effects in animal models of spinal cord injury (SCI), yet their clinical translation remains challenging. Significant evidence suggests that the supporting matrix of NSC grafts has a crucial role in regulating NSC effects. Here we demonstrate that grafts based on porous collagen-based scaffolds (PCSs), similar to biomaterials utilized clinically in induced regeneration, can deliver and protect embryonic NSCs at SCI sites, leading to significant improvement in locomotion recovery in an experimental mouse SCI model, so that 12 weeks post-injury locomotion performance of implanted animals does not statistically differ from that of uninjured control animals. NSC-seeded PCS grafts can modulate key processes required to induce regeneration in SCI lesions including enhancing NSC neuronal differentiation and functional integration in vivo, enabling robust axonal elongation, and reducing astrogliosis. Our findings suggest that the efficacy and translational potential of emerging NSC-based SCI therapies could be enhanced by delivering NSC via scaffolds derived from well-characterized clinically proven PCS.

npj Regenerative Medicine (2020)5:12 ; https://doi.org/10.1038/s41536-020-0097-0

INTRODUCTION

Traumatic spinal cord injury (SCI) results in devastating disabilities that affect millions of patients worldwide. Current clinical treatment of SCI is limited to surgical intervention for spinal cord decompression[1] and the delivery of methylprednisolone, a corticosteroid of controversial efficacy[2]. The development of effective SCI treatments is still an unmet clinical need, as no treatment has demonstrated consistent efficiency and safety[3].

The multifactorial, complex nature of SCI[4] motivated the development of combinatorial treatments that would integrate the effects of diffusible factors (small molecules, neurotrophic factors, and biologics[5,6]), cell therapies, and biomaterials. In particular, cell-based treatments utilize stem cells to replace cells lost during SCI and enhance axonal elongation and synaptic plasticity[7]. Among several types of stem cells evaluated, neural stem cells (NSCs) are of particular interest, as they can differentiate to both neurons and glia, secrete neurotrophic factors, and their application does not suffer from the safety concerns of pluripotent stem cells[8]. Indeed, several NSC-based grafts have provided encouraging results in rodent and primate SCI models[9–12].

However, the clinical translation of NSC treatments remains challenging. The first phase I clinical trial of a human NSC cell line in chronic SCI patients reported encouraging safety results but very limited efficacy[13], possibly due to NSC delivery in suspension. Indeed, several studies have demonstrated that NSC delivery at SCI sites without a supporting matrix results in extensive cell death, poor neuronal differentiation, and suspension leak away from the lesion site[14,15]. Several of these obstacles can be overcome by delivering NSCs inside biomaterials. Biomaterials can enhance NSC therapies by localizing cell delivery at the injury site, filling the lesion cavity volume, protecting delivered cells from immune attack, and enhancing axonal elongation by providing adhesion cues and downregulating deleterious inflammation and scar formation[16–20]. Although certain NSC grafts have utilized biomaterials (e.g., fibrin hydrogels, collagen gels), none of them has received regulatory approval before[9–11,21].

On the other hand, porous collagen-based scaffolds (PCSs) have revolutionized the clinical treatment of severe injuries in skin and peripheral nerves. However, 40 years after the discovery of their ability to induce dermis regeneration[22], PCS have not managed to impact the clinical treatment of central nervous system (CNS) injuries, including SCI. Cell-free PCS grafts applied to full-transection rat SCI models managed to reduce and favorably align the resulting collagenous scar tissue and reduce cyst cavity formation at the lesion site[16,19]. In the same rat transection SCI model, NSC-seeded PCS grafts did not induce significant functional improvement compared with cell-free grafts, possibly due to the difficult-to-reverse nature of full-transection SCI or the use of adult (instead of embryonic) NSCs. Despite the large number of studies that report effects on NSCs by various biomaterials, including a few that utilized porous scaffolds (in this work, the term "scaffold" refers to a porous biomaterial fabricated in dry state, therefore excludes hydrogels)[23,24], these reports usually have lack detailed characterization of the biomaterial used (e.g., structure, in-vivo degradation, surface chemistry) and cannot be used to draw conclusions on the specific biomaterial features that have significant regenerative effects in SCI in vivo. No prior study has described in detail the effects of PCS

[1]Department of Pharmacology, School of Medicine, University of Crete, Heraklion 71003, Greece. [2]Institute of Molecular Biology and Biotechnology, Foundation for Research and Technology–Hellas, Heraklion 71003, Greece. [3]Department of Mechanical Engineering, Massachusetts Institute of Technology, Cambridge, MA 02139, USA. [4]Department of Biology, University of Crete, Heraklion 71003, Greece. [5]Institute of Electronic Structure and Laser, Foundation for Research and Technology–Hellas, Heraklion 71003, Greece. [6]These authors contributed equally: Alexandra Kourgiantaki, Dimitrios S. Tzeranis, Kanelina Karali. ✉email: gravania@uoc.gr

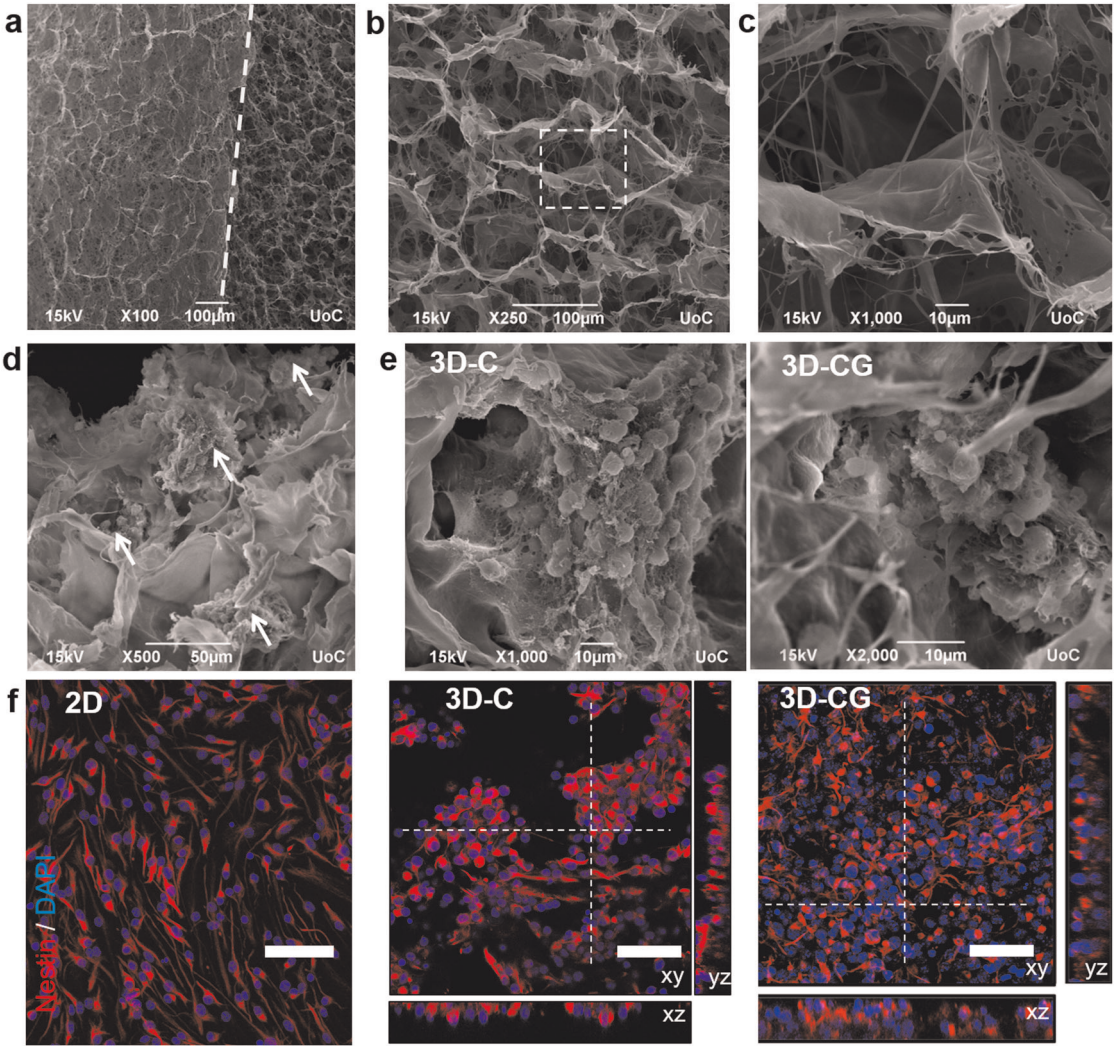

Fig. 1 3D culture of mouse embryonic neural stem cells inside porous collagen-based scaffolds. a SEM image highlighting the interface (dashed line) between the scaffold surface (left) and the scaffold interior (right). **b** SEM image of a porous collagen-GAG scaffold highlighting its porous structure. **c** High-magnification image of the region shown in **b**. **d** SEM image of neurospheres (white arrows) grown inside a collagen-GAG (3D-CG) scaffold at 3 DIV. **e** SEM images of neurospheres grown inside collagen (3D-C) or collagen-GAG (3D-CG) scaffolds at 3 DIV. **f** Representative confocal fluorescence images of nestin$^+$ NSCs (red) grown on a PDL-laminin-coated coverslip (2D), inside a collagen scaffold (3D-C) or inside a collagen-GAG scaffold (3D-CG) at 3 DIV. Scale bars, 50 µm.

on potent NSCs and the ability of PCS to provide NSCs an appropriate support matrix at SCI sites. Motivated by the in-vivo effects of fibrin hydrogels to NSCs[9–11], and by the ability of keratinocyte-seeded Dermis Regeneration Template to accelerate epidermis formation in large skin wounds[22,25], here we evaluate whether PCS grafts could host NSCs and leverage the regenerative potential of NSCs in SCI in vivo.

The present study demonstrates that grafts based on well-characterized PCS[26,27], similar to Food and Drug Administration (FDA)-approved scaffolds utilized in regenerative medicine[22,25,28], can deliver and protect embryonic NSCs at SCI sites, leading to a statistically significant improvement in locomotion recovery in a mouse dorsal column crush SCI model, so that 12 weeks post-injury locomotion performance was not statistically different than uninjured animals. Extensive in vitro and in-vivo data demonstrate the ability of PCS grafts to modulate key processes required to induce regeneration in CNS lesions. PCS grafts protected NSCs and enabled NSC neural differentiation and functional integration in vivo, facilitated axonal elongation at the lesion site and through the lesion boundary, enabled NSC migration into the surrounding tissue, and reduced astrogliosis. Our findings suggest the development of a new generation of SCI grafts that will deliver NSCs via optimized scaffolds derived from well-characterized clinically proven PCS.

RESULTS

Establishment of 3D culture of NSCs inside PCSs in vitro

To study PCS–NSC interactions and prepare PCS grafts for implantation at SCI sites, a three-dimensional (3D) culture system based on PCS was established. NSCs were seeded and studied inside cylindrical samples of collagen scaffolds (denoted as 3D-C) similar to grafts utilized in peripheral nerve regeneration[27], or inside samples of porous collagen-glycosaminoglycan (GAG) scaffolds (denoted as 3D-CG) similar to grafts utilized in skin regeneration[22,25]. Compared with 3D-C, 3D-CG scaffolds contain chondroitin-6-sulfate (Ch6S). Both the PCS types were fabricated using identical protocols, leading to sponges of 0.5% mass fraction, 3-week in-vivo degradation half-life, and ≈95 µm mean pore diameter (Fig. 1a-c)[26,27]. NSCs were seeded in single-cell

suspension and easily infiltrated inside PCS pores, where they adhered to PCS struts as single cells (Fig. 1d, f) or formed neurosphere-like aggregates (Fig. 1e, f). After 3 days in vitro (DIV), >99% of cells stained for nestin (Fig. 1f). NSC activity did not cause detectable scaffold degradation after 10 DIV, suggesting that once seeded in PCS, NSCs can be manipulated for several days before grafting the resulting tissue construct into an SCI site.

Regulation of NSC proliferation, survival, and differentiation by PCSs in vitro

The effect of PCS composition on NSC proliferation and viability was evaluated by quantifying the fraction of nuclei that stain positively for Ki67 and propidium iodine (PI), respectively, in NSCs grown inside PCS or on poly-D-lysine (PDL)-laminin-coated coverslips (two-dimensional (2D) control). The fraction of $Ki67^+$ nuclei decreased progressively between 3 DIV and 10 DIV (Fig. 2a, b and Supplementary Fig. 1a). At 3 DIV, the fraction of $Ki67^+$ nuclei was significantly higher in NSCs grown on 2D (2D: 74.3 ± 3.3%, $n = 3$; 3D-C: 42.7 ± 8.1%, $n = 3$, $P < 0.05$; 3D-CG: 44.7 ± 5.9%, $n = 3$, $P < 0.05$; $P_{1\text{-way-ANOVA}} = 0.0187$). At 10 DIV, the fraction of $Ki67^+$ nuclei was significantly larger in 3D-CG culture (3D-CG: 23.0 ± 1.2%, $n = 3$; 3D-C: 8.3 ± 0.6%, $n = 3$; 2D: 16.3 ± 0.3%, $n = 3$; $P_{1\text{-way-ANOVA}} < 0.0001$). The fraction of PI^+ nuclei at 3 DIV was similar in all groups and progressively increased between 3 DIV and 7 DIV (Fig. 2c and Supplementary Fig. 1b). The effect of PCS composition on the fraction of PI^+ nuclei became statistically significant at 5 DIV (3D-CG: 33.4 ± 0.9%, $n = 3$; 3D-C: 10.8 ± 1.2%, $n = 3$, $P < 0.01$; 2D: 6.0 ± 0.1%, $n = 3$, $P < 0.01$; $P_{1\text{-way-ANOVA}} = 0.0002$). Overall, growing NSCs on laminin-coated coverslips or inside collagen-GAG scaffolds favored cell survival and proliferation compared with growing NSCs inside collagen scaffolds.

The effect of PCS chemical composition on NSC differentiation was investigated by growing NSCs inside porous scaffolds or on PDL-laminin-coated coverslips (2D culture control) for 3 days in complete medium and then 4 more days in a differentiation medium formulation that supports simultaneous NSC differentiation towards neurons, astrocytes, and oligodendrocytes. At 7 DIV, NSCs had differentiated mainly towards Glial fibrillary acidic protein $(GFAP)^+$ cells (glial-restricted progenitors and astrocytes) and less towards $Olig2^+$ (oligodendrocyte lineage) cells or $Tuj1^+$ neurons (Fig. 2d, e), in agreement with previous reports[29]. NSC differentiation in 2D culture resulted in a larger fraction of $Tuj1^+$ neurons than that of 3D-C culture (2D: 9.8 ± 0.4%, $n = 3$; 3D-C: 3.2 ± 0.14%, $n = 3$, $P = 0.0054$). NSC differentiation in 3D-CG resulted in significantly larger fraction of $Olig2^+$ cells (3D-CG: 36.3 ± 2.3%, $n = 3$; 2D: 23.0 ± 0.5%, $n = 3$, $P = 0.0319$).

Regulation of neuronal differentiation by PCSs in vitro

Maturation of NSC-derived neurons was initially evaluated by quantifying two morphological features (neurite branching, mean length of neuron dendrites) of $Tuj1^+$ neurons at 7 DIV (Fig. 2f-h). Interestingly, NSC-derived neurons in 3D-C culture exhibited significantly higher axonal branching (3D-C: 9.3 ± 0.8, $n = 27$; 3D-CG: 4.5 ± 0.9, $n = 20$; $P = 0.0364$; Fig. 2g) and sustained significantly longer neuronal dendrites (3D-C: 120.3 ± 9.2 μm, $n = 27$; 3D-CG: 78.3 ± 7.2 μm, $n = 20$; $P = 0.0377$; Fig. 2h) compared with NSC-derived neurons in 3D-CG culture.

We further evaluated the maturation of NSC-derived neurons by quantifying their spontaneous activity. Field recordings revealed low level of spontaneous activity in neurospheres formed in 3D-C, 3D-CG cultures, and 2D (standard NSC neurosphere culture) at 3, 5, and 7 DIV (Fig. 3a). Given the significant role of $GABA_A$ signaling in neuronal differentiation and maturation during embryonic neurogenesis[30], we investigated whether bicuculline, a $GABA_A$ antagonist, could affect spontaneous activity measurements. Although at 5 DIV no group was responsive to bicuculline, at 7 DIV neurospheres grown inside collagen scaffolds (3D-C) profoundly increased their spontaneous activity in response to bicuculline (5 DIV: 0.32 ± 0.06 events per second, $n = 8$; 7 DIV: 1.23 ± 0.04 events per second, $n = 8$; $P < 0.05$; Fig. 3b, c).

To quantify spontaneous activity in single cells located inside scaffolds, we utilized time-lapsed confocal fluorescent microscopy to monitor cytosolic Ca^{+2} fluctuations in fluo3-stained NSCs at 5 and 7 DIV. Single-cell analysis revealed that a fraction of cells exhibited periodic oscillations of cytosolic Ca^{+2}, consisting of repeated Ca^{+2} events (Fig. 3d, e). Such oscillations were observed only in neurospheres or in cell-rich scaffold regions, and not on isolated cells, suggesting that cell–cell interactions were required for their generation. At 5 DIV, NSCs grown in collagen scaffolds exhibited more frequent (smaller period T between events) and sharper [smaller event full width at half maximum (FWHM) d] Ca^{+2} events compared with NSCs grown in collagen-CG scaffolds (Fig. 3f-g and Supplementary Video 1), indicative of more advanced neural maturation. Between 5 DIV and 7 DIV, both T and d decreased in both 3D-C and 3D-CG cell culture groups ($P < 0.001$). Multiple-factor analysis revealed a significant effect of scaffold type ($P < 0.05$) on both T and d. On the other hand, bicuculline treatment did not affect significantly duration d or period T.

Porous collagen scaffolds support the formation of networks of functional neurons in vitro

We then evaluated the ability of collagen scaffolds to support the formation of networks of functional terminally differentiated neurons inside them, a process requiring significant axon elongation and synapse formation. Five days after seeding E13.5 mouse dorsal root ganglia (DRG) cells inside collagen scaffolds, cells had attached extensively on the scaffold and neurons had extended long neurites with synaptic activity along the scaffold surface (Supplementary Fig. 2a-c). At DIV 7, a 3D network of DRG neurons had formed inside the scaffold (Fig. 3g), consisting of long axons, and stained positive for neurofilament heavy chain and the presynaptic marker synaptophysin (Supplementary Fig. 2d, e). The ability of neuronal cells to elongate axons into collagen scaffolds was not limited to primary cells. Preliminary experiments suggest that spinal cord neural cells derived from mouse embryonic stem cells can adhere and grow axons through the pores of collagen scaffolds (Supplementary Fig. 2f).

NSC-seeded collagen scaffolds significantly improved locomotion recovery after dorsal column crush SCI in mice

NSC-seeded porous collagen scaffolds were further evaluated in a mouse dorsal column crush model, a SCI model known to cause irreversible coordination dysfunction and hind limb instability[31]. The experimental design consisted of five animal groups (Fig. 4a, b). In the "uninjured control" group ($n = 8$ animals), following laminectomy, the dura matter was cut but the exposed spinal cord was not injured. In the "crush" group ($n = 8$ animals), the dorsal column of the exposed spinal cord was crushed using forceps. In the "scaffold + NSC" group ($n = 10$ animals), immediately following dorsal column crush, the lesion site was grafted with a porous collagen scaffold seeded with Bromodeoxyuridine (BrdU)-pulsed embryonic NSCs. In the "scaffold-only" control group ($n = 8$ animals), the lesion site was grafted with a cell-free porous collagen scaffold. Finally, in the "scaffold + NIH-3T3" control non-NSC group ($n = 8$ animals), the lesion site was grafted with a porous collagen scaffold seeded with mouse NIH-3T3 cells. NIH-3T3 fibroblast cells were chosen due to their proliferative capacity, end-term differentiation state (thus, as a non-NSC cell model), and robust fibroblast adhesion to PCS[25,28].

Histology revealed that NSC-seeded scaffolds integrated well with the surrounding tissue and no gaps were observed between the scaffold and the surrounding tissue 6, 9, and 12 weeks post injury (Figs. 4c, d, 5, and 6, and Supplementary Fig. 3). In the scaffold-only group, grafts had drifted away from the lesion site in

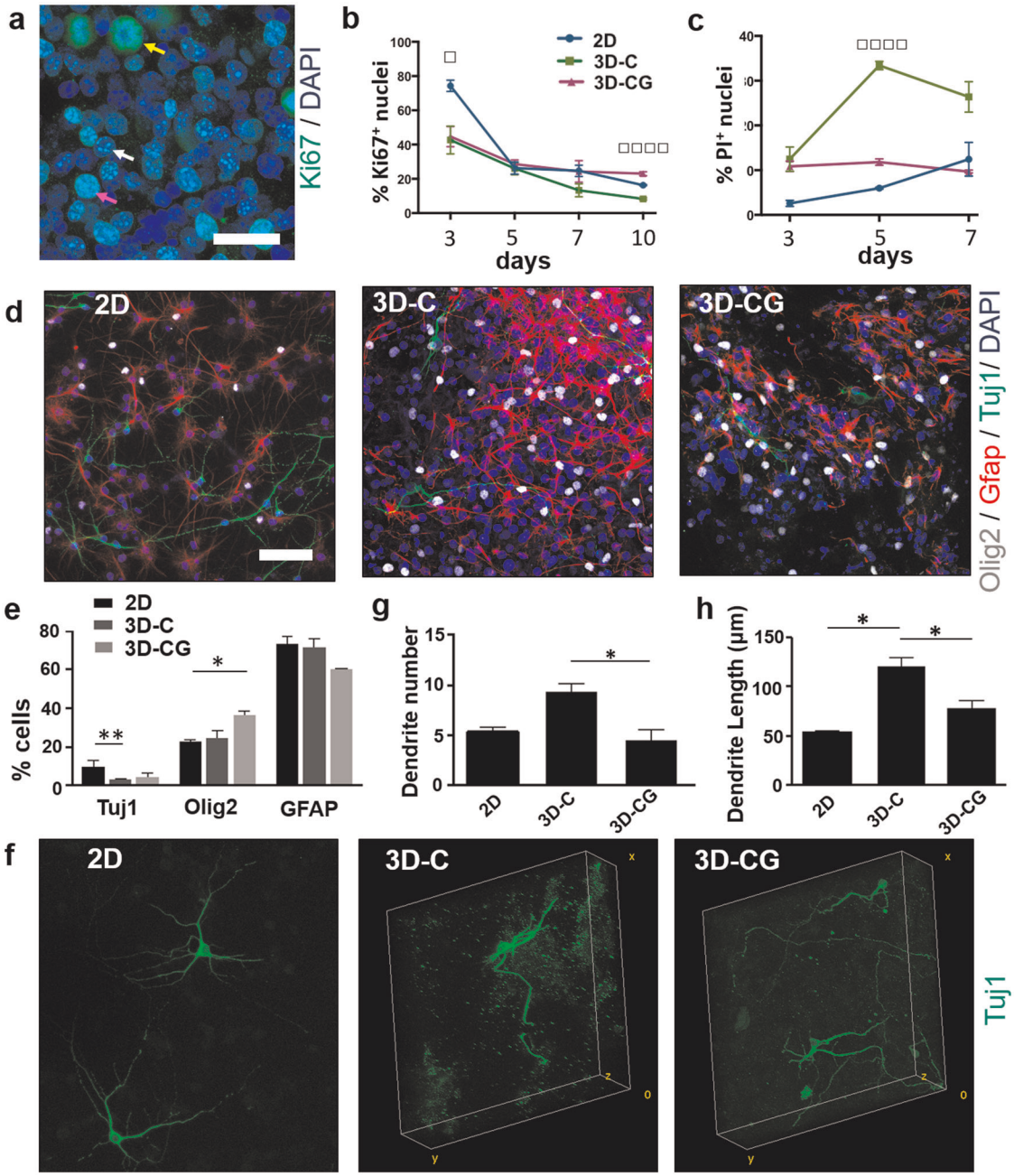

Fig. 2 Regulation of NSC proliferation, viability, and differentiation by PCS composition in vitro. a Fluorescence image of Ki67$^+$ NSCs inside a porous collagen-GAG scaffold at 3 DIV. Arrows highlight cells at the early S phase (white arrow), the late S phase (purple arrow), or mitosis (yellow arrow). Scale bar, 30 µm. **b** Fraction of Ki67$^+$ nuclei in the three NSC culture groups at 1, 3, 5, 7, and 10 DIV ($n = 3$). **c** Fraction of PI$^+$ nuclei in the three NSC culture groups at 1, 3, 5, and 7 DIV ($n = 3$). **d** Representative confocal images of cells immunostained for Tuj1 (neurons; green), Olig2 (oligodendrocytes; gray), and Glial fibrillary acidic protein (GFAP, astrocytes; red) in 2D, 3D-C, and 3D-CG cultures at 7 DIV. Scale bar, 50 µm. **e** Fractions of Tuj1$^+$, Olig2$^+$, and GFAP$^+$ cells in the three cell culture groups at 7 DIV. **f** 3D reconstruction of confocal *z*-stacks of NSC-derived Tuj1$^+$ neurons growing on laminin-coated coverslips (2D) or inside porous scaffolds (3D-C, 3D-CG) at 7 DIV. Box size: 263 × 263 × 80 µm. **g** Number of dendrites per Tuj1$^+$ neuron in the three NSC culture groups ($n = 30$). **h** Mean dendrite length per Tuj1$^+$ neuron in the three NSC culture groups ($n = 30$). Results are expressed as mean ± SEM. $^*P < 0.05$, $^{**}P < 0.01$, $^{\square}P_{1\text{-way-ANOVA}} < 0.05$, $^{\square\square\square\square}P_{1\text{-way-ANOVA}} < 0.001$.

four out of four animals examined 6 weeks post injury (Fig. 4c, d and Supplementary Fig. 3). In the scaffold + NIH-3T3 group, four out of eight animals showed signs of poor health and distress (weight loss, back feet paralysis, and heavy abdominal breathing) and were killed 2 weeks post injury. Post-mortem tissue histological evaluation of the killed animals showed extended damage and overt inflammatory response of the tissue surrounding the lesion (Supplementary Fig. 4a, b). Despite NSC proliferative capacity, such complications were not observed in the scaffold + NSC group. The remaining four animals of the scaffold + NIH-3T3 group were monitored for locomotion recovery and were used for histological analysis. Six weeks post injury, in surviving "scaffold + NIH-3T3" group animals scaffold drift was not observed, the scaffold was integrated with the surrounding tissue;

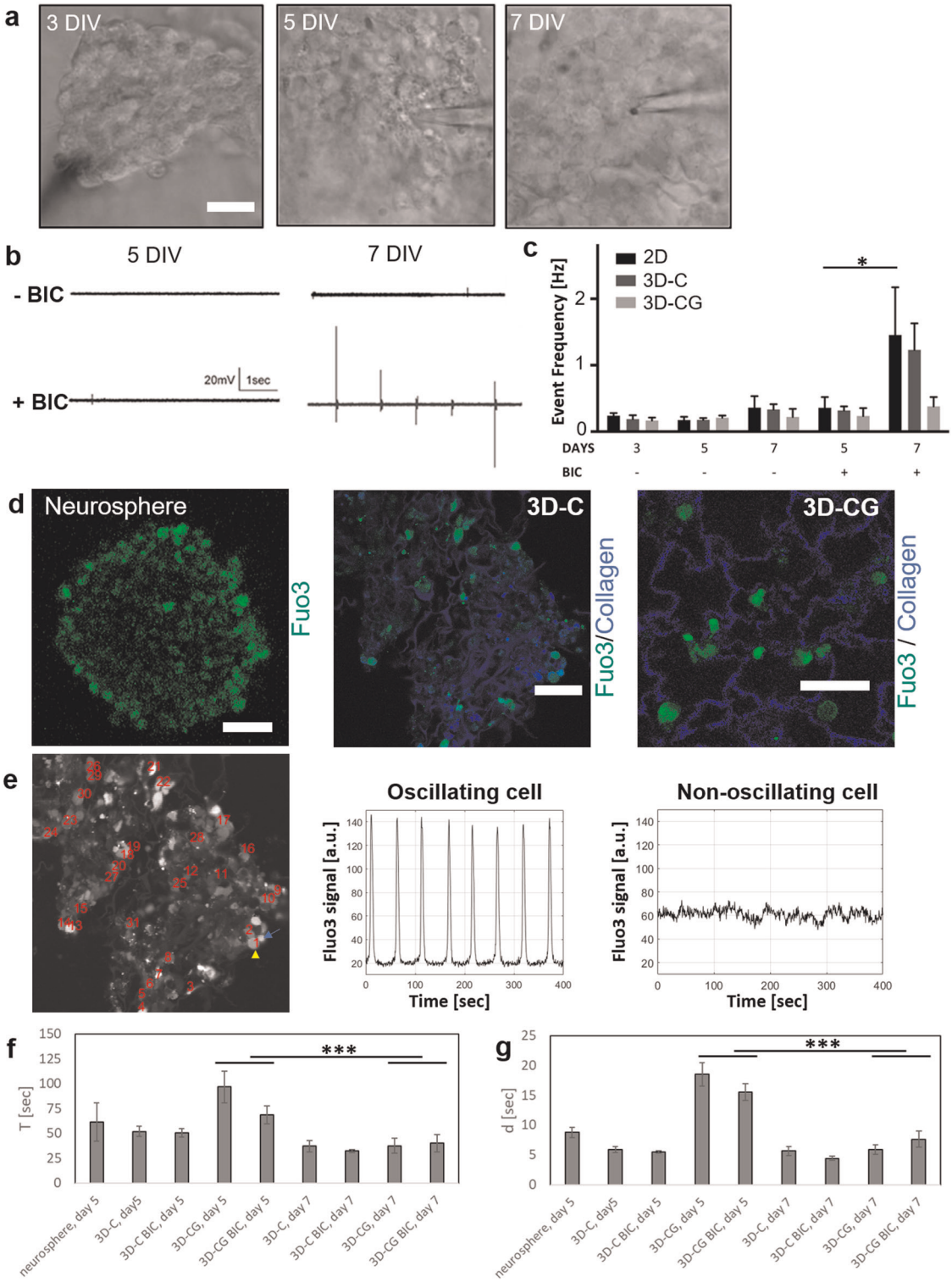

Fig. 3 Porous collagen scaffolds enhance NSC neural differentiation in vitro. a Representative bright-field microscopy images of neurospheres grown in PCS during electrophysiological recordings at 3, 5, and 7 DIV. Scale bar, 20 μm. **b** Representative field recordings of spontaneous activity acquired in neurospheres grown inside collagen scaffolds (3D-C) before (top row) and after (bottom row) bicuculline treatment, at 5 and 7 DIV. **c** Quantification of spontaneous activity event frequency in neurospheres grown in 2D or 3D cultures at 3, 5, and 7 DIV ($n = 6$). **d** Representative fluorescent image of Fluo3 emission (green) in neurospheres grown in suspension or NSCs seeded in collagen or collagen-GAG scaffolds (blue) at 5 DIV. Scale bars, 50 μm. **e** Representative time profiles of Ca^{+2}-induced Fluo3 signal in single cells grown inside a porous collagen scaffold. Comparison of profiles in two neighboring cells, one of which displays Fluo3 oscillation (yellow arrowhead) and one does not (cyan arrow). **f**, **g** Quantification of Ca^{+2} oscillations: mean period T between spontaneous events (**f**) and FWHM d of event duration (**g**) in NSC grown inside collagen or collagen-GAG scaffolds at 5 or 7 DIV, in the presence or absence of bicuculline ($n = 3$ to 5). Results are expressed as mean ± SEM. $^{*}P < 0.05$, $^{***}P < 0.001$.

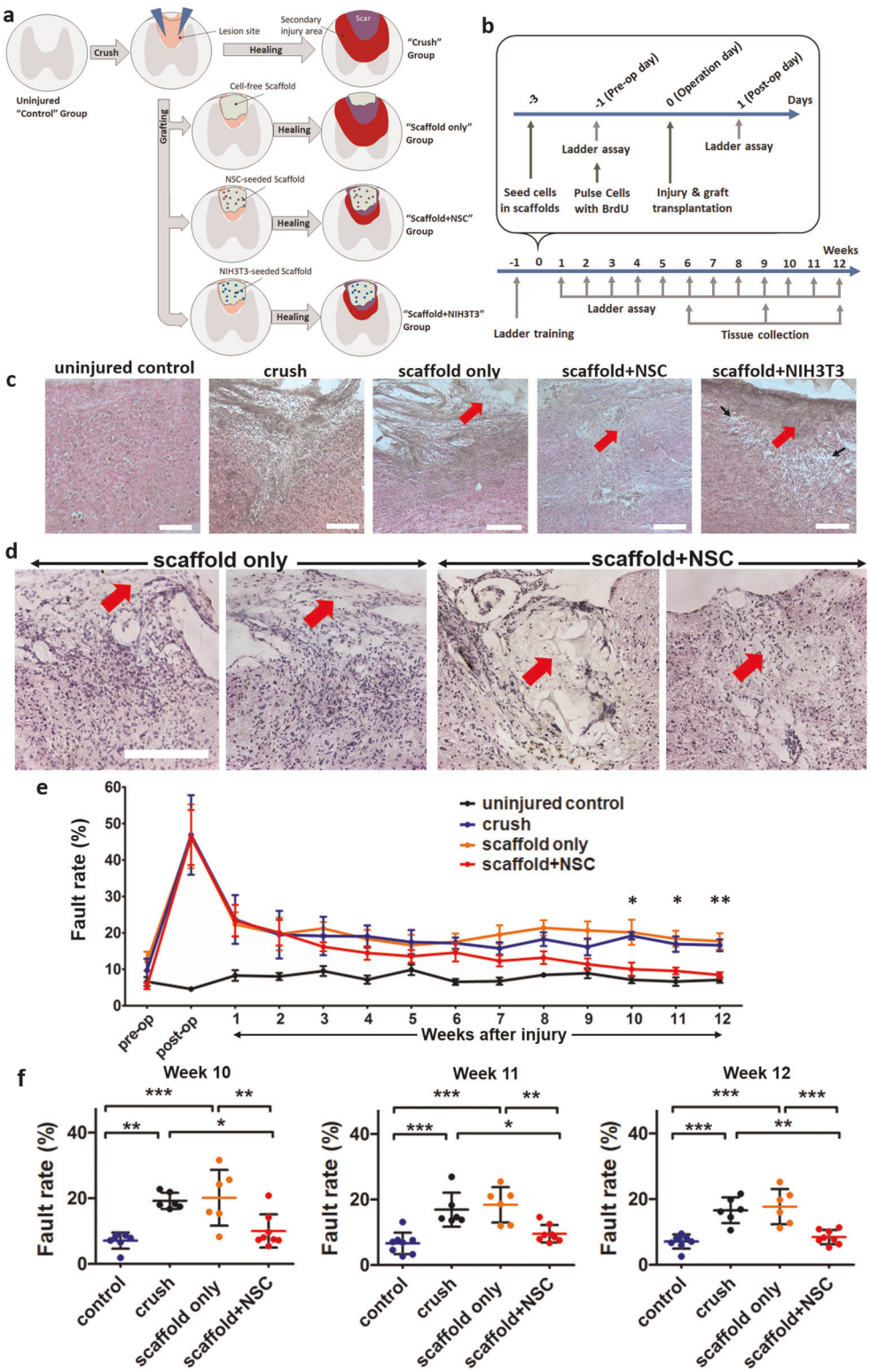

Fig. 4 Porous collagen scaffolds seeded with embryonic NSCs enhanced locomotion recovery in a mouse dorsal column crush SCI model. **a** Schematic of the injury model and the three animal groups considered in this study. **b** Timeline of animal experiments, demonstrating BrdU labeling, injury and grafting, locomotion recovery quantification, and animal killing for histology. **c** H&E staining of spinal cord parasagittal sections from all animal groups 6 weeks post injury. Red arrows indicate residual scaffold and black arrows indicate areas of cavitation. Scale bars, 200 μm. **d** Higher-magnification images of spinal cord cross-sections stained by H&E from the scaffold-only and scaffold + NSC animal groups 6 weeks post injury. The location of residual scaffold is highlighted using arrows. Cell-free scaffolds had drifted away from the lesion site. Scale bars, 200 μm. **e** Locomotion recovery after SCI quantified by the Horizontal Ladder Walking Assay. Fault rates are presented as mean ± SEM ("uninjured control" and "scaffold + NSC" groups: $n = 8$ animals, "crush" and "scaffold-only" groups: $n = 6$ animals). The complete dataset is available in Supplementary Figs. 5b and 6). $^{*}P_{1\text{-way-ANOVA}} < 0.05$, $^{**}P_{1\text{-way-ANOVA}} < 0.01$. **f** Dot plot of locomotion fault rate at 10, 11, and 12 weeks post injury. Fault rates are presented as mean ± SD. $^{*}P < 0.05$, $^{**}P < 0.01$, $^{***}P < 0.001$ (Tukey's post-hoc pairwise test assuming $P_{1\text{-way-ANOVA}} < 0.05$).

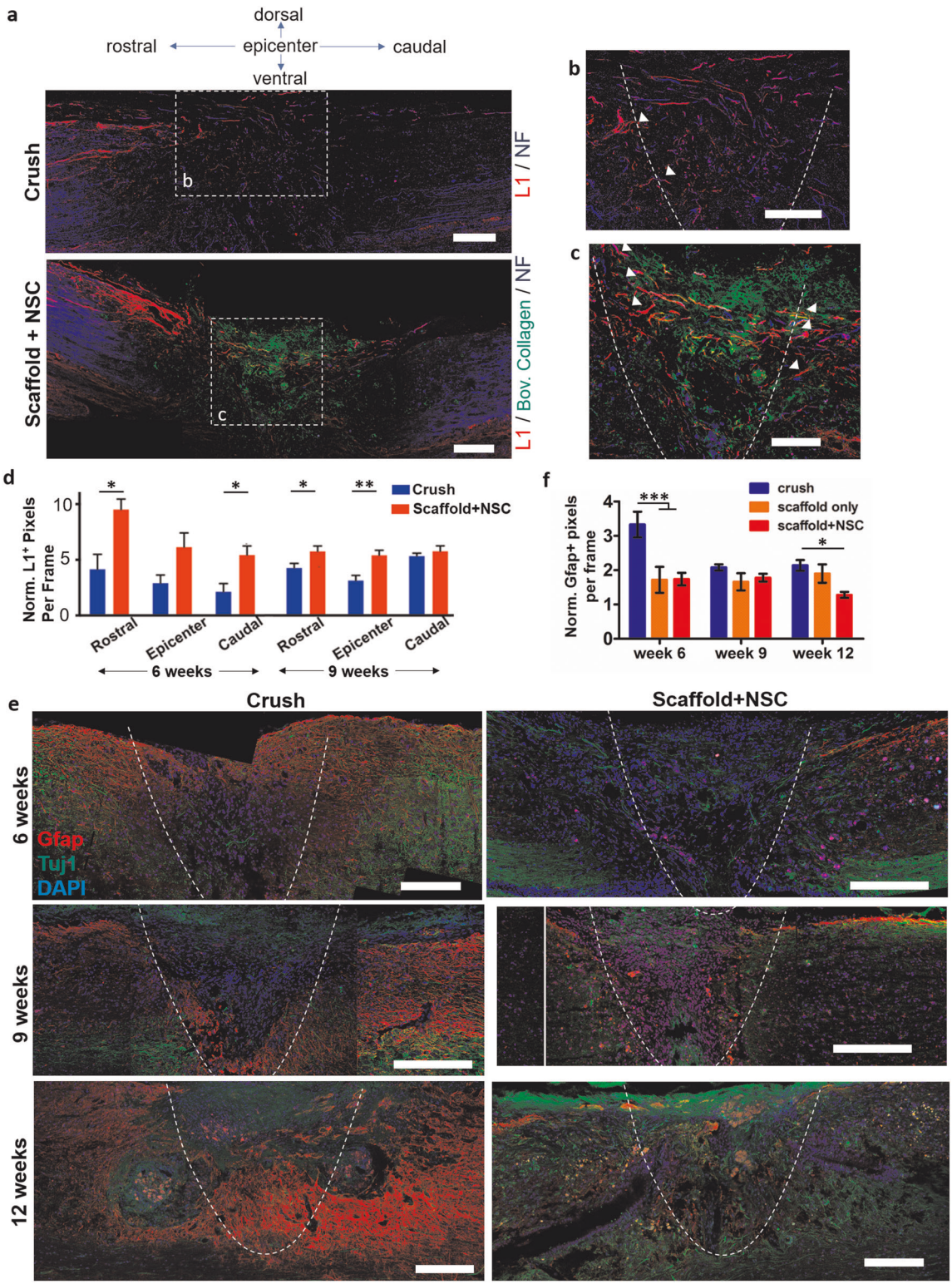

Fig. 5 Porous collagen scaffolds seeded with embryonic NSCs increased axonal elongation and reduced astrogliosis at the lesion site after dorsal column crush. a Representative fluorescence images of parasagittal sections from crush and scaffold + NSC groups immunostained for neurofilament heavy chain, bovine collagen I and L1, 6 weeks post injury. Scale bars, 200 μm. **b**, **c** High-magnification images of regions shown in **a** highlight axons that stain for NF and L1 at the lesion (inside the graft) or on the approximate lesion boundary (dashed lines). Examples of $L1^+$ axons crossing the approximate lesion boundary are marked by triangles. Scale bars, 100 μm. **d** Quantification of $L1^+$ pixel density in crush and scaffold + NSC groups, caudally, in the epicenter, and rostrally to the lesion, at 6 and 9 weeks post injury. Results are normalized with respect to the uninjured control group and are presented as mean ± SEM. **e** Fluorescence imaging of parasagittal sections stained for Tuj1 and GFAP at the lesion 6, 9, and 12 weeks post injury. The approximate lesion boundary is shown using dashed lines. Bars: 200 μm. **f** Quantification of $GFAP^+$ pixel density in the crush and scaffold + NSC groups at 6, 9, and 12 weeks post injury. Results are normalized with respect to the uninjured control group and are presented as mean ± SEM. "Uninjured control" and "scaffold-only" groups: $n = 3$. "Crush" and "scaffold + NSC" groups: $n = 5$. $^*P < 0.05$, $^{***}P < 0.001$ (Bonferroni post-hoc pairwise test assuming $P_{1\text{-way-ANOVA}} < 0.05$).

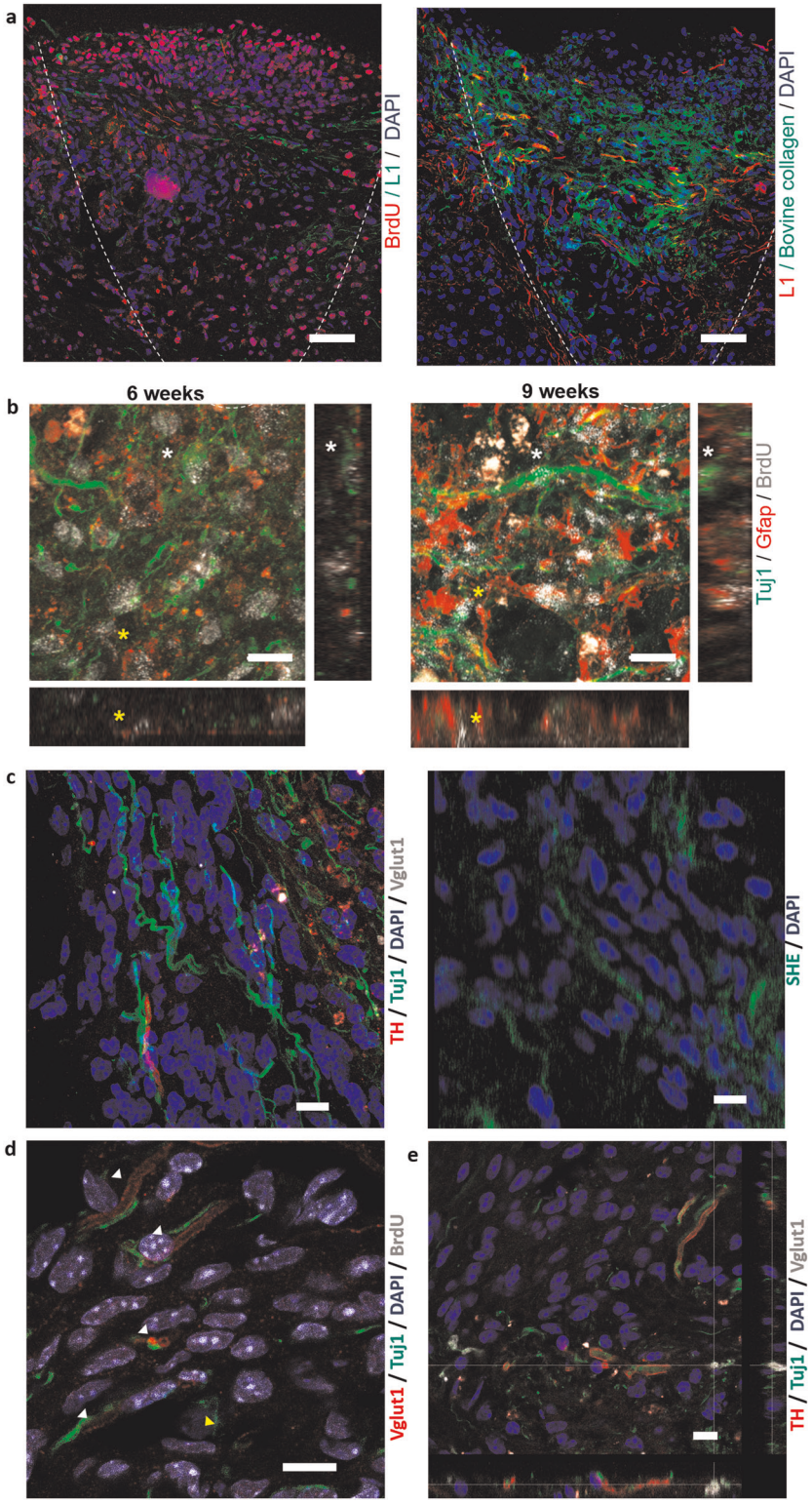

Fig. 6 Porous collagen scaffolds safely delivered embryonic NSCs at the SCI lesion and enabled NSC differentiation towards both neurons and astrocytes in vivo. a Representative immunofluorescence images of sagittal sections stained for bovine collagen I, BrdU, and L1 at the lesion epicenter, 6 weeks post injury. Dashed line indicates the approximate lesion boundary. Scale bars, 50 μm. **b** High-magnification immunofluorescence images and orthogonal views at the lesion epicenter, 6 and 9 weeks post injury. Cellular colocalization of $BrdU^{+}$ nuclei with cytoplasmic Tuj1 or GFAP are marked by white and yellow asterisks, respectively. Scale bar, 10 μm. **c** Immunofluorescence images of a parasagittal section acquired inside the graft 6 weeks post injury. Left: section stained for TH, Vglut1, and Tuj1. Right: second harmonic emission by residual scaffold collagen in the same location. Scale bar, 10 μm. **d**, **e** Immunofluorescence image of a parasagittal section acquired inside the graft 6 weeks post injury. The sections were stained for Vglut1, Tuj1, and BrdU (**d**) or Vglut1, Tuj1, and TH (**e**). Scale bars, 10 μm.

however, there were extended areas of cavitation in the tissue surrounding the scaffold (Fig. 4c).

Following SCI, locomotion recovery was quantified by the horizontal ladder walking assay over a period of 12 weeks post injury (Fig. 4e, f, Supplementary Figs. 4 and 5, and Supplementary Video 2). Locomotion fault rate (percentage of misplaced steps) remained unchanged in the uninjured (laminectomy-only) control group ($\mu = 7.5\%$, $\sigma = 3.2\%$) over the 12-week evaluation period. The response of the four SCI groups (crush, scaffold + NSC, scaffold-only, and scaffold + NIH-3T3) were not statistically different 1 day ($P_{1\text{-way-ANOVA}} = 0.433$, $F = 0.955$) and 1 week ($P_{1\text{-way-ANOVA}} = 0.726$, $F = 0.44$) post injury, indicating that SCI groups suffered from the same degree of injury. Overall, the vast majority of detected misplacements were classified as "correction" and mainly as "partial placement" (Supplementary Fig. 5b), indicative that dorsal column crush mainly affects fine motility. Severe foot misplacements were observed up to 2 weeks post injury in four SCI groups. Over a 12-week post-injury period, there was a significant overall effect of the treatment ($P_{\text{Repeated Measures 2-way-ANOVA}} = 0.0002$, $F[2,238] = 8.822$, 3.57% of variation). Some spontaneous locomotion restoration was observed in all four SCI groups (significant overall effect of time, $P_{\text{Reapeted Measures 2-way-ANOVA}} < 0.0001$, $F[13,238] = 8.822$, 44.38% of variation) in agreement with similar studies[32]. Starting at 3 weeks post injury, locomotion performance in the scaffold + NSC group was consistently better compared with the crush group. These differences became statistically significant at 10 (10.0 ± 1.8% vs. 19.2 ± 1.0%, $P_{\text{Tukey}} < 0.05$; $P_{1\text{-way-ANOVA}} = 0.0072$, $F = 6.69$), 11 (9.6 ± 0.9% vs. 16.9 ± 2.1%, $P_{\text{Tukey}} < 0.05$; $P_{1\text{-way-ANOVA}} = 0.0031$, $F = 8.27$) and 12 (8.4 ± 0.8% vs. 16.6 ± 1.6%, $P_{\text{Tukey}} < 0.01$; $P_{1\text{-way-ANOVA}} = 0.0005$, $F = 12.33$) weeks post injury (Fig. 4f). Scaffold + NSC was the only animal group where the slope α of the linear trendline that fits locomotion performance between 3 and 12 weeks post injury was negative and statistically non-zero (Scaffold + NSC: $\alpha = -0.79\%$/week; $P_{\text{slope}} = 1.5 \times 10^{-5}$. Scaffold-only: $\alpha = -0.014\%$/week; $P_{\text{slope}} = 0.96$. Crush: $\alpha = -0.18\%$/week; $P_{\text{slope}} = 0.52$. Uninjured control: $\alpha = -0.13\%$/week; $P_{\text{slope}} = 0.34$; Supplementary Fig. 6). Finally, scaffold + NSC was the only SCI group whose locomotion performance at 12 weeks post injury was not statistically different from one of the uninjured (laminectomy-only) control group (8.4 ± 0.8% vs 7.1 ± 0.8%, $P_{2\text{-sided } t\text{-test}} > 0.2$; Fig. 4f). Similar trends were observed in the response of the Foot Fault Score (Supplementary Fig. 5a), an alternative metric of locomotion performance that considers the type of foot misplacements. No improvement in locomotion recovery compared with the crush (injured, not grafted) group was observed in animals treated with porous scaffolds seeded with non-NSC NIH-3T3 cells (Supplementary Fig. 4c).

NSC-seeded collagen scaffolds improved axonal elongation and reduced astrogliosis at the lesion site

Axon elongation through the lesion site is a key prerequisite for functional restoration after SCI. No significant axonal elongation was observed at SCI sites grafted with cell-free PCS grafts[16,19,23]. Six weeks post injury, NF^+ axons were present caudally and rostrally of the lesion site. $L1^+$ axons were present in the dorsal column adjacent to the lesion and in the lesion epicenter (Fig. 5a-d and Supplementary Fig. 7). At 6 weeks post injury, the scaffold + NSC group displayed significantly higher density of $L1^+$ pixels compared with the crush group caudally (scaffold + NSC: 952 ± 4%, crush: 416 ± 134%, $n = 5$, $P < 0.05$) and rostrally (scaffold + NSC: 543 ± 82%, crush: 213 ± 74%, $n = 5$, $P < 0.05$; Fig. 5d). At 9 weeks post injury, the scaffold + NSC group displayed significantly higher density of $L1^+$ pixels rostrally (scaffold + NSC: 580 ± 49%, crush: 489 ± 42%, $n = 5$, $P < 0.05$) and at the lesion epicenter (scaffold + NSC: 545 ± 45%, crush: 315 ± 47%, $n = 5$, $P < 0.01$). High-magnification images at the lesion epicenter 6 weeks post injury revealed significant numbers of NF^+ axons inside the scaffold, many of which stain for L1, and multiple $L1^+$ axons crossing the scaffold-tissue interface both rostrally and caudally (Fig. 5c).

Astrogliosis at the lesion site was evaluated by immunostaining for GFAP and calculating the fraction of $GFAP^+$ pixels around the approximate lesion boundary. Six weeks post injury, intense GFAP staining was localized rostrally and caudally of the lesion epicenter in the crush group, a characteristic pattern of astrogliosis (Fig. 5e, f and Supplementary Fig. 8a, b). The fraction of $GFAP^+$ pixels in the scaffold + NSC group was significantly smaller compared with the crush group at 6 weeks post injury (scaffold + NSC: 174 ± 18%, crush: 332 ± 37%, $n = 5$, $P < 0.001$) and at 12 (scaffold + NSC: 128 ± 9%, crush: 214 ± 16%, $n = 3$, $P < 0.05$) weeks post injury (Fig. 5f and Supplementary Fig. 8c), suggesting that the graft managed to reduce astrogliosis around the lesion. Microgliosis was also evaluated in the crush and scaffold + NSC groups by quantifying the fraction of pixels that stain for IBA1, a marker of microglia and recruited monocytes/macrophages. Images reveal that $IBA1^+$ cells of phagocytotic morphology are attracted in the lesion site in both groups (Supplementary Fig. 9a). No statistically significant difference in the fraction of $IBA1^+$ pixels was observed between the crush and scaffold + NSC groups (Supplementary Fig. 9b). Second harmonic emission (SHE) imaging revealed that although the graft did not manage to completely block the formation of a collagenous scar, in the scaffold + NSC group the collagen fibers of scar were localized mostly at the lesion boundary and not inside the scaffold (Supplementary Fig. 10).

Neural differentiation of NSCs inside porous collagen scaffolds in vivo

To track the fate of NSCs delivered inside PCS at the SCI lesion site, NSC-seeded collagen scaffolds were pulsed with BrdU prior to their grafting (Fig. 4a, b). Immunostaining revealed that most $BrdU^+$ nuclei were located inside the scaffold suggesting that PCS achieved localized delivery of NSCs at the lesion site (Fig. 6a). Manual counting in confocal *z*-stacks (stack volume $2.69 \pm 0.38 \times 10^5\ \mu m^3$) from five animals of the scaffold + NSC group 6 weeks post injury revealed 375.4 ± 74.5 nuclei per imaging stack corresponding to cell density $1.37 \pm 0.15 \times 10^6$ cells/μl. The majority of these nuclei (86.6 ± 1.5%) stained for BrdU, corresponding to a density of $1.19 \pm 0.14 \times 10^6$ $BrdU^+$ cells/μl. Although it is not possible to calculate the survival rate of implanted NSCs (due to NSC proliferation and scaffold degradation), the high density of BrdU cells and the lack of cell debris inside the scaffold (Fig. 6c-e) suggest that the scaffold managed to protect NSCs from the harsh conditions of SCI. Furthermore, a few $BrdU^+$ nuclei were observed within 200 μm from the scaffold boundary, suggesting that the porous nature of PCS enabled NSC migration and integration into the surrounding tissue in vivo. No ectopic NSC colonies were observed within 1 mm away from the lesion site.

To evaluate whether NSCs seeded inside PCS can differentiate in vivo in the SCI site, sections from the scaffold + NSC group were simultaneously stained for BrdU, Tuj1, and GFAP. Imaging and manual cell counting revealed that 6 weeks post injury, a significant fraction of $BrdU^+$ cells stained positively for either Tuj1 (22.9 ± 2.4%, $n = 5$) or GFAP (6.0 ± 1.4%, $n = 5$; Fig. 6b). As NSCs at the day of implantation stained positively for nestin (Fig. 1f), our results provide evidence that NSCs differentiated towards both neuronal or glial fates inside PCS after graft implantation in vivo, a prerequisite for developing NSC-based relay treatments for SCI.

Finally, to probe the nature of the neurons and axons present at the lesion site 6 weeks post injury, parasagittal sections from the scaffold + NSC animal group were immunostained for Vglut1 (marker of excitatory glutamatergic neurons), TH (marker of dopaminergic neurons), and GAD65/67 (marker of inhibitory GABAergic neurons). Imaging revealed the presence of both

Vglut1, TH, and GAD65/67 staining in the lesion epicenter (Fig. 6c-e and Supplementary Figs. 11 and 12). Superimposing confocal images with SHE images verifies that Vglut1, TH, and GAD65/67 signals were indeed located inside the collagen scaffold (Fig. 6c and Supplementary Fig. 11). Simultaneous labeling of Vglut1 and BrdU suggests that several NSC-derived neurons could be excited by glutamatergic neurons (Fig. 6d). Very few $BrdU^+$ neurons expressed TH or GAD65/67 (Fig. 6e and Supplementary Fig. 12). Overall, these findings suggest the presence of both excitatory and inhibitory neurons inside the scaffold in the lesion epicenter 6 weeks post injury.

DISCUSSION

The development of effective clinical treatments for SCI is an important unmet medical need due to the severe consequences of SCI to patients. Existing clinical treatments (small molecules and surgical procedures) have limited efficacy and short-term effects. Several methods utilized clinically to replace injured organs (e.g., transplantation and allografts) cannot be applied in the injured spinal cord. Induced regeneration appears to be a promising, yet challenging alternative for providing SCI patients valuable functional and sustainable recovery. Indeed, over the past two decades, much research focused on developing novel regenerative medicine treatments for SCI. Among them, cell therapy promises to utilize the emerging understanding on stem cell biology to replace lost cells at SCI sites[7]. In particular, SCI grafts based of embryonic NSCs have demonstrated impressive effects on axonal elongation and synapse formation in rodent and primate SCI models[9–11]. However, significant development is required to safely deliver NSCs at SCI lesions and harvest their potential in clinical practice. Strong evidence, including the poor efficacy reported in the first clinical trial of human NSCs in SCI patients[13], suggests that the supporting matrix is a key mediator of NSC effects[10]. Although several biomaterials have demonstrated ability to regulate NSC phenotypes in vitro[24], little is known on the underlying mechanisms that could guide the development of effective SCI grafts. Furthermore, those biomaterials that have demonstrated positive effects to NSC in SCI grafts[9–11,21] have not received regulatory approval before, adding another obstacle towards the clinical translation of NSC treatments. Meanwhile, the few biomaterials that have been translated in the clinical practice of induced organ regeneration, including porous collagen-based scaffolds (PCS), have not contributed to the development of effective SCI grafts. Despite the ability of PCS to induce regeneration in peripheral nerve injuries, cell-free PCS grafts have provided limited results in SCI[16,19]. Little is known about the ability of PCS to harvest the regenerative capability of potent NSCs in SCI. In this study, we demonstrate that PCS can safely deliver and regulate embryonic NSCs at SCI sites leading to significant locomotion recovery in a mouse SCI model. We focused on the two seminal PCS due to their established clinical application in regenerative medicine and their proven ability to modulate wound healing[22,27]. Finally, we utilized mouse embryonic cortical NSCs due to their proliferative capacity, trilineage differentiation, easy availability (ensures the reproducibility of our findings), and relatively easy isolation and expansion.

The first part of the study quantified the effects of the two seminal PCS on key phenotypes of NSCs (proliferation, viability, and neuronal differentiation) and NSC-derived neurons (axonal elongation) in vitro. Seeded NSCs adhered robustly on PCS struts either as single cells or formed neurosphere-like aggregates inside PCS pores (Fig. 1d-f). Collagen-GAG scaffolds enhanced NSC proliferation and survival compared with GAG-free collagen scaffolds (Fig. 2b, c), in agreement with previous in vitro and in-vivo reports[33,34]. We hypothesize that Ch6S can emulate the extracellular matrix of the NSC niche at the adult sub-ventricular zone or the embryonic telencephalon, where abundant GAGs and proteoglycans regulate NSC fate and the migration of newly born neurons[35]. The presence of Ch6S in PCS did not affect the fraction of NSCs that differentiated towards $Tuj1^+$ neurons (Fig. 2d, e). However, GAG-free PCS enhanced the maturation of NSC-derived neurons compared with collagen-GAG scaffolds (evaluated by morphological assays; Fig. 2f-h), in agreement with the inhibitory role of chondroitin sulfate proteoglycans (CSPGs) in neuronal synapse maturation[36]. Neural maturation was further evaluated by quantifying the spontaneous activity of NSC-derived neurons inside PCS. Field recordings revealed that at 7 DIV the frequency of spontaneous events in bicuculline-treated neurospheres formed inside collagen scaffolds was significantly larger compared with neurospheres formed inside collagen-GAG scaffolds (Fig. 3a-c). Here, the inhibitory/excitatory state of $GABA_A$ receptors was utilized as a developmental marker. Although in the adult CNS $GABA_A$ receptors are inhibitory, in the early stages of development $GABA_A$ receptors have excitatory effects[37]. Our finding that at 7 DIV spontaneous activity was increased in response to bicuculine in NSCs grown in collagen scaffolds but not in collagen-GAG scaffolds suggests that $GABA_A$ receptors had already switched into becoming inhibitory in 3D-C but not in 3D-CG.

Fluorescence imaging of cytosolic Ca^{+2} in NSCs grown inside PCS revealed the presence of periodic Ca^{+2} events, whose duration and mean period was significantly smaller in collagen scaffolds compared with collagen-GAG scaffolds at 5 DIV (Fig. 3d-g), in agreement with the delayed neural differentiation observed in CG scaffolds via electrophysiology measurements. Although we did not identify whether cells participating in such oscillations were neurons or astrocytes, this results support the hypothesis that collagen scaffolds favor the functional maturation of NSC-derived neural cells and demonstrate neural activity in NSC-derived neural cells inside PCS in vitro. Finally, the ability of GAG-free PCS to support the functional maturation of neurons was further supported by the formation of functional networks of interacting (synaptophysin-positive) primary DRG neurons inside porous collagen scaffolds (Supplementary Fig. 2).

The second part of the study evaluated the ability of PCS grafts to safely deliver NSCs at SCI lesion sites and enhance locomotion recovery in a clinically relevant model of SCI. GAG-free porous collagen scaffolds were solely utilized due to their superior ability to support neuronal differentiation in vitro and also due to the reported adverse effects of CSPGs on axonal elongation[38]. Previous studies on PCS graft effects in SCI utilized transection models, which provide unambiguous conditions for quantifying axonal regeneration; however, they are much more severe than common SCI in human patients (usually contusions). Here, PCS grafts (cell-free or seeded with NSCs or non-NSCs (NIH-3T3 cells)) were evaluated in a mouse dorsal column crush SCI model (Fig. 4a, b), known to irreversibly affect both ascending and descending pathways (including the challenging corticospinal tract). The chosen SCI model provides a lesion volume where a graft can be implanted and therefore has been utilized previously to quantify graft effects[21,39]. Histology revealed that both types of cell-seeded grafts remained in the lesion site, whereas cell-free PCS drifted away from the lesion site (Fig. 4c, d and Supplementary Fig. 3). These results clearly suggest that seeded cells were critical for graft adhesion with the surrounding spinal cord tissue, a prerequisite for direct interactions between the scaffold and host neural cells. However, the type of cells seeded inside scaffold proved to be critical as NIH-3T3 cells, in sharp contrast to NSCs, did not induce any locomotion recovery and even induced complications and mice mortality (Supplementary Fig. 4).

Locomotion recovery in the crush, scaffold-only and scaffold + NIH-3T3 groups over a 12-week period after SCI was partial (locomotion performance did not reach the one of the uninjured control group). Grafting the SCI lesion site with cell-free scaffolds or NIH-3T3-seeded scaffolds did not induce any improvement compared with the crush (injured but not grafted) group, in

agreement with previous studies (Fig. 4e and Supplementary Fig. 4b)[16,19]. On the other hand, starting at 3 weeks post injury, animals grafted with NSC-seeded scaffolds had consistently lower fault rate compared with the crush group (Fig. 4e). The ~8% absolute improvement in fault rate induced by the scaffold + NSC group (corresponding to a statistically non-zero slope of 0.79%/week; Supplementary Fig. 6) became statistically significant compared with the crush group at 10, 11, and 12 weeks post injury (Fig. 4f). Noticeably, at 12 weeks post injury, the locomotion fault rate of the scaffold + NSC group was not statistically different from the uninjured control group.

To gain insight on how NSC-seeded PCS grafts can improve locomotion recovery, we quantified graft effects on four key elementary processes of SCI wound healing: cell-scaffold interactions, NSC survival and differentiation, axonal elongation, and astrogliosis. A significant fraction of grafted scaffolds remained non-degraded at the lesion site at 6 weeks post injury, in agreement with the reported 3-week in-vivo degradation half-life of PCS[27]. In contrast to cell-free scaffolds, NSC-seeded scaffolds made firm contact with the surrounding tissue (Fig. 4c, d) and no void spaces were observed either inside the graft or at the graft–tissue interface. Extensive scaffold contact with the surrounding tissue (a pattern observed in PCS-induced regeneration in skin and peripheral nerves[25,28]) can facilitate interactions of host neurons with grafted cells or the scaffold itself.

A major finding of our study is that PCS grafts safely delivered NSCs at SCI lesion sites, where they supported NSC neuronal differentiation and functional integration with the surrounding tissue. Delivered NSCs were confined within the lesion site as evident by the high density of $BrdU^+$ cells ($1.19 \pm 0.14 \times 10^6$ $BrdU^+$ cells/μl.) observed inside the non-degraded scaffold 6 weeks post injury (Fig. 6a). Several studies have reported safety concerns regarding the formation of ectopic colonies when NSC suspensions are delivered at lesion sites via a syringe[40]. No ectopic colonies were observed in this study within 1 mm from the lesion site, possibly because NSC delivery via PCS avoids applying high pressure to tiny suspension volumes and does not suffer from NSC suspension leak away from the lesion site (during grafting, NSCs adhere robustly to the surrounding PCS). Furthermore, several $BrdU^+$ nuclei were observed within 200 μm away from the approximate lesion boundary. We hypothesize that the porous nature of PCS and the robust PCS-tissue contact discussed above, facilitates NSC migration into the surrounding tissue, which can greatly enhance the functional integration of NSC-derived cells with the surrounding tissue. A significant fraction of $BrdU^+$ cells double-stained either for Tuj1 ($22.9 \pm 2.4\%$) or for GFAP ($6.0 \pm 1.4\%$), suggesting that seeded NSCs managed to differentiate towards both neurons and astrocytes in vivo (Fig. 6b) inside PCS in the harsh conditions of a SCI site. Immunolabeling for markers relevant to neurotransmitter expression revealed the presence of $Vglut1^+$ synapses of excitatory glutamatergic neurons, dopaminergic neurons and inhibitory GABAergic neurons inside the scaffold (visualized by SHE; Fig. 6d-e and Supplementary Figs. 11 and 12). Verification of the nature of NSC-derived $BrdU^+$ neurons was more challenging, as very few neurons triple stained for BrdU, Tuj1, and one of the markers utilized (Vglut1, TH, GAD65/67). Further research is required to trace the nature of the observed NSC-derived $Tuj1^+$ cells and their functional integration with the surrounding spinal cord tissue.

In agreement with our in vitro observations, NSC-seeded PCS grafts proved to be a permissible substrate for axonal elongation in vivo. Animals treated with grafts had significantly more $L1^+$ staining elongating axons at the lesion site compared with animals of the crush group at 6 and 9 weeks post injury (Fig. 5a-d). In the scaffold + NSC group, large numbers of $L1^+$ axons were observed inside the graft, whereas several $L1^+$ axons crossed the approximate lesion boundary (Fig. 5c). By facilitating axonal growth at the lesion site, NSC-seeded PCS can potentially enhance the functional integration of NSC-derived neurons with neurons of the surrounding spinal cord tissue. Further research is required to trace the origin of the observed $L1^+$ axons and verify whether NSC-derived neurons inside PCS grafts formed synapses with axons originating from the surrounding tissue. Although collagen I is not a component of spinal cord extracellular matrix and is associated with scar, this study provides evidence that primary neurons, NSCs, and NSC-derived neuronal cells adhered well to PCS, and that neurons can grow long axons on scaffold struts both in vitro (Fig. 1d-f, 2d, f, and 3d, and Supplementary Fig. 2) and in vivo (Fig. 5a-c and 6b-e, and Supplementary Figs. 11 and 12), in agreement with previous reports[21,41].

Finally, NSC-seeded PCS significantly reduced astrogliosis, a major barrier of axonal elongation. Significantly less GFAP staining was observed around the lesion boundary in the scaffold + NSC group compared with the crush animal group 6 weeks post injury (Fig. 5e, f), in agreement with reports of reduced astrogliosis in rat SCI models treated with cell-PCS[16]. Second harmonic imaging of collagen fibers revealed the presence of several collagen scar fibers at the lesion boundaries but few inside the remaining scaffold (Supplementary Fig. 10). Collagenous scar is a hallmark of failed regeneration in adult organs[28] and a consequence of increased astrogliosis. Furthermore, IBA1 staining revealed that the scaffold did not manage to significantly decrease microgliosis; however, it also did not exacerbate the inflammatory response at the lesion (Supplementary Fig. 9b).

The major implication of our findings is to suggest that a new generation of NSC treatments for SCI can be developed based on PCS, similar to FDA-approved scaffolds already utilized in the clinical practice of induced regeneration in severe skin and peripheral nerve wounds. Compared with NSC grafts that utilize hydrogels[9–11,13,21], SCI grafts based on PCS offer several advantages: first, PCS provide both effective spatial confinement of NSCs and easy migration of NSCs into the surrounding tissue. Second, PCS physicochemical parameters (pore structure, chemical composition, and cross-linking) can be easily tuned to better modulate specific SCI pathophysiological processes (including astrogliosis and wound contraction[22,28]), enhance axonal elongation in challenging tracts, and improve NSC differentiation and functional integration[23]. Emerging bioengineering technologies (e.g., 3D printing, microfabrication, and chemical functionalization) can further customize graft structure to better match the structure of the surrounding neural tissue or adapt to the needs of individual patients[23,42–44]. Third, the long in-vivo degradation half-life of PCS enables elegant manipulation of seeded NSCs prior to graft implantation. Such manipulations can use emerging protocols for directing NSCs towards specific lineages[45] in order to enhance graft effects on specific spinal cord tracts[11,44]. Finally, PCS-based SCI grafts could greatly benefit the clinical translation of emerging NSC technologies for SCI (derivation of safe patient-specific NSCs and optimization of NSC manipulations) by exploiting the extensive regulatory and clinical experience of existing FDA-approved PCS grafts.

METHODS

Scaffold fabrication

Porous collagen and collagen-GAG scaffold sheets were fabricated as described previously[26], by lyophilizing a 5 mg/ml microfibrillar collagen I suspension or a 5 mg/ml microfibrillar collagen I suspension supplemented with 0.44 mg/ml Ch6S, respectively. The resulting 2.5 mm-thick dry sheets were cross-linked via dehydro-thermal treatment (105 °C, 50 mTorr, 24 h). Scaffold structure was verified by SEM. Cylindrical scaffold samples (3 mm diameter) were cut using a biopsy punch.

Primary neural cell isolation and culture

Animal experimentation protocols 27300 and 262272 were approved by the Veterinary Directorate of the Region of Crete and FORTH ethics

committee. Experiments were carried out in compliance with EU guidelines 2010/63/EU. Reagents were obtained from Thermo Fisher Scientific unless otherwise noted. C57/BL6 mice were maintained on a 12 h light/dark cycle with ad libitum access to food and water.

For NSC isolation, pregnant mice (gestational day 13.5) were killed via cervical dislocation, embryos were carefully removed and washed gently in HBSS + P/S [Hanks' balanced salt solution (HBSS), 5% penicillin/streptomycin], and NSCs were isolated by mechanically dissociating cortical hemispheres in NSC complete medium [Dulbecco's modified Eagle's medium (DMEM)/F12 (Sigma), N2 supplement, 2 mM L-glutamine, 0.6% D-glucose, 100 µg/ml primocin (InvivoGen), 20 ng/ml FGF2 (R&D), 20 ng/ml EGF (R&D)]. NSCs (2.5×10^5) in 5 ml complete medium were seeded in T25 flasks. One milliliter of fresh medium was added every other day. Neurospheres formed within 2 days. Neurospheres were dissociated by accutase (Sigma) at day 4 or 5. Dissociated NSCs were either passaged or used for experiments (passage 3–8).

For DRG cell isolation, ~200 ganglia from 8 embryos settled for 5 min in HBSS + P/S medium on ice inside sterile 1.5 ml tubes, were incubated in 0.25% trypsin at 37 °C for 5 min prior to dissociation into single neurons by pipetting using a fire-polished Pasteur pipette in DRG medium (RPMI, 10% fetal bovine serum (FBS), 1% P/S, 100 ng/ml NGF (Millipore)). Cells from three dissociated ganglia were seeded in 3 mm-diameter scaffold samples. DRG medium was changed every other day until day 7.

Cell culture inside PCS or on coverslips

Three-dimensional NSC culture utilized PCS samples (3 mm diameter and 2.5 mm height) maintained as floating sponges in 48-well plates. The day before cell seeding, wells were coated by air-drying 0.1% agarose overnight inside a sterile hood. NSCs were seeded in each scaffold by first placing the scaffold on agarose-coated wells, pipetting a 10 µl drop containing 3×10^4 NSCs on the scaffold, incubating at 37 °C for 10 min, and finally adding 300 µl NSC complete medium. Two-dimensional NSC culture took place by plating 2.5×10^4 NSCs on sterile coverslips coated with PDL and laminin (Sigma). In survival and proliferation experiments, NSCs were grown in complete medium. NSCs were fixed for immunocytochemistry at 3, 5, 7, and 10 DIV. In differentiation experiments, NSCs were grown in complete medium for 3 days and then in Neurocult differentiation medium (Stem Cell Technologies) for 4 more days, fixed, stained, and imaged. For each experimental treatment, at least three scaffold samples were quantified.

Immunocytochemistry, confocal microscopy, and cytometry

At indicated days, NSCs grown on coverslips or inside porous scaffolds were washed twice in phosphate-buffered saline (PBS) and fixed by 4% paraformaldehyde (PFA) in PBS for 15 min at 4 °C. Samples were washed in PBS, blocked in 5% bovine serum albumin (BSA) in PBST (0.3% Triton X-100 in PBS) at room temperature for 1 h, incubated in primary antibodies (Ki67: 1:500 Abcam ab16667; β3 tubulin: 1:1000 Biolegend MMS-453P (Tuj1 clone); Olig2: 1:500 Novus NBP1-28667; GFAP: 1:1000 Millipore AB5541; Neurofilament heavy chain: 1:1000 Abcam ab4680; Synaptophysin: 1:500 Abcam ab7837; and Nestin: 1:1000 Novus NB100-1604) diluted in PBST overnight at 4 °C, washed twice in PBS, incubated in fluorophore-conjugated secondary antibodies (Thermo) diluted 1:1000 in PBST for 1 h at room temperature, washed twice in PBS, and counterstained with 4′,6-diamidino-2-phenylindole (DAPI). In viability experiments, samples were also counterstained with 1 µM propidium iodide.

Fluorescently labeled samples were imaged in a Leica TCS SP8 inverted confocal microscope using a ×20 oil-immersion objective lens (Leica Microsystems, Wetzlar, Germany). Three *z*-stacks per sample (1 µm spacing) were acquired. Images were processed by custom MATLAB software (Mathworks, Natick MA; available upon request) that consisted of three steps as follows: (1) identification of cell nuclei at each plane by h-min morphological filtering on the DAPI channel, followed by user inspection and correction. (2) Identification of unique cell nuclei over the complete *z*-stack based on the localization of nuclei centroids and nuclei size statistics. (3) Single-cell calculation of markers of interest (Ki67 and propidium iodide). Threshold levels, chosen manually by two expert users, were applied to all images. In differentiation experiments, $GFAP^+$, $Tuj1^+$, and $Olig2^+$ cells were counted manually based on confocal *z*-stacks due to staining pattern complexity. For the assessment of neurite branching, the number of dendrites emerging from the main neuronal axon were counted manually. Neuron axon length was calculated by tracing 30 axons stack-by-stack using Fiji software. For the assessment of BrdU/Tuj1/GFAP double labeling, three confocal stacks (~$129 \times 129 \times 6$ µm each) per animal ($n = 5$ animals) were acquired within the scaffold. Cell nuclei were counted based on distinct DAPI objects. Cell density (cells/mm^3) was calculated based on the volume of the acquired *z*-stack. $Tuj1^+/BrdU^+$ neurons or $GFAP^+/BrdU^+$ astrocytes were counted manually based on $BrdU^+/DAPI^+$ nuclei surrounded by Tuj1 or GFAP staining.

Scanning electron microscopy

All steps took place at 4 °C. Cell-seeded scaffolds were washed twice in 0.1 M sodium cacodylate buffer (SCB) for 15 min, fixed in 2% glutaraldehyde, 2% formaldehyde in 1% SCB for 1 h, washed twice in 1% SCB for 15 min, and dehydrated in serial ethanol solutions. Samples were sputter-coated by a 10 nm-thick gold layer (Humme Technics, Inc., Alexandria, VA, USA) and imaged in a JEOL 7000 scanning electron microscope (JEOL, Tokyo, Japan) at 15 kV voltage.

Electrophysiology

Field recordings were performed on NSC neurospheres grown in 2D, 3D-C, and 3D-CG cultures at 3, 5, and 7 DIV. Artificial cerebrospinal fluid (125 mM NaCl, 7.5 mM KCl, 26 mM $NaHCO_3$, 3 mM $CaCl_2$, 10 mM glucose pH 7.4, 315 mOsm/l) oxygenated with 95% O_2 was continuously perfused during recordings. An extracellular recording electrode filled with 2 M NaCl was placed inside neurospheres identified via DIC bright-field microscopy using an Axioskop 2FS microscope (Carl Zeiss, Inc., Jena, Germany). Voltage responses were amplified by a BVC-700A amplifier (Dagan Corp., Minneapolis, MN, USA) and digitized by a ITC-18 board (Instrutech, Inc.) on a PC. Data were acquired and analyzed using custom scripts in IgorPro software (Wavemetrics, Inc., Lake Oswego, OR, USA). Spontaneous field excitatory postsynaptic potential traces were acquired for 20 min before the addition of bicuculine (Tocris) and for 30 min after. Spontaneous events were identified as voltage responses larger than four times the SD σ_b of the background signal. The average number of spontaneous events for each sample was calculated from traces covering the last 5 min before the addition of bicuculine and the last 5 min of the 30 min recording period after the addition of bicuculline.

Calcium imaging

NSCs were seeded in collagen or collagen-GAG scaffold samples and grown for 5 or 7 days in NSC complete medium. Samples were stained by 4 µM Fluo3 in NSC complete medium for 45 min, washed twice, placed in complete medium supplemented with 7.5 mM KCl on a glass-bottom petri dish, and imaged in a SP8 confocal microscope or in a custom-built multiphoton microscope based on an Axio Observer Z1 (Carl Zeiss, Inc.) employing a Pharos-SP fs oscillator (Light Conversion, Vilnius, Lithuania) at 1030 nm, 70–90 fs, 76 MHz. Confocal images were acquired by a ×40/1.2NA water-immersion objective (300 µs pixel dwell time, 2 fps, 256×256 pixels). Multiphoton images were acquired by a 20×/0.8NA objective (320 µs pixel dwell time, 3 fps, 250×250 pixels). Videos were processed by custom MATLAB software. Regions of interest (ROIs) corresponding to cells where Ca^{+2} oscillations took place were identified manually. For each ROI, the time profile of Fluo3 emission was analyzed in order to measure event duration (FWHM) and mean inter-event periodicity.

Spinal cord injury model

The week prior to injury, mice (male C57/BL6, 1.5–2 months old) settled down in the animal facility and walked through the ladder to become familiarized. Three days prior to injury, 3×10^4 cells (NSCs in the "scaffold-NSC" group and NIH-3T3 in the "scaffold-NIH-3T3" group) were seeded into $1 \times 1 \times 1.5$ mm collagen scaffold samples in medium (complete NSC medium for NSCs, DMEM supplemented with FBS, and pen/strep for NIH-3T3). Starting 2 days prior to injury and repeating once every 12 h, cell-seeded scaffolds were pulsed with 10 nM BrdU. Prior to implantation, grafts were washed for 30 min in PBS.

All surfaces, tools, and instruments utilized in the following procedure had been sterilized carefully. Before anesthesia, a drop of metacam was introduced per os. Mice were anesthetized by 2.5:1 isoflurane:oxygen mix inhalation for 5 min in a scavenger box until breathing slowed down. After verifying the absence of paw reflexes, each mouse was shaved in the level of the humpback and the exposed skin was disinfected with Hibiscrub. Each mouse was then transferred on a heat-pad, ophthalmic ointment was applied to avoid eye dryness and 2:1 isoflurane:oxygen mix was applied to maintain deep anesthesia via a mask. A skin incision was made from the

base of the humpback until the higher point of the rib cage, and exposed muscles were carefully torn. After removing surrounding ligaments, the bone of T10 vertebra was removed and an incision was made in the dura matter above the T13 segment. The dorsal column crush was applied by inserting Dumont #5 fine forceps 1 mm deep into the white matter and keeping them closed for 10 sec. This step was repeated once, to create an ~1 mm^3 pocket (lesion). In the crush animal group, the lesion was not grafted. In the scaffold-only group, a cell-free collagen scaffold was placed in the pocket. In scaffold + NSC and scaffold + NIH-3T3 groups, a cell-seeded collagen scaffold was placed in the pocket. In all animal groups, the exposed spinal cord was covered by a hemostatic sponge (Geistlich Bio-Gide) to protect the exposed spinal cord tissue, the muscles and skin were sutured, the skin was disinfected, and metacam was provided for the next 3 days.

Functional evaluation of locomotion recovery via the ladder walking assay

Mice walked along a horizontal ladder consisting of two parallel 100 × 25 cm acrylic sheets connected by ø2 mm aluminum rods spaced ~1 cm. The ladder was elevated at cage height above ground. Animals were trained to cross the ladder from a neutral cage to their home cage in the same direction. Before each session, mice crossed the ladder twice for habituation. Each animal run the assay five times per session. Videos of walking mice were analyzed in frame-by-frame by two researchers blind to the condition (group, week) of the animal analyzed to identify locomotion errors, defined as steps where a hind limb missed or slipped off or was misplaced on a rod. Each fault was classified using a 7-category scale (0: total miss, 1: deep slip, 2: slight sleep, 3: replacement, 4: correction, 5: partial placement, 6: correct placement) as described previously[46]. Locomotion performance was described via the fault rate (fraction of steps classified in categories 0–5) or via the Foot Fault Score[46]. The last step before and the first step after a stop were excluded; only consecutive steps were included in the analysis. Only animals where statistically significant (fault step rate > 15%) locomotion deterioration was observed 1 day or 1 week post injury were considered for further ladder assay analysis and histological evaluation.

Histological evaluation of recovery after SCI

Six, 9, or 12 weeks post SCI, mice were deeply anesthetized using 2.5:1 isoflurane:oxygen mix and transcardially perfused with ice-cold heparinized (10 U/mL) saline followed by 4% PFA in PBS. Spinal cords were dissected, post-fixed in 4% PFA at 4 °C for 1 h, washed in PBS, and immersed in 30% sucrose solution in 0.1 M PB for 24 h at 4 °C. The 2 mm-long part of the spinal cord tissue centered around the lesion was frozen in isopentane at −70 °C and 20 µm-thick parasagittal sections were cut in superfrost slides.

For histological analysis, slides were placed in ice-cold acetone for 5 min, air-dried for 10 min in laminar flow, washed twice in PBS, fixed for 15 min in 4% PFA in PBS at 4 °C, washed in PBS, blocked in PBST (0.3% Triton X-100 in PBS) supplemented with 5% BSA at room temperature for 1 h, and incubated in primary antibodies (L1: 1:000 rabbit polyclonal antibody; GFAP: 1:1000 Millipore AB5541; BrdU: 1:200 Abcam ab6326; β3 tubulin: 1:1000 Biolegend MMS-453P (Tuj1 clone); Neurofilament heavy chain: 1:1000 Abcam ab4680; IBA1: 1:1000 Wako 019-19741; Vglut1: 1:400 Synaptic systems 135304; Tyrosine Hydroxylase: 1:1000 Abcam ab6211; GAD65/67: 1:1000 Abcam ab11070-50; and Collagen I: 1:100 Novus Biologicals NB600-1408) diluted in PBST overnight at 4 °C, washed twice with PBS, incubated with fluorophore-conjugated secondary antibodies (Thermo) diluted 1:1000 in PBST for 1 h at room temperature, washed twice in PBS, mounted, and counterstained with DAPI. For $BrdU^+$ quantification, sections were incubated in 2 N HCl at 37 °C for 30 min, rinsed in 0.1 M sodium tetraborate pH 8.5 for 10 min, and rinsed twice in PBS before blocking. Stained sections were imaged in a Leica TCS SP8 inverted confocal microscope.

Immunostained parasagittal sections were imaged at the epicenter, caudally and rostrally to the lesion. Positive staining (L1, GFAP, or IBA1) was defined by thresholding using a common value chosen by an expert user. Measurements from four randomly selected fields were averaged per section. Results from six sections were averaged per animal. Axonal elongation was quantified by calculating the percentage of pixels that stained positively for L1 in the dorsal column in the immediate proximity (caudally and rostrally) of the lesion boundary and in the lesion epicenter. Care was taken to avoid the background L1 staining observed in the spared tissue, mostly in the gray matter (Supplementary Fig. 7). Astrogliosis was quantified by calculating the percentage of pixels that stained positively for GFAP immediately rostrally and caudally to the lesion boundary. Microgliosis was quantified by calculating the percentage of pixels that stained positively for IBA1 in the lesion epicenter. All pixel measurements were normalized to the mean measurement of the uninjured control animal group.

For visualization, acquired images were processed as follows: (1) for each channel (corresponding to a specific fluorophore or SHE), the mean of the background signal (calculated in a region where no signal is expected) was subtracted from the signal intensity. (2) Channel intensity was then scaled linearly with respect to a common intensity value (chosen usually as 90–98% of peak intensity).

Statistical analysis

Experimental data are expressed as mean ± SEM. Statistical analysis was performed using the Prism software (Graphpad, La Jolla, CA, USA). Statistical significance was assessed by unpaired two-tailed Student's *t*-tests (two-group comparisons) or analysis of variance (ANOVA) followed by Tukey's or Bonferroni's post-hoc test (multi-group comparisons) assuming a statistical significance level of 0.05. To minimize type II error, statistical comparison of locomotion performance against the uninjured control group was assessed by unpaired two-tailed Student's t-tests assuming a significance level of 0.1. For in-vivo experiments, the sample size required was estimated based on the number of groups and the expected effect size using the G*power software (Düsseldorf, Germany). Due to the lack of published data on experimental variability in dorsal column crush injuries treated with biomaterial grafts, initially power was chosen at 80%.

Reporting summary

Further information on research design is available in the Nature Research Reporting Summary linked to this article.

DATA AVAILABILITY

All relevant data supporting the findings of this study are available within the paper, its supplementary information and from the corresponding authors upon reasonable request.

Received: 16 August 2018; Accepted: 29 April 2020;
Published online: 15 June 2020

REFERENCES

1. Carlson, G. D. et al. Early time-dependent decompression for spinal cord injury: vascular mechanisms of recovery. *J. Neurotrauma* **14**, 951–962 (2009).
2. Evaniew, N. et al. Methylprednisolone for the treatment of patients with acute spinal cord injuries: a systematic review and meta-analysis. *J. Neurotrauma* **33**, 468–481 (2016).
3. Silva, N. A., Sousa, N., Reis, R. L. & Salgado, A. J. From basics to clinical: a comprehensive review on spinal cord injury. *Prog. Neurobiol.* **114**, 25–57 (2014).
4. O'Shea, T. M., Burda, J. E. & Sofroniew, M. V. Cell biology of spinal cord injury and repair. *J. Clin. Invest.* **127**, 3259–3270 (2017).
5. Schnell, L. & Schwab, M. E. Axonal regeneration in the rat spinal cord produced by an antibody against myelin-associated neurite growth inhibitors. *Nature* **343**, 269–272 (1990).
6. Bradbury, E. J. et al. Chondroitinase ABC promotes functional recovery after spinal cord injury. *Nature* **416**, 636–640 (2002).
7. Assinck, P., Duncan, G. J., Hilton, B. J., Plemel, J. R. & Tetzlaffm, W. Cell transplantation therapy for spinal cord injury. *Nat. Neurosci.* **20**, 637–647 (2017).
8. Lu, P., Jones, L. L., Snyder, E. Y. & Tuszynski, M. H. Neural stem cells constitutively secrete neurotrophic factors and promote extensive host axonal growth after spinal cord injury. *Exp. Neurol.* **181**, 115–129 (2003).
9. Lu, P. et al. Long-distance growth and connectivity of neural stem cells after severe spinal cord injury. *Cell* **150**, 1264–1273 (2012).
10. Kadoya, K. et al. Spinal cord reconstitution with homologous neural grafts enables robust corticospinal regeneration. *Nat. Med.* **22**, 479–487 (2016).
11. Rosenzweig, E. S. et al. Restorative effects of human neural stem cell grafts on the primate spinal cord. *Nat. Med.* **24**, 484–490 (2018).
12. Jin, Y., Bouyer, J., Shumsky, J. S., Haas, C. & Fischer, I. Transplantation of neural progenitor cells in chronic spinal cord injury. *Neuroscience* **320**, 69–82 (2016).

13. Curtis, E. et al. A first-in-human, phase I study of neural stem cell transplantation for chronic spinal cord injury. *Cell Stem Cell* **22**, 941–950 (2018).
14. Cao, Q. et al. Pluripotent stem cells engrafted into the normal or lesioned adult rat spinal cord are restricted to a glial lineage. *Exp. Neurol.* **167**, 48–58 (2001).
15. Zhu, Y., Uezono, N., Yasui, T. & Nakashima, K. Neural stem cell therapy aiming at better functional recovery after spinal cord injury. *Dev. Dyn.* **247**, 75–84 (2018).
16. Spilker, M. H. et al. The effects of tubulation on healing and scar formation after transection of the adult rat spinal cord. *Restor. Neurol. Neurosci.* **18**, 23–38 (2001).
17. Teng, Y. D. et al. Functional recovery following traumatic spinal cord injury mediated by a unique polymer scaffold seeded with neural stem cells. *Proc. Natl Acad. Sci. USA.* **99**, 3024–3029 (2002).
18. Yoshii, S. et al. Restoration of function after spinal cord transection using a collagen bridge. *J. Biomed. Mater. Res.* **70**, 569e75 (2004).
19. Cholas, R. H., Hsu, H. P. & Spector, M. The reparative response to cross-linked collagen-based scaffolds in a rat spinal cord gap model. *Biomaterials* **33**, 2050–2059 (2012).
20. Okada, S. The pathophysiological role of acute inflammation after spinal cord injury. *Inflamm. Regen.* **36**, 20 (2016).
21. Bonner, J. F. et al. Grafted neural progenitors integrate and restore synaptic connectivity across the injured spinal cord. *J. Neurosci.* **31**, 4675–4686 (2011).
22. Yannas, I. V., Burke, J. F., Orgill, D. P. & Skrabut, E. M. Wound tissue can utilize a polymeric template to synthesize a functional extension of skin. *Science* **215**, 174–176 (1982).
23. Li, X. et al. Promotion of neuronal differentiation of neural progenitor cells by using EGFR antibody functionalized collagen scaffolds for spinal cord injury repair. *Biomaterials* **34**, 5107–5116 (2013).
24. Skop, N. B., Calderon, F., Cho, C. H., Gandhi, C. D. & Levison, S. W. Improvements in biomaterial matrices for neural precursor cell transplantation. *Mol. Cell Ther.* **2**, 19 (2014).
25. Yannas, I. V., Lee, E., Orgill, D. P., Skrabut, E. M. & Murphy, G. F. Synthesis and characterization of a model extracellular matrix which induces partial regeneration of adult mammalian skin. *Proc. Natl Acad. Sci. USA* **86**, 933–937 (1989).
26. O'Brien, F. J., Harley, B. A., Yannas, I. V. & Gibson, L. Influence of freezing rate on pore structure in freeze-dried collagen-GAG scaffolds. *Biomaterials* **25**, 1077–1086 (2004).
27. Yannas, I. V., Tzeranis, D. S., Harley, B. A. & So, P. T. Biologically active collagen-based scaffolds: advances in processing and characterization. *Philos. Trans. A Math. Phys. Eng. Sci.* **368**, 2123–2139 (2010).
28. Soller, E. C., Tzeranis, D. S., Miu, K., So, P. T. & Yannas, I. V. Common features of optimal collagen scaffolds that disrupt wound contraction and enhance regeneration both in peripheral nerves and in skin. *Biomaterials* **33**, 4783–4791 (2012).
29. Reynolds, B. A. & Rietze, R. L. Neural stem cells and neurospheres–re-evaluating the relationship. *Nat. Methods* **2**, 333–336 (2005).
30. Ge, S. et al. GABA regulates synaptic integration of newly generated neurons in the adult brain. *Nature* **439**, 589–593 (2006).
31. Kanagal, S. G. & Muir, G. D. Bilateral dorsal funicular lesions alter sensorimotor behaviour in rats. *Exp. Neurol.* **205**, 513–524 (2007).
32. Gulino, R., Dimartino, M., Casabona, A., Lombardo, S. A. & Perciavalle, V. Synaptic plasticity modulates the spontaneous recovery of locomotion after spinal cord hemisection. *Neurosci. Res.* **57**, 148–156 (2007).
33. Faissner, A. & Steindler, D. Boundaries and inhibitory molecules in developing neural tissues. *Glia* **13**, 233–254 (1995).
34. von Holst, A., Sirko, S. & Faissner, A. The unique 473HD-chondroitinsulfate epitope is expressed by radial glia and involved in neural precursor cell proliferation. *J. Neurosci.* **26**, 4082–4094 (2006).
35. Kazanis, I. & ffrench-Constant, C. Extracellular matrix and the neural stem cell niche. *Dev. Neurobiol.* **71**, 1006–1017 (2011).
36. Pizzorusso, T. et al. Reactivation of ocular dominance plasticity in the adult visual cortex. *Science* **298**, 1248–1251 (2002).
37. Ganguly, K. et al. GABA itself promotes the developmental switch of neuronal GABAergic responses from excitation to inhibition. *Cell* **105**, 521–532 (2001).
38. Rhodes, K. E. & Fawcett, J. W. Chondroitin sulphate proteoglycans: preventing plasticity or protecting the CNS? *J. Anat.* **204**, 33–48 (2004).
39. Steward, O., Zheng, B., Ho, C., Anderson, K. & Tessier-Lavigne, M. The dorsolateral corticospinal tract in mice: an alternative route for corticospinal input to caudal segments following dorsal column lesions. *J. Comp. Neurol.* **472**, 463–477 (2004).
40. Steward, O., Sharp, K. G. & Matsudaira Yee, K. Long-distance migration and colonization of transplanted neural stem cells. *Cell* **156**, 385–387 (2014).
41. Carbonetto, S., Gruver, M. M. & Turner, D. C. Nerve fiber growth in culture on fibronectin, collagen, and glycosaminoglycan substrates. *J. Neurosci.* **3**, 2324–2335 (1983).
42. Kim, H., Zahir, T., Tator, C. H. & Shoichet, M. S. Effects of dibutyryl cyclic-AMP on survival and neuronal differentiation of neural stem/progenitor cells transplanted into spinal cord injured rats. *PLoS ONE* **6**, e21744 (2011).
43. Khademhosseini, A. & Peppas, N. A. Micro- and nanoengineering of biomaterials for healthcare applications. *Adv. Health. Mater.* **2**, 10–12 (2013).
44. Koffler, J. et al. Biomimetic 3D-printed scaffolds for spinal cord injury repair. *Nat. Med.* **25**, 263–269 (2019).
45. Dulin, J. N. et al. Injured adult motor and sensory axons regenerate into appropriate organotypic domains of neural progenitor grafts. *Nat. Commun.* **9**, 84 (2018).
46. Metz, G. A. & Wishaw, I. Q. Cortical and subcortical lesions impair skilled walking in the ladder run walking test: a new task to evaluate fore- and hildlimb stepping, placing, and co-ordination. *J. Neurosci. Methods* **115**, 169–179 (2002).

ACKNOWLEDGEMENTS

We thank Professor J. Fawcett and Dr. S. Soleman (Cambridge University, UK) for providing training on the SCI mouse model, Professor F. Rathjen (Max-Delbrück-Centrum für Molekulare Medizin, Germany), and Professor D. Karagogeos (University of Crete) for the L1 antibody, M. Nikou for assistance in Ca^{+2} imaging, F. Moschogiannaki for assistance in scaffold fabrication, and X. Mallios, M. Kyriakidou, M. Michaelidou, and E. Droulou for quantifying Horizontal Ladder Walking Assay videos. We thank the Non-linear microscopy lab of IESL-FORTH and especially Dr M. Mari for conducting SHE and MPEF imaging. This work was supported by the Hellenic General Secretariat of Research and Technology ERC01 grant "3D NEUROSCAFFOLDS" (ERC National Initiative) to A.G., the People Programme (Marie Curie Actions) of European Union Horizon 2020 (REA DLV-658850) to D.S.T., and by the Hellenic Foundation for Research and Innovation (HFRI) and the General Secretariat for Research and Technology (GSRT) under grant agreement number 1635 to D.S.T.

AUTHOR CONTRIBUTIONS

A.K., D.S.T., and K.K. (co-first authors) designed and conducted experiments, analyzed data, and wrote the manuscript. K.S., K.G., S.P., and E.B. conducted experiments and analyzed data. I.V.Y. provided critical materials and consultation. E.S. provided facilities and consultation. I.C. and A.G. designed experiments, supervised project, and wrote the manuscript.

COMPETING INTERESTS

Prof. I.V. Yannas has participated in the founding of Integra LifeSciences, Plainsboro, NJ. He currently has no financial connection with the company and owns no stock of Integra LifeSciences. The rest of the authors declare that there are no competing interests.

ADDITIONAL INFORMATION

Supplementary information is available for this paper at https://doi.org/10.1038/s41536-020-0097-0.

Correspondence and requests for materials should be addressed to A.G.

Reprints and permission information is available at http://www.nature.com/reprints

Publisher's note Springer Nature remains neutral with regard to jurisdictional claims in published maps and institutional affiliations.

Open Access This article is licensed under a Creative Commons Attribution 4.0 International License, which permits use, sharing, adaptation, distribution and reproduction in any medium or format, as long as you give appropriate credit to the original author(s) and the source, provide a link to the Creative Commons license, and indicate if changes were made. The images or other third party material in this article are included in the article's Creative Commons license, unless indicated otherwise in a credit line to the material. If material is not included in the article's Creative Commons license and your intended use is not permitted by statutory regulation or exceeds the permitted use, you will need to obtain permission directly from the copyright holder. To view a copy of this license, visit http://creativecommons.org/licenses/by/4.0/.

© The Author(s) 2020